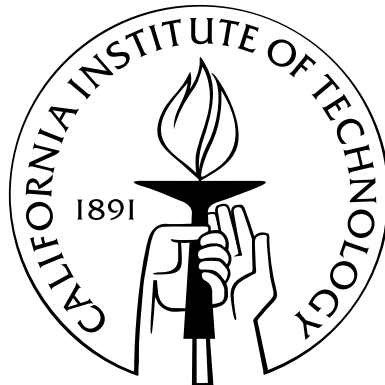


Measurement of the neutron beta decay asymmetry using ultracold neutrons

Thesis by
Michael Praetorius Mendenhall

In Partial Fulfillment of the Requirements
for the Degree of
Doctor of Philosophy



California Institute of Technology
Pasadena, California

2014
(Defended December 4, 2013)



Michael Praetorius Mendenhall, 2014

this work is released into the public domain by the author,
with all copyrights waived to the extent allowed by law
as per CC0 1.0 Universal Public Domain Dedication
<https://creativecommons.org/publicdomain/zero/1.0/>

in memory of Winifred Moehle Mendenhall (1926-2011)

Acknowledgements

The research presented in this dissertation is the product of a wide-ranging collaboration. I am grateful for many people; not only for their contributions to scientific knowledge, but also for my personal benefit from the privilege of working alongside them. The mentorship and guidance of these colleagues has been the best material from which my graduate education could be made.

I would especially like to acknowledge the Kellogg Radiation Laboratory research group at Caltech, including my advisor Brad Filippone, (former) postdocs Jianglai Liu and Brad Plaster; Bob Carr, Pat Huber, and fellow graduate students Kevin Hickerson and Riccardo Schmid. Also, the graduate students from collaborating institutions, with whom I shared many long night shifts on the experiment: Robbie Pattie, Adam Holley, Leah Broussard, Raymond Rios, Brittney VornDick, and Bryan Zeck. The Los Alamos researchers and staff: Andy Saunders, Mark Makela, Takeyasu Ito, Chris Morris, Susan Seestrom, Scott Currie; and Albert Young at NCSU.

Thanks also to my parents, Marcus and Cheryl Mendenhall, who preceded me through the experience of graduate studies at Caltech; and to my church family in Pasadena at Trinity Lutheran.

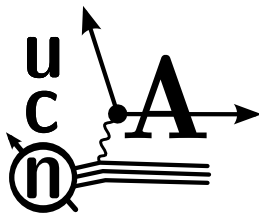


Figure 1: Logo of the UCNA Collaboration.

Abstract

The free neutron beta decay correlation A_0 between neutron polarization and electron emission direction provides the strongest constraint on the ratio $\lambda = g_A/g_V$ of the Axial-vector to Vector coupling constants in Weak decay. In conjunction with the CKM Matrix element V_{ud} and the neutron lifetime τ_n , λ provides a test of Standard Model assumptions for the Weak interaction. Leading high-precision measurements of A_0 and τ_n in the 1995–2005 time period showed discrepancies with prior measurements and Standard Model predictions for the relationship between λ , τ_n , and V_{ud} . The UCNA experiment was developed to measure A_0 from decay of polarized ultracold neutrons (UCN), providing a complementary determination of λ with different systematic uncertainties from prior cold neutron beam experiments. This dissertation describes analysis of the dataset collected by UCNA in 2010, with emphasis on detector response calibrations and systematics. The UCNA measurement is placed in the context of the most recent τ_n results and cold neutron A_0 experiments.

Contents

Acknowledgements	iv
Abstract	v
Contents	vi
List of Figures	xiii
List of Tables	xvi
1 Historical context for neutron beta decay measurements	1
1.1 Development of Weak interactions theory	1
1.1.1 Beta decay	1
1.1.1.1 Fermi's decay theory	1
1.1.1.2 Konopinski-Uhlenbeck modification	2
1.1.1.3 What interaction form?	2
1.1.2 The Weak interaction	3
1.1.2.1 Universal Weak interaction	3
1.1.2.2 Parity-violating interaction terms	3
1.1.2.3 Decay correlations	4
1.1.2.4 $V - A$ structure	5
1.1.2.5 Conserved Vector Current hypothesis	6
1.1.2.6 Free neutron beta decay correlations	7
1.1.2.7 Induced couplings	8
1.1.2.8 Weak Magnetism	8
1.1.2.9 Second-class currents	8
1.1.2.10 Electromagnetic corrections	9
1.1.3 Connection to quark model	10
1.1.3.1 Quarks	10
1.1.3.2 Cabibbo mixing angle and the charm quark	11
1.1.3.3 CKM matrix and unitarity	11
1.1.4 Beta decay in the Standard Model	12
1.2 β -decay asymmetry experiments	12
1.2.1 Early A measurements at Argonne	13
1.2.2 High rate experiments with PERKEO at ILL	14

1.2.3	PNPI and ILL TPC measurements	14
1.2.4	PERKEO II	15
1.3	Ultracold neutrons	15
1.3.1	Slow neutron scattering	15
1.3.2	Ultracold neutrons	16
1.3.3	Early experimental UCN sources	17
1.3.4	High flux UCN turbine sources	17
1.3.5	LANL SD ₂ superthermal UCN source	18
1.4	The UCNA experiment	18
1.4.1	Initial development	18
1.4.2	Neutron lifetime discrepancy	18
1.4.3	2009 proof of principle result	19
1.4.4	2010 result	19
1.4.5	2013 result	20
2	UCNA experimental overview	21
2.1	Apparatus	21
2.1.1	UCN production	21
2.1.2	UCN transport	24
2.1.3	Polarization	25
2.1.4	β -decay spectrometer	26
2.1.5	Wirechambers	27
2.1.5.1	Wire planes	27
2.1.5.2	Gas volume	27
2.1.5.3	Wirechamber electronics	28
2.1.6	Scintillator calorimeters	29
2.1.6.1	PMT electronics	29
2.1.7	Auxiliary detectors	29
2.1.8	DAQ	30
2.1.8.1	Trigger	30
2.2	Data collection	33
2.2.1	Super-ratio asymmetry	33
2.2.2	Run sequence	33
2.2.2.1	Depolarization runs	34
2.2.2.2	Run lengths	35
2.2.3	Blinding	35

3	Calibrations overview	37
3.1	System response model	37
3.1.1	Inverse model	37
3.1.2	Energy variables	38
3.1.3	Scintillator response	39
3.1.4	Backscattering categorization	39
3.2	Calibrations approach	41
3.2.1	Interdependence and orthogonality	41
3.2.2	Iterative calibrations	42
3.3	Inverting the Response Model	43
3.3.1	E_{vis} from ADC	43
3.3.1.1	Individual PMT energy	43
3.3.1.2	Combining PMT results	43
3.3.2	Backscatter classification	43
3.3.2.1	Initial classification	44
3.3.2.2	Type II/III separation	44
3.3.3	E_{recon} from E_{vis}	46
3.4	Calibration data sources	47
3.4.1	Sealed sources	47
3.4.1.1	Conversion electrons	49
3.4.2	Activated Xenon	50
3.4.3	^{207}Bi gain monitoring pulser	52
3.4.4	Light Emitting Diode scans	52
3.4.4.1	LED system properties	53
3.4.4.2	LED in 2010 data	53
3.4.4.3	Post-2010 LED system	53
4	Simulation of spectrometer physics	54
4.1	Detector geometry	54
4.1.1	Components in detector geometry model	54
4.1.2	Irregularities	58
4.1.2.1	Wirechamber window bowing	58
4.1.2.2	Kevlar string fraying	58
4.1.2.3	Decay trap foil wrinkles	60
4.1.3	Calibration source foil	60
4.2	Magnetic field	61
4.2.1	Motion of electrons in a magnetic field	61
4.2.2	Spectrometer field in GEANT4 model	63
4.2.3	Simulating with 2010 measured field	63
4.3	Electric field	64
4.4	Physics list	65
4.5	Event generation	66
4.5.1	Neutron decay	66
4.5.2	Radioactive nuclides	66

4.5.2.1	Conversion electrons	66
4.5.2.2	Nuclear beta decays	67
4.5.2.3	Auger electrons	69
4.6	Track data reduction	70
4.6.1	Scintillator quenched energy	70
4.6.2	Detector hit positions	71
4.6.3	Entry/exit variables	72
4.7	MC Tuning	73
4.7.1	Production cuts	73
4.7.2	Dead layer	73
4.8	Simulation and Data	74
4.8.1	Matching simulations to data	74
4.8.1.1	Asymmetry weighting	74
4.8.1.2	Octet data “cloning”	75
4.8.2	MC/data agreement	75
4.8.2.1	Beta decay backscatter spectra	76
5	Scintillator calibration	77
5.1	PMT readout electronics calibration	77
5.1.1	PMT pedestals	77
5.1.1.1	Data selection	77
5.1.1.2	Data processing	77
5.1.1.3	Results	78
5.1.1.4	Response model pedestal terms	78
5.1.2	Scintillator event trigger	78
5.1.2.1	Independent trigger model	80
5.1.2.2	Single PMT average trigger probability	80
5.1.2.3	Shortcomings of independent trigger model	81
5.2	PMT gain stability	83
5.2.1	²⁰⁷ Bi pulser	84
5.2.1.1	Method	84
5.2.1.2	Results	85
5.2.2	Beta endpoint stabilization	85
5.2.2.1	Beta spectrum endpoint fitting for energy scale comparison	85
5.2.2.2	Fit sensitivity to energy resolution	87
5.2.2.3	Analytical approximation for spectrum smearing	89
5.3	Scintillator light transport	90
5.3.1	Mapping with activated xenon	90
5.3.1.1	Spectrum composition	91
5.3.1.2	Mapping method	91
5.3.2	Associated uncertainties	92
5.3.2.1	Statistics	92
5.3.2.2	Smearing correction	92
5.3.2.3	Energy dependent position reconstruction	94

5.3.2.4	Interpolation error	94
5.3.2.5	Coupling to wirechamber accuracy	94
5.4	PMT linearity and energy resolution	95
5.4.1	Data/simulation comparison principle	95
5.4.2	Spectrum feature fitting	96
5.4.3	2010 linearity curves	97
5.4.3.1	Energy calibration uncertainty envelope	98
5.4.4	Energy resolution	99
5.4.4.1	Energy resolution model	99
5.4.4.2	Energy resolution from calibration source peak data	100
5.4.4.3	Four-PMT crosstalk correlation	100
5.4.4.4	Energy resolution accuracy	101
5.5	PMT signal correlations	101
5.5.1	Underlying physics correlation	101
5.5.2	Extracting correlation from the data	101
5.5.3	Correlation contributions model	103
5.5.4	Measurement with LED data	104
5.5.4.1	LED mean output estimation	104
5.5.4.2	LED output width	105
5.5.4.3	Pedestal correlations	106
6	Wirechamber calibration	108
6.1	Wirechamber energy calibration	108
6.1.1	MC expectations	108
6.1.2	Calibrations plan	109
6.1.3	Pedestals	109
6.1.4	Total charge signal	110
6.1.5	Charge signal position dependence	112
6.1.6	Gain calibration	113
6.2	Software wirechamber trigger	116
6.2.1	Trigger cut possibilities	116
6.2.2	False negative effects	117
6.2.3	False positive effects	117
6.3	Position reconstruction	117
6.3.1	Overview	117
6.3.2	Input data	118
6.3.3	Initial position estimate	119
6.3.3.1	Parabola center	119
6.3.3.2	Adjusted Gaussian center	120
6.3.3.3	Direct Gaussian center	120
6.3.3.4	Pair and edge wires	121
6.3.4	Uniformity correction	121
6.3.4.1	Cathode relative gain normalization	121
6.3.4.2	Cathode segment uniformity	125

6.3.5	Localized position reconstruction quality	127
6.3.6	Towards a first-principles wirechamber response model	127
6.4	East-West position offsets	130
6.4.1	Offset measurement	130
6.4.2	Offset effects	131
7	Asymmetry extraction and uncertainties	132
7.1	Asymmetry calculation from data	132
7.1.1	Super-ratio asymmetry	132
7.1.1.1	Incorporation of backscatter data	134
7.1.2	Extracting A_0 from A_{SR}	135
7.1.2.1	Statistical weighting and energy window	136
7.1.2.2	Extracted A_0 , corrections, and uncertainties	136
7.1.2.3	Statistical sensitivity approximation	136
7.2	Polarization	137
7.2.1	Measurement procedure	138
7.2.2	2010 polarimetry results	138
7.2.3	Impact on asymmetry	139
7.3	Montecarlo Corrections	139
7.3.1	Extraction of MC corrections	140
7.3.2	Backscattering	140
7.3.2.1	Comparison to prior analyses	141
7.3.3	Angle and energy acceptance	141
7.3.4	Magnetic field	144
7.3.5	Wirechamber efficiency	145
7.3.6	Estimation of MC uncertainties	145
7.3.6.1	Comparison of analysis choices	146
7.4	Energy Calibration Systematics	147
7.4.1	Constant energy distortions	147
7.4.1.1	Common mode errors	147
7.4.1.2	Differential mode errors	148
7.4.1.3	2010 energy calibration uncertainty	148
7.4.2	Variable energy distortions	149
7.4.2.1	2010 gain fluctuation uncertainty	149
7.4.2.2	Pedestal fluctuation uncertainty	150
7.5	Backgrounds	150
7.5.1	Background effects on A	150
7.5.2	Avoiding background contributions	151
7.5.3	Ambient gamma ray background	151
7.5.4	Cosmic ray muon background	152
7.5.5	Subtracting residual background	154
7.5.5.1	Systematic uncertainty from background subtraction	155
7.5.6	Neutron-generated background	159
7.6	Theory contributions	162

7.6.1	Recoil order effects	164
7.6.1.1	Additional BSM terms	164
7.6.2	Radiative effects	165
7.7	2010 asymmetry extraction	165
7.7.1	Data selection cuts	165
7.7.1.1	Timing cuts	165
7.7.1.2	Position cuts	166
7.7.2	Extracted asymmetry	166
7.7.2.1	Blinding factor removal	166
7.7.2.2	Octet asymmetries	166
7.7.2.3	Complete dataset	166
7.7.2.4	Combined result	170
8	Conclusion	171
8.1	Looking behind	171
8.2	Looking ahead	171
8.2.1	UCNA 2011-2013 dataset	173
8.2.1.1	Polarimetry improvements	173
8.2.1.2	Reduction of MC correction uncertainties	173
8.2.1.3	Energy calibration	174
8.2.2	Next-generation decay measurements	174
8.2.3	Future UCN source prospects	174
A	Sealed source calibration radioisotopes	175
A.1	2010 conversion electron sources	175
A.1.1	^{139}Ce	175
A.1.2	^{113}Sn	177
A.1.3	^{207}Bi	177
A.2	Post-2010 additional sources	179
A.2.1	^{114m}In	179
A.2.2	^{109}Cd	180
A.2.3	^{137}Cs	180
A.3	Compton scatter electrons	182
B	Combining measurements with correlated errors	184
C	Generation of correlated random fluctuations	186
D	Segmenting and Interpolating a Circular Region	188
D.1	Segmenting	188
D.2	Interpolating	188
	Bibliography	191

List of Figures

1	Logo of the UCNA Collaboration.	iv
1.1	Dependence of neutron decay correlations on $\lambda \equiv g_A/g_V$	7
1.2	History of A experimental results through 2010.	13
1.3	State of Weak interactions experimental field in 2010, V_{ud} - λ phase space.	19
2.1	UCNA experimental hall layout.	22
2.2	Sketch of UCN source.	23
2.3	Sketch of SCS magnet and detectors.	26
2.4	Sketch of SCS detector package.	27
2.5	PMT signal chain.	31
2.6	UCNA DAQ schematic.	32
3.1	Backscattering event topologies.	40
3.2	Optimization of wirechamber energy cut for Type II/III event separation.	45
3.3	Optimum Type II/III separation wirechamber energy cut.	45
3.4	Predicted Type II/III separation accuracy.	46
3.5	$E_{\text{vis}} \rightarrow E_{\text{true}}$ curves.	47
3.6	Detector hit positions with three sealed sources in holder.	48
3.7	A menagerie of Xenon isotopes, as seen by the UCNA spectrometer (simulated).	51
4.1	MC detector geometry.	55
4.2	MC source holder geometry.	57
4.3	MC energy deposition in wrinkled foils.	60
4.4	Energy loss of ^{241}Am 5485.56 keV α decays through aluminized Mylar foils.	61
4.5	Sketch of an electron's trajectory in an expanding magnetic field.	62
4.6	Spectrometer magnetic field maps using Hall probe array.	64
4.7	Spectrum and corrections for ^{135}Xe $\frac{3}{2}^+$ beta decay.	68
4.8	Corrections to the shape of the neutron beta decay spectrum.	69
4.9	MC of scintillator quenching effects for ^{207}Bi calibration source.	72
4.10	GEANT4 MC backscatter rates versus data.	76
5.1	Typical PMT pedestal distributions.	78
5.2	PMT pedestal values history.	79
5.3	Single-PMT trigger efficiency determination.	82
5.4	Observed trigger efficiency versus independent trigger expectations.	83

5.5	^{207}Bi pulser spectrum.	84
5.6	^{207}Bi pulser gain monitor history.	86
5.7	Sensitivity of Kurie fit to energy resolution, versus fit range upper end.	88
5.8	Sensitivity of Kurie fit to energy resolution, versus fit range lower end.	88
5.9	Decomposition of observed Xe spectra into isotope components.	90
5.10	Xenon spectrum composition change over time.	91
5.11	Scintillator light transport maps.	93
5.12	Example calibration source peak fits.	97
5.13	Example PMT linearity curve from calibration source scan.	98
5.14	Energy reconstruction errors for all 2010 calibrations.	99
5.15	Example observed versus expected calibration peak widths.	100
5.16	Errors in source peak width predictions.	102
5.17	Multi-sweep determination of LED averaged output applied to one sweep.	105
5.18	Observed scatter in LED sweep data.	106
5.19	Estimated LED output fluctuation contribution to total observed E_s fluctuations. . .	107
6.1	Examples of wirechamber pedestals.	110
6.2	Cathode pedestal histories.	111
6.3	Cathode charge cloud size versus anode signal.	112
6.4	Anode ADC spectra.	113
6.5	Anode ADC spectra most probable values, by position and scintillator energy.	114
6.6	Wirechamber energy deposition most probable value by scintillator energy.	114
6.7	Position dependence of wirechamber charge signal magnitude.	115
6.8	Wirechamber energy deposition, data versus MC.	115
6.9	Anode gain calibration factor history.	116
6.10	Characteristics of cathode segment readout.	119
6.11	Cathode segment event counts prior to gain adjustment.	122
6.12	Normalized cathode signal distribution, and sketch of effect of cathode gain changes. .	123
6.13	Cathode segment gain adjustments.	124
6.14	Cathode segment event counts after gain correction.	124
6.15	Wirechamber positioning correction coefficients.	126
6.16	Wirechamber beta decay event positions, before and after uniformity correction. . . .	127
6.17	Wirechamber beta decay event 2D distribution, before and after uniformity correction.	128
6.18	Example position reconstructions of localized event distributions from sealed sources. .	128
6.19	Data and simulated cathode charge distributions.	129
6.20	East-West event position offsets.	130
6.21	East-West event position offsets history.	130
7.1	Simulated detector efficiency $\eta_s(E)$	134
7.2	Neutron beta decay statistical sensitivity for extracting asymmetry A_0	137
7.3	Accumulated neutron decay statistics for 2010 dataset.	138
7.4	MC Backscattering corrections for 2010 geometry.	142
7.5	MC acceptance correction Δ_3 and combined $\Delta_2 + \Delta_3$ for 2010 geometry.	144
7.6	Extracted asymmetries for various analysis choices.	146

7.7	Energy calibration related uncertainties on A in 2010 data analysis.	147
7.8	Gamma ray events spectra.	152
7.9	Timing coincidence spectra from muon veto detectors.	153
7.10	Muon veto scintillator event spectra.	153
7.11	Muon-tagged events energy spectra.	154
7.12	Muon-tagged event rate in 2010 beta decay runs.	154
7.13	Subtracted background energy spectra by identified event type.	156
7.14	Background runs event positions.	157
7.15	Subtracted background event rate within beta decay analysis cuts.	158
7.16	Muon veto efficiency fluctuation uncertainty for 2010 data.	158
7.17	Neutron generated backgrounds simulation.	160
7.18	Data/MC comparison for high energy excess beta events after background subtraction.	162
7.19	MC estimated neutron generated background.	163
7.20	Recoil order and radiative theory modifications to observed asymmetry.	163
7.21	Event radial position distributions.	167
7.22	Asymmetries for subsets of 2010 data.	168
7.23	Beta decay energy spectrum from 2010 dataset.	169
7.24	Combined asymmetry from 2010 dataset.	169
8.1	Weak decay parameter discrepancies, before and after the UCNA results publication.	172
8.2	History of A experimental results.	172
A.1	^{139}Ce decay source.	177
A.2	^{113}Sn decay source.	178
A.3	^{207}Bi decay source.	178
A.4	^{114m}In decay source.	180
A.5	^{109}Cd decay source.	181
A.6	^{137}Cs decay source.	181
A.7	Simulated detected event positions from gamma rays in sealed source holder.	183
A.8	Simulated Compton electron spectra from gamma rays originating in a sealed source.	183
C.1	Square root and inverse square root components for special case matrix.	187
D.1	Scheme for dividing a circle into smaller sections.	189

List of Tables

1.1	Neutron potentials from material, magnetic, and gravitational interactions.	17
2.1	Beta decay data collection sequences.	34
3.1	System response model, connecting initial physics to collected data.	38
3.2	Observed backscatter classification.	44
3.3	Electron source radioisotopes useful for UCNA calibration.	49
3.4	Binding energies for selected conversion electron sources.	49
3.5	Xenon isotopes accessible by neutron capture on stable xenon.	50
4.1	MC detector geometry materials in electron path.	57
4.2	GEANT4 simulated energy losses in spectrometer material volumes.	59
4.3	Backscatter fractions, GEANT4 MC versus data.	76
5.1	Pedestal correlations between PMT pairs.	107
7.1	UCNA 2010 asymmetry corrections and uncertainties.	133
7.2	Neutron polarizations for the 2010 dataset.	139
7.3	Neutron-generated background counts, data and simulation.	161
A.1	BrIcc conversion electron predictions.	176

Chapter 1

Historical context for neutron beta decay measurements

1.1 Development of Weak interactions theory

1.1.1 Beta decay

1.1.1.1 Fermi's decay theory

Enrico Fermi's 1934 "*Versuch einer Theorie der β -Strahlen*" ("Attempt at a theory of β -rays") [Fer34] (available in translation [Wil68]) provides a remarkable starting point for the study of beta decays. Fermi describes the interaction through the Hamiltonian

$$H = H_{\text{h.p.}} + H_{\text{l.p.}} + H_{\text{int}}, \quad (1.1)$$

constructed from the heavy particle (nucleon) energies $H_{\text{h.p.}}$, light particle (lepton) energies $H_{\text{l.p.}}$, and an interaction term H_{int} , which permits transition between the initial and final states in perturbation theory. Following a series of simplifying assumptions for the form of the interaction, Fermi concludes a plausible form for changing between a neutron and proton while producing an electron and antineutrino,

$$H_{\text{int}} = g[Q(-\psi_1\phi_2 + \psi_2\phi_1 + \psi_3\phi_4 - \psi_4\phi_3) + Q^*(-\psi_1^*\phi_2^* + \psi_2^*\phi_1^* + \psi_3^*\phi_4^* - \psi_4^*\phi_3^*)], \quad (1.2)$$

where g is the coupling strength constant, Q and Q^* are operators changing a proton to a neutron and vice-versa, ψ_i are the four components of the relativistic Dirac wavefunction for annihilation (ψ_i^* for creation) of the electron, and ϕ_i for the (anti)neutrino. The particular combination of ψ 's and ϕ 's chosen came from analogy to the electromagnetic interaction $H_{\text{EM}} = eJ_\mu A_\mu$, treating the lepton term as transforming like electromagnetic vector four-potential component A_0 (and taking the nucleus' contribution J_μ in the nonrelativistic limit). In more modern notation, Fermi's Vector interaction would be written:

$$H_{\text{int}} = g(\bar{\psi}_p \gamma_\mu \psi_n)(\bar{\psi}_e \gamma_\mu \psi_{\nu_e}) + \text{H.C.} \quad (1.3)$$

From this reasoning, and incorporating Coulomb interactions for the outgoing electron based on hydrogen atom wavefunctions, Fermi proposed the electron energy spectrum form resulting in

$$S_{\text{Fermi}}(W)dW \equiv G^2|M|^2F(Z, W)(W_0 - W)^2\sqrt{W^2 - 1}WdW, \quad (1.4)$$

where W is the electron total energy in $m_e c^2$ units, W_0 is the decay endpoint energy, $|M|^2$ is the matrix element between initial and final nuclear states, G an overall coupling constant for the interaction, and $F(Z, W)$ is the Fermi function incorporating Coulomb interaction effects on the electron's decay phase space:

$$F(Z, W) \equiv \frac{4}{\Gamma(3 + 2\gamma)}(2p\rho)^{2\gamma}e^{\pi\alpha ZW/p}|\Gamma(1 + \gamma + i\alpha ZW/p)|^2, \quad \gamma \equiv \sqrt{1 - (\alpha Z)^2} - 1, \quad p = \sqrt{W^2 - 1}, \quad (1.5)$$

where ρ is the radius of the nucleus.

1.1.1.2 Konopinski-Uhlenbeck modification

Comparing Fermi's decay spectrum form with available experimental data, Konopinski and Uhlenbeck published a 1935 article [KU35] noting a systematic tendency for measured spectra to show a more asymmetric form (biased towards lower energies) than Fermi's proposed form. They proposed a modification to the "statistical factor" for the decay phase space S (produced by assuming coupling to the neutrino wavefunction's gradient rather than its value), changing Fermi's prediction for the decay spectrum to a re-weighted form:

$$S_{\text{Fermi}}(W)dW \rightarrow S_{\text{K-U}}(W)dW \equiv G^2|M|^2F(Z, W)(W_0 - W)^4\sqrt{W^2 - 1}WdW. \quad (1.6)$$

The Konopinski-Uhlenbeck spectrum shape, with its additional factor of $(W_0 - W)^2$, generally produced better agreement with experimental beta spectra shapes at the time, and gained widespread popularity in the beta decay physics community. However, as experimental technique improved over the next several years, beta decay spectra "shifted" from agreeing better with the K-U form back towards Fermi's original theory.

In a 1943 review article on beta decay, Konopinski writes:

"Thus, the evidence of the spectra, which has previously comprised the sole support for the K-U theory, now definitely fails to support it." [Kon43]

Among the main culprits identified by Konopinski for the discrepancies between earlier and later experimental results were extra energy losses in older thick decay source samples, distorting the spectrum towards the K-U form; development of newer, thin decay samples agreed better with Fermi's predictions.

1.1.1.3 What interaction form?

Fermi's original theory chose a Vector form for the interaction from familiar analog to electromagnetic theory, though leaving open the possibility of any other interaction form in the same formalism. The Vector form would impose selection rules for allowed decays of $\Delta J = 0$, no parity change. Gamow and Teller argued in a 1936 article [GT36] that this selection rule was contradicted by experimental

evidence from thorium beta decays, which instead favored the Gamow-Teller (G-T) selection rules of $\Delta J = 0, \pm 1$ (except $0 \rightarrow 0$), no parity change. Either a Tensor or Axial-Vector decay form would produce the G-T selection rule, while both Vector and Scalar forms produce the Fermi selection rule. A Pseudoscalar interaction would produce $\Delta J = 0$ with parity change.

As Konopinski discusses in [Kon43], each individual interaction form would produce the same allowed beta decay spectrum shape. However, a 1937 paper by Markus Fierz [Fie37] noted that the simultaneous presence of both Tensor and Axial-vector terms, or of both Scalar and Vector terms, would produce interference cross-terms modifying the spectrum shape. Which interaction forms actually dominated in beta decay would remain an open question for the next 15 years, with confusing and contradictory experimental evidence.

1.1.2 The Weak interaction

1.1.2.1 Universal Weak interaction

In 1949, Tiomno and Wheeler commented on a striking similarity between the interactions $n \rightarrow p + e + \bar{\nu}_e$, $\mu^- \rightarrow e + \bar{\nu}_e + \nu_\mu$, and $\mu^- + p \rightarrow n + \nu_\mu$:

“We note that the *three coupling constants determined quite independently agree with one another within the limits of error of experiment and theory*. We apparently have to do in all three reaction processes with phenomena having a much closer relationship than we can now visualize.” [TW49]

A contemporaneous letter by Lee, Rosenbluth, and Yang commented on the same coincidence:

“One can perhaps attempt to explain the equality of these interactions in a manner analogous to that used for the Coulomb interactions, i.e. by assuming these interactions to be transmitted through an intermediate field with respect to which all particles have the same “charge.” The “quanta” of such a field would have a very short lifetime and would have escaped detection.” [LRY49]

Progress in experimental measurements of such interactions solidified the hypothesis of a common mechanism, named the “Weak” interaction in comparison to the higher energy scales and faster decays of the Strong nuclear interaction. Fermi’s theoretical framework for beta decay now came to encompass a wide variety of four-Fermion Weak interactions.

1.1.2.2 Parity-violating interaction terms

In an October 1956 paper [LY56], Lee and Yang proposed expanding the terms in the Weak interaction neutron decay Hamiltonian:

$$\begin{aligned}
H_{\text{int}} = & (\bar{\psi}_p \psi_n)(C_S \bar{\psi}_e \psi_{\nu_e} + C'_S \bar{\psi}_e \gamma_5 \psi_{\nu_e}) \\
& + (\bar{\psi}_p \gamma_\mu \psi_n)(C_V \bar{\psi}_e \gamma_\mu \psi_{\nu_e} + C'_V \bar{\psi}_e \gamma_\mu \gamma_5 \psi_{\nu_e}) \\
& + \frac{1}{2}(\bar{\psi}_p \sigma_{\lambda\mu} \psi_n)(C_T \bar{\psi}_e \sigma_{\lambda\mu} \psi_{\nu_e} + C'_T \bar{\psi}_e \sigma_{\lambda\mu} \gamma_5 \psi_{\nu_e}) \\
& - (\bar{\psi}_p \gamma_\mu \gamma_5 \psi_n)(C_A \bar{\psi}_e \gamma_\mu \psi_{\nu_e} + C'_A \bar{\psi}_e \gamma_\mu \gamma_5 \psi_{\nu_e}) \\
& - (\bar{\psi}_p \gamma_5 \psi_n)(C_P \bar{\psi}_e \psi_{\nu_e} + C'_P \bar{\psi}_e \gamma_5 \psi_{\nu_e}) + \text{H.C.},
\end{aligned} \tag{1.7}$$

in which the C_i coupling constants prefix the Scalar, Vector, Tensor, Axial-vector, and Pseudo-scalar terms of prior Fermi theory. The C'_i couplings, however, introduce new parity-violating terms. In the case $C'_i = \pm C_i$, the $(1 \pm \gamma_5)$ terms indicate maximal parity violation in which only one helicity of the leptons participates — right-handed neutrinos for $(1 + \gamma_5)$ and left-handed for $(1 - \gamma_5)$, with the electron helicity identical in the V and A cases, or opposite in S , T , P .

Parity violation had been excluded in Strong interactions with stringent experimental limits, and thus it had not been previously considered in Weak decay theory. However, Lee and Yang noted that there had been no conclusive experimental tests of parity conservation in Weak decays. Furthermore, parity violation could solve an open puzzle about experimentally observed “ τ^+ ” and “ θ^+ ” particles, which appeared to have the same masses and lifetimes, but decayed to states with opposite parity. “One way out of the difficulty,” wrote Lee and Yang, “is to assume that parity is not strictly conserved, so that θ^+ and τ^+ are two different decay modes of the same particle, which necessarily has a single mass value and a single lifetime.” Lee and Yang proposed a variety of experimental observables that would result from parity violation, including:

“A relatively simple possibility is to measure the angular distribution of the electrons coming from β decays of oriented nuclei. If θ is the angle between the orientation of the parent nucleus and the momentum of the electron, an asymmetry of distribution between θ and $180^\circ - \theta$ constitutes an unequivocal proof that parity is not conserved in β decay.”

Prompted by Lee and Yang, Chien-Shiung Wu quickly assembled an experiment to test the theory. In January 1957, Wu published a measurement of the parity-violating electron asymmetry in polarized ^{60}Co beta decay [Wu+57]. Experimental evidence indicated not only that parity violation occurred in Weak decays, but also that parity violation was maximal within experimental uncertainties. Lee and Yang shared the 1957 Nobel Prize in Physics, and the “ θ^+ ” and “ τ^+ ” mesons are known today as the Kaon K^+ . The apparent completeness of parity violation led Lee and Yang to propose a two-component neutrino theory in which only one neutrino handedness was produced in beta decay [LY57] (though it was not known which one).

1.1.2.3 Decay correlations

Decay angular correlations (and improved experimental capabilities to measure them) opened up a new window for understanding Weak interactions beyond spectrum shapes and decay lifetimes. Jackson, Trieman, and Wyld considered a variety of other experimentally observable correlations in a pair of papers early in 1957 [JTW57b; JTW57a] (with additional correlation terms I , K' , M , S , T , U , V , W enumerated in a follow-up article by Ebel and Feldman [EF57]). The β^\mp -decay rate for an ensemble of nuclei with charge $Z \mp 1$, angular momentum \mathbf{J} in direction \hat{j} , as a function of electron momentum and energy \mathbf{p}_e and E_e , neutrino momentum and energy \mathbf{p}_ν and E_ν (experimentally accessible through recoiling proton and electron observables by energy and momentum conservation),

and electron spin $\boldsymbol{\sigma}$, would be [JTW57b; JTW57a; EF57]:

$$\begin{aligned}
\omega(\langle \mathbf{J} \rangle, \boldsymbol{\sigma} | E_e, \Omega_e, \Omega_\nu) dE_e d\Omega_e d\Omega_\nu = & \\
\frac{1}{2} \frac{F(\pm Z, E_e)}{(2\pi)^5} p_e E_e (E^0 - E_e)^2 dE_e d\Omega_e d\Omega_\nu \xi & \\
\times \left\{ 1 + a \frac{\mathbf{p}_e \cdot \mathbf{p}_\nu}{E_e E_\nu} + b \frac{m}{E_e} + \frac{\langle \mathbf{J} \rangle}{J} \cdot \left[A \frac{\mathbf{p}_e}{E_e} + B \frac{\mathbf{p}_\nu}{E_\nu} + D \frac{\mathbf{p}_e \times \mathbf{p}_\nu}{E_e E_\nu} \right] \right. & \\
+ \left[\frac{J(J+1) - 3 \langle (\mathbf{J} \cdot \hat{\mathbf{j}})^2 \rangle}{J(2J-1)} \right] \left(c \left[\frac{1}{3} \frac{\mathbf{p}_e \cdot \mathbf{p}_\nu}{E_e E_\nu} - \frac{(\mathbf{p}_e \cdot \hat{\mathbf{j}})(\mathbf{p}_\nu \cdot \hat{\mathbf{j}})}{E_e E_\nu} \right] + I \left[\frac{1}{3} \frac{\boldsymbol{\sigma} \cdot \mathbf{p}_\nu}{E_\nu} - \frac{(\boldsymbol{\sigma} \cdot \hat{\mathbf{j}})(\mathbf{p}_\nu \cdot \hat{\mathbf{j}})}{E_\nu} \right] \right) & \\
+ K' \frac{\boldsymbol{\sigma} \cdot \mathbf{p}_e}{E_e + m} \left[\frac{1}{3} \frac{\mathbf{p}_e \cdot \mathbf{p}_\nu}{E_e E_\nu} - \frac{(\mathbf{p}_e \cdot \hat{\mathbf{j}})(\mathbf{p}_\nu \cdot \hat{\mathbf{j}})}{E_e E_\nu} \right] + M \left[\frac{1}{3} \frac{\boldsymbol{\sigma} \cdot (\mathbf{p}_e \times \mathbf{p}_\nu)}{E_e E_\nu} - \frac{(\boldsymbol{\sigma} \cdot \hat{\mathbf{j}})(\mathbf{p}_e \times \mathbf{p}_\nu \cdot \hat{\mathbf{j}})}{E_e E_\nu} \right] & \\
+ \boldsymbol{\sigma} \cdot \left[G \frac{\mathbf{p}_e}{E_e} + H \frac{\mathbf{p}_\nu}{E_\nu} + K \frac{\mathbf{p}_e}{E_e + m} \frac{\mathbf{p}_e \cdot \mathbf{p}_\nu}{E_e E_\nu} + L \frac{\mathbf{p}_e \times \mathbf{p}_\nu}{E_e E_\nu} + N \frac{\langle \mathbf{J} \rangle}{J} + Q \frac{\mathbf{p}_e}{E_e + m} \frac{\langle \mathbf{J} \rangle \cdot \mathbf{p}_e}{J E_e} \right. & \\
+ R \frac{\langle \mathbf{J} \rangle \times \mathbf{p}_e}{J E_e} + S \frac{\langle \mathbf{J} \rangle}{J} \frac{\mathbf{p}_e \cdot \mathbf{p}_\nu}{E_e E_\nu} + T \frac{\mathbf{p}_e}{E_e} \frac{\langle \mathbf{J} \rangle \cdot \mathbf{p}_\nu}{J E_\nu} + U \frac{\mathbf{p}_\nu}{E_\nu} \frac{\langle \mathbf{J} \rangle \cdot \mathbf{p}_e}{J E_e} & \\
\left. + W \frac{\mathbf{p}_e}{E_e + m} \frac{\langle \mathbf{J} \rangle \cdot (\mathbf{p}_e \times \mathbf{p}_\nu)}{J E_e E_\nu} \right] + V \frac{\langle \mathbf{J} \rangle \cdot (\boldsymbol{\sigma} \times \mathbf{p}_\nu)}{J E_\nu} \left. \right\}. & \\
\end{aligned} \tag{1.8}$$

Each correlation coefficient is related to the Lee-Yang couplings, along with nuclear transition matrix elements $|M_F|^2$ and $|M_{GT}|^2$ for Fermi and Gamow-Teller selection rule decays. The overall rate is set by the contributions to each selection rule,

$$\xi = |M_F|^2 (|C_S|^2 + |C_V|^2 + |C'_S|^2 + |C'_V|^2) + |M_{GT}|^2 (|C_T|^2 + |C_A|^2 + |C'_T|^2 + |C'_A|^2), \tag{1.9}$$

plus the interference term b predicted by Fierz [Fie37] if both coupling types for one selection rule are present:

$$b\xi = \pm 2 \text{Re} (|M_F|^2 (C_S C_V^* + C'_S C_V'^*) + |M_{GT}|^2 (C_T C_A^* + C'_T C_A'^*)). \tag{1.10}$$

Jackson, Trieman, and Wyld discuss how experimental correlation measurements could narrow down the couplings in Lee and Yang's very general Hamiltonian. Invariance under Charge conjugation (C) requires the couplings C to be pure real, and the C' to be pure imaginary (up to an overall phase), while a C-odd interaction would have C and C' in-phase. Parity (P) invariance would require either the C or C' couplings to be zero, with P-odd maximal parity violation at $C = \pm C'$. Time reversal (T) invariance would require the C and C' couplings to be real (up to an overall phase), which could be tested by correlation terms such as $D \langle \mathbf{J} \rangle \cdot \mathbf{p}_e \times \mathbf{p}_\nu$.

1.1.2.4 $V - A$ structure

By the mid-1950s, general consensus in the scientific community held that the Weak interaction was primarily driven by Scalar and Tensor coupling terms. Sudarshan and Marshak proposed, at a September 1957 conference [SM57], that a Vector/Axial-vector form could also explain experimental data, with various notable exceptions — several of which were quickly overturned. By January 1958, Sudarshan and Marshak were able to publish their claim [SM58] on solid experimental ground that

Weak decays involved Vector and Axial-vector couplings, with coupling constants approximately equal in magnitude and opposite in sign, called the “ $V - A$ structure” of the Weak interaction.

1.1.2.5 Conserved Vector Current hypothesis

A 1955 article by USSR theorists Gershtein and Zeldovich [GZ56] had noted a special property of Vector interaction contributions to Weak decay. However, due to the presumed Scalar/Tensor form at the time, Gershtein and Zeldovich’s observation received little immediate attention:

“It is of no practical significance but only of theoretical interest that in the case of the vector interaction type V we should expect the equality

$$g_{F(V)} \equiv g'_{F(V)}$$

to any order of the meson-nucleon coupling constant, taking nucleon recoil into account and allowing also for the interaction of the nucleon with the electromagnetic field, etc. This result might be seen by analogy with Ward’s identity for the interaction of a charged particle with the electromagnetic field; in this case virtual processes involving particles (self-energy and vertex parts) do not lead to charge renormalization of the particle.”

Renewed interest in Vector interactions, along with experimental evidence, prompted Feynman and Gell-Mann to independently rediscover Gershtein and Zeldovich’s observation. Feynman and Gell-Mann begin a 1958 article [FGM58] noting the agreement between the muon lifetime calculated using the coupling constant G derived from $O^{14} \beta^+$ decay, $\tau_\mu = 192\pi^3/G^2\mu^5 = (2.26 \pm 0.04) \times 10^{-6}$ seconds, and the direct experimental measurement of $\tau_\mu = (2.22 \pm 0.02) \times 10^{-6}$ seconds:

“It might be asked why this agreement should be so good. Because nucleons can emit virtual pions there might be expected to be a renormalization of the effective coupling constant. On the other hand, if there is some truth in the idea of an interaction with a universal constant strength it may be that *the other interactions are so arranged so as not to destroy this constant*. We have an example in electrodynamics.”

Feynman and Gell-Mann proposed that, analogous to conserved electric charge, the Weak decay vector coupling was associated with a current that “is conserved, and, like electricity, leads to a quantity whose value (for low energy interactions) is unchanged by the interaction of pions and nucleons.” This principle came to be named the “Conserved Vector Current” (CVC) hypothesis.

With the Vector coupling constant g_V free from modification by renormalization, convention assigns it the value $g_V = 1$, absorbing the overall coupling strength into the definition of G_F . The Axial-vector coupling g_A , not free from renormalization effects, must be experimentally determined for a particular particle interaction of interest. The ratio of the two coupling constants is frequently given the name $\lambda \equiv g_A/g_V \approx -1$, though sign conventions vary, with $\lambda \equiv |g_A/g_V| \approx 1$ alternatively used in the literature.

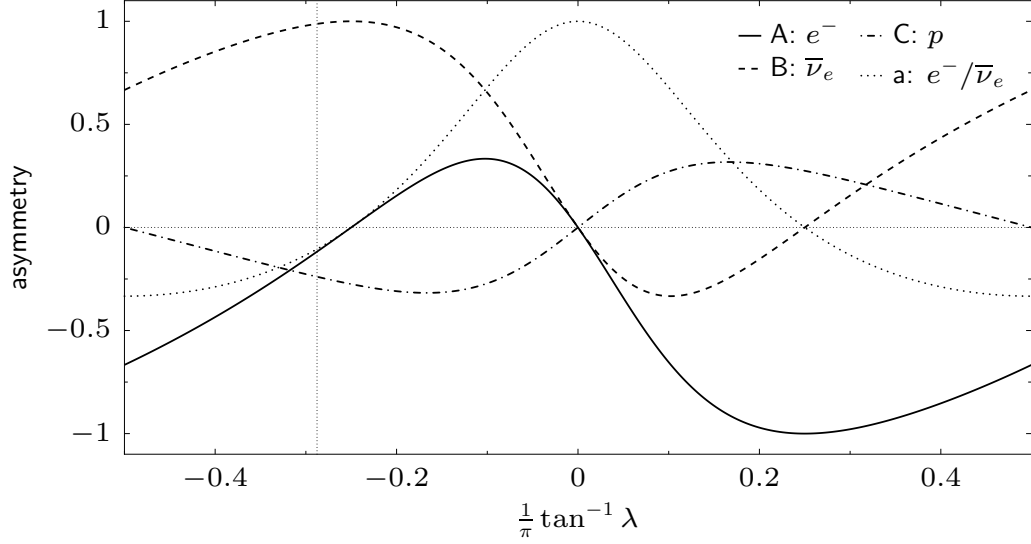


Figure 1.1: Correlations for neutron decay versus $\lambda \equiv g_A/g_V$, for full range of V and A mixtures from pure-Fermi at $\lambda = 0$ to pure-GT at $\lambda = \pm\infty$ ($\tan^{-1} \lambda = \pm\frac{\pi}{2}$). Vertical line marks experimental value of $\lambda \approx -1.27$.

1.1.2.6 Free neutron beta decay correlations

In the particular case of free neutron decay, where $J^\pi = \frac{1}{2}^+ \rightarrow \frac{1}{2}^+$, both Fermi and G-T selection rules are possible. The neutron-proton transition defines the normalization for the Fermi and G-T transition matrix elements, with $|M_F|^2 \equiv 1$ and $|M_{GT}|^2 \equiv 3$ requiring no further knowledge of strong interaction details necessary to calculate matrix elements for nuclei with more than one nucleon. The correlation A between neutron spin and electron direction given by [JTW57a] in terms of the Lee-Yang Hamiltonian (Equation 1.7) coupling constants is then:

$$A\xi = \frac{4}{3}|M_{GT}|^2 \text{Re}(C_T C_T'^* - C_A C_A'^*) + \frac{2}{\sqrt{3}} M_F M_{GT} \text{Re}(C_S C_T'^* + C_S' C_T^* - C_V C_A'^* - C_V' C_A^*), \quad (1.11)$$

where ξ is given by Equation 1.9. Letting $C' = C$ be pure real for T-even, P-odd symmetry, and taking the $V - A$ interaction structure, this reduces to

$$A = \frac{-4(C_A^2 + C_A C_V)}{2C_V^2 + 6C_A^2} = \frac{-2\lambda(1 + \lambda)}{1 + 3\lambda^2}, \quad \lambda \equiv \frac{C_A}{C_V} = \frac{g_A}{g_V}. \quad (1.12)$$

Additional correlations B between neutron spin and neutrino direction, and a between electron and neutrino directions, are given by:

$$a = \frac{1 - \lambda^2}{1 + 3\lambda^2}; \quad B = \frac{-2\lambda(1 - \lambda)}{1 + 3\lambda^2}; \quad C = -0.27848 \cdot (A + B). \quad (1.13)$$

Here C is the correlation between neutron spin and proton recoil direction, which is derived by kinematics from the A and B electron and neutrino correlations. Figure 1.1 plots the dependence of these correlations on λ .

The correlation parameters as given above neglect higher-order contributions from nucleon recoil effects, electromagnetic effects, etc.; effectively, they are for a final state with an infinitely massive,

neutrally charged, pointlike proton. To distinguish this “bare model parameter” value from the physical asymmetry that will be observed in the lab, the A of Equation 1.12 is often denoted “ A_0 .”

1.1.2.7 Induced couplings

Goldberger and Treiman published a Physical Review article in 1958 [GT58] noting that, while the Weak decay Lagrangian contained only $V - A$ terms for the lepton couplings, additional terms with different symmetries could be induced in decay matrix elements by Strong interaction effects. While these induced couplings would likely be “negligible in β decay,” the higher momentum transfer in μ capture interactions might demonstrate induced pseudoscalar terms.

1.1.2.8 Weak Magnetism

In the same edition of Physical Review containing Goldberger and Treiman’s article on induced couplings, Gell-Mann followed the Weak interaction’s analogous mathematical structure to electromagnetism to note that the Vector interaction also

“...gives rise to ‘weak magnetism’ analogous to the magnetic effects that induce the emission of M1 photons. This ‘weak magnetism’ obeys Gamow-Teller selection rules and interferes with the A coupling...” [GM58]

Gell-Mann proceeds to calculate the effect on the $e^- - \bar{\nu}$ angular correlation and the electron energy spectrum.

Bilen’kiĭ *et al.* [Bil+60] expanded the calculation to other neutron β -decay observables. They found that the neutron β -decay correlation coefficient A would pick up an energy dependence from the recoil-order terms:

$$A^{\text{RO}}(E) = A_0 + \frac{2(\lambda + \mu)}{(1 + 3\lambda^2)^2} \frac{1}{M} \left[\left(\lambda^2 + \frac{2}{3}\lambda - \frac{1}{3} \right) E_0 - \left(\lambda^3 + 3\lambda^2 + \frac{5}{3}\lambda - \frac{1}{3} \right) E - 2\lambda^2(\lambda - 1) \frac{m_e^2}{E} \right], \quad (1.14)$$

where $\mu \equiv \mu_p - \mu_n$, with $\mu_p \approx 2.79$ and $\mu_n \approx -1.91$ as the proton and neutron magnetic moments, E as the decay electron’s total energy, and $\lambda \equiv |g_A/g_V|$. The net effect is an $\sim 1.5\%$ increase of the physical asymmetry over A_0 , shown in Figure 7.20.

1.1.2.9 Second-class currents

Unlike the Strong interaction, the Weak interaction had been demonstrated to violate Parity symmetry. Weinberg considers in [Wei58] the implications of applying another Strong interaction symmetry, $G \equiv C e^{i\pi I_2}$ (the product of charge symmetry and charge conjugation), to the Weak interaction. Weinberg divides the various possible currents in the Weak interaction into two classes. The currents in Feynman–Gell-Mann Weak interaction theory fall in the first class, behaving under G like the Strong interactions; additional “second-class” currents will not occur if G symmetry applies to Weak interactions.

Following the formalism of [Byr82], the matrix element for neutron decay can be written as the contraction of lepton and nucleon transition current amplitudes,

$$M_\beta = \frac{G_\beta}{\sqrt{2}} (2\pi)^4 j_\mu^l j_\mu^n; \quad j_\mu^l \equiv \langle e^- \bar{\nu}_e | J_\mu^l(0) | 0 \rangle = -i \langle \bar{u}_e | \gamma_\mu (1 + \gamma_5) | u_{\nu_e} \rangle, \quad j_\mu^n \equiv \langle p | J_\mu^n(0) | n \rangle. \quad (1.15)$$

The nucleon current can be written as the sum of components transforming like a Vector or Axial-vector,

$$\begin{aligned} j_\mu^n &\equiv j_\mu^V + j_\mu^A \\ j_\mu^V &= i \langle \bar{u}_p | g_V \gamma_\mu - \frac{g_M - g_V}{2M_n} \sigma_{\mu\nu} q_\nu - \frac{ig_S}{2M_n} q_\mu | u_n \rangle \\ j_\mu^A &= i \langle \bar{u}_p | g_A \gamma_5 \gamma_\mu - \frac{g_{II}}{2M_n} \sigma_{\mu\nu} \gamma_5 q_\nu - \frac{ig_P}{2M_n} \gamma_5 q_\mu | u_n \rangle. \end{aligned} \quad (1.16)$$

The leading g_V and g_A terms correspond to first-class currents, along with the recoil-order weak magnetism (pseudotensor) contribution $\frac{g_M - g_V}{2M_n}$ and the induced pseudoscalar $\frac{g_P}{2M_n}$. Second-class currents produce the g_S Scalar term, which, contributing to the Vector current of the interaction, is ruled out if the CVC hypothesis holds, and the Tensor coupling g_{II} . There is no experimental evidence for the presence of g_{II} ; however, appearing at recoil order suppressed by $1/M_n$, neither are there particularly stringent experimental limits against it [Wil00; Bha+12]. The presence of g_{II} would be observable in energy-dependent modifications to the neutron beta decay asymmetry (see subsection 7.6.1.1).

1.1.2.10 Electromagnetic corrections

In addition to Weak magnetism and recoil corrections, neutron β -decay is also influenced by electromagnetic effects (*e.g.* Coulomb interactions between the electron and proton and bremsstrahlung radiation). The Coulomb attraction between the proton and electron was already incorporated by Fermi into the beta decay phase space of [Fer34]. Sirlin published a 1967 paper [Sir67] considering additional order- α electromagnetic corrections to the β -decay spectrum. Sirlin argues that calculable, model-independent Coulomb effects can be separated from the difficult, model-dependent portions involving details of the Strong and Weak interactions. The high-energy, model-dependent corrections will be insensitive to the relatively low energies and momenta of the decay products, and thus are effectively constants that can be absorbed into the definition of the coupling constants. Sirlin calculates the model-independent portion of the Coulomb corrections $\frac{\alpha}{2\pi} g(E)$ to the unpolarized neutron β -decay spectrum, capturing the dependence on the outgoing electron's energy.

A following paper by Shann in 1971 [Sha71] considers the impact of these electromagnetic corrections on polarized neutron decay. Shann calculates the order- α radiative corrections $\frac{\alpha}{2\pi} h(E)$ to the observable electron asymmetry $A(E)$. Including the Sirlin and Shann corrections, the polarized neutron decay rate is

$$\begin{aligned} \Gamma_{n \rightarrow p e \bar{\nu}}(E, \theta) &\propto 1 + \frac{\alpha}{2\pi} g(E) + \left(1 + \frac{\alpha}{2\pi} h(E)\right) A \beta \cos \theta \\ &= \left(1 + \frac{\alpha}{2\pi} g\right) \left(1 + \left[1 + \frac{\alpha}{2\pi} (h - g) + O(\alpha^2)\right] A \beta \cos \theta\right), \end{aligned} \quad (1.17)$$

which modifies the observable asymmetry by the factor $\frac{\alpha}{2\pi}(h - g) \sim 10^{-3}$,

$$h - g = 4 \left(\frac{\tanh^{-1} \beta}{\beta} - 1 \right) \left(1 - \beta^2 + \frac{E_0 - E}{8E} \right) \frac{E_0 - E}{3E\beta^2} + \frac{\tanh^{-1} \beta}{\beta} \left(2 - 2\beta^2 - \frac{(E_0 - E)^2}{6E^2} \right), \quad (1.18)$$

where E_0 is the neutron β -decay endpoint, and E , $\beta \equiv \frac{v}{c}$ are the electron's total energy and speed. The result is an $\sim 0.1\%$ increase of the physical asymmetry over A_0 , shown in Figure 7.20.

1.1.3 Connection to quark model

1.1.3.1 Quarks

By mid-century, particle physics experiment had uncovered a large and still growing catalog of new particles. Shoichi Sakata commented in a 1956 letter:

“It seems to me that the present state of the theory of new particles is very similar to that of the atomic nuclei 25 years ago. At that time, we had known a beautiful relation between the spin and the mass number of the atomic nuclei. Namely, the spin of the nucleus is always integer if the mass number is even, whereas the former is always half integer if the latter is odd. But unfortunately we could not understand the profound meaning for this even-odd rule.” [Sak56]

As the discovery of the neutron led to an explanation for nuclear properties in terms of proton and neutron constituents, Sakata was hopeful that properties of the zoo of newly discovered particles could likewise be explained:

“In our model, the new particles are considered to be composed of four kinds of fundamental particles in the true sense, that is, nucleon, antinucleon, Λ^0 and anti- Λ^0 .”

Murray Gell-Mann and Yuval Ne’eman (independently) developed a more advanced replacement for Sakata’s four-constituent model, associating the organization of baryons and mesons with the mathematical structure of direct products of $SU(3)$ groups, which Gell-Mann named the “eightfold way”. Gell-Mann distanced the “eightfold way” theory from Sakata’s concept of physical fundamental constituent particles “in the true sense,” emphasizing that the group-theoretical approach was a mathematical abstraction rather than a combination of physical constituents:

“Unitarity symmetry may be applied to the baryons in a more appealing way if we abandon the connection with the symmetrical Sakata model and treat unitarity symmetry in the abstract. (An abstract approach is, of course, required if there are no “elementary” baryons and mesons.)” [GM62]

The “Eightfold Way” was simultaneously developed in 1964 into George Zweig’s “aces” [Zwe64] and Gell-Mann’s “up,” “down,” and “strange” quarks [GM64], three fractionally charged members of a unitarity triplet which combine in pairs and triads to form observable mesons and baryons. While the quarks were still primarily treated purely as mathematical abstractions, Gell-Mann countenanced the possibility that quarks might be physical particles:

“It is fun to speculate about the way quarks would behave if they were physical particles of finite mass (instead of purely mathematical entities as they would be in the limit of infinite mass). Since charge and baryon number are exactly conserved, one of the quarks (presumably $u^{\frac{2}{3}}$ or $d^{-\frac{1}{3}}$) would be absolutely stable, while the other member of the doublet would go into the first member very slowly by β -decay or K-capture.” [GM64]

1.1.3.2 Cabibbo mixing angle and the charm quark

Experimental measurements of Weak interactions of new particles placed a strain on the CVC hypothesis, indicating higher Vector coupling for particles with strangeness inconsistent with the “universality” of the interaction. In 1963, Nicola Cabibbo extended the CVC hypothesis [Cab63] to account for strangeness-nonconserving decays by describing the Weak interaction Vector current as a mixing of $\theta_c \approx 0.26$ between $\Delta S = 0$ and $\Delta S = 1$ currents such that the strength of the combined vector current $j = j_{\Delta S=0} \cos \theta_c + j_{\Delta S=1} \sin \theta_c$ would still be “universal.” For Weak decays of particles without strangeness, the Vector decay rate would be scaled down by a factor of $\cos^2 \theta_c$.

Björken and Glashow proposed adding a fourth, heavier “charm” quark, incorporating Cabibbo’s mixing angle into the model, explaining the masses of observed mesons, and predicting new decays:

“The model is vulnerable to rapid destruction by the experimentalists. The main prediction is the existence of the charmed $S_{p,v}^+$ and $D_{p,v}^{+,0}$ mesons which can be produced in pairs in $\pi - p$, $K - p$ and $\bar{p} - p$ reactions, followed by weak but rapid decays into both Y-conserving and Y-violating channels.” [BG64]

Following experiments contradicted Björken and Glashow’s decay predictions, providing “rapid destruction” for the model. A 1970 paper revived the possibility of the charm quark with the “Glashow-Iliopoulos-Maiani” (GIM) mechanism [GIM70], which re-introduced the fourth quark to explain experimentally observed suppression of $\Delta S = 2$ decays, while also justifying the prior lack of evidence for charm decays:

“such events will necessarily be of very complex topology, involving the plentiful decay products of both charmed states. Charmed particles could easily have escaped notice.”

Independent experiments at BNL [Aub+74] and SLAC [Aug+74] simultaneously announced the discovery of a new particle decay in November 1974, which turned out to be the same $c\bar{c}$ “ J/ψ ” meson. Burton Richter and Samuel Ting, the lead investigators for each experiment, shared the 1976 Nobel Prize in Physics for the discovery.

1.1.3.3 CKM matrix and unitarity

Meanwhile, a 1973 paper by Kobayashi and Maskawa [KM73] argued that CP-violating Weak decays could only be incorporated into the existing theoretical framework by extending Cabibbo’s two-element mixing angle θ_c to a 3×3 unitary mixing matrix — later named the Cabibbo-Kobayashi-Maskawa (CKM) matrix with elements V_{ij} — consequently predicting the existence of yet another generation of quarks. CP violation had been observed in rare $K_2^0 \rightarrow \pi\pi$ decays in 1964 [Chr+64], for which James Cronin and Val Fitch shared the 1980 Nobel Prize. The 1977 “observation of a Dimuon resonance at 9.5 GeV” at BNL [Her+77] provided experimental evidence for the lighter

“bottom” quark in the new pair, while observation of the heavier “top” quark by the D0 [Aba+95] and CDF [Abe+95] experiments was published in 1995. Kobayashi and Maskawa shared in the 2008 Nobel Prize for predicting the third quark generation.

With three generations of quarks discovered, an obvious question is whether there are yet more to be found (extending the CKM matrix to a 4×4 mixing). If interactions with a fourth generation are possible, then the existing 3×3 CKM matrix would not be unitary. The first row of the CKM matrix, involving the most common decays coupling to the u quark, provides the most stringent experimental limits on unitarity, *i.e.* whether $|V_{ud}|^2 + |V_{us}|^2 + |V_{ub}|^2 = 1$.

1.1.4 Beta decay in the Standard Model

Lee and Yang’s effective Hamiltonian model for Weak decays can now be understood in terms of Standard Model quark interactions. Following a 2010 review paper by Towner and Hardy [TH10], the total decay rate for nuclear beta decays will be:

$$\Gamma = \tau^{-1} = \frac{G_F^2 g_V^2 m_e^5}{2\pi^3} V_{ud}^2 f[|M_F|^2 + \lambda^2 |M_{GT}|^2], \quad (1.19)$$

where f is a phase space integral over the decay spectrum shape,

$$f \equiv \int_1^{W_0} (W_0 - W)^2 p W F(W, Z) S(W, Z) dW; \quad p \equiv \sqrt{W^2 - 1}, \quad (1.20)$$

where W is the total electron energy (in electron mass units) out to the spectrum endpoint W_0 , $F(W, Z)$ is the Fermi function Coulomb correction, and $S(W, Z) \approx 1$ is all other fine shape corrections.

The Fermi coupling constant $G_F/(\hbar c)^3 = 1.1663787(6) \cdot 10^{-5} \text{ GeV}^{-2}$ [Ber12] is experimentally determined from the muon decay lifetime ($\mu^- \rightarrow \nu_\mu + \bar{\nu}_e + e^-$), taking advantage of the universality of the Weak interaction to extract this parameter from a decay independent of nuclear structure considerations. The best experimental measurements of V_{ud} come from from superallowed $0^+ \rightarrow 0^+$ nuclear decay rates, which selection rules guarantee to be pure Fermi decays ($|M_{GT}|^2 = 0$). Combining several experimental results gives the best estimate [HT09] $V_{ud} = 0.97425(22)$.

Free neutron beta decay provides an ideal system for precision measurements of parameters related to Axial-vector contributions to decay, as the nuclear matrix elements are known by definition ($|M_F|^2 \equiv 1$, $|M_{GT}|^2 \equiv 3$), rather than requiring difficult and uncertain nuclear structure calculations. For free neutron beta decay, this yields the relation between V_{ud} , neutron lifetime τ_n , and $\lambda \equiv \frac{g_A}{g_V}$ [TH10]:

$$V_{ud}^2 = \frac{(4908.7 \pm 1.9) \text{ s}}{\tau_n (1 + 3\lambda^2)}, \quad (1.21)$$

with neutron decay experiments providing both the lifetime τ_n and the Axial-vector/Vector coupling ratio λ via the polarized decay correlation A .

1.2 β -decay asymmetry experiments

Figure 1.2 shows the history of A_0 measurements through 2010, described in the following sections. Prior to the UCNA experiment, all measurements were performed using collimated beams of cold

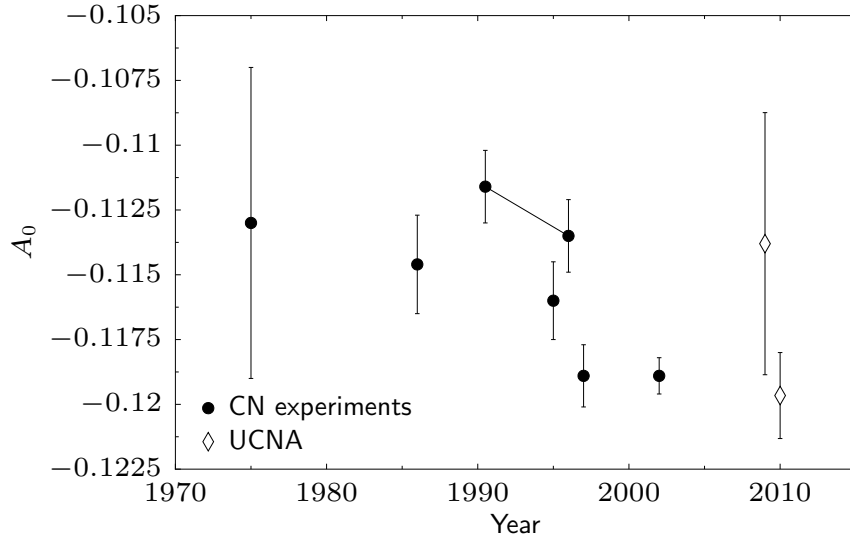


Figure 1.2: History of A experimental results through 2010 (see Figure 8.2 for inclusion of latest results). In time order as shown: [KR75; Bop+86; Ero+90; Sch+95; Yer+97; Abe+97; Abe+02; Pat+09; LMH+10].

neutrons (CN) from nuclear reactors.

1.2.1 Early A measurements at Argonne

The first experimental measurement of A was carried out at Argonne National Laboratory and published by Burgy *et al.* in September 1957 [Bur+57]. A collimated beam of reactor neutrons was polarized to $87 \pm 7\%$ by glancing reflection from a magnetized cobalt-iron mirror. The neutrons' polarization could be reversed by reversing the magnetizing field applied to the mirror, and subsequently depolarized by insertion of an 0.010 inch thick steel plate in the beam path. The neutron beam passed through a decay region with a scintillator beta detector on one side, and a 12 kV accelerating potential to collect protons on a proton-sensitive cathode (a red-hot beryllium copper ellipse replacing the photocathode at the start of a PMT electron-multiplying dynode stack). Electron-proton coincidence rates (of ~ 9 counts per hour) with the neutron polarization directed towards or away from the beta scintillator, or depolarized by the steel plate, indicated a decay asymmetry of $A = -0.37(11)$.

Incremental improvements to the Argonne apparatus produced a series of increasingly precise A results. From measuring the recoiling proton, the apparatus could also be reconfigured for sensitivity to the correlations $B \frac{\langle \mathbf{J} \cdot \mathbf{p}_\nu \rangle}{JE_\nu}$ and $D \frac{\langle \mathbf{J} \cdot (\mathbf{p}_e \times \mathbf{p}_\nu) \rangle}{JE_e E_\nu}$. With an improved proton detector, moved closer to the neutron beam for increased collection efficiency, the Argonne group produced a result of $A = -0.11(02)$ in 1960 [Bur+60]. With a new polarizing mirror and magnetic guiding fields, this was refined to $A = -0.115(008)$ in 1970 [CKR70]. By the final Argonne publication in 1975 [KR75], the measured even rate was up to ~ 7 counts per minute, completing the datasets for a combined (statistics limited) Argonne result of $A = -0.113(6)$.

1.2.2 High rate experiments with Perkeo at ILL

A new experimental design, the PERKEO spectrometer, was built at the Institut Laue-Langevin (ILL) research reactor in Grenoble, and published its first measurement in 1986 [Bop+86]. A beam of cold neutrons (thermalized in a 23 K deuterium moderator volume near the reactor core) was polarized to $> 97\%$ by reflection from a supermirror polarizer. A “current-sheet non-adiabatic spin flipper” could flip the neutron polarization on demand. The polarized neutron beam was directed along the central axis of a 1.7 m long solenoid magnet. At both ends of the solenoid, the magnetic field bent out of the neutron beam path, towards a pair of electron-detecting plastic scintillators. Electrons from neutron decay in the solenoid were confined by the magnetic field and directed towards the detectors on either side. This allowed for a much larger neutron decay region than the Argonne apparatus, with $2 \times 2\pi$ angular coverage for electron detection. An unprecedented beta decay detection rate of ~ 100 Hz allowed a precision measurement of $A_0 = -0.1146(19)$. However, the “bent” magnetic field configuration produced an $\sim 10\%$ correction to A_0 for magnetic mirroring of electrons from decays in the field bend regions.

1.2.3 PNPI and ILL TPC measurements

Meanwhile, at the research reactor of the Leningrad Institute of Nuclear Physics (later renamed the Petersburg Nuclear Physics Institute, PNPI), a new liquid hydrogen cold neutron source with an iron-cobalt polarizing mirror was built in 1985. A neutron decay asymmetry experiment at the cold neutron source collected data in 1989–1990, and published results in 1990–1991 [Ero+90; Ero+91]. The detector apparatus was similar to the Argonne experiment, using coincidences between an electron scintillator detector and a proton collector. At a detected event rate of ~ 3 Hz, the PNPI experiment had much greater statistical reach than the Argonne measurements, without the large magnetic mirroring systematic corrections of the higher-rate PERKEO spectrometer. With a measured result of $A_0 = -0.1116(14)$, however,

“A comparison of the results with the most recent measurements of the neutron lifetime and the angular-correlation constant A shows an appreciable deterioration in the consistency of these data.” [Ero+90]

In order to resolve the discrepancy, a differently designed apparatus was built at ILL [Sch+95; Lia+97]. The polarized cold neutron beam passed through a gas-filled drift chamber between two scintillator plates. The gas volume operated as a Time Projection Chamber (TPC), in which the ionization paths left by a decay electron drifted out (at a known rate) to crossed anode and cathode wires, allowing 3-D reconstruction of the electron’s path. The scintillators measured the energy of the electron. The experimental result of $A_0 = -0.1160(15)$ was in agreement with PERKEO, but 2.2σ from PNPI.

A correction to the 1990 PNPI result was published in 1997 [Yer+97]. Re-analysis of the data accounted for previously ignored distortion of the neutron beam energy spectrum from passage through aluminum windows and air gaps in the beam line. Differences in beam line geometry between the setup for measuring neutron polarization and the setup for beta decay meant that neutron polarization during asymmetry measurement was different from that directly measured. The re-analyzed result of $A_0 = -0.1135(14)$ was in agreement with both the PERKEO [Bop+86] and TPC [Sch+95] measurements.

1.2.4 Perkeo II

In 1997, a newly designed PERKEO II spectrometer at ILL published its first measurement [Abe+97]. Unlike the original PERKEO spectrometer, in PERKEO II the magnetic solenoid is placed perpendicular to the cold neutron beam. Electron detectors at each end of the solenoid are further from the neutron beam (reducing backgrounds), and because the magnetic field does not need to curve out of the neutron beam path, the large magnetic mirroring corrections are eliminated. The experimental result of $A_0 = -0.1189(12)$, however, was in 3σ disagreement with the prior world average.

The PERKEO II collaboration worked to double-check their main experimental systematics (polarization, backgrounds, and detector energy response), publishing a new higher precision measurement in 2002 [Abe+02]. The 2002 PERKEO II measurement agreed with their 1997 number — producing a combined result of $A_0 = -0.1189(7)$ — still in stark disagreement with the preceding PDG world average. The paper was provocatively titled “Is the Unitarity of the Quark-Mixing CKM Matrix Violated in Neutron β -Decay?”

1.3 Ultracold neutrons

This discrepancy between cold neutron beam measurements of neutron decay parameters encouraged the development of alternative experimental methods that would not share common sources of systematic uncertainty. Ultracold neutrons (UCN) offered such a possibility.

1.3.1 Slow neutron scattering

Enrico Fermi published a long article in the Italian journal *La Ricerca Scientifica* in 1936 entitled “*Sul moto dei neutroni nelle sostanze idrogenate*” (“On the motion of neutrons in hydrogenous substances”) [Fer36]. In this paper, Fermi developed a theory to trace the interaction of neutrons with hydrogen-bearing materials (specifically paraffin), all the way from high-velocity elastic and inelastic scattering to final capture to deuterium. Section (10) of Fermi’s paper, “*Urto di neutroni contro atomi di idrogeno legati*” (“Scattering of the neutron from bound hydrogen atoms”), focuses on the < 1 eV scattering regime where the hydrogen nuclei are held in place by chemical forces in the solid. Fermi develops an approximation based around an intermediate length scale R , which is simultaneously much greater than the neutron-proton interaction range ρ and much smaller than the de Broglie wavelength scale λ for the neutron and proton.

In this regime, the fine details of nucleon interactions may be approximated by a steep-edged potential well, characterized by a single “scattering length” $a \ll \lambda$. In the limit where the hydrogen nucleus is free to recoil, conservation of momenta indicates acute-angle scattering of the neutron with differential cross section

$$\sigma d\omega = 4a^2 \cos \theta d\omega \Rightarrow \sigma_{\text{tot}} \equiv \int \sigma d\omega = 4\pi a^2, \quad (1.22)$$

where $\theta \in (-\frac{\pi}{2}, \frac{\pi}{2})$ is the angle between incoming and outgoing neutron momenta in the center-of-mass frame, as if scattering from a hard sphere of radius $|a|$. When the nucleus is rigidly held in

place by chemical bonds in matter, the scattering becomes isotropic with increased cross section

$$\sigma d\omega = \left(\frac{M_n a}{\mu}\right)^2 d\omega \Rightarrow \int \sigma d\omega = 4\pi \left(\frac{M_n a}{\mu}\right)^2, \quad (1.23)$$

as if the “hard sphere” potential had expanded to the “bound nucleus scattering length” $a_B \equiv \frac{M_n}{\mu} a$ [GRL91], where $\mu \equiv \frac{M_n M_N}{M_n + M_N}$ is the reduced mass of the neutron-nucleus system.

When a neutron with wavelength larger than inter-atomic spacings encounters an array of nuclei in matter, coherent scattering over the many individual nuclei produce an effective “Fermi potential” averaged over individual interactions [GRL91],

$$V_F = \frac{2\pi\hbar^2}{M_n} n a_B \quad (1.24)$$

where n is the number density of the nucleus with bound scattering length a_B . For materials with multiple types of nuclei, this may be summed over each variety. Neutrons incident on a material surface with perpendicular kinetic energy lower than the Fermi potential will be entirely reflected. Experiments by Fermi and Zinn in 1946 [FZ46] and Fermi and Marshall in 1947 [FM47], using neutron beams at glancing incidence on various material surfaces, verified Fermi’s low-velocity neutron-scattering theory.

1.3.2 Ultracold neutrons

Zeldovich first published the idea of completely trapping neutrons using the Fermi potential in 1959:

“Let us place neutrons in a cavity surrounded on all sides by graphite. The neutrons of speed higher than critical will rapidly leave the cavity, but neutrons of less than critical speed are blocked in the cavity and vanish only as they decay, with a half-life of approximately 12 minutes.” [Zel59]

The low-kinetic-energy range of neutrons that may be completely trapped by material potentials came to be called “ultracold neutrons” (UCN). Table 1.1 lists the Fermi potential for several materials, along with magnetic and gravitational neutron interactions. Typical Fermi potentials on the order of 200 neV indicate that trapped UCN will have velocities $\lesssim 6$ m/s. In addition to reflection from material Fermi potentials, UCN lie in a kinetic energy range where gravitational and magnetic $\boldsymbol{\mu} \cdot \mathbf{B}$ interactions are significant. The magnetic interaction of ± 60 neV/T means that several Tesla fields available in the lab can be used to manipulate and sort UCN by spin state. The gravitational potential of 102 neV/m allows acceleration and deceleration of UCN populations by meter-scale drops and rises in containing guides.

Practical realization of Zeldovich’s proposed trapping would be slow in coming, for a variety of reasons. The first difficulty, discussed in the Zeldovich paper, is obtaining in the first place a flux of sufficiently slow neutrons — in a room-temperature thermal distribution, only a tiny portion of neutrons ($\sim 10^{-8}$) are in the UCN range that can be completely trapped. Thermalization to liquid helium temperatures increases the fraction to $\sim 10^{-5}$. Beyond the initial difficulty of UCN production, immense care must be taken in the construction of storage volumes to avoid rapid neutron losses to unintended material interactions.

material	potential [neV]
^{58}Ni	335
diamond	304
beryllium	252
beryllium oxide	261
stainless steel	188
graphite	180
copper	168
aluminum	54
1T magnetic field $\boldsymbol{\mu}_n \cdot \boldsymbol{B}$	± 60
1m rise $m_n g h$	102
1m/s velocity $\frac{1}{2} m_n v^2$	5.2

Table 1.1: Neutron interaction Fermi potentials for various materials [GRL91], along with magnetic and gravitational potentials and kinetic energy.

1.3.3 Early experimental UCN sources

Much of early UCN research took place in the USSR, starting with the first observation of UCN in moderated reactor neutrons [Lus+69; Ign90]. Early experiments used solid-state “converter” sources [Ign90], cooled blocks of moderating material with low Fermi potential (such as aluminum) allowing UCN in the tail of the Maxwell spectrum to escape. Advancements in converter materials and design improved the efficiency of extracting neutrons from the low-temperature tail of the Maxwellian distribution; however, these methods produced experimental UCN fluxes typically measured in counts per hour.

1.3.4 High flux UCN turbine sources

To circumvent the limitations of the Maxwell distribution, Steyerl constructed a “neutron turbine” in 1975 at the FRM reactor in Munich [Ste75], in which a cold neutron beam is incident on the high-Fermi-potential vanes of a quickly rotating turbine. Another UCN turbine was built by Kashoukeev in the same year [Kas+75] at the Institute of Nuclear Research and Nuclear Energy of the Bulgarian Academy of Sciences. The turbine vanes move in the direction of the neutron beam; cold neutrons moving forward slightly faster than the turbine vanes (with UCN velocities relative to the vanes’ reference frame) are reflected to lower velocities in the lab frame, and inward towards slower-moving portions of the vanes nearer the turbine axis. After several reflections, cold neutron portions of the incident Maxwellian distribution — with considerably higher flux than the UCN tail — are converted to UCN. The Steyerl design uses a curved blade geometry with UCN extracted opposite the incoming beam, while the Kashoukeev turbine uses flat blades and extracts UCN from a guide along the turbine axis.

In 1986, a new version of the Steyerl turbine was combined with the high flux liquid deuterium moderated cold neutron source at ILL [Ste+86]. The ILL turbine presently delivers the highest available UCN flux to experiments.

1.3.5 LANL SD₂ superthermal UCN source

An alternate method for “superthermal” UCN production (boosting the UCN density above the thermal equilibrium distribution) was proposed by Golub and Pendlebury in 1975 [GP75]. Incoming cold neutrons enter a cryogenic crystal, with phonon vibration modes in the right energy-momentum ranges that a neutron scattering off the crystal lattice will dump most of its kinetic energy into exciting a phonon and be left in the UCN velocity range. Because downscattering to UCN can occur for neutrons entering the crystal from a wide range of directions (rather than the collimated cold neutron beam geometry required by turbines), more UCN can be generated from a lower initial cold neutron flux. This permits UCN production from a small pulsed spallation target source, rather than a reactor neutron port.

A prototype solid deuterium (SD₂) source was built and tested at the Los Alamos Neutron Science Center (LANSCE) at Los Alamos National Labs (LANL) in 1998–2000 [Liu02]. A few μA from the LANSCE 800MeV proton accelerator, striking a spallation tungsten target, provided the initial free neutrons, subsequently thermalized in layers of cold polyethylene before downscattering in the SD₂ volume (see Figure 2.2 and subsection 2.1.1). Continued development of the LANL UCN source [Sau+04; Sau+13] turned the prototype source into a facility for experimental neutron research.

1.4 The UCNA experiment

1.4.1 Initial development

Motivated by the discrepant state of cold neutron A measurements in 1998, the UCNA experiment was proposed to the DOE in April 2000, to use the LANL SD₂ UCN source to measure A . Progress from design to prototype to data-ready experiment is described in [Yua06].

Employing ultracold neutrons for the measurement held the prospect of greatly reducing, or at least providing independent alternatives to, the major systematic concerns associated with cold neutron beam experiments. Backgrounds would be significantly reduced by operating the apparatus away from the higher-radiation environments produced in the path of neutron beams. Neutron polarization would be independent from the systematic uncertainties of beam polarization techniques (though new approaches would be needed for assessing bottled neutron depolarization). The design choice to include a position-tracking wirechamber would trade some additional electron energy losses and backscattering for the advantage of a well-defined fiducial volume and ability to analyze position-dependent detector response. In addition, the wirechambers would provide strong suppression of gamma ray backgrounds.

1.4.2 Neutron lifetime discrepancy

While the UCNA experiment was in its research and development stage, publication of a new neutron lifetime measurement in 2005 [Ser+05] further exacerbated the experimental discrepancies in the Weak sector. The lifetime measurement by Serebrov’s group, bottling neutrons from the ILL UCN source in a high-Fermi-potential oil-coated trap, provided the highest precision result to date ($878.5 \pm 0.7_{\text{stat}} \pm 0.3_{\text{sys}}$ s) — but in 6σ discrepancy with the prior world experimental average

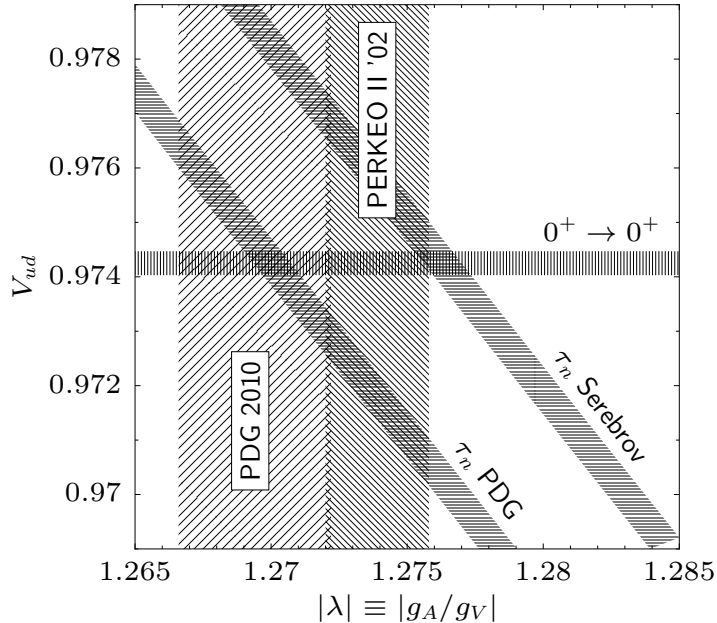


Figure 1.3: State of Weak interactions experimental field in 2010, V_{ud} - λ phase space. PDG 2010 τ_n , V_{ud} , and λ [Nak10], versus PERKEO II 2002 λ [Abe+02] and Serebrov 2005 τ_n [Ser+05].

(885.7 ± 0.7) s. Serebrov’s lifetime measurement allowed much smaller corrections for non-decay neutron losses than prior experimental work — but was it correct? Figure 1.3 shows the state of the experimental field in 2010, with the intersection of V_{ud} and PERKEO II λ ambiguously favoring the Serebrov result over prior τ_n measurements. The importance of producing new (systematically independent) experimental results to clarify the discrepancies had now grown even higher than before.

1.4.3 2009 proof of principle result

Decay data collected in 2007 provided the first proof-of-principle A measurement using UCN, published in January 2009 [Pat+09]: $A_0 = -0.1138(46)_{\text{stat}}(21)_{\text{syst}}$. The result was strongly statistics-limited, due to a very short useful decay data collection period. Systematics were dominated by detector energy response linearity uncertainty ($\pm 1.3\%$) and neutron polarization ($\pm 1.1\%$). Energy reconstruction uncertainty was high on account of apparent highly nonlinear detector response to a pair of conversion electron calibration sources (^{113}Sn and ^{207}Bi), and uncertainty in how detector response varied as a function of position over the fiducial volume. Neither the nonlinearity nor the position response could be precisely mapped out with the data available for the 2009 publication. Nonetheless, relative to the large statistical uncertainty, energy reconstruction was more than sufficiently accurate.

1.4.4 2010 result

The second UCNA result, using new data collected in 2008–2009, was published in October 2010 [LMH+10]: $A_0 = -0.11966(89)_{\text{stat}}(_{-140}^{+123})_{\text{syst}}$. A greatly expanded data set pushed the experiment

from statistically to systematically limited, despite significant improvements in systematics. As before, the largest systematic uncertainties came from polarization (${}_{-0}^{+0.52}\%$) and energy reconstruction ($\pm 0.47\%$). Rising in relevance were systematic uncertainties in Monte Carlo based corrections for backscattering and electron-pitch-angle-dependent detector response, at the $\sim 0.4\%$ level. Energy reconstruction uncertainty was reduced thanks to a more comprehensive calibration scheme, using several conversion electron line sources to map out the nonlinear detector response, combined with the more abundant beta decay data to map position-dependent response. An in-depth discussion of the data analysis behind the 2010 result was published in a comprehensive Physical Review C article in 2012 [Pla+12]. While insufficiently precise to definitively resolve the discrepancy between earlier *A* measurements and the PERKEO II 1997 and 2002 results, UCNA 2010 supported the PERKEO II conclusions.

1.4.5 2013 result

The most recent UCNA result, using data collected in 2010, was published in March 2013 [Men+13], and is the primary topic for this dissertation.

Chapter 2

UCNA experimental overview

This chapter describes the UCNA experiment, starting with a description of the hardware, proceeding in order from UCN production to beta decay and detection in the spectrometer. Then, an overview of the raw datasets collected, and how they are converted to “physically meaningful” information.

2.1 Apparatus

The UCNA experiment resides on Line B of the proton linear accelerator at the Los Alamos Neutron Science Center (LANSCE), at Los Alamos National Labs (LANL). The apparatus consists of:

- a solid deuterium (“SD₂”) UCN source [Liu02; Sau+04; Sau+13],
- guides to transport the UCN [Mak05; Mam10],
- a polarizing magnet and adiabatic fast passage spin flipper (AFP) [Hol12; Hol+12],
- a neutron decay trap in a $2 \times 2\pi$ spectrometer [Pla+08; Ito+07; Rio+11], and
- a data acquisition system (DAQ) for recording the data [Yua06].

Figure 2.1 shows the layout of the components in the UCNA experimental hall. The following subsections indicate the literature in which extensive details on each component may be found, followed by a brief summary of key points.

2.1.1 UCN production

The operating principles of the UCN source are detailed in [Liu02]. Initial prototype performance in 2004 is described in [Sau+04], and the present status in [Sau+13]. Figure 2.2 shows a sketch of the UCN source.

Spallation neutrons are produced by running $\sim 5 \mu\text{A}$ average current from the LANSCE 800MeV proton beam into a tungsten spallation target. This average current arrives in pulse bunches at 5 s intervals, with each bunch consisting of five $\sim 625 \mu\text{s}$ pulses at a 20 Hz repetition rate (each of which in turn has its own internal micropulse structure). The spallation target area is surrounded by beryllium blocks, acting as a reflector to concentrate more of the neutron flux into the UCN source

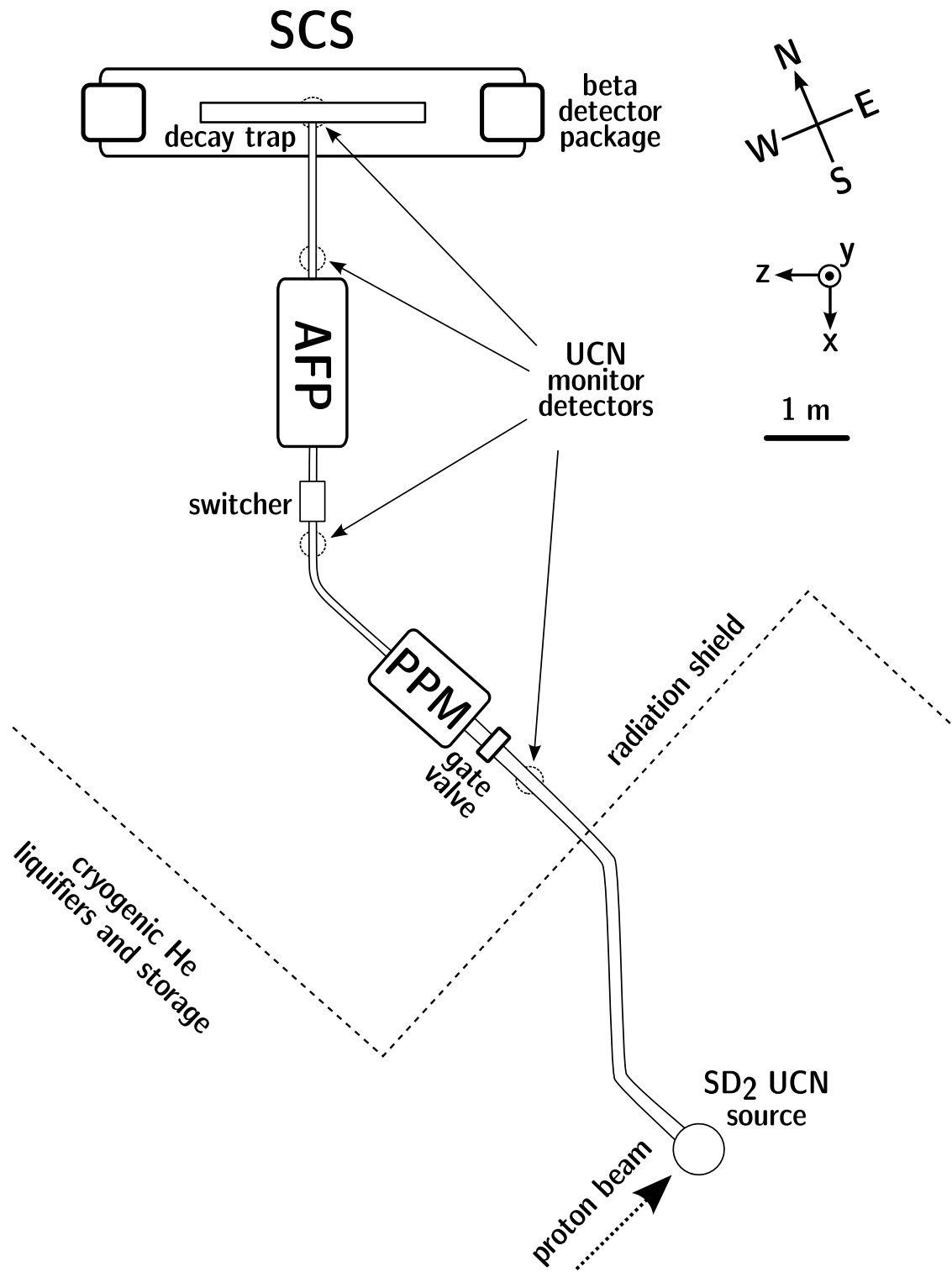


Figure 2.1: UCNA experimental hall layout.

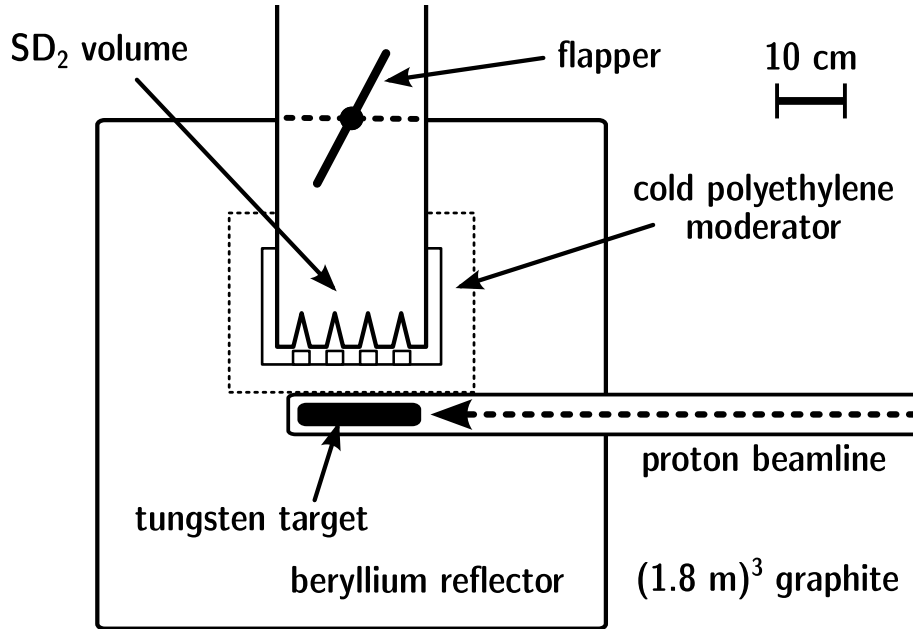


Figure 2.2: Sketch of UCN source, $\sim 1 : 10$ scale.

volume. Outside the beryllium reflector, a $(1.8\text{ m})^3$ graphite block slows stray neutrons, followed by several meters of steel and concrete shielding.

A layer of polyethylene beads, cooled to $\sim 20\text{ K}$ to 100 K by the return flow of cryogenic helium from the solid deuterium source, thermalizes part of the spallation neutron flux into lower velocity cold neutrons (CN). The CN flux enters a 19.7 cm -diameter ^{58}Ni -coated UCN-reflecting volume, containing a few centimeter thick block of solid deuterium frozen at $\sim 5.5\text{ K}$ to 8 K onto the crenellated bottom of the volume. The energy-momentum dispersion curves of phonon vibration modes in the D_2 crystal intersect the energy-momentum range of incoming cold neutrons. A cold neutron can, by transferring its kinetic energy into exciting a phonon, be left nearly at a standstill, becoming an UCN.

Once downscattered into the UCN velocity range, neutrons are especially vulnerable to being lost through capture (with cross-sections typically scaling $\propto \frac{1}{v}$) or upscatter back into the thermal neutron range. UCN loss mechanisms in the UCNA SD_2 source are described and measured in [Mor+02]. The major limiting factors are capture on deuterium or ^1H contamination, upscattering by phonons in the SD_2 (“frozen out” at sufficiently low temperatures), and spin exchange with para-deuterium molecules. The spin and orbital angular momentum $S = J = 0$ ortho-deuterium state is the ground state configuration of D_2 . The para-deuterium state with $S = J = 1$ lies about 7.5 meV higher; spin-exchange interaction with UCN results in a spin flip to ortho-deuterium and the 7.5 meV energy release kicking the neutron into the thermal range. Ortho-deuterium is the stable state at cryogenic temperatures ($kT \sim 1\text{ meV}$), and metastable at room temperature ($kT \sim 25\text{ meV}$) in the absence of spin exchange mechanisms, permitting storage without excessive conversion to para-deuterium for many months as a room temperature gas in a non-magnetic stainless steel gas tank. The system for converting and monitoring the ortho/para composition of deuterium for UCNA is described in [Liu+03], with para-deuterium fractions $\lesssim 2.5\%$ desirable for UCN production. Under

optimal conditions, UCN lifetimes in SD_2 before loss to upscatter or capture of ~ 25 ms are achieved [Mor+02].

Because of the limited lifetime before loss in SD_2 , UCN production is maximized by separating the UCN from the SD_2 as soon as possible. The 5 s pulsed proton beam delivery is designed to permit this. A ^{58}Ni -coated “trap door” above the frozen deuterium (called the “flapper”) is open during each beam pulse, and swings shut shortly after, preventing UCN that have escaped the D_2 from returning. This “flapping” production mode results in a roughly threefold increase in UCN production compared to leaving the D_2 volume continuously open to the guides. The pulsed beam operation also allows prompt beam-correlated backgrounds in experiment detectors to be vetoed by timing cuts. Under typical operating conditions, the average UCN density in the SD_2 source volume below the flapper is ~ 200 UCN/cm³ [Sau+13].

The source volume extends ~ 1 m above the SD_2 before joining the horizontal UCN guide leading out of the shielding stack. The gravitational potential difference cancels out the 102 neV kinetic energy boost imparted to UCN exiting the Fermi potential of the SD_2 . A typical UCN density at the guide exit from the shielding stack of 44 ± 5 UCN/cm³ was measured by neutron capture on a vanadium foil [Sau+13].

The section of the system containing the SD_2 UCN source, which will be filled with atmospheric-pressure D_2 while freezing in or melting out the source, needs to be an isolated pressure volume from the “downstream” vacuum sections, while still allowing UCN transit between. A vacuum-tight metal foil strong enough to withstand potential pressure differentials separates the two sides of the system. The foil is located in the 6 T magnetic field of the “Pre-Polarizer Magnet” (PPM), which accelerates UCN in the “high-field-seeking” polarization state through the foil, while slowing or reflecting low-field-seeking UCN. Exiting the high field region on the other side, UCN slow back down to their initial velocity spectrum. Initially, an aluminum window was used, but it was later changed to stronger, thinner zirconium for improved UCN transmission. A vacuum gate valve immediately preceding the PPM also allows the flow of UCN to be entirely shut off to the downstream apparatus.

2.1.2 UCN transport

The production of Diamond-Like Carbon (DLC) coated quartz UCN guides, and corresponding discussion of UCN transport, is the topic of [Mak05]. Further development of UCN guide coatings, including the DLC-coated copper guides used in 2010, is described in [Mam10].

A good UCN guide needs a surface with a high Fermi potential and low cross sections for UCN capture and upscattering. Since the primary UCN reflecting surface may have minor imperfections or damage from manufacture and installation, a moderately neutron-friendly substrate is also useful for minimizing the impact of small scrapes and dents. Furthermore, a “shiny” surface with specular neutron reflection is beneficial, allowing UCN to transit the guide in a more direct path with fewer potentially lossy surface interactions than the longer random meander produced by diffuse reflections. Stability of the reflecting surface is also important — preferably, it will not rapidly degrade in air, or flake off under thermal and mechanical stress.

Before entering the polarizing magnetic fields, UCN from the SD_2 source are initially contained by ^{58}Ni -coated stainless steel (high Fermi potential and good stability, but expensive to manufacture). Starting 1 m above the source (thus 102 neV lower typical neutron energies), the guide system

switches to electropolished stainless steel (lower potential, but readily available thanks to use in the dairy industry) guides. High stability is especially important for guides near the UCN source, enclosed under heavy radiation shielding, and thus difficult to access and replace.

For sections of the apparatus handling polarized neutrons (everything past the PPM foil), only strictly non-magnetic materials can be used to prevent depolarization on local magnetic impurities. Copper tubing, finished by mechanical polishing followed by electropolishing, was widely used for this purpose in earlier stages of the experiment. Diamond-like carbon (DLC) coatings provide a higher Fermi potential than copper, though with additional difficulty to manufacture, and fragility of the produced surface. DLC coating is used on quartz tubing passing through the RF spin flipper [Mak05], where an electrically non-conductive guide is necessary. As new coating processes were developed, DLC-coated copper gradually replaced bare copper guides in the system [Mam10], including the spectrometer decay trap in 2010.

The endcaps of the spectrometer decay trap must reflect UCN while allowing β -decay electrons to pass with minimal interaction. A UCN-reflecting Beryllium coating on a thin foil ($0.7\ \mu\text{m}$ Mylar in 2010) is used here, minimizing the total mass of material, and the Z^2 -proportional electron scattering cross section for heavier nuclei. Beryllium is near ideal as a UCN reflecting surface, but the health hazards associated with manufacturing and installing beryllium components preclude wider use in the system.

2.1.3 Polarization

A full explanation of how the polarization of UCN is controlled by an Adiabatic Fast Passage (AFP) spin flipper, and polarization purity is measured in the UCNA experiment, is found in [Hol12]. The AFP spin flipper is further described in [Hol+12], with a brief summary following below.

After the 6 T field bump and vacuum volume separation foil in the PPM mostly separate out the high-field-seeking polarization neutrons, a 7 T high-field region near the entrance to the AFP magnet reflects back any remaining low-field-seeking neutrons. The 7 T field produces a $\pm 420\ \text{neV}$ potential for low/high-field-seeking neutrons. This is designed to be substantially higher than the Fermi potential of the preceding UCN guide system, so that any neutrons fast enough to transit the field in low-field-seeking polarization ($> 420\ \text{neV}$ kinetic energy in zero field) would already have escaped the system. A 60° “elbow” bend in the guide path between the PPM and AFP assures that there is no direct line-of-sight for faster neutrons. Between the elbow and the AFP (see Figure 2.1), the UCN guide enters a “switcher,” which can change the guide configuration to redirect the UCN by switching between two differently-directed guide segments on a pneumatically actuated slide. In the normal position for data collection, the switcher connects the elbow straight through to the AFP. When “switched,” the upstream elbow end is left disconnected, and the downstream end (toward the AFP and spectrometer decay trap) is connected to a port leading to a UCN counting detector (subsection 2.1.7), which is used in the polarization measurement process.

The 7 T field bump drops down to a $\sim 1\ \text{T}$ region with a small, smooth field gradient. The guide in this region is surrounded by a “birdcage” RF resonator coil [Hol+12]. The RF coil can be switched on to produce a tuned RF field largely orthogonal to the main field, operating at a frequency that matches a neutron’s Larmor precession frequency ($\sim 28.5\ \text{MHz}$) at some point along the magnetic field gradient. In the adiabatic limit, where the neutron has time to precess $n \gg 1$ times around

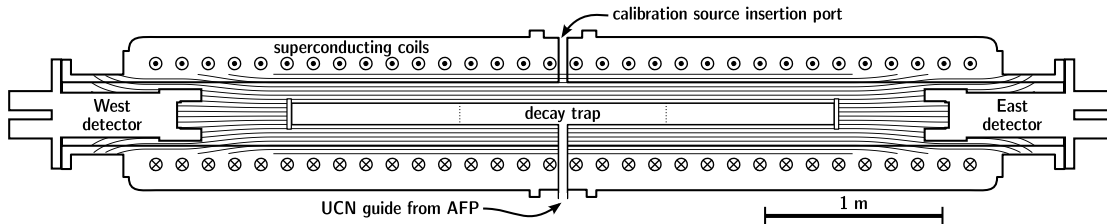


Figure 2.3: Sketch of SCS magnet and detectors, at $\sim 1 : 40$ scale.

the main field compared to slower rotation around the smaller applied RF field, a neutron passing through the RF region resonant with its Larmor frequency undergoes a rotation by π around the RF field to emerge in the opposite spin state on the other side. Thus, by turning the AFP spin flipper on or off, UCN exiting the AFP magnet toward the spectrometer can be set to either polarization.

Between the 1 T field of the AFP spin flipper region and the 1 T field of the decay spectrometer, the magnetic field drops significantly, but is kept sufficiently high to preserve polarization by the fringe fields of the AFP and spectrometer magnets, along with strategically placed permanent magnets. Polarization measurements indicate polarizations of $\langle P \rangle \sim 99.5 \pm 0.5\%$, with potential future improvements to the $99.9 \pm 0.1\%$ level.

When the AFP spin flipper is activated, flipping from high- to low-field-seeker in a 1 T field boosts a neutron’s potential energy by 240 neV, which is converted to kinetic energy as the low-field-seeking neutron accelerates into the lower fields outside the AFP. With the spin flipper on, the UCN enter the spectrometer with a higher velocity spectrum — corresponding to a higher loss rate from more frequent wall bounces or escaping the guides’ Fermi potential. The result is an $\sim 30\%$ reduction in trapped UCN density (thus total neutron decay rate) in the spectrometer compared to the spin flipper off state.

2.1.4 β -decay spectrometer

The beta decay spectrometer is described in [Pla+08]. The spectrometer is housed in the 35-cm-diameter warm bore of the Superconducting Solenoid (SCS) magnet (Figure 2.3), with a 1 T field in the central region containing the 3 m-long, 62 mm-radius UCN decay trap. Typical observed neutron decay rates on the order of ~ 20 Hz indicate a population of $\sim 2 \cdot 10^4$ neutrons in the ~ 50 mm-radius fiducial volume visible to the detectors, at a density of ~ 1 neutron per cm^3 . At either end of the spectrometer (named “East” and “West” for their locations in the experimental hall, with UCN entering the decay trap from the South), the magnetic field expands out to 0.6 T, where the beta decay electron detector packages are located at $\sim \pm 2.2$ m. The field expansion reduces asymmetry-diluting electron backscattering from the detectors, both by forward-directing electron momenta and magnetically mirroring $\sim 80\%$ of the electrons that do backscatter (see subsection 4.2.1).

The detector packages on each side consist of a multi-wire proportional chamber (MWPC) and a plastic scintillator calorimeter read out by four photomultiplier tubes (PMTs). A set of muon vetoes ([Rio+11] and subsection 7.5.4) surrounding the SCS aid in suppression of cosmic ray backgrounds. Figure 2.4 shows a sketch of one detector package.

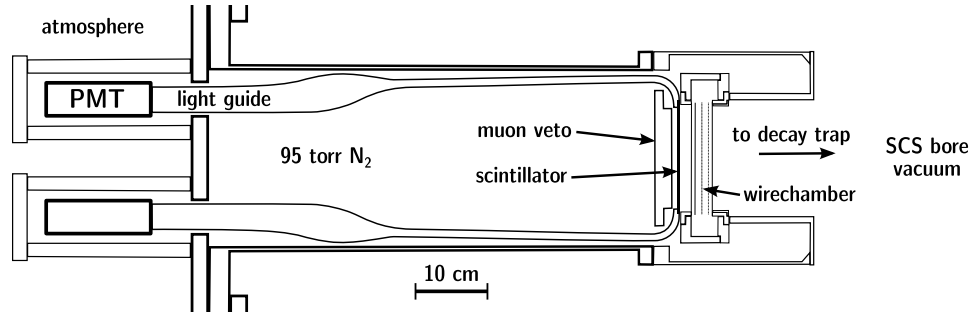


Figure 2.4: Sketch of SCS detector package, at $\sim 1 : 10$ scale.

2.1.5 Wirechambers

The MWPCs (see [Ito+07]) consist of a 100 torr neopentane ($C(CH_3)_4$) gas volume containing two orthogonal cathode wire planes on either side of a central anode wire plane, separated from the spectrometer vacuum by aluminized Mylar windows. Charge signals on the cathode planes indicate the position of events passing through the wirechamber. This allows position cuts to exclude events where wall interactions may occur, and also calibration of the position-varying light transport in the scintillator. The wirechamber is relatively insensitive to gamma rays, allowing gamma backgrounds to be strongly suppressed by requiring a wirechamber coincidence with scintillator signals (subsection 7.5.3). The 7 cm radius circular entrance window frame to the wirechamber sets the ~ 50 mm radius fiducial volume for observable decays in the decay trap (noting that the field expansion from 1 T to 0.6 T expands particle trajectories to cover a $\sqrt{0.6} \times$ larger physical region at the detectors).

2.1.5.1 Wire planes

Each wire plane has 64 wires, spaced 0.1 inches apart; the planes are 1 cm apart. The anode is oriented with the wires vertical; one cathode plane has vertical wires, and the other horizontal. The anode plane in the middle uses $10 \mu\text{m}$ -diameter gold-plated tungsten wires; the small diameter was selected to produce sufficiently high electric fields in the vicinity of the wires for electron-multiplying gas gain, and the material was chosen for sufficient strength. The cathode plane wires were designed to minimize backscattering. Since a high electric field is not needed at the cathode, larger-diameter wires of weaker but lighter and lower- Z gold-plated aluminum were used. The original wirechamber design specified $50 \mu\text{m}$ -diameter wires; a shortage of $50 \mu\text{m}$ wire resulted in the substitution of $70 \mu\text{m}$ diameter wire in some replacement cathode planes in 2011–2013.

2.1.5.2 Gas volume

The neopentane wirechamber fill gas was selected for high electron density (high detection efficiency) with low Z (backscattering minimization) and pressure (allowing containment by thin entrance and exit windows). The pressure is maintained by a PID-controlled gas flow system to well within ± 5 torr variations from nominal. For some brief periods, due to shortages of neopentane, the same pressure of isobutane was used, with no major changes in wirechamber performance seen.

The wirechamber gas volume is separated from the spectrometer vacuum by a $6 \mu\text{m}$ aluminized Mylar entrance window, mechanically supported against the 100 torr pressure differential by 200

denier (22.2 mg/m) Kevlar multi-strand strings spaced at 5 mm intervals. To isolate the scintillators from the neopentane (out of concern for long-term degradation from reaction with the gas), a rear window (also 6 μm aluminized Mylar) separates the neopentane volume from the scintillator volume. The scintillator volume is filled with nitrogen at 5–10 torr lower pressure than the neopentane, to minimize the differential pressure across the rear window, while assuring that the window will not bow inwards and hit the cathode plane. The Mylar windows are nominally 5 mm from the cathode planes, with the rear window 0.5 inches from the scintillator face, though bowing under pressure might change these dimensions by an additional ~ 5 mm.

2.1.5.3 Wirechamber electronics

The wirechambers are typically run with the anode held at $\sim +2700$ V relative to grounded cathode planes and gas volume enclosure (an aluminum box with the aluminized Mylar entrance/exit windows). The West wirechamber, for unknown reasons, runs at higher gain for a given voltage, so it is often operated with the anode at $+2600$ V. Occasionally, the wirechambers become temperamental, and repeatedly trip off their HV supplies by drawing current above an $0.1 \mu\text{A}$ trip setpoint; when this is happening, the chambers may be operated at 50 V to 100 V lower bias (and consequent lower gain).

Charge collected on the anode and cathode planes is routed to the input of a Multi Channels System PA3300 charge-sensitive preamplifier/shaping amplifier module. The PA3300 modules are located within the scintillator nitrogen volume to allow a short signal path from the wirechamber planes. Wirechamber HV breakdown events sometimes burned out individual PA3300 modules. Unfortunately, accessing the modules requires a lengthy (and risky to delicate windows and wirechambers) venting of the system, and substantial disassembly of detector components. Due to the difficulty of replacement, some periods of running were taken with non-functional readout for various anode and cathode signals, requiring additional care in data analysis.

All 64 anode plane wires are connected together for a single readout, connected through an HV isolation coupling capacitor to a PA3300 module. During the 2011–2013 data collection period, the last working replacement anode preamplifier module was burned out. The unamplified West anode signal was eventually routed to a feedthrough connector out of the detector package. A different external and easily accessible Ortec charge-sensitive preamplifier and shaping amplifier replaced the original anode preamplifier electronics.

The 64 cathode wires in each plane are connected together in adjacent groups of 4, to create 16 segment readouts. Each segment is connected to a PA3300 preamplifier module, which includes input isolation up to 500V (potentially allowing the cathode planes to be run at positive bias voltage for additional charge collection from outside the planes, though this has not been done during regular data collection). The group of 16 preamplifier modules for each cathode plane is connected by twisted-pair ribbon cable to a feedthrough out of the detector volume.

Some of the cathode PA3300 modules were found to have a negative DC offset on their output. To compensate for this, the signals are passed through a unity-gain amplifier circuit with adjustable DC offset en-route to the V785 PADC inputs (via twisted-pair ribbon cable). An offset (typically adjusted to 140 mV to 160 mV, then slowly drifting in the 100 mV to 200 mV range) is added to keep the signal pedestal at an appropriately positive value. In addition to cathode PA3300 module damage

from HV breakdown events, the DC offset circuitry also has its own reliability issues, contributing to the portion of runs taken without working readouts for one or more cathode segments.

2.1.6 Scintillator calorimeters

The scintillator calorimeter [Yua06; Pla+08] in each detector package is a 15 cm-diameter, 3.5 mm-thick disk of “EJ-204” plastic scintillator from Eljen Technology. The design thickness is enough to fully stop any electrons with energies up to the 782 keV neutron beta decay endpoint (converting kinetic energy to scintillation light), and most electrons up to 1 MeV kinetic energy. Twelve light guides surrounding the periphery connect the scintillator to four PMTs outside the 0.6 T magnetic field (protected from fringe fields by concentric iron and mumetal shields, and a field-canceling “bucking coil” solenoid). The scintillator and PMT volume, filled with 95 torr of N₂, is separated from the MWPC neopentane by a 6 μm aluminized Mylar exit window on the MWPC. The original detector, used through the 2009 data set, used Burle 8850 PMTs. These had suffered damage from use (likely from arcing in the PMT bases), requiring calibration for large nonlinearities in the 2009 data analysis [LMH+10; Pla+12]. For 2010, these were replaced with new Hamamatsu R7725 PMTs and custom-designed bases [Hic12]. In addition, a “²⁰⁷Bi pulser” gain monitoring system was added to each PMT (section 5.2).

2.1.6.1 PMT electronics

Bias voltage for the PMTs is supplied by a LeCroy HV4032 power supply, with independent HV settings for each PMT (typically 1100 V to 1300 V) manually set to place PMT output levels in the appropriate range for DAQ readout electronics. In a new addition for 2010, PMT output signals are routed through a capacitor coupling box which suppresses issues with drifting DC offsets encountered in prior years. A preamplifier then boosts signal gain by a factor of 10. A LeCroy 428F linear fan-in/fan-out NIM module produces multiple copies of the PMT signal for trigger discrimination and charge-integrated readout.

2.1.7 Auxiliary detectors

Various additional sensors allow monitoring of the apparatus state while collecting data. A solenoidal loop around the proton beamline directed towards the spallation target monitors proton beam current. Temperatures, pressures, magnet fill levels, etc., related to the cryogenics and vacuum systems are periodically (30 s to 60 s) recorded to a database. These data points are not integrated into the subsequent data analysis procedures, but are used by the on-shift experimenters operating the apparatus.

Four UCN-counting detectors [Mor+09] hang 1 m below sampling holes in the UCN guides, using gravitational acceleration to accelerate UCN through an aluminum window into a wirechamber containing ³He and CF₄, where $n + {}^3\text{He} \rightarrow p + {}^3\text{H} + 764 \text{ keV}$. The 764 keV kinetic energy released into recoiling nuclei is converted to ionization in the CF₄, which is collected and read out from an anode wire plane. A single-channel pulse-height analyzer (SCA) generates a trigger for anode charge signals in the range indicating neutron capture.

The locations of the UCN monitors are marked in Figure 2.1. One UCN monitor sits just upstream of the gate valve before the PPM, measuring the UCN flux arriving from the SD₂ source.

The second sits on the alternate branch of the UCN guide “switcher,” to count UCN unloaded from the decay trap during polarization measurements. The third is between the AFP and SCS magnets, covered by a magnetized iron foil that preferentially transmits high-field-seeking polarization UCN, used for tuning the spin flipper to optimal performance [Hol12]. The fourth is below the SCS decay trap.

2.1.8 DAQ

The data acquisition system (DAQ) [Yua06] is based around readout from VME crate modules, connected by a fiber optic link to a computer running MIDAS [Mid] data acquisition software. Additional NIM modules provide signal preamplification and fan-outs as necessary. VME modules used include:

- CAEN V895 16-channel edge discriminator with programmable threshold, used to produce 8 individual PMT triggers,
- CAEN V792AA 32-input, 12-bit charge integrating ADC, used to read out the PMT signals,
- CAEN V785 32-input, 12-bit peak-sensing ADC, used for wirechamber signal readout,
- CAEN V775AA 32-input, 12-bit, 1200 ns-range TDC, used for timing between PMT signals on the two detector sides, and coincidence timing with muon vetoes, and
- SIS 3600 Multi Event Latch, used to record the originating subsystems contributing to the global trigger.

A 1 MHz clock signal connected to scalers reset at the start of each data collection run and at each beam pulse provides event time stamps (in μ s increments) within each data collection run. Figure 2.5 shows a schematic of the signal chain starting from one PMT, with the overall DAQ layout shown in Figure 2.6.

2.1.8.1 Trigger

Triggers for recording an event from the DAQ may come from multiple sources, and are collected and processed into a single global trigger by a CAEN V495 programmable logic unit. Trigger inputs producing a global trigger include:

- coincidence between two PMTs on one detector side above threshold in the V895 discriminator;
- a single PMT above a high threshold, used for the “ ^{207}Bi pulser” gain monitoring system;
- a UCN monitor SCA trigger; and
- a trigger from an LED pulser system (subsection 3.4.4) for injecting light pulses into the scintillator via fiber optic cable.

The global trigger results in the readout of all data-collecting VME modules. TDCs for detector timing information are operated in common-stop mode, starting their “stopwatches” at triggers from their individual subsystems, and stopping the count at the global trigger plus a fixed delay.

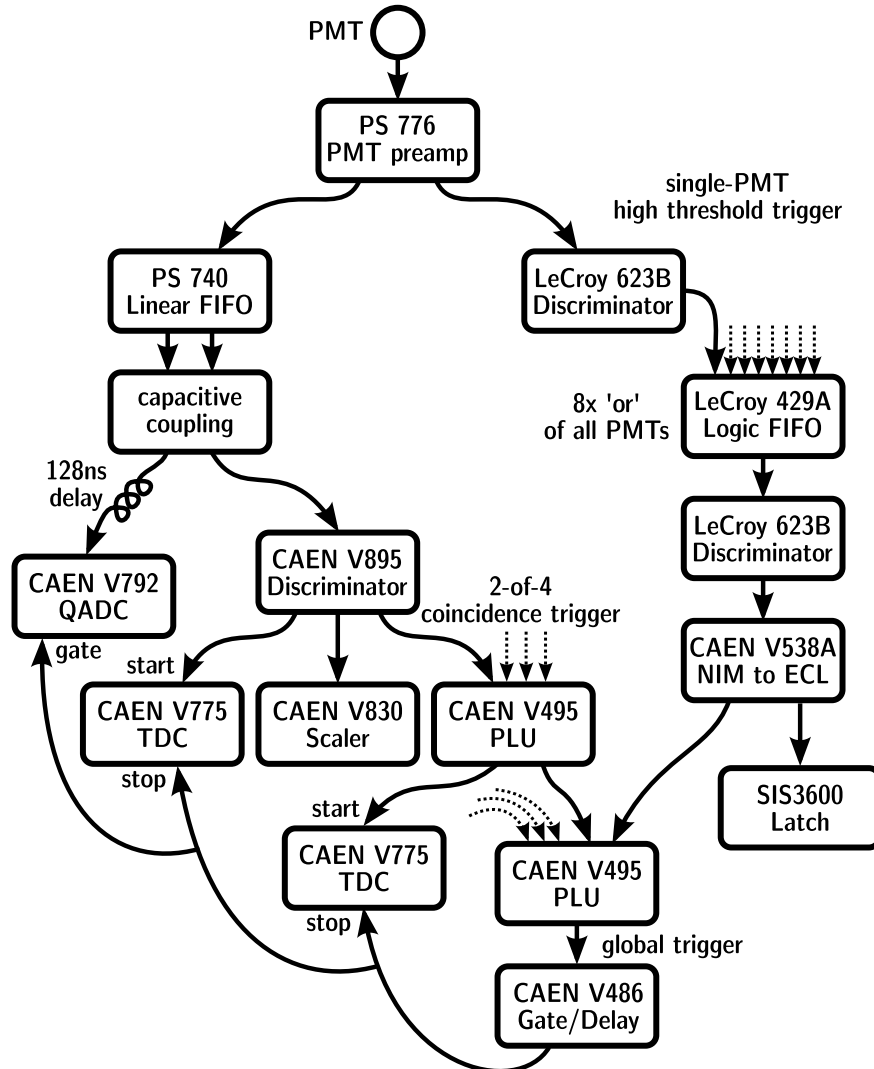


Figure 2.5: Simplified schematic of signal chain for one PMT. Additional logic for suppressing trigger generation while DAQ is “busy” reading out a preceding event is shown in Figure 2.6.

Detector Signals Generating DAQ Triggers

Fast DAQ Trigger Logic

Last Revised: September 29, 2007

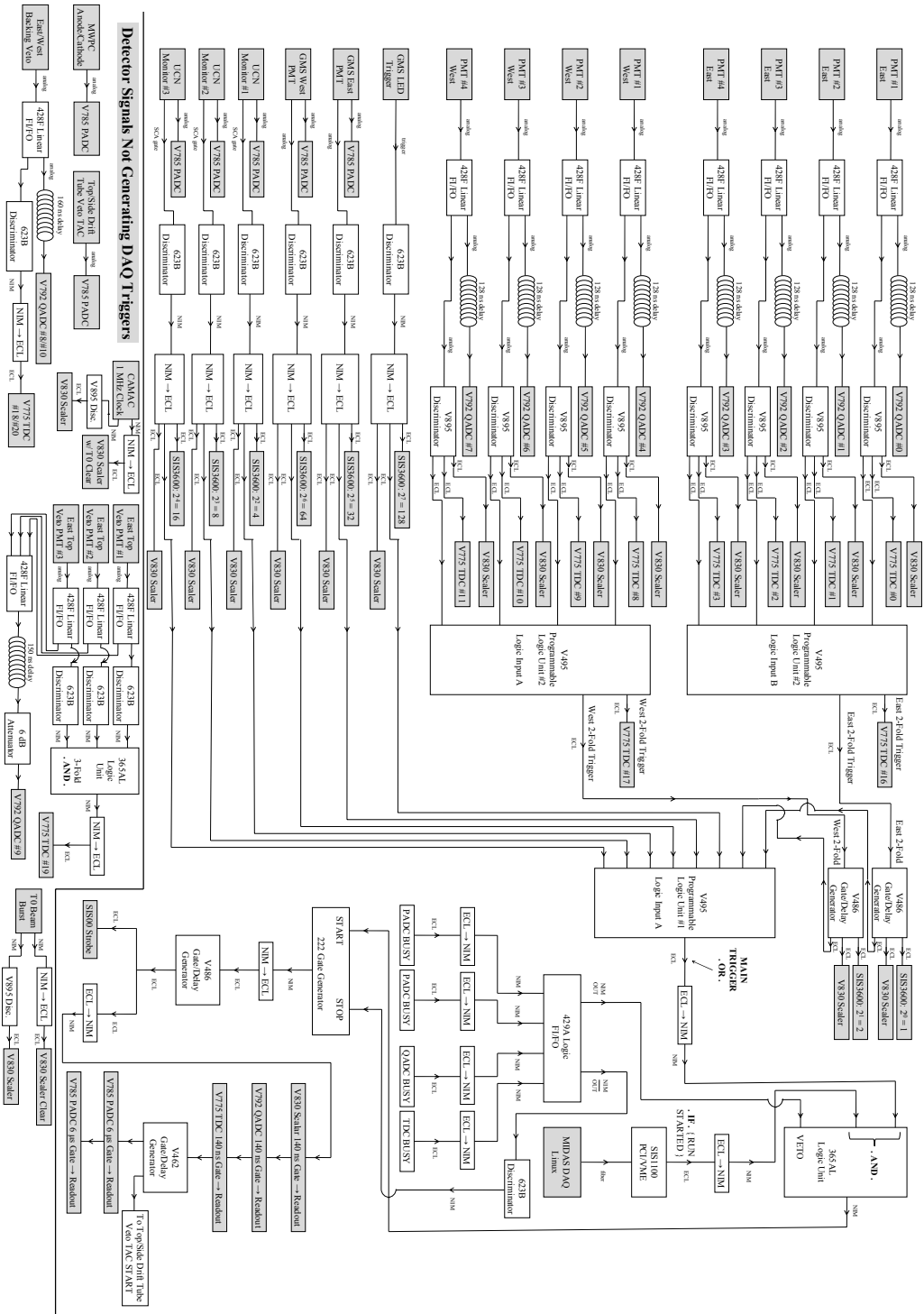


Figure 2.6: UCNA DAQ schematic (as of 2007). Present configuration is largely identical, though with the addition of a high-threshold individual PMT trigger (show in Figure 2.5).

2.2 Data collection

Data is collected in individually numbered runs, lasting from a few minutes up to about an hour (beyond a certain number of events, MIDAS automatically starts a new numbered run). In beta decay data taking mode, runs follow the sequence described in subsection 2.2.2. Additional special-purpose runs are taken to provide calibration data outside the beta decay sequence.

2.2.1 Super-ratio asymmetry

Beta decay data is collected for both neutron polarizations, allowing the asymmetry to be extracted via a detector-efficiency-cancelling “super-ratio asymmetry.” Given a measurement of detected event rates Γ^E, Γ^W on the East and West sides for only one neutron polarization, the simple “bonehead” asymmetry

$$A_{\text{BH}} \equiv \frac{\Gamma_E - \Gamma_W}{\Gamma_E + \Gamma_W} \quad (2.1)$$

mixes the underlying physics asymmetry together with any instrumental asymmetries in detector efficiency. However, given (background-subtracted) rates $\Gamma_{\text{off}}^E, \Gamma_{\text{off}}^W, \Gamma_{\text{on}}^E, \Gamma_{\text{on}}^W$ for both detector sides and for the spin flipper off or on, a “super-ratio” R and “super-ratio asymmetry” A_{SR} may be formed:

$$R \equiv \frac{\Gamma_{\text{off}}^E \Gamma_{\text{on}}^W}{\Gamma_{\text{on}}^E \Gamma_{\text{off}}^W}, \quad A_{\text{SR}} \equiv \frac{1 - \sqrt{R}}{1 + \sqrt{R}}. \quad (2.2)$$

The super-ratio asymmetry should recover an underlying physics asymmetry while canceling out spin flipper independent detector efficiencies and spin flipper dependent total decay rate differences (“trap loading efficiency”). Specifically, consider the case in which the two sides have detection efficiencies η^E and η^W , and there is a total decay rate of $2\Gamma_{\text{off}}$ and $2\Gamma_{\text{on}}$ for the spin flipper off and on states, divided into $(1 \pm A)\Gamma$ electrons heading towards the East and West detectors, respectively, depending on the spin flipper state, then

$$\begin{aligned} \Gamma_{\text{off}}^E &= (1 - A)\eta^E \Gamma_{\text{off}}, \quad \Gamma_{\text{off}}^W = (1 + A)\eta^W \Gamma_{\text{off}}, \quad \Gamma_{\text{on}}^E = (1 + A)\eta^E \Gamma_{\text{on}}, \quad \Gamma_{\text{on}}^W = (1 - A)\eta^W \Gamma_{\text{on}} \\ &\Rightarrow R = \left(\frac{1 - A}{1 + A} \right)^2, \quad A_{\text{SR}} = A. \end{aligned} \quad (2.3)$$

The discussion above applies equally with “rates” exchanged for “counts,” as the conversion factor of time between the two also cancels out. Details of asymmetry extraction via super-ratio are given in subsection 7.1.1.

2.2.2 Run sequence

Runs for beta decay are taken in an alternating sequence of beta decay, background, and depolarization measurement runs, in each spin flipper state. Beta, background, and depolarization runs are taken in groups of three, termed “triads,” with the depolarization run immediately following the beta decay run (starting with a neutron-filled trap from the beta run, and ending with an empty system ready for whatever run type follows). Two triads in opposite spin states form a “pulse pair,” the minimal unit from which a detector-efficiency-canceling “super-ratio” asymmetry can be determined (subsection 2.2.1). Pulse pairs are taken in pairs that alternate the order of beta and background runs and spin flipper states, termed “A” or “B” sequences (each containing twelve runs

	A	B
1	background off	background on
2	beta off	beta on
3	depol off→on	depol on→off
4	background on	background off
5	beta on	beta off
6	depol on→off	depol off→on
7	beta on	beta off
8	depol on→off	depol off→on
9	background on	background off
10	beta off	beta on
11	depol off→on	depol on→off
12	background off	background on

Table 2.1: Beta decay run sequences A1...A12 and B1...B12. “On” and “off” indicate the state of the spin flipper for background, beta decay, and depolarization measurement (“depol”) runs (which include a transition between flipper states).

in four triads). See Table 2.1 for the order of runs in each sequence. Two sequences in either in A→B or B→A order form an “octet” (containing eight beta decay runs, and associated depolarization and background runs). The choice of A→B or B→A order for taking each octet is determined by a coin flip.

Within the sequence, beta and background runs are assured to always start with a “clean” system empty of neutrons from a preceding background or depolarization run. The alternating spin flipper and beta/background run order will also help cancel out some “slowly varying” systematic effects. For example, a slow linear change in detected background rates (due either to real background changes or detector efficiency), which would result in systematic over- or under-subtraction of backgrounds were beta and background runs always taken in the same order, will be canceled out by the alternating beta/background order over an A or B half-octet. The effectiveness of this cancellation is not relied on for determining experimental systematics; however, it provides an additional “margin of safety” for many potential time-varying effects.

2.2.2.1 Depolarization runs

Full details of depolarization measurements are given in [Hol12]. Briefly, the “depol” runs are intended to provide an “*in situ*” measurement of depolarized event fractions produced during beta decay data collection, when combined with a variety of additional “*ex situ*” runs taken to characterize UCN transport properties of the system. A depol run begins with the trap filled with the equilibrium distribution of neutrons produced in the preceding beta decay run. Correctly polarized neutrons are free to traverse the entire length of the guide system. Depolarized neutrons in the trap, however, are blocked by the 7 T field bump of the AFP magnet. Closing the gate valve and switching the switcher drains the correctly polarized neutrons into the UCN counting monitor at the switcher port. After some time necessary to clear the correctly polarized neutrons out of the system, the spin flipper state is reversed; remaining depolarized neutrons in the trap are now of the appropriate polarization to pass the 7 T barrier and be counted by the UCN monitor. Additional “*ex-situ*” system characterization measurements taken outside the normal beta decay measurement cycle are used to translate the observed counts into a depolarized fraction.

2.2.2.2 Run lengths

The length of time taken for beta and background runs was selected by whoever was on data-taking shift to fit within available time constraints. Typically, a length of one hour was used for beta runs when pressing time constraints were not imposed, with shorter runs of ~ 30 minutes to 45 minutes to fit an octet in shorter shifts. Depolarization runs take a fixed time, of ~ 5 minutes. The length of background runs is approximately determined from the signal:background ratio. Given a fixed length of time t available to take both a background run with event rate Γ_b , and a foreground run with combined signal and background $\Gamma_s + \Gamma_b$, dividing the time into lengths $l \cdot t$ for foreground and $(1 - l)t$ for background, and assuming \sqrt{N} counting statistics dominate the uncertainty, the measured background-subtracted rate will be

$$\begin{aligned}\Gamma_{\text{meas}} &= \frac{(\Gamma_s + \Gamma_b)lt \pm \sqrt{(\Gamma_s + \Gamma_b)lt}}{lt} - \frac{\Gamma_b(1-l)t \pm \sqrt{\Gamma_b(1-l)t}}{(1-l)t} \\ &= \Gamma_s \pm \frac{1}{\sqrt{t}} \sqrt{\frac{\Gamma_s + \Gamma_b}{l} + \frac{\Gamma_b}{1-l}} \equiv \Gamma_s \pm \sigma.\end{aligned}\quad (2.4)$$

Minimizing the uncertainty as a function of l gives the optimum use of time

$$\frac{d\sigma^2}{dl} = 0 = \frac{1}{t} \left[\frac{\Gamma_b}{(1-l)^2} - \frac{\Gamma_s + \Gamma_b}{l^2} \right] \Rightarrow \frac{l}{1-l} = \sqrt{\frac{\Gamma_s}{\Gamma_b} + 1}, \quad l = \frac{\sqrt{\Gamma_s/\Gamma_b + 1}}{1 + \sqrt{\Gamma_s/\Gamma_b + 1}}. \quad (2.5)$$

Thus, for a typical signal:background ratio of $\sim 40 : 1$, the beta runs should be roughly $\sqrt{41} \approx 6.4$ times longer than background runs. This guideline was approximately adhered to, though typically erring on the side of slightly longer background runs, closer to 1:5 of the beta run time.

2.2.3 Blinding

To deter experimenter bias pushing the asymmetry analysis toward some subconsciously desired value, calculations of the super-ratio asymmetry prior to “locking in” all analysis methods and corrections were performed including a randomly-generated blinding factor. To circumvent being canceled out in the super-ratio asymmetry, a blinding procedure needs to modify the extracted rates entering the asymmetry by some factor that varies both by detector side and spin flipper state. Blinding was achieved by including separate “East” and “West” event time-stamps t_E and t_W in the data, independently adjusted from the true time-stamp t by a blinding factor δ ,

$$t_E \equiv (1 \pm \delta)t, \quad t_W \equiv (1 \mp \delta)t, \quad (2.6)$$

where the sign of the blinding factor δ switches according to the spin flipper state for the run. The blinding factor δ is selected randomly (and left unknown to experimenters) from a range large compared to expected experimental uncertainties — $\pm 5\%$ for the 2010 data. The resulting “blinded” timestamps are used for calculating the rates entering the super-ratio, changing the resulting super-ratio asymmetry by

$$\begin{aligned}R^{\text{blinded}} &= \frac{\Gamma_{\text{off}}^E/(1+\delta) \cdot \Gamma_{\text{on}}^W/(1+\delta)}{\Gamma_{\text{on}}^E/(1-\delta) \cdot \Gamma_{\text{off}}^W/(1-\delta)} = \left(\frac{1-\delta}{1+\delta} \cdot \frac{1-A}{1+A} \right)^2 = \left(\frac{1-(A+\delta)/(1+A\delta)}{1+(A+\delta)/(1+A\delta)} \right)^2 \\ &\Rightarrow A_{\text{SR}}^{\text{blinded}} = \frac{A+\delta}{1+A\delta} \approx A + \delta.\end{aligned}\quad (2.7)$$

This blinding method does not secure against “malicious” unblinding by a researcher intent on thwarting the system, as it relies on compliance with calculating asymmetries in the blinded manner using the separate clocks. Implementing a “secure” blinding protocol resistant to intentional circumvention is difficult for the UCNA dataset. Restricting access to a small subset of the data prior to unblinding would overly limit statistics for studies of many non-asymmetry features of the data. One potential blinding method would be to remove a small proportion of the events, in a detector side- and spin flipper-dependent manner (based on simplistic approximations of detector event side), from the accessible data. However, the collaboration has deemed such an approach unnecessarily complicated and potentially error-prone.

Chapter 3

Calibrations overview

The data directly collected by the UCNA experiment begins as a long list of numbers read out by the DAQ from dozens of ADC/TDC channels per event. The goal of detector calibration is to establish the correspondence between this jumble of bits and the initial physics processes causing them, building a “system response model” that recreates observed DAQ outputs in response to known physics inputs.

3.1 System response model

The presumed connection between “initial physics” and data recorded at the DAQ is described by the system response model outlined in Table 3.1. The model is broken into three main stages:

1. Event generation, corresponding each physics event to a cluster of primary particles generated with particular momenta at some vertex position. For the UCNA experiment, electrons and gamma rays are considered, while recoiling nuclei and neutrinos are ignored. Event generators are described in more detail in section 4.5.
2. Simulation of particle transport (and corresponding energy deposition) in the detector geometry. Two independent versions of the simulation, based on GEANT4 and PENELOPE codes, have been developed, allowing cross-checks between the two. The GEANT4 code is primarily used for most calibration-related simulations besides free neutron decay, with spot-checks against PENELOPE, while full GEANT4 and PENELOPE simulations are generated for neutron decay. The GEANT4 physics MC is described in chapter 4.
3. Detector response converting deposited energy to ADC/TDC readouts by the DAQ. Details of the detector response model are described in chapter 5. The detector response model is implemented as a set of C++ classes in the UCNA analysis code repository, with model parameters stored in a calibrations database (using MySQL).

3.1.1 Inverse model

The model as described above proceeds in the “forward” direction from initial physics to DAQ readout. Having DAQ data in hand, the inverse process (to recover the initial physics) is of interest. However, the forward process from physics to DAQ is “lossy,” preventing a 1-to-1 inversion mapping

initial physics		
↓	event generators	
E_{true}		E_{recon}
↓	electron transport GEANT4, PENELOPE MC	detector geometry energy deposition scintillator quenching
		↑
E_{dep}, E_Q		E_{vis}
↓	detector response calibrations code and DB	light transport PE statistics PMT linearity PMT gain pedestals triggering quantization
		↑
DAQ readout		

Table 3.1: System response model, connecting initial physics to collected data.

from DAQ readouts to initial physics. Information is lost both by projecting a higher-dimensional initial parameter space onto a lower-dimensional set of observables (for example, the pitch angle of initial events is unobservable, and intertwined with energy loss), and by the stochastic nature of electron transport and detector readout. However, inversion can be approximated in a mean or most probable sense. So long as the inversion is carried out in a consistent manner, the fine details of inversion have negligible impact on final results. The inversion is largely for “cosmetic” purposes, allowing results to be plotted against a physically meaningful calibrated energy scale, which aids intuitive and conceptual understanding of the data. Approximate correctness is useful, to the extent that it minimizes avoidable “mixing” of events with different initial characteristics (such as energy and direction), which would otherwise need to be accounted for by larger simulation-based corrections.

3.1.2 Energy variables

For understanding what is occurring at each stage of the model, one can examine intermediate quantities between the stages (which may be extracted from the simulated model, but not directly observed in data). In particular, two quantities related to the energy of the event are of interest:

- the “true” kinetic energy E_{true} of an electron generated at the beginning of an event;
- the deposited energy E_{dep} in various detector volumes, such as the wirechamber, scintillator, and windows. In the case of scintillator energy deposition, it is useful to also include the effects of scintillator quenching here, producing a “quenched energy” variable E_Q , described in subsection 4.6.1.

Proceeding in the inverse direction starting from DAQ readouts (section 3.3) yields energy quantities observable from the data, approximately corresponding to E_Q and E_{true} in mean sense:

- a “visible energy” $E_{\text{vis}} \approx E_Q$ (subsection 3.3.1);
- a “reconstructed energy” $E_{\text{recon}} \approx E_{\text{true}}$ (subsection 3.3.3).

3.1.3 Scintillator response

The core of the detector response portion of the system response model is the conversion of the “quenched energy” E_Q (proportional to scintillation light) predicted by the MC electron transport model to ADC readouts recorded by the DAQ. The scintillator is viewed simultaneously by four PMTs, each of which is calibrated independently. To first order, the PMT signal chains can be considered fully independent, though correlations between the signals from the PMTs are possible. Correlations are discussed in section 5.5. The “master equation” for a single PMT output in response to quenched energy E_Q deposited at position (x, y) in the scintillator is:

$$\text{ADC} = \lfloor f(E_Q \cdot \eta(x, y) \pm \Delta L) \cdot g + p \pm \Delta p + 0.5 \rfloor, \quad (3.1)$$

in which

- ADC is the DAQ readout for the charge-integrating ADC channel for the PMT,
- $\eta(x, y)$ is the light transport efficiency from the event position in the scintillator (section 5.3),
- $\pm\Delta L$ is photoelectron counting statistics fluctuations (subsubsection 5.4.4.1),
- f is the PMT linearity response (section 5.4),
- g is a time-varying gain factor (section 5.2),
- p is the signal pedestal mean value (subsection 5.1.1),
- $\pm\Delta p$ is a random electronics noise contribution producing the width of the pedestal distribution (subsection 5.1.1), and
- $\lfloor \dots + 0.5 \rfloor$ is quantization to the nearest integer value by the 12-bit ADC.

In this arrangement, variations in the normalization of $\eta(x, y)$ can be absorbed into f . The placement of the gain factor g “outside” of the linearity curve f rather than “inside” is somewhat arbitrary; for the most general case, one would need to distinguish gain changes occurring before or after any nonlinear response stages. However, to the extent that f is nearly linear, the order does not matter.

To rough approximation, 1 ADC channel corresponds to 1 keV of energy deposited at the center of the scintillator. Counting statistics fluctuations $\pm\Delta L$ correspond to ~ 400 photoelectrons per MeV deposited in the scintillator, divided between the four PMTs.

In addition to the ADC output, the scintillator response model also includes DAQ trigger efficiency, described in subsection 5.1.2.

3.1.4 Backscattering categorization

In addition to event “continuous” quantities such as the energy variables described above, modeled events can also be discretely classified by backscattering topology. There are an infinite number of potential backscatter topologies, with multiple bounces back and forth. However, these can be classified according to a finite number of combinations of energy deposition in the detector packages on both sides, in relation to the initial direction of the primary electron, with more complicated multiple-bounce events being lumped together with their simpler counterparts. Figure 3.1 shows various backscatter types schematically. The named event topologies are:

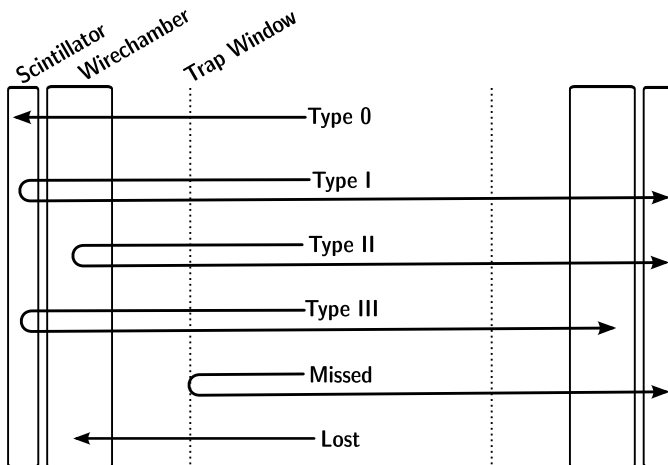


Figure 3.1: Schematic of backscattering events topology; all events initially heading left.

Type 0 (“correct”): energy is deposited exclusively in the wirechamber and scintillator on the side towards which the electron was initially heading.

Type I: energy is deposited in scintillators and wirechambers on both sides of the spectrometer, in the initial direction scintillator first. This typically results from a backscatter within the scintillator, such that the particle is able to reach the opposite side.

Type II: energy is deposited first in the initial direction wirechamber but not scintillator, and then in the wirechamber and scintillator on the opposite side. This typically results from backscatter within the initial direction wirechamber.

Type III: energy is deposited first in the wirechamber and scintillator in the initial direction, and in the opposite side wirechamber. Similar to Type I, but with the electron not making it all the way through the wirechamber to the scintillator on the opposite side.

Missed backscatter: electron reverses direction before depositing energy in any detector, reproducing the observable energy deposition pattern of one of the above (most frequently “Correct”), except with sides reversed relative to initial direction. Results from additional undetectable backscattering off of magnetic field nonuniformities, decay trap endcap foil, wirechamber entrance window, etc.

Lost event: energy is not deposited in either scintillator, so the event will not produce a DAQ trigger and be detected.

Based on observed detector response, informed guesses can be made at the event backscattering topology. Events are classified into observed backscattering classes intended to correspond to their true backscattering topologies, based on scintillator and wirechamber signals for each event (subsection 3.3.2). While the initial side of Type I events can be clearly distinguished using the trigger timing between scintillators (with a minimum transit time of $\gtrsim 15$ ns for electrons crossing between detectors), Type II and III events are only partially distinguishable based on wirechamber energy deposition.

3.2 Calibrations approach

The task of calibrations is to pin down all free parameters in the response model, and evaluate remaining uncertainty. In general, calibration is performed by putting in known initial physics on one side, recording the observed DAQ readouts on the other, and then adjusting free parameters in the model to obtain the same relationship between simulated physics events and DAQ response as observed. Schematically, this can be represented by:

$$\begin{aligned}
 \text{Phys} \rightarrow \text{DAQ}^{\text{obs}} \rightarrow M_{DR}^{-1}(\text{DAQ}^{\text{obs}}) \\
 \updownarrow \\
 M_{DR}(M_{MC}(\text{Phys})) = \text{DAQ}^{\text{exp}} \rightarrow M_{DR}^{-1}(\text{DAQ}^{\text{exp}}),
 \end{aligned}
 \tag{3.2}$$

where “Phys” is known physics introduced into the system (such as a radioisotope sealed source), and DAQ^{obs} is the observed DAQ response. The system response model is represented by a Monte Carlo component M_{MC} and a detector response component M_{DR} , which, together, produce an expected DAQ response DAQ^{exp} to the known input physics. The observed and expected DAQ responses could be compared directly. However, for clarity, it is often helpful to make the comparison in more “physical” units, by applying the approximate detector response inverse M_{DR}^{-1} , so that one is comparing, e.g., $E_{\text{vis}}^{\text{obs}}$ with $E_{\text{vis}}^{\text{exp}}$. Note that, because the stochastic nature of M_{DR} means the inverse M_{DR}^{-1} can only be done in an average sense, $M_{DR}^{-1} \circ M_{DR} \neq 1$ acts to apply the detector’s energy resolution smearing and trigger efficiency to input deposited energy spectra.

Reliance on the neutron beta decay spectrum as a calibration input is avoided where possible, leaving the beta decay results independent from “circular” calibration concerns. Alternate sources of initial “known physics,” outlined in section 3.4, provide the bulk of the calibration data, including scintillator position-dependent light transport and PMT linearity (to which the beta decay spectrum had contributed in prior analyses). The one remaining major calibrations use of beta decay data is a PMT gain adjustment for groups of runs described in section 3.4.

3.2.1 Interdependence and orthogonality

Because only the endpoints of input physics and output DAQ response are subject to direct control and observation, the intermediate stages can never be evaluated in strict isolation. The results observed are always a convolution of effects from every stage in the system.

To some extent, errors in modeling one portion of the chain can be corrected in another. Some overall normalization factors can “float” between different parts of the model with no overall impact whatsoever. For example, absolute measurements of scintillator light transport are irrelevant, as an overall factor can be absorbed into the conversion factor from transported light to photo-electrons. Other model components can only be approximately corrected elsewhere. For example, nonlinearity in scintillator response from quenching, or errors in “dead material” energy losses, can partially be absorbed into PMT nonlinearity, though not perfectly, since position-dependent light transport differences will place the signal at different locations along a PMT nonlinearity curve. In general, mis-attribution of the source of effects will result in a greater spread in the distribution of differences between observed and expected values, even if these can be corrected to coincide on average for a set of observations.

Calibration techniques that maximize orthogonality, allowing one model component to be measured with as little interference as possible from other stages, are preferable when possible. For example, measurement of energy from an isolated mono-energetic line is preferable to locating the endpoint of a continuous spectrum, as the latter will be more sensitive to “smearing” from detector resolution effects, and will depend on detector linearity calibration over a wide range of energies.

In addition, the choice of how to represent model parameters can help with orthogonality. For example, consider how to express a PMT energy resolution parameter in the model. An obvious approach might be to represent this by the number of photo-electrons per keV of deposited energy at the center of the scintillator. However, this approach mixes together effects from many other parameters, such as the light transport efficiency and the conversion factor between energy and ADC channels. A more “orthogonal” parameter representation is to record the energy resolution as a width in ADC channels at a particular ADC channel. This parametrization is more independent of other effects — the observed width of a peak in ADC channels is a stable feature of the calibration data that does not move around if changes are made to other model parameters. The more physical description of energy resolution, in terms of photo-electrons per keV, can be calculated on demand by combining the underlying parameter representation (width in ADC channels) with the other model components (light transport, linearity, energy calibration, etc.), and will improve in accuracy as the other model parameters are better pinned down.

In practice, a perfectly orthogonal set of model parameters and calibration methods is not available, so allowance must be made for some level of interdependence between different parts.

3.2.2 Iterative calibrations

Comparison between $M_{DR}^{-1}(\text{DAQ}^{\text{obs}})$ and $M_{DR}^{-1} \circ M_{DR}(M_{MC}(\text{Phys}))$ provides guidance for adjusting the detector response model for a better match between observed and expected. However, because of the complicated and interconnected nature of M_{DR} , one cannot produce an analytical formula for exactly how to modify model parameters to perfectly match observed and expected data. Nonetheless, one can typically make a decent approximation for how to improve the model, by temporarily ignoring the finer interdependent subtleties.

This motivates an “iterative” approach to calibrations. Rather than attempting to determine every model parameter in “one pass” from a comparison of every available piece of calibration data at once, approximate improvements are made to refine one part of the model at a time. The same data analysis for one model component is revisited repeatedly after working on others, producing small tweaks for interdependent effects. Such an approach relaxes the demands on calibration methods to produce a “perfect” answer on the first attempt. So long as residual discrepancies between observed and expected results are sufficiently reduced at each stage, the process will converge to a stable, well-calibrated point.

Formal proof of stability and convergence of the calibration procedure from first principles would be an ambitious task. However, the convergence and stability of calibrations can be checked during the process, and from the final quality of agreement between observation and model expectations achieved.

3.3 Inverting the Response Model

3.3.1 E_{vis} from ADC

3.3.1.1 Individual PMT energy

Inverting Equation 3.1 so far as possible (by dropping “lossy” stochastic terms), individual PMT energy estimates are obtained from observed ADC values by

$$E_{\text{vis}} = f^{-1}((\text{ADC} - p)/g)/\eta(x, y) \approx E_Q, \quad (3.3)$$

where p , g , η , and f are retrieved from the Calibrations DB, having been determined by the calibration methods described in chapter 5.

3.3.1.2 Combining PMT results

Given the four PMT estimates for the visible energy, these can be combined in a weighted sum to produce a four PMT combined energy. A simple average (equal weights of $\frac{1}{4}$) could be employed. However, selecting a more statistically optimal weighting will increase the energy resolution of the combined result.

Consider an event depositing E_Q at position (x, y) . Some fraction $\eta_i(x, y)E_Q$ of this light reaches each PMT, where it is converted into $\tilde{N}_i = N_i \pm \sqrt{N_i}$ photoelectrons according to the quantum efficiency C_i of the PMT, such that $N_i = C_i\eta_i E_Q$. The ADC signal for PMT i is converted to the single-PMT energy estimate $E_i = E_Q \pm \frac{E_Q}{\sqrt{N_i}}$, corresponding to $\tilde{N}_i \equiv C_i\eta_i E_i$. Statistically optimal $1/\sigma^2$ weights would thus be $\frac{N_i}{E_Q^2} = \frac{C_i\eta_i}{E_Q}$. Thus,

$$E_Q \approx \frac{\sum_i \frac{C_i\eta_i}{E_Q} E_i}{\sum_i \frac{C_i\eta_i}{E_Q}} \pm \frac{1}{\sqrt{\sum_i \frac{C_i\eta_i}{E_Q}}} = \frac{\sum_i \tilde{N}_i}{\sum_i C_i\eta_i} \pm \sqrt{\frac{E_Q}{\sum_i C_i\eta_i}} \equiv E_{\text{vis}} \pm \delta E_{\text{vis}}, \quad (3.4)$$

showing that the statistically optimal estimate for the energy comes from counting the total number of observed photoelectrons for an event $\tilde{N}_{\text{tot}} \equiv \sum_i \tilde{N}_i$, and multiplying by a (position dependent) photoelectrons-to-energy conversion factor $K(x, y) \equiv 1/\sum_i C_i\eta_i(x, y)$. Note that position dependence only appears in the summed combination $\sum_i C_i\eta_i$, which is a smoother function of position than the individual PMT light transport maps, which are thus less sensitive to errors in position reconstruction. Note also that the coefficients C_i , derived from observed energy resolution of each PMT, appear only as weighting factors on the individual-PMT energy estimates E_i . Errors in determining C_i — changing the weighting selected for each PMT — have no impact on the mean reconstructed energy.

3.3.2 Backscatter classification

Refer to Figure 3.1 for the backscatter topology type definitions. Lost backscatters (including any event that does not pass trigger-producing threshold in either scintillator) will be absent from the recorded data. Missed backscatters will be unidentifiable, and distributed among the other backscatter classes. Other backscatters are categorized as described below.

1 st Scint.	1 st WC	2 nd WC	2 nd Scint.	Type
+	+	-	-	0
+	at least 1		+	I
+	+	+	-	II/III
+	-	-	?	gamma
+	-	+	-	gamma

Table 3.2: Observed backscatter classification, based on whether each scintillator and wirechamber triggers (+), does not trigger (-), or “?” for either. 1st and 2nd side determined by scintillator timing when both scintillators trigger, otherwise is side of sole triggering scintillator.

3.3.2.1 Initial classification

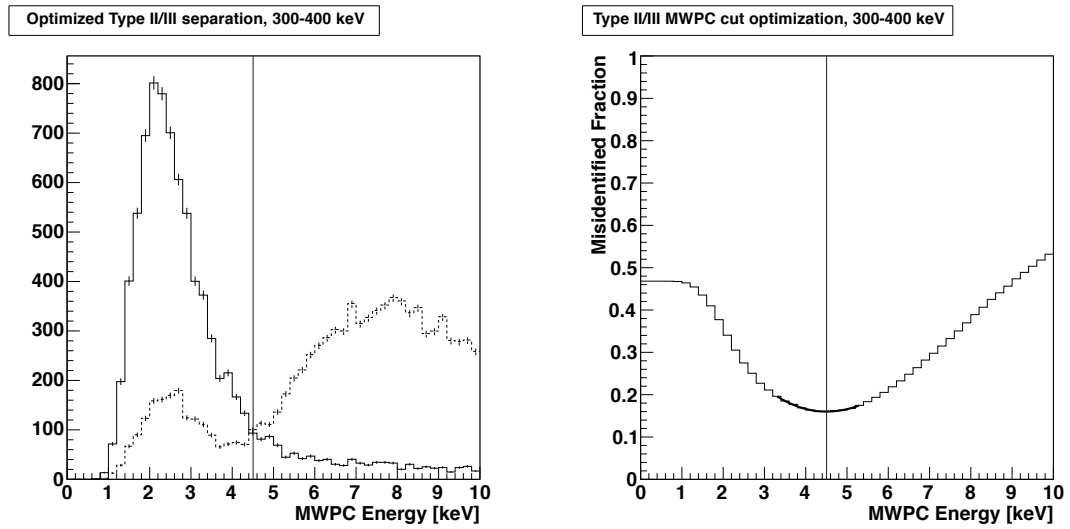
Backscatter classification depends on which detector subsystems are marked as having triggered during the event. See subsection 5.1.2 for scintillator trigger criteria, and section 6.2 for the wirechambers. The scintillator which triggers for an event, or the first scintillator to trigger based on DAQ timing information, is designated as the “primary” side for the event, with the other side designated “secondary.” Table 3.2 shows the resulting classification scheme. For all event types except Type II, the primary side also indicates the likely initial direction of the electron. Note that events lacking a scintillator/wirechamber trigger pair on at least one side are tagged as gamma rays (designated by “TYPE_IV_EVENT” in the analysis code). Type II and III events are ambiguously distinguishable, as no precision timing information is available from the wirechambers. They are approximately separated as described below.

3.3.2.2 Type II/III separation

Type II and III events are separated according to scintillator and wirechamber signals based on MC predictions. The goal of a separation scheme is to maximize the fraction of events which are assigned to their true initial direction (equivalently, to minimize the misidentified event fraction). In general, Type III events will deposit more energy in the primary side scintillator (from making a double pass) than Type II events. However, there is a substantial amount of overlap between the observable spectra for the two event types.

Given some observable parameter space, such as primary side scintillator and wirechamber energy, optimal separation efficiency is achieved by placing cut boundaries in that parameter space along contours of equal probability for Type II and III events. Simulations indicate that there is virtually no useful information for improving separation efficiency from the secondary side wirechamber — secondary side wirechamber energy deposition spectra from Type II and III events are practically identical. Useful separation information comes from primary-side scintillator and wirechamber energy deposition.

Simulated Type II/III beta decay events are binned by scintillator energy (100 keV-wide bins) and true initial direction, with corresponding wirechamber spectra generated for each energy bin. For each energy bin, histograms are made for primary side wirechamber energy deposition (Figure 3.2a) for events with each true initial direction. To optimize the separation cut position, the misidentified event fraction as a function of cut location is calculated from the histograms, and the minimum is located by a cubic polynomial fit (Figure 3.2b). This fitting procedure permits interpolation of the crossover point between histograms, which might be “noisy” from limited statistics.



(a) Wirechamber spectra for true Type II (solid line) and III (dashed) events, with vertical line at optimal cut position. (b) II/III misidentified fraction as a function of cut position, with cubic fit around minimum to locate optimum cut (vertical line).

Figure 3.2: Optimization of wirechamber energy cut for maximizing Type II/III event separation efficiency. Plots for simulated beta decays with 300 keV to 400 keV scintillator energy.

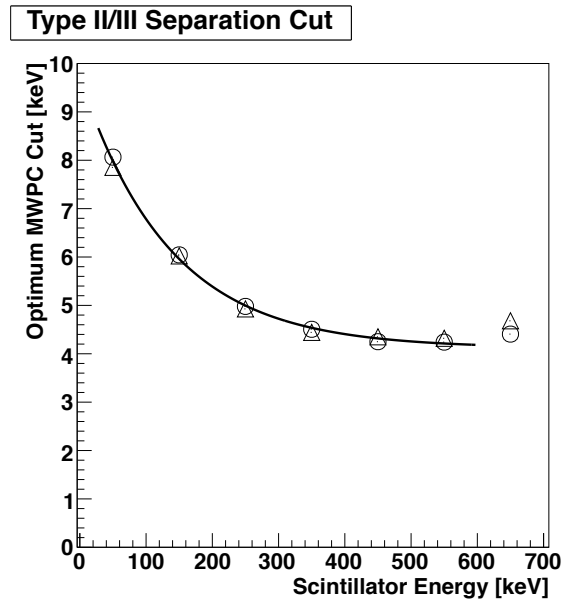


Figure 3.3: Optimum Type II/III wirechamber energy cut position as a function of scintillator energy, and fit curve. Circles = East side primary scintillator events; triangles = West.

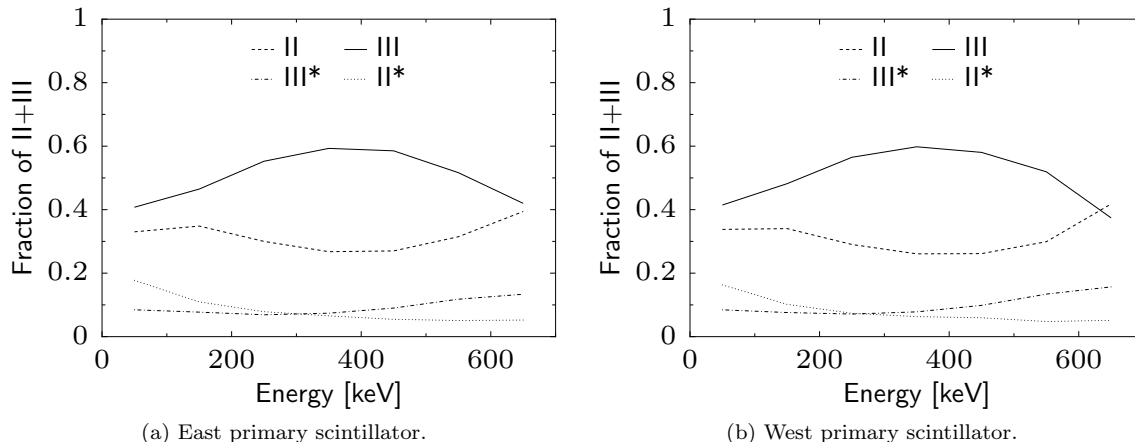


Figure 3.4: Predicted separation accuracy for 2010 data using optimized cut. Type II and III indicate correctly identified events; II* stands for IIs misidentified as IIIs, and likewise for III*.

Figure 3.3 shows the optimum cut position extracted by this method as a function of energy for the 2010 data analysis. The cut position is fit by a curve of the form

$$E_{\text{cut}} = C_1 + C_2 e^{-E_{\text{vis}}/C_3} = 4.0 + 5.4 e^{-E_{\text{vis}}/149 \text{ keV}} \text{ keV} \quad (3.5)$$

to define the cut as a continuous function of E_{vis} . The East and West detector sides show very similar behavior, so a common curve was fit to both. Figure 3.4 shows the correctly and incorrectly identified fractions of Type II/III events predicted by simulation using this optimized cut.

3.3.3 E_{recon} from E_{vis}

The E_{vis} determined above is intended to correspond to the quenched energy E_Q deposited in the scintillators, after energy losses in preceding material and signal reduction due to quenching. From here, we wish to get reasonably close to the “original” energy of the event, before such loss mechanisms. In the case of major changes to detector response, a separate mapping might be employed for different sets of runs; this was not deemed necessary for the 2010 data analysis, which used the same detector geometry with only minor PMT response changes throughout. A more sophisticated approach to energy reconstruction might develop a function in multiple variables, depending on observed energy deposition in both scintillators and wirechambers. For this work, a simple function mapping from $E_{\text{vis}} \approx E_Q$ to reconstructed energy $E_{\text{recon}} \approx E_{\text{true}}$ (separately for each backscatter type) was employed.

To do this, an approximate map is determined from simulation between initial E_{true} and resulting mean E_{vis} . Simulated beta decays are run forward through the detector response model to simulated DAQ readouts, then reconstructed back to E_{vis} by the same processing chain as the data. Events are binned by E_{true} , and the mean E_{vis} produced for each original E_{true} bin is determined. This is done separately for events identified as Type 0, I, or II/III backscatters, as different backscatter types correspond to significantly different mean energy losses and quenching impacts.

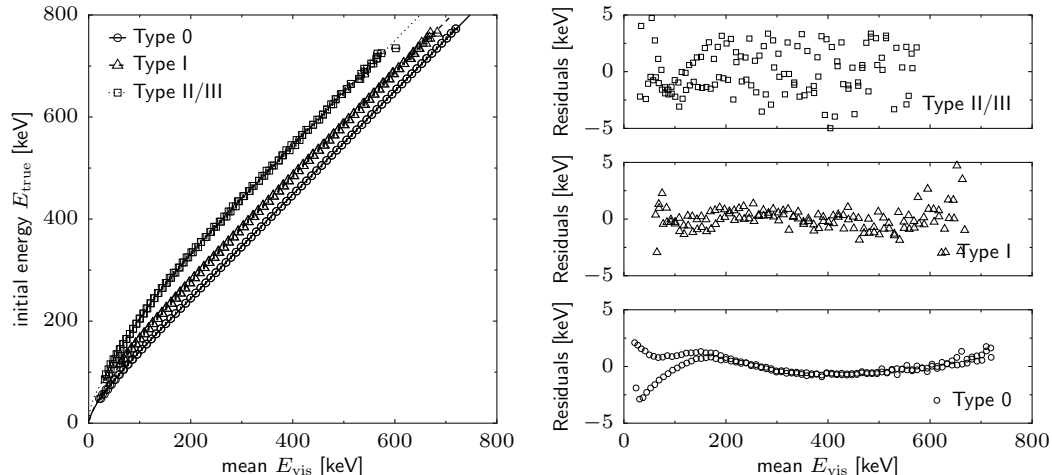


Figure 3.5: $E_{\text{vis}} \rightarrow E_{\text{true}}$ curves from simulation for the 2010 data, and residuals from fits. Note that the split in Type 0 residuals below 200 keV is due to different East/West detector behaviors, which are averaged together by the fit.

The E_{true} versus mean E_{vis} points for each backscatter class are fit with a smooth curve, which is uploaded to the Calibration DB. The form of the fit curve employed is

$$E_{\text{recon}} = c_0 + c_1 E_{\text{vis}} + \frac{c_{-1}}{E_{\text{vis}}} + \frac{c_{-2}}{E_{\text{vis}}^2} \quad (3.6)$$

down to the E_{vis} of the lowest data point with sufficient statistics (≥ 50 points produced by simulation), and then extended smoothly to $(0, 0)$ using a power law form cE_{vis}^α matching first derivative, at the point of juncture with the fit curve. Using this curve, events are assigned a reconstructed energy $E_{\text{recon}} \approx E_{\text{true}}$ as a function of their E_{vis} and backscatter type. Figure 3.5 shows the curves determined by this method for the 2010 data analysis, which were simulated based on the detector response for a single “representative” run and averaged over the two detector side responses.

3.4 Calibration data sources

This section describes the properties of various e^- sources with “known initial physics” that are useful for characterizing the UCNA detector. The specifics of how each item is used in calibrations are reserved for the following chapters on each detector subsystem.

3.4.1 Sealed sources

Electron-emitting radioisotope decay sources provide well-characterized localized sources of beta particles. Sealed between thin aluminized Mylar foils for safe handling, such sources can be inserted into the UCNA spectrometer. The UCNA decay trap is designed with a removable plug in the wall of the center section (opposite the incoming UCN guide). This plug can be removed, allowing sealed sources to be inserted into the center of the decay trap, in a holder (accommodating three sources in a row) on a sliding rod. Figure 3.6 shows the three-source holder, as seen by the UCNA

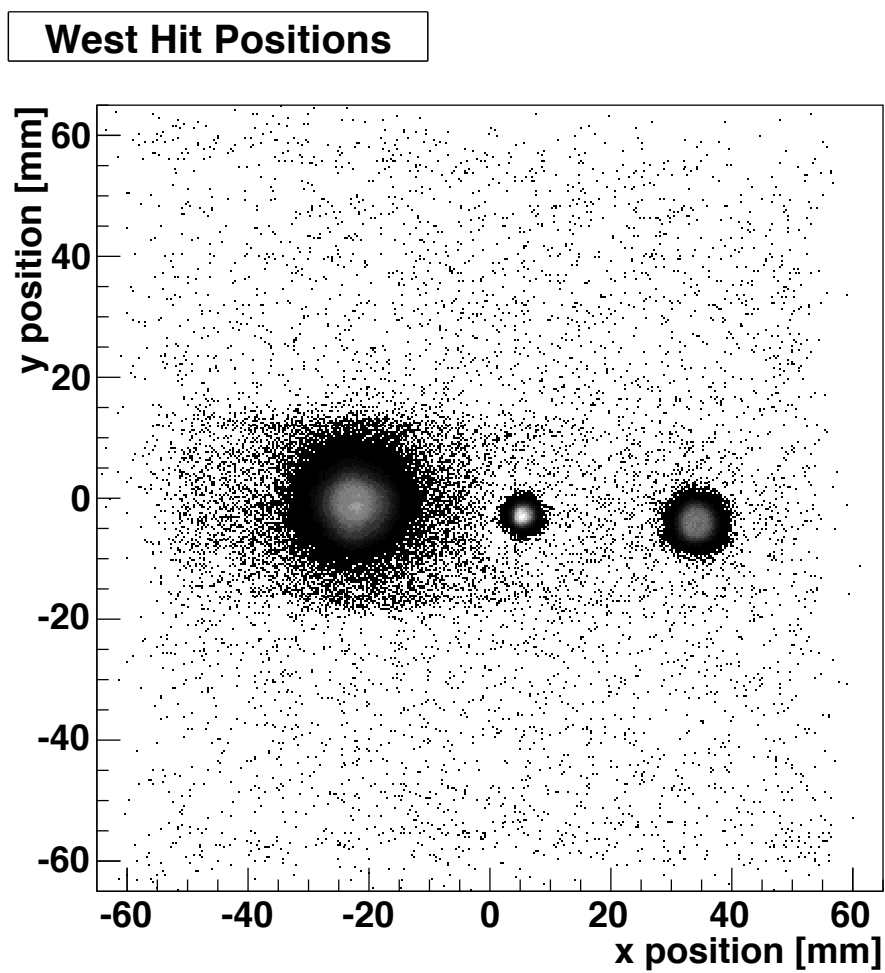


Figure 3.6: Detector hit positions with three sealed sources in holder (left to right: ^{207}Bi , ^{139}Ce , ^{113}Sn). The body of the source holder around ^{207}Bi is visible in Compton scatter electron counts; see section A.3.

Source	Half-life	Feature	Decay %
$^{109}_{48}\text{Cd}$	461 d	75 keV CE	98%
$^{139}_{58}\text{Ce}$	138 d	132 keV CE	20%
$^{114m}_{49}\text{In}$	49.5 d	175 keV CE 1989 keV β^-	80% 99%
$^{113}_{50}\text{Sn}$	115 d	368 keV CE	36%
$^{207}_{83}\text{Bi}$	31.6 y	56.7 keV Auger 502 keV CE 995 keV CE	2.9% 2.1% 9.6%
$^{137}_{55}\text{Cs}$	30.1 y	630 keV CE 514 keV β^- 1176 keV β^-	9.6% 95% 5.3%

Table 3.3: Electron source radioisotopes useful for UCNA calibration. Conversion electron energies are averaged over shell splittings.

Z	K	L ₁	L ₂	L ₃	M ₁	M ₂	M ₃	M ₄	M ₅
47 Ag	25.51	3.81	3.52	3.35	0.72	0.60	0.57	0.37	0.37
49 In	27.94	4.24	3.94	3.73	0.83	0.70	0.66	0.45	0.44
56 Ba	37.44	5.99	5.62	5.25	1.29	1.14	1.06	0.80	0.78
57 La	38.92	6.27	5.89	5.84	1.36	1.20	1.12	0.85	0.83
82 Pb	88.00	15.86	15.20	13.04	3.85	3.55	3.07	2.59	2.48

Table 3.4: Inner electron shells binding energy in keV from [BB67], for UCNA conversion electron sources’ final state nuclei.

wirechamber. The holder can be slid back and forth in the x direction, allowing the sources to be placed at various locations along a line across the detector.

Isotopes of interest are those with distinct electron lines in the $\lesssim 1$ MeV range applicable to beta decay. The isotopes must also be sufficiently long-lived to allow use over a few months of data gathering. Table 3.3 lists six isotopes of interest for UCNA data calibrations, along with their main electron features. Details of each isotope’s decay are given in Appendix A, along with example measured energy spectra. For the 2010 data analysis, three conversion electron sources were used: ^{139}Ce , ^{113}Sn , and ^{207}Bi . Three additional calibration sources (^{114m}In , ^{109}Cd , and ^{137}Cs) were incorporated into the calibrations routine in 2011–2013, extending the lower energy end of the calibrations range and filling in “gaps” between the three 2010 sources.

3.4.1.1 Conversion electrons

Conversion electron sources are especially useful for energy calibration, as they provide distinct energy lines. Conversion electrons are emitted at the energy of the gamma associated with the transition, minus the binding energy of the inner-shell electron emitted. Table 3.4 shows binding energies for the K, L, and M shells for nuclei involved in UCNA calibration sources. The UCNA detectors’ energy resolution is insufficient to resolve the splitting between electron shell lines, though the presence of multiple lines does modify the shape of observed source peaks. Uncertainty in the splitting ratios (primarily between K and L shells) translates into uncertainty in the average energy of the conversion electron peak observed by the detector, which is generally small (~ 0.1 keV) compared to overall calibration uncertainty.

Nucleus, J^π	$T_{1/2}$	P.A.	Features
$^{125}\text{Xe } 1/2^+$	16.9 hours	0.095%	53.8 keV CE 0.58%
			84.5 keV CE 0.25%
			159.6 keV CE 7.3%
			215.6 keV CE 2.4%
$^{127}\text{Xe } 1/2^+$	36.3 days	0.089%	452.5 keV CE 0.06%
			119.1 keV CE 2.0%
			143.0 keV CE 4.2%
			174.2 keV CE 7.8%
$^{129m}\text{Xe } 11/2^-$	8.88 days	1.91%	346.5 keV CE 0.35%
$^{131m}\text{Xe } 11/2^-$	11.84 days	4.07%	119.1 keV CE 2.0%
$^{133}\text{Xe } 3/2^+$	5.25 days	26.9%	143.0 keV CE 4.2%
			50.0 keV CE 62.9%
$^{133m}\text{Xe } 11/2^-$	2.20 days		174.2 keV CE 7.8%
$^{135}\text{Xe } 3/2^+$	9.14 hours	10.4%	171.9 keV CE 95.5%
			218.6 keV CE 6.6%
$^{135m}\text{Xe } 11/2^-$	15.3 min.		140.7 keV CE 98.1%
$^{137}\text{Xe } 7/2^-$	3.82 min.	8.86%	207.7 keV CE 89.9%
			423.9 keV CE 0.43%
			3718 keV β^- 31%
			4173 keV β^- 67%

Table 3.5: Xenon isotopes accessible by neutron capture on stable xenon. P.A. = parent nucleus abundance in natural isotopic composition.

3.4.2 Activated Xenon

A calibration method added for the 2010 dataset is using neutron-activated xenon as a decay source. The activated xenon is produced by freezing a small quantity of natural xenon into the volume normally holding UCNA’s solid deuterium UCN source. The frozen xenon is subjected to the thermalized spallation neutron flux in the source for several minutes, and then warmed up and pumped out into a storage volume. Portions of this activated xenon can then be injected into the spectrometer vacuum, filling the entire system volume and producing decay products visible in the UCNA detectors. Table 3.5 lists the xenon isotopes, and their main decay features, which are accessible from neutron capture on natural xenon and long enough lived to make it into the spectrometer.

The xenon produced in this manner is a mixture of all these isotopes, in quantities evolving with time. Figure 3.7 shows a simulation of how each individual species would appear in the UCNA detectors. Most species contribute to a 100 keV to 200 keV peak, the precise shape of which will depend on the mixture. Note that the strange shape of the $^{137}\text{Xe } 7/2^-$ spectrum (observable only from “freshly made” activated xenon) is due to most of the electrons from its multi-MeV beta decays punching through the 3.5 mm UCNA scintillator, approximately producing a minimum ionizing particle energy distribution. The one distinct long-lived feature in the mix is the 915 keV endpoint beta spectrum of $^{135}\text{Xe } 3/2^+$. Details of the observed spectrum and its time-evolving composition are discussed in section 5.3.

While not providing distinct lines useful for energy calibration, activated xenon has the useful attribute of covering the entire detector fiducial area with a uniform decay spectrum. Large amounts

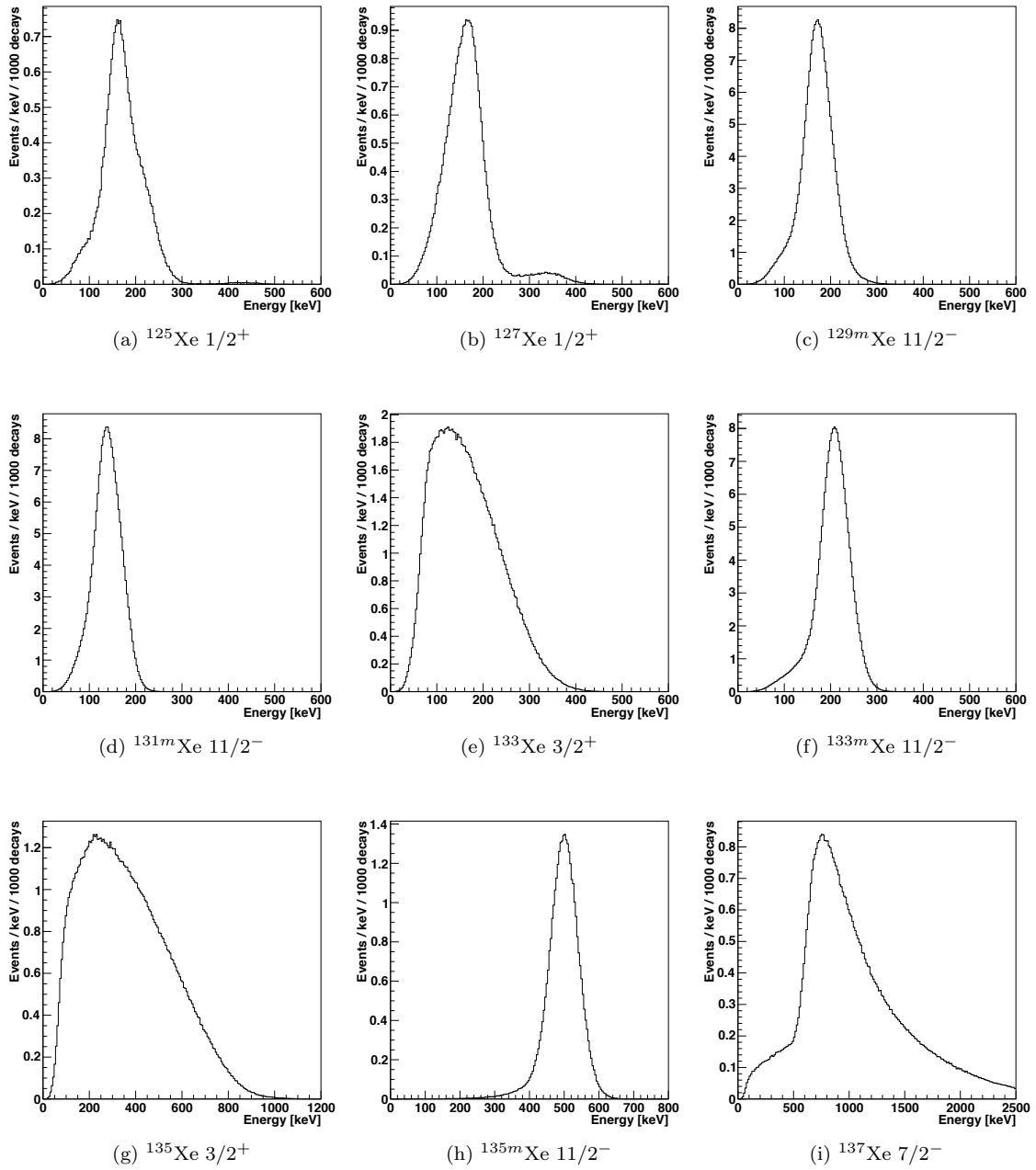


Figure 3.7: A menagerie of Xenon isotopes, as seen by the UCNA spectrometer (simulated).

of xenon data can be accumulated, running at ~ 1 kHz detected decay rates for many hours, providing high-statistics indicators of detector response as a function of position.

3.4.3 ^{207}Bi gain monitoring pulser

With the installation of new PMTs at the start of the 2010 run, a new gain monitoring device was added to the system, based on the concept of attaching a constant-output scintillating “light pulser” to each PMT described in [MBM76]. Each “pulser” consists of a dab of ^{207}Bi inside a hole drilled into a small block of scintillator. All but one side of the pulser block are covered in white light-reflective material, and the remaining surface is covered by an optical attenuator to roughly match the light output to that coming from the beta scintillator. A pulser is glued to the face of each PMT next to the light guide coming from the beta scintillator.

At the DAQ electronics cabinet, signals from the individual PMTs are split off to a discriminator with a much higher threshold than the discriminators for the individual PMT triggers forming the 2-fold coincidence trigger. A new type of event trigger is added to the DAQ, for large amplitude single PMT events (which would be ignored by the 2-fold coincidence trigger).

The light attenuation for signals from the pulsers was less than originally intended, resulting in the 1 MeV line in the ^{207}Bi spectrum falling at roughly the equivalent of 3 MeV events from the scintillator. Keeping this peak within the 12-bit ADC range results in compressing “normal” signals into the bottom third of the range. However, this is not highly problematic, as ADC resolution and small-signal noise is still far from the limiting factor in system resolution. Indeed, running the system at lower gain to accommodate the pulser peak provides a comfortable amount of “headroom” to assure that all other scintillator signals remain below clipping. While the pulser peak lies outside the signal range calibrated for linearity, the good linearity of the PMTs installed for 2010 within the calibrated range indicates that there is no cause for worry about severe nonlinearity interfering with gain stabilization.

The ^{207}Bi pulser provides what should be a constant spectrum of light flashes to each PMT, barring changes in light transport efficiency. This spectrum allows fluctuations in PMT gain to be monitored and corrected, as discussed in subsection 5.2.1.

During 2011–2013 data taking, some problems with the pulser system arose. The signal from one pulser rapidly decreased in magnitude and disappeared (while PMT output to other signals remained normal). This was initially presumed to indicate that the pulser glue joint had separated from the PMT face. However, the pulser signal came back during a period when the magnet was ramped down. The amplitude of the pulser signal showed strong dependence on the PMT bucking coil settings, differently from PMT response to other signals. It is possible that the light from the pulser is entering and hitting a different portion of the PMT photocathode than light arriving through the scintillator light guide.

3.4.4 Light Emitting Diode scans

The UCNA scintillators have an optical fiber glued onto the back at the center, leading to a fiber feedthrough on the detector vacuum flange. This allows light pulses from a Light Emitting Diode (LED) to be injected into the scintillator and observed by the PMTs. The DAQ includes an LED trigger input, so LED pulse events can be recorded.

3.4.4.1 LED system properties

Various attempts prior to the 2010 dataset had been made to use the LED for gain stability and linearity measurements. However, the long fiber and multiple optical connections between the light source and the scintillator input hamper the long-term stability of the signal. Also, controlling the light output from the LED in a predictable way, with highly nonlinear output, is challenging. A variable optical attenuator was tried as a method for precisely controlling the light level; however, the repeatability and accuracy of the attenuator itself left much to be desired.

Despite shortcomings as a method for measuring gain stability or linearity, the LED has provided useful data. The LED pulser has several properties of particular interest:

- The LED provides an independent trigger from the usual PMT 2-fold coincidence, allowing a range of small-signal events which might not otherwise trigger a DAQ event to be produced and captured.
- Though long-term stability is dubious, pulse-to-pulse short term stability is excellent. The LED provides a near perfectly sharp “monoenergetic” line source not possible with electron energy deposition events (which are always broadened by variable dead material energy losses and backscattering).
- This narrow line can be set to any brightness, from zero to beyond what the scintillator can typically capture from single electrons.
- The four PMTs see the light from LED pulses in fixed proportion to each other (without the position dependence of light transport from other sources). This means that, though the brightness can be set to any level (for all four PMTs at once), the LED does not cover the whole space of signal combinations produced in beta decay data (with varying ratios between the PMTs).

3.4.4.2 LED in 2010 data

In the 2010 configuration, a single LED was connected to a fiber splitter near the middle of the spectrometer, with fibers running to the detectors on both sides. The LED was employed erratically throughout the 2010 data set; in many runs, the system was entirely disabled. Towards the end of the beta decay collection, runs 16097–16216, the LED was left running in “ramping” mode, with LED pulses generated at ~ 10 Hz, and the LED brightness swept up from zero to beyond the PMT ADC range in a repeating ~ 25 s “sawtooth” pattern. Applications of this data to studying DAQ triggering and signal correlations are presented in subsection 5.1.2.3 and subsection 5.5.4.

3.4.4.3 Post-2010 LED system

After 2010, the LED system has been expanded and improved by Kevin Hickerson, in the process of prototyping systems for the UCNb experiment. A beam splitter arrangement allows for two LEDs (in different wavelengths) to be used, and a photodiode was added to measure LED light output (potentially allowing linearity measurements against the PMTs). LED data is thus available more consistently in post-2010 data, with various interleaved pulsing patterns between the two LEDs. A detailed analysis of the calibration potential of this new system has yet to be done.

Chapter 4

Simulation of spectrometer physics

Simulation of electron transport and energy deposition in the UCNA spectrometer is important both for calibrations and the asymmetry measurement. The UCNA Collaboration uses two independently developed Monte Carlo simulation codes (to provide cross-checks on MC results). A simulation based on GEANT4 [Ago+03] was developed and maintained at Caltech (see [Yua06] and this work). Collaborators at NC State University developed the complementary simulation based on PENELOPE [Pat12; Sem+97].

For calibration purposes, the energy deposition (and, to second order, position distribution) of electrons in the scintillator is of primary interest. Note, however, that perfect accuracy at predicting energy losses is not essential — unanticipated energy losses in materials common to neutron beta decays and calibration source events will be “calibrated out” by the normal calibrations process. The only component for which accuracy of the model is especially critical is energy losses in the extra materials enclosing calibration sources, which are not shared in common with beta decay events. The effective thickness of the source foil has been directly measured, as described in subsection 4.1.3. The GEANT4 simulation was primarily used for calibrations work because it was most available and familiar to the author of this dissertation; however, no substantial difference would be expected from the adaptation of PENELOPE to the same tasks.

Determining corrections for the experimentally measured beta decay asymmetry poses a greater challenge to MC simulations. Here, the fine finicky details of backscattering and angle-dependent energy losses (largely irrelevant for the reproduction of calibration source energy peaks) compose the entirety of MC-reliant corrections. Both GEANT4 and PENELOPE simulations are produced for beta decay and the corresponding detector corrections, with the discrepancy between them serving as one guide to the general reliability of the MC-based corrections.

The following sections describe the GEANT4-based simulations for the UCNA spectrometer, as used for analysis of the 2010 dataset.

4.1 Detector geometry

4.1.1 Components in detector geometry model

The detector geometry used in the GEANT4 model is sketched in Figure 4.1. The geometry consists of three major components: the decay trap unit, and two detector modules, identical besides rotation

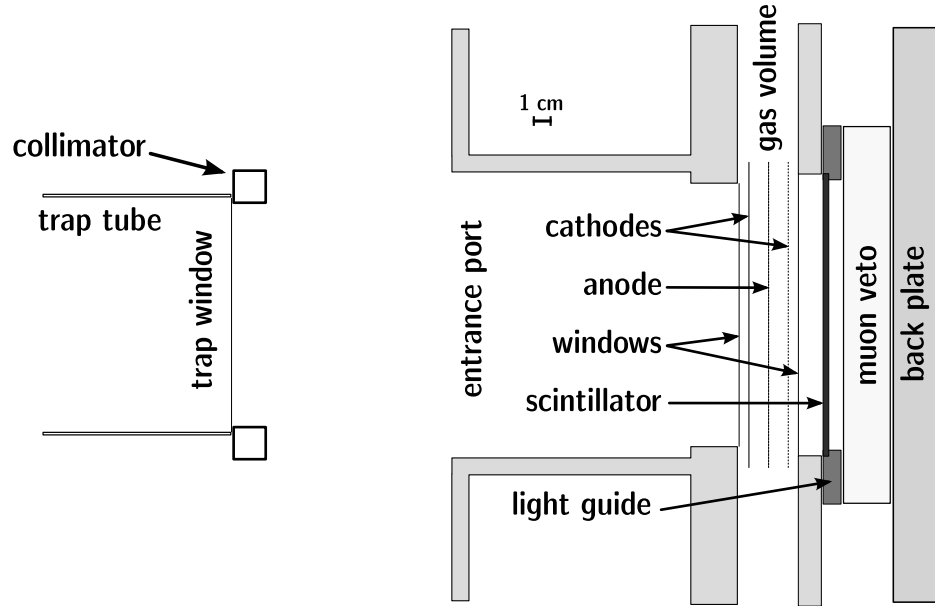


Figure 4.1: MC detector geometry (sketched at approximately $\frac{1}{4}$ scale), cross-section through decay trap end and detector package. See text for details. Note that the magnetic field expansion region in ~ 0.5 m gap between the decay trap end and detector package (not drawn to scale) expands the position scale of electron trajectories by $1/\sqrt{0.6} \approx 1.29$.

and placement on opposite ends of the trap. Details of the geometry follow below. The odd mix of metric and imperial units in which dimensions are specified reflects the different places and times in which the individual components were designed.

The decay trap consists of:

- Decay trap (Cu cylinder), 3 m length, 2.45'' IR, 2 mm wall thickness,
- Trap window coating (Be), $0.3 \mu\text{m}$ thick,
- Trap window (Mylar), $0.7 \mu\text{m}$ thick, and
- Collimator (Polyethylene cylinder), 2.3'' IR, $(0.8'') \times (0.8'')$ square cross section.

The detector packages on each side are constructed by the same code, then duplicated and rotated to a mirror-symmetric pair. The detectors are positioned so that the front surface of the scintillator is at $z = \pm 2.2$ m from the decay trap center $x = y = z = 0$; the detector packages can also be optionally offset and rotated in the x - y plane to match observed offsets in backscatter data (section 6.4). The entrance port to the wirechambers is built from a cylinder with an annular plate on the front entrance facing the trap,

- Entrance port tube (Al cylinder), 3'' IR, $\frac{3}{8}$ '' wall thickness, 5'' depth, and
- Front flange face on trap-facing side of entrance port (Al cylinder), 6'' OR and $\frac{3}{8}$ '' wall thickness.

The front wirechamber window frame and wirechamber box wall are defined as a single annular plate behind the entrance port, with the 7 cm inner radius generally determining the observable decay fiducial volume (accepting electron trajectories from a $7 \cdot \sqrt{0.6} \approx 5.42$ cm radius at the decay trap due to magnetic field expansion),

- Wirechamber entrance plate, 7 cm IR, 6" OR, 1" thick.

The wirechamber section consists of

- Kevlar window support strings (see subsection 4.1.2.2),
- Front window (Mylar), 6 μm thick (aluminum coating is neglected in model),
- Front neopentane volume, 5 mm nominal + 5 mm "bowing" thickness (see subsection 4.1.2.1),
- Front cathodes, 64 vertical wires at 0.1" center-to-center spacing, 50 μm diameter including Al core plus 0.2 μm -thick Au plating, and
- "Live" neopentane volume, 2 cm thick, including at the center:
- Anode plane, 64 vertical wires at 0.1" spacing, 10 μm diameter tungsten (Au coating is neglected for similarity to tungsten),
- Rear cathodes, same as front but horizontally oriented,
- Rear neopentane volume, 5 mm thick, and
- Rear Mylar window, same as front.

Behind the rear window is the wirechamber rear window frame and wall unit (modeled as an annular plate), surrounding the rear nitrogen volume. Behind this, the scintillators consisting of:

- Wirechamber exit plate, 7.5 cm IR (nitrogen filled), 6" OR, 0.5" thick,
- Optional scintillator dead layer (originally 3 μm , but set to 0; see subsection 4.7.2),
- Beta scintillator, 7.5 cm radius and 3.5 mm thick,
- Light guide (treated as same plastic as scintillator), surrounding scintillator edge with a lip on the back protruding inward 3.5mm,
- Nitrogen gap, 6.5 mm,
- Backing veto, 10 cm radius and 1" thick, and
- Back plate representing all the mass behind the detectors, 1" thick 304 stainless steel, 6" radius.

An optional calibration decay source holder may be inserted at the center of the decay trap (Figure 4.2), consisting of:

- Retaining ring (aluminum annulus), 1" OD, (1"-6 mm) ID, 3.2 mm thick,

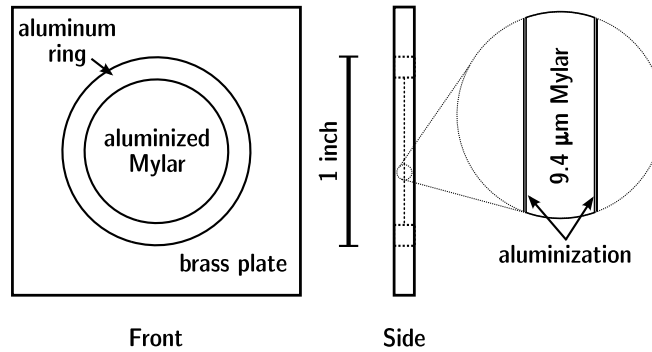


Figure 4.2: MC source holder geometry; see text for details.

Volume	Material	Density	Thickness
Vacuum	“Air,” 78:22 N:O	15.9 pg/cm ³	~ 2 m
Trap window	Beryllium	1.848 g/cm ³	0.3 μm
	Mylar (C ₅ H ₄ O ₂) _n	1.4 g/cm ³	0.7 μm
MWPC Windows			6 μm × 2
MWPC Kevlar	Kevlar (C ₁₄ H ₁₀ N ₂ O ₂) _n	1.44 g/cm ³	3.08 μm *
MWPC Gas	Neopentane C ₅ H ₁₂	0.388 mg/cm ³	3.5 cm
Cathode planes	Aluminum	2.7 g/cm ³	0.76 μm × 2 *
	Gold	19.3 g/cm ³	12 nm × 2 *
Anode plane	Tungsten	19.3 g/cm ³	31 nm *
Dead volume	Nitrogen	0.143 mg/cm ³	13 mm
Scintillator	n = 4.68:5.15 C:H	1.032 g/cm ³	3.5 mm
Dead layer			0–3 μm
Backing veto			1"
Source holder foil	Mylar	1.4 g/cm ³	4.7 μm
Holder foil coating	Aluminum	2.7 g/cm ³	0.1 μm

Table 4.1: MC detector geometry materials in electron path. *: mean thickness for wires/strings.

- Source sealing foil (Mylar) spanning ring ID, 9.4 μm total thickness (with centered source decays escaping through half),
- 0.1 μm Aluminum coating on either side of source sealing foil, and
- 1.5" × 1.5" square brass holder, with central hole containing ring, same thickness as ring.

Table 4.1 summarizes the primary materials used in the simulation. The wirechamber fill neopentane is treated, for density, as an ideal gas at 100 torr and 298 K. The nitrogen volume is likewise at 95 torr. Vacuum is nominally 10⁻⁵ torr “air” (78:22 nitrogen to oxygen by mass) at 293 K. Brass for the source holder is modeled as 70:30 Cu:Zn by mass, with density 8.5 g/cm³. 304 Stainless for the back material is modeled as 70:20:10 Fe:Cr:Ni by mass, with density 8.03 g/cm³.

Table 4.2 shows the mean (and RMS spread) energy losses in each model component encountered by beta decay electrons. Note that the inner window shows somewhat higher mean energy losses

than the outer, as scattering in the intermediate wirechamber gas leaves beta electrons less forward directed, and lower in kinetic energy, than when first entering. The Kevlar strings and wirechamber planes show low average energy losses, but with larger RMS spreads, due to the “hit-or-miss” nature of electron trajectories passing the material (see subsection 4.1.2.2).

4.1.2 Irregularities

The geometry of the actual detector varies in many small ways from the idealized construction in the MC code. Tests, described in the sections below, were made to assess the impact of several known geometrical irregularities of the actual detector. The precise parameters of these irregularities are difficult to ascertain, but reasonable guesses for their magnitude can be made. The tests check that the impact of these irregularities is negligible within the bounds of reasonable expectation.

4.1.2.1 Wirechamber window bowing

Because of the pressure differentials, the wirechamber windows will bow outward from the neopentane region, increasing the distance electrons travel through neopentane. The front window between neopentane and vacuum is supported by Kevlar strings; while highly inelastic, the Kevlar supports are not stretched tight, and may allow a few millimeters of bulging. The rear wirechamber window between neopentane and nitrogen remains taut with no signs of inelastic stretching when utmost care is taken while venting or filling the wirechamber to avoid excessive pressure excursions. However, actual operation of the wirechamber often results in additional wear on the rear window, leaving it visibly stretched from use. The wirechamber neopentane region is thus likely to be wider than the nominal 3 cm design width.

The effects of increasing the neopentane volume due to window bowing were tested in MC by adding 10 mm to the neopentane volume width. The 10 mm extra neopentane width results in ~ 1 keV additional energy loss, with no significant impact on backscattering. Since this extra energy loss is shared between calibration sources and beta decays, it is “calibrated out” to first order (contributing only to smaller backscatter and low-energy efficiency effects). For regular simulations, 5 mm of bowing is added to the vacuum-facing window.

4.1.2.2 Kevlar string fraying

The support strings for the front wirechamber window are 200 denier ($=0.022$ g/m) Kevlar at 5 mm intervals [Yua06]. At a nominal density of 1.44 g/cm³, this corresponds to a 140 μ m-diameter Kevlar cylinder. Inspection of the actual strings, however, show that they are composed of many smaller fibers, which have come untwisted and frayed with use. Rather than cohering as a 140 μ m cylinder, the smaller fibers are spread out more thinly over a wider area.

To model this spreading in the MC, the cylindrical strings were replaced with an equal cross-sectional area rectangular strip with a 16:1 aspect ratio. For beta decay events, cylindrical Kevlar strings intersect the paths of $\sim 3.3\%$ of events, for which they account for a most probable value energy loss of 32 keV and a mean of 44.7 keV. The 16:1 aspect ratio Kevlar strips intercept $\sim 10.6\%$ of events, with a 9.4 keV most probable value energy loss and a 16.0 keV mean energy loss. The overall difference between the spectrum shape and backscattering probabilities for the two configurations is negligible.

E_{prim} range	0–100 keV	100–200 keV	200–300 keV	300–400 keV	400–500 keV	500–600 keV	600–700 keV	700–800 keV
$\langle E_{\text{prim}} \rangle$	85.03 (10.6)	153.95 (28.2)	250.09 (28.8)	348.63 (28.8)	447.06 (28.7)	544.69 (28.4)	639.38 (27.1)	721.14 (16.2)
scintillator	57.61 (16.4)	126.93 (37.3)	226.12 (42.3)	328.07 (41.6)	428.47 (40.5)	527.19 (39.6)	622.45 (38.8)	704.43 (33.2)
quenching	11.91 (2.4)	17.16 (3.7)	22.39 (3.5)	26.35 (2.9)	29.44 (2.5)	31.97 (2.3)	34.10 (2.1)	35.75 (2.0)
trap foil	1.48 (1.8)	1.41 (2.1)	1.21 (2.0)	1.09 (1.9)	1.03 (1.9)	1.01 (1.9)	0.98 (1.9)	0.99 (2.0)
Kevlar strings	0.35 (2.7)	1.78 (6.8)	1.98 (7.9)	1.72 (7.2)	1.54 (6.6)	1.42 (6.3)	1.36 (5.9)	1.33 (5.5)
outer window	4.51 (2.7)	4.22 (5.6)	3.76 (6.6)	3.24 (6.3)	2.89 (5.8)	2.68 (5.4)	2.55 (5.3)	2.46 (5.0)
inner MWPC	7.60 (4.2)	7.04 (8.0)	5.98 (9.2)	5.04 (8.6)	4.47 (8.0)	4.11 (7.4)	3.90 (7.1)	3.77 (7.2)
outer MWPC	4.13 (2.7)	3.79 (4.7)	3.22 (5.2)	2.72 (4.9)	2.42 (4.5)	2.23 (4.2)	2.11 (4.0)	2.05 (4.1)
wire planes	0.02 (0.7)	0.51 (4.9)	0.93 (7.0)	0.86 (6.6)	0.77 (6.0)	0.71 (5.5)	0.65 (5.0)	0.64 (5.0)
inner window	6.25 (4.9)	5.38 (7.0)	4.21 (6.8)	3.46 (6.1)	3.05 (5.6)	2.80 (5.3)	2.64 (5.0)	2.55 (5.0)
N ₂ volume	4.77 (5.0)	3.61 (5.5)	2.64 (4.8)	2.13 (4.2)	1.87 (3.8)	1.71 (3.6)	1.61 (3.5)	1.54 (3.3)
Total lost	29.11 (9.6)	27.75 (16.5)	23.93 (18.5)	20.26 (17.1)	18.05 (15.7)	16.66 (14.7)	15.81 (14.0)	15.33 (13.7)

Table 4.2: GEANT4 simulated energy loss for Type 0 events in spectrometer volumes, for beta decay spectrum in 100 keV initial energy bins. Quantities are in units of keV, mean and (RMS spread). “Quenching” indicates the effective reduction in light output due to scintillator quenching (see subsection 4.6.1). “Inner” and “outer” MWPC indicate neopentane between and outside the cathode planes; “outer” and “inner” windows indicate the decay-trap-facing and scintillator-facing MWPC windows, respectively. “Total lost” is total energy deposition outside the scintillator.

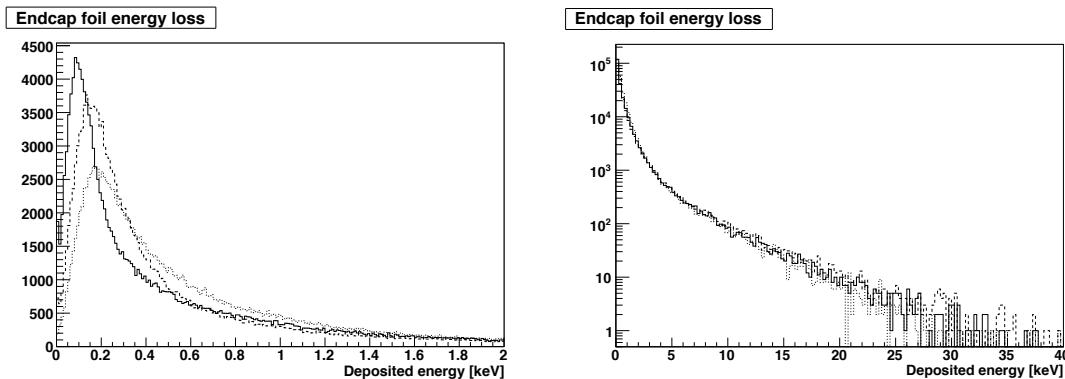


Figure 4.3: MC energy deposited in decay trap foil for ^{113}Sn source events. Solid line: extra wrinkly ($\pi/2$) foil; dashed: wrinkly ($\pi/4$) foil; dotted: flat foil. Although the low-energy deposition peak varies with the amount of wrinkle, high energy deposition event distributions remain identical.

4.1.2.3 Decay trap foil wrinkles

The beryllium-coated decay trap endcap foils are visibly wrinkled from stretching during spectrometer vent/pump cycles. An MC test of the impact of these wrinkles was conducted by changing the endcap foil model from a flat plane to a corrugated surface built from arcs of cylindrical tubes. Wrinkling angles of $\theta = 0, \pi/4$, and $\pi/2$ were tested, retaining the same total volume of endcap material in all cases by thinning the material in proportion to the increased length of the wrinkled foil (11% longer for the $\pi/4$ wrinkles and 57% for the $\pi/2$).

Figure 4.3 shows energy deposition in the endcap foil by simulated ^{113}Sn source events for the varying levels of wrinkliness. Although the shape of the energy loss distribution changes, the difference in average energy loss between the flat and $\pi/2$ extra wrinkly foil is only 0.1 keV. The tail of high energy loss events (where significant modifications to the spectrum shape and backscattering occur) is identical for all wrinkling levels; hence, Type I and II/III backscattering fractions are identical regardless of wrinkling, and the observable energy spectrum (even for low energy events like the 57 keV ^{207}Bi Auger K line) is unchanged to the 0.1 keV level.

4.1.3 Calibration source foil

The one energy loss not shared by calibration sources and beta decays (thus not corrected by regular energy calibrations) is the foil enclosing sealed source calibration radioisotopes. University of Washington collaborators Ran Hong and Troy MacDonald set up a collimated ^{241}Am α source (5485.56 keV decay energy) with a silicon detector to measure energy losses through thin foils over a ~ 1 mm spot. The Sn, Bi, and Ce calibration sources used for the 2010 dataset were all measured over a grid of points around the deposited source spot. All three foils, at all positions, showed energy losses in the 1080 keV to 1160 keV range. For comparison, a sample of the $6 \mu\text{m}$ aluminized Mylar foil used for the wirechamber windows showed an energy loss of 690 keV.

Matching GEANT4 simulations were produced for 5485.56 keV α particles passing through various thickness of aluminized ($0.1 \mu\text{m}$ each side) Mylar foil. The results are shown in Figure 4.4. The GEANT4 prediction was consistent with the $6 \mu\text{m}$ wirechamber window foil, measured at 690 keV

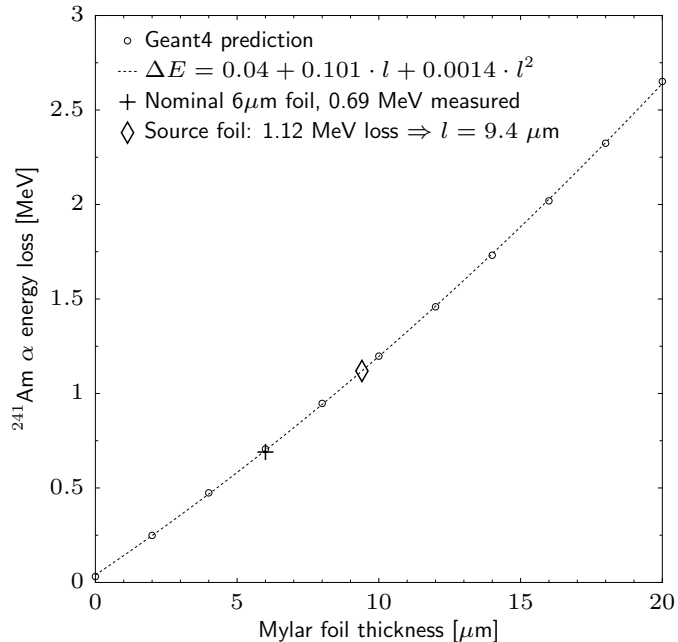


Figure 4.4: Energy loss of ^{241}Am 5485.56 keV α decays through aluminized Mylar foils, simulation and measured points. X axis is Mylar thickness between fixed-thickness ($0.1 \mu\text{m} \times 2$) aluminization, producing the 40 keV energy loss at zero foil thickness.

energy loss and predicted at 699 keV. Based on a middle value of 1.12 MeV energy loss measured in the source foils, setting a thickness of $9.4 \mu\text{m}$ in the simulation will reproduce the measured energy loss. The nominal foil thickness from manufacturer specifications was $7.6 \mu\text{m}$; the different measured thickness corresponds to an ~ 0.5 keV additional energy loss for calibration source electrons passing through the $\sim 1 \mu\text{m}$ extra material on either side. Using the corrected $9.4 \mu\text{m}$ source foil thickness, MC uncertainty for mean energy losses particular to the source foil may be assumed to be < 0.1 keV.

4.2 Magnetic field

4.2.1 Motion of electrons in a magnetic field

Though electron propagation in the magnetic field is fully handled by GEANT4, an overview of key points is given below to aid intuition.

An electron moving in a uniform magnetic field B follows a helical path, winding around the magnetic field lines with a Larmor radius

$$r = \frac{p_{\perp}}{q_e B} \approx \frac{p_{\perp}/(\text{MeV}/c)}{B/\text{T}} \cdot 3.34 \text{ mm}, \quad (4.1)$$

where p_{\perp} is the component of the relativistic momentum perpendicular to the field. The cyclotron frequency of completing loops around the field lines, for an electron with Lorentz factor γ , will be

$$f = \frac{q_e B}{2\pi\gamma m_e} \approx \frac{B/\text{T}}{\gamma} \cdot 28.0 \text{ GHz}. \quad (4.2)$$

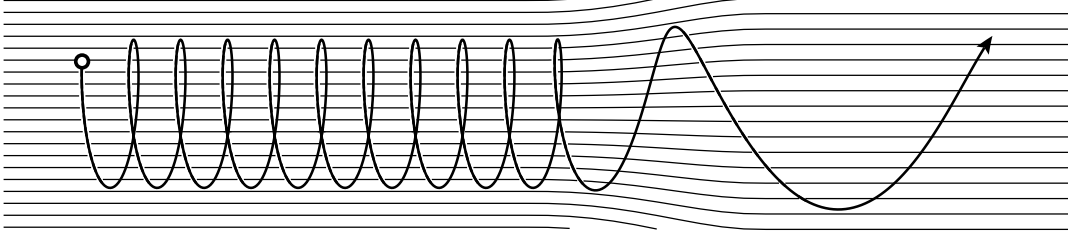


Figure 4.5: Sketch of an electron's trajectory in an expanding magnetic field.

Note that this implies a lower limit n_{\min} on the number of loops per forward distance d traveled for even the most forward-directed electrons:

$$\frac{n_{\min}}{d} = \frac{f}{v} = \frac{q_e B}{2\pi\beta\gamma m_e c} \approx \frac{B/\text{T}}{\beta\gamma} \cdot 93.4 \text{ m}^{-1}, \quad (4.3)$$

so electrons traversing the UCNA wirechambers will always complete > 1 loops (and nearly so much again before reaching the scintillator).

Now consider an electron moving in a static magnetic field (and zero electric field) with gradual spatial variation, so the electron sees $|\frac{\Delta B}{B}| \ll 1$ on timescales $\frac{1}{f}$. The electron takes a helical path following a central field line, with the parallel component of motion described by [NT60]:

$$\frac{dp_{\parallel}}{dt} = -\frac{M}{\gamma} \frac{\partial B}{\partial s}; \quad M \equiv \frac{p_{\perp}^2}{2m_e B}, \quad (4.4)$$

where the magnetic moment M is an invariant of the motion, and ∂s is distance parallel to the field. Combining the invariance of M with the Larmor radius indicates that the flux enclosed by the helical path $\pi r^2 B$ is also constant, providing an intuitive image of the helical trajectory enclosing a constant bundle of field lines:

$$p_{\perp}^2 = 2m_e B M \Rightarrow \pi r^2 B = \frac{2\pi m_e}{q_e^2} M \approx \frac{p_{\perp}^2 / (\text{MeV}/c)^2}{B/\text{T}} \cdot 35.0 \text{ T} \cdot \text{mm}^2. \quad (4.5)$$

Combining the invariance of M with conservation of total momentum p ($p^2 = p_{\perp}^2 + p_{\parallel}^2$) indicates that p_{\parallel} must make up the difference as B varies, with $p_{\perp} \propto \sqrt{B}$. Moving into an expanding magnetic field (decreasing B), the electron becomes more forward directed as momentum shifts from p_{\perp} to p_{\parallel} . Figure 4.5 sketches an electron's trajectory through a field expansion. As a field pinches down (increasing B), the electron is directed into a more steeply pitched trajectory as p_{\parallel} decreases, which can only go so far until $p_{\parallel} = 0$, and the electron is magnetically mirrored back towards the lower field region. The magnetic field required for mirroring (where the electron's momentum is entirely $p = p_{\perp}$) is thus

$$B_M = \frac{p^2}{2Mm_e}. \quad (4.6)$$

Alternately, for a particle starting in field B_0 with momentum components p_{\perp}, p_{\parallel} , mirroring occurs when the particle encounters a field B_M , such that

$$\frac{p_{\parallel}}{p_{\perp}} = \sqrt{\frac{B_M - B_0}{B_0}}. \quad (4.7)$$

4.2.2 Spectrometer field in Geant4 model

The spectrometer magnetic field is taken to be radially symmetric around the decay trap axis, to have no B_ϕ component, and to have a constant B_z component as a function of radius. These assumptions, combined with Maxwell's equations, fully define the magnetic field from its value $B_z(z)$ along the central axis:

$$B_z(z, r, \phi) = B_z(z); \quad B_\phi(z, r, \phi) = 0; \quad \nabla \cdot \mathbf{B} = 0 = \frac{\partial B_z}{\partial z} + \frac{1}{r} \frac{\partial}{\partial r} [r B_r] \Rightarrow B_r(z, r, \phi) = -\frac{r}{2} \frac{dB_z}{dz}. \quad (4.8)$$

The $B_z(z)$ field is defined at a discrete set of points, and the field between them is smoothly interpolated by a half-wave of a cosine:

$$\begin{aligned} B_z(z_1) \equiv B_1, \quad B_z(z_2) \equiv B_2 \Rightarrow B_z(z \in [z_1, z_2]) &= \frac{B_1 + B_2}{2} + \frac{B_1 - B_2}{2} \cos\left(\frac{z - z_1}{z_2 - z_1} \pi\right) \\ \Rightarrow B_r(z \in [z_1, z_2], r) &= \frac{B_1 - B_2}{z_2 - z_1} \frac{\pi r}{4} \sin\left(\frac{z - z_1}{z_2 - z_1} \pi\right). \end{aligned} \quad (4.9)$$

The “default” field is fixed at 1 T between ± 1.5 m, expanding out to 0.6 T at ± 2.2 m. Measured fields from the Hall probe array (defining 15 evenly spaced points over ± 1.5 m) can also be applied. For measured fields over the decay trap region, $\left| \frac{B_1 - B_2}{z_2 - z_1} \right| \lesssim 10^{-2}$ T/m, so the radial component in the decay trap is small: $|B_r| \lesssim 10^{-3}$ T. Measured fields typically have a mean value of ~ 0.96 T over the decay trap region (the SCS is usually run slightly below the full 1 T design field); the 0.6 T field expansion region is scaled down proportionally. See Figure 4.6 for an example of measured fields, cosine interpolated as above.

Geant4 offers several options for the algorithm for tracking the motion of charged particles in electromagnetic fields. The `G4HelixImplicitEuler` stepper was selected based on somewhat faster computation for measured fields compared to the other option (`G4HelixHeum`) for pure B-fields.

4.2.3 Simulating with 2010 measured field

In 2010, the field profile was measured a few times (after major events, such as re-ramping the magnet) using the Hall probe array in the spectrometer bore. Figure 4.6 shows two of the field profiles. For the purpose of simulation, the October 28 map was adopted as representative for the whole dataset, as the difference between field maps was not large enough to require the effort of separate simulations.

For simulating 2010 beta decay, the realistic field map was not included in the main high-statistics simulation, but rather relegated to a secondary lower-statistics run, for two main reasons. The first reason is to separate the particular impact of field ripples from other factors. The second reason is practicality — running simulations with “wiggly” field profiles is far more computationally intensive than propagating electrons in an idealized, flat field.

In the 10^{-5} torr vacuum pressure used by default for uniform-field UCNA simulations, an individual electron trapped in a field dip can require a few minutes of computer time to simulate bouncing back and forth before encountering enough residual gas to scatter out. This makes simulation of tens of millions of decays quite impractical, even if only a small percentage are initially trapped. The solution is to crank up the simulated spectrometer residual gas pressure to 10^{-3} torr. So long as electrons still require $\gg 1$ bounces to escape trapping, there is little change to the outcome of

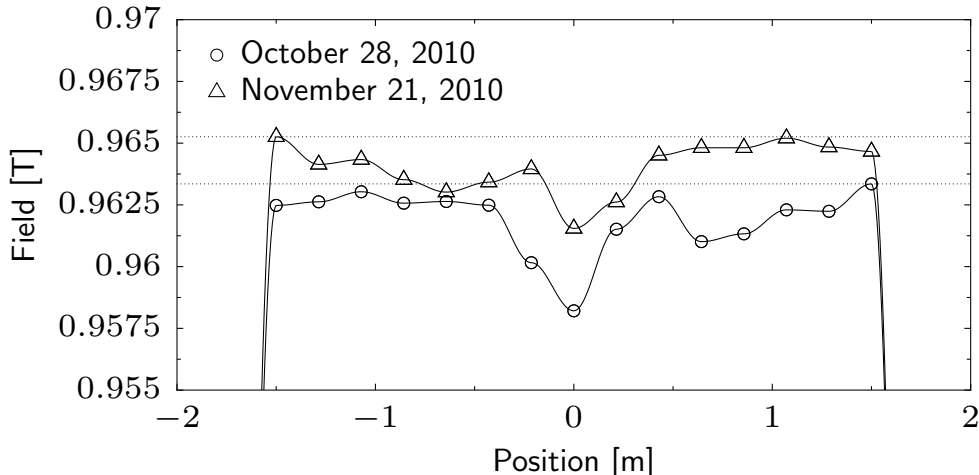


Figure 4.6: Two spectrometer magnetic field maps from 2010 using the Hall probe array. Dotted lines indicate highest field point. Curve connecting points is cosine interpolation per Equation 4.9.

trapping from speeding up the process to a more manageable timescale. At such pressures, the extra gas typically traversed by (untrapped) electrons becomes comparable to encountering an extra couple hundred nanometers of decay trap window. A third set of simulations, with an idealized uniform decay trap field and the 10^{-3} torr vacuum, is also generated to separate the effects of increased residual gas from those of incorporating the realistic field shape.

Note that for simulations of calibration sealed source radioisotopes, with the source holder sitting in the typical central field dip, the source holder provides abundant material interactions to prevent long-term trapping of electrons. Thus, calibration source simulations are always done with the nonuniform field map enabled (without elevated vacuum pressure), which produces slightly more events in the tail distributions below source peaks, in improved agreement with the data.

4.3 Electric field

The exact shape of the electric field in the wirechamber due to the 2600 V to 2700 V potential between the anode and cathode planes is an analytically intractable problem. However, a simple analytic approximation can be made. The electric field at distance l from an isolated wire with charge per unit length λ is, by Gauss' Law, $E = \frac{\lambda}{2\pi\epsilon_0 l}$ radially outward from the wire. Now consider an infinite plane of charged parallel wires of radius r and distance $d \gg r$ apart, and the field at distance l away from the plane and shifted by a from the center of one wire. Define $E_0 \equiv \frac{\lambda}{2\epsilon_0 d}$, the field produced by a uniform plane with equal surface charge λ/d . Summing over the contributions from all wires (neglecting the smaller distortion of the charge distribution on each wire due to the others, which vanishes for $d \gg r$), the field has components perpendicular and parallel to the plane

$$E_{\perp}(l, a) = \frac{\lambda}{2\pi\epsilon_0} \sum_{n=-\infty}^{\infty} \frac{l}{l^2 + (a + nd)^2} = \frac{\sinh \frac{2\pi l}{d}}{\cosh \frac{2\pi l}{d} - \cos \frac{2\pi a}{d}} E_0 \quad (4.10)$$

$$E_{\parallel}(l, a) = \frac{\lambda}{2\pi\epsilon_0} \sum_{n=-\infty}^{\infty} \frac{a + nd}{l^2 + (a + nd)^2} = \frac{\sin \frac{2\pi a}{d}}{\cosh \frac{2\pi l}{d} - \cos \frac{2\pi a}{d}} E_0 \quad (4.11)$$

(note that the positive and negative halves of the E_{\parallel} sum individually diverge; by combining terms to pair off wires in the positive and negative directions, a manifestly convergent sum is produced). For regions inside the wire, $\mathbf{E} = 0$. Additional corrections for the finite wire diameter coupling to the field from other wires appear only at quadrupole and higher orders and can safely be neglected, thanks to the symmetric cancellation of fields from wires on each side.

The potential at the surface of a wire relative to a point perpendicular distance $l = L \gg d$, $a = 0$ away is

$$\begin{aligned} V &= \int_r^L \frac{\sinh \frac{2\pi l}{d}}{\cosh \frac{2\pi l}{d} - 1} E_0 dl = \frac{d}{\pi} E_0 \int_{\pi r/d}^{\pi L/d} \coth(x) dx \\ &= \frac{d}{\pi} E_0 \ln \frac{\sinh(\pi L/d)}{\sinh(\pi r/d)} \approx E_0 \left[L + \frac{d}{\pi} \ln \frac{d}{2\pi r} \right]. \end{aligned} \quad (4.12)$$

Thus, to model the wirechamber anode plane distance $L = 1\text{cm}$ from the grounded cathodes, with wire radius $r = 5\mu\text{m}$ and spacing $d = 2.54\text{mm}$, the field is set to

$$E_0 = \frac{\pi V/d}{\ln \frac{\sinh(\pi L/d)}{\sinh(\pi r/d)}} = 0.738 \cdot \frac{V}{\text{cm}}. \quad (4.13)$$

To simplest approximation, the cathode planes can be modeled as a uniform conductive plane by sharply cutting off the field to zero past distance L from the anode. If a more accurate field near the cathodes is also desired, the same approach as above can be applied, selecting a cathode field to produce $\mathbf{E} = 0$ at infinity by $E_0^{\text{cathode}} = -\frac{1}{2}E_0^{\text{anode}}$ for each of the planes. In addition, the (near uniform) field from the anodes induces a charge distribution on the cathode wires equivalent to a dipole outside the wire surface.

Inclusion of the wirechamber electric field in the MC turns out to have negligible impact on simulation results, so the even simpler approximation $\mathbf{E} = 0$ is equally suitable.

4.4 Physics list

Physics included in the MC was based around GEANT4's "Livermore" low-energy electromagnetic physics list [Iva+11] (as of GEANTversion 4.9.5). The "Livermore" physics list was designed to replicate a large variety of electromagnetic scattering experiments, covering the energy range of interest for UCNA. Particular processes of interest included in the physics list are [Col11]:

- e^- multiple scattering using the "UrbanMsc95" model,
- e^- ionization by "LowEnergyIoni" up to 100 keV, then "MollerBhabha" above,
- e^- bremsstrahlung by "AngularGen2BS,"
- γ Compton scattering by "LivermoreCompton," and
- γ Rayleigh scattering by "LivermoreRayleigh."

As recommended for the physics list, an energy cutoff of 250 eV was used for producing and tracking electrons and photons, along with a range cut of $1\ \mu\text{m}$ for photons and 500 nm for electrons. In denser materials in the geometry (e.g. aluminum), the range cut dominated, pushing the energy cutoff for electrons into the 500 eV to 1 keV range. However, in the scintillator, Mylar, beryllium, and wirechamber gas, the 250 eV energy cutoff was applied.

4.5 Event generation

MC simulations begin with the specification of primary particles (vertex position and momenta) for each “event.” Event generators were developed for throwing the electrons and gamma rays associated with neutron decay and other calibration sources in the UCNA detector. Appropriate initial event vertex position distributions are then produced for the particles (such as neutrons uniform through the decay trap, or a dot of sealed calibration source material in the source holder).

4.5.1 Neutron decay

Neutron decay events are generated according to an isotropic, uncorrected, “plain phase space” beta decay spectrum for electrons alone, $\Gamma_e(1 \leq W \leq W_0) \propto \sqrt{W^2 - 1}W(W_0 - W)^2$, where W is the total electron energy in units of electron rest mass energy, and $W_0 = (782.347 + 511.00)/511.00$ the endpoint energy of beta decay in the same units. The initial kinetic energy and emission angle of the electron is recorded, so that fine corrections to the beta spectrum shape and polarization-dependent anisotropy can be applied later via event-by-event weighting factors in analyzing the MC data.

4.5.2 Radioactive nuclides

For calibration sources and possible neutron-activated materials, a general-purpose event generator was written which reads a list of energy levels, decay types, and probabilities from configuration files for each isotope. The event generator follows the decay chains specified, potentially generating multiple electrons and gamma rays within a single event as needed. Event generation includes gamma rays, conversion electrons, auger electrons, and beta decays involved in the process. Angular correlations between multiple primaries in an event are not accounted for (all primaries are independently isotropic into 4π). For decays with long-lived (compared to the $6\ \mu\text{s}$ DAQ readout window) intermediate states, the portions of the decay chain up to and after the intermediate state are treated as independent decay possibilities produced in separate simulation events. There were no decays considered in which intermediate products were not either much longer- or much shorter-lived than the DAQ window.

4.5.2.1 Conversion electrons

Conversion electrons are generated by specifying two energy levels between which the transition occurs, and a conversion probability broken down by electron subshells. The energy of the conversion electron is taken to be the difference between nuclear energy levels, less the appropriate electron shell binding energy as tabulated in [BB67].

4.5.2.2 Nuclear beta decays

The shape of allowed beta decay spectra are modeled according to a series of review papers by D. H. Wilkinson [Wil82; Wil89; Wil90; Wil93; Wil95a; Wil95b; Wil97; Wil98]. The spectrum is taken as a function of electron total energy W , endpoint W_0 , final-state nucleus A and Z , from which an approximate radius $R \approx A^{1/3}R_0$ and mass $M \approx ZM_p + (A - Z)M_n$ are determined. Throughout the following section, we adopt the “natural units” $\hbar = c = m_e = 1$ used by Wilkinson, in which system:

$$M_p \equiv \frac{m_p}{m_e} \approx 1836.1; \quad M_n \equiv \frac{m_n}{m_e} \approx 1838.7; \quad R_0 \equiv \frac{1.2 \text{ fm}}{\hbar/m_e c} \approx 0.0031; \quad W_0^n \equiv M_n - M_p \approx 2.531. \quad (4.14)$$

The decay rate for allowed beta decays of unpolarized nuclei as a function of electron energy is:

$$\omega(W; W_0, A, Z) = \frac{G_F^2 m_e^5 c^4}{2\pi^3 \hbar^7} |V_{ud}|^2 (|M_F|^2 + |M_{GT}|^2 \lambda^2) g_V^2 \cdot S_0 \cdot F_0 \cdot L_0 \cdot C \cdot \left[1 + \frac{\alpha}{2\pi} g\right] \cdot R \cdot Q. \quad (4.15)$$

S_0 is the standard beta decay phase space factor,

$$S_0(W; W_0) \equiv pW(W_0 - W)^2; \quad p \equiv \sqrt{W^2 - 1}. \quad (4.16)$$

F_0 is the Fermi function Coulomb-force correction [Wil82; Wil89]:

$$F_0(Z, W, R) \equiv \frac{4(2pR)^{2(\gamma-1)} e^{\pi\alpha ZW/p}}{\Gamma(2\gamma+1)^2} |\Gamma(\gamma + i\alpha ZW/p)|^2; \quad \gamma \equiv \sqrt{1 - (\alpha Z)^2}, \quad (4.17)$$

where the Γ function of the complex argument can be calculated by [Wil93]:

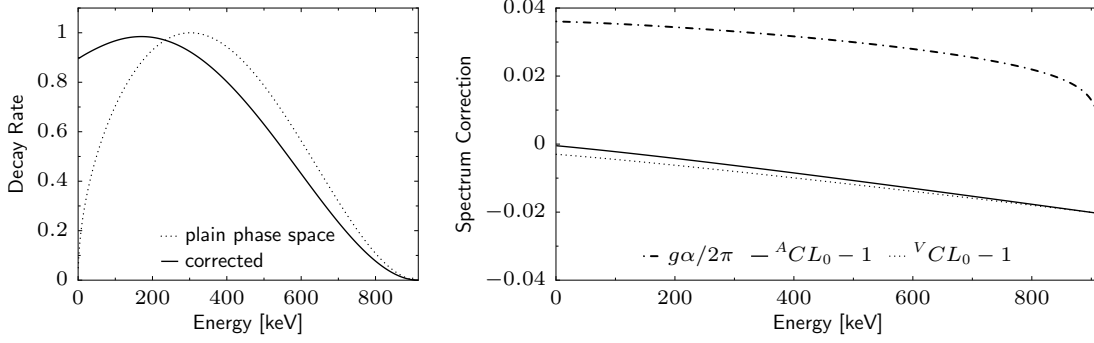
$$\begin{aligned} \ln |\Gamma(\gamma + iy)|^2 &= \sum_{n=0}^{N-1} \left(\ln \frac{n^2 + ay^2}{(n + \gamma)^2 + y^2} \right) + \ln \frac{\pi(N^2 + ay^2)}{ay \sinh \pi ay} - (2N + 1) \ln a \\ &+ (1 - \gamma) \left[2 - \ln [(N + \gamma)^2 + y^2] + \frac{2y}{N + \gamma} \arctan \frac{y}{N + \gamma} + \frac{1}{6a} \frac{1}{(N + \gamma)^2 + y^2} \right] \\ a &\equiv \frac{N + 1}{N + \gamma}, \end{aligned} \quad (4.18)$$

taking the sum to $N = 3$ terms sufficing for accuracy.

L_0 corrects the Fermi function for the nonzero size of the nuclear charge, and C is similarly a correction for the convolution of the electron wavefunction against the finite-sized nucleus. $L_0(Z, W, R)$ is given by a series approximation in [Wil90], which also describes C . C takes slightly different values for Vector (Fermi) or Axial-Vector (Gamow-Teller) decays,

$$\begin{aligned} {}^V C &= 1 - \frac{233(\alpha Z)^2}{630} - \frac{(W_0 R)^2}{5} - \frac{6W_0 R \alpha Z}{35} + \left[-\frac{13R \alpha Z}{35} + \frac{4W_0 R^2}{15} \right] W \\ &+ \left[\frac{2\gamma W_0 R^2}{15} + \frac{\gamma R \alpha Z}{70} \right] \frac{1}{W} - \frac{4R^2}{15} W^2 \end{aligned} \quad (4.19)$$

$${}^A C = 1 - \frac{233(\alpha Z)^2}{630} - \frac{(W_0 R)^2}{5} + \frac{2W_0 R \alpha Z}{35} + \left[-\frac{21R \alpha Z}{35} + \frac{4W_0 R^2}{9} \right] W - \frac{4R^2}{9} W^2, \quad (4.20)$$



(a) “Plain phase space” and fully corrected beta decay spectra, normalized to equal area. (b) Radiative and finite nuclear size corrections. The Axial-Vector ($^A C$) corrections are appropriate for this decay; the Vector corrections (also shown) are similar.

Figure 4.7: Spectrum and corrections for the 915 keV endpoint beta decay of $^{135}\text{Xe } \frac{3}{2}^+$ to $^{135}\text{Cs } \frac{5}{2}^+$.

or an appropriate mixture of the two for decays with both Fermi and Gamow-Teller components. The L_0 and C corrections, on the order of several percent for larger nuclei, work in opposite directions, canceling out to leave a smaller combined finite-size correction on the order of -1% .

g is Sirlin’s order- α radiative correction [Sir67], with the divergent term $\ln(W_0 - W)$ “repaired” as in [RW83; Wil95b]:

$$g(W, W_0, M) = 3 \ln M - \frac{3}{4} + 4 \left[\frac{\text{atanh } \beta}{\beta} - 1 \right] \left[\frac{W_0 - W}{3W} - \frac{3}{2} + \ln 2 \right] + \frac{4}{\beta} L \left(\frac{2\beta}{1 + \beta} \right) + \frac{\text{atanh } \beta}{\beta} \left[2(1 + \beta^2) + \frac{(W_0 - W)^2}{6W^2} - 4 \text{atanh } \beta \right] + \frac{2\pi}{\alpha} \left\{ (W_0 - W)^{\frac{2\alpha}{\pi}} \left[\frac{\text{atanh } \beta}{\beta} - 1 \right] \right\}, \quad (4.21)$$

where $\beta \equiv \frac{p}{W}$ is the electron’s velocity, $\text{atanh } x \equiv \frac{1}{2} \ln \frac{1+x}{1-x}$, and $L(x)$ is the Spence function

$$L(-1 \leq x \leq 1) \equiv \int_0^x \frac{\ln(1-t)}{t} dt = - \sum_{n=1}^{\infty} \frac{x^n}{n^2}. \quad (4.22)$$

There are additional corrections for nuclear recoil: Q for the impact on the Coulomb interactions, and R for the effect on phase space. The correction from Q is generally negligibly small, being of order $\frac{\alpha}{M}$ [Wil82]:

$$Q(Z, W, W_0, M) = 1 - \frac{\pi\alpha}{Mp} \left(1 + \frac{1 - \lambda^2}{1 + 3\lambda^2} \frac{W_0 - W}{3W} \right). \quad (4.23)$$

The R correction is of order $\frac{1}{M}$, thus also quite small for all but the lightest nuclei. As with C , R takes different forms for Vector and Axial-Vector decays: [Wil82; Wil90]:

$$R^V(W, W_0, M) = 1 + \frac{W_0^2}{2M^2} + \frac{W_0}{3M^2} \frac{1}{W} + \left[\frac{2}{M} - \frac{4W_0}{3M^2} \right] W + \frac{16}{3M^2} W^2 \quad (4.24)$$

$$R^A(W, W_0, M) = 1 - \frac{2W_0}{3M} - \frac{W_0^2}{6M^2} - \frac{77}{18M^2} + \left[-\frac{2}{3M} + \frac{7W_0}{9M^2} \right] \frac{1}{W} + \left[\frac{10}{3M} - \frac{28W_0}{9M^2} \right] W + \frac{88}{9M^2} W^2. \quad (4.25)$$

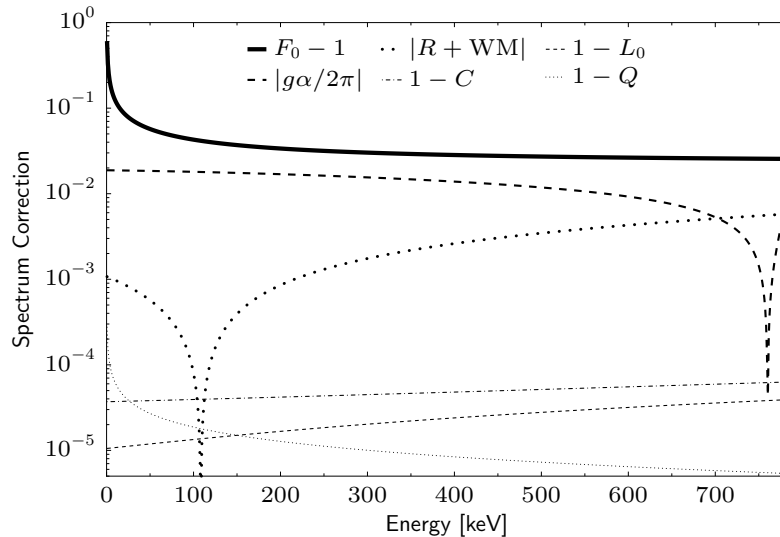


Figure 4.8: Corrections to the shape of the neutron beta decay spectrum. The recoil correction R is merged into the recoil and Weak magnetism correction of [Bil+60], denoted by “ $R + WM$,” which is positive above ~ 110 keV. The radiative correction g is also positive below ~ 750 keV.

An example of these corrections is shown in Figure 4.7, considering the 915 keV endpoint beta decay of ${}_{54}^{135}\text{Xe } \frac{3}{2}^+$ to ${}_{55}^{135}\text{Cs } \frac{5}{2}^+$. Figure 4.8 shows the spectrum shape corrections for free neutron beta decay. For this very small nucleus, the C and L corrections are negligible, as is Q . The recoil correction R , less strongly suppressed by $\frac{1}{M}$, rises in prominence. Combining the Vector and Axial-Vector components in Equation 4.24 and Equation 4.25 as appropriate for free neutron decay, and neglecting smaller $\frac{1}{M^2}$ terms,

$$R_n(W) \equiv \frac{R^V + 3\lambda^2 R^A}{1 + 3\lambda^2} \approx 1 + \frac{1}{1 + 3\lambda^2} \frac{1}{M_p} [-2\lambda^2 W_0 + 2(5\lambda^2 + 1)W - 2\lambda^2/W]. \quad (4.26)$$

This recoil correction was calculated along with effects from Weak Magnetism (introducing the additional terms in μ) by Bilen’kiĭ *et al.* [Bil+60] to produce a combined correction:

$$R_n^{R+WM}(W) \equiv 1 + \frac{1}{1 + 3\lambda^2} \frac{1}{M_p} [-2\lambda(\lambda + \mu)W_0^n + 2(5\lambda^2 + 2\lambda\mu + 1)W - 2\lambda(\mu + \lambda)/W], \quad (4.27)$$

where $\mu \equiv \frac{\mu_p - \mu_n}{\mu_N} \approx 2.792847356 - (-1.9130427)$ is the difference between the proton and neutron total magnetic moments.

First-forbidden Axial-Vector beta decays ($|M_F|^2 = 0$) are multiplied by an additional shape factor $C_{1T}(W, W_0, Z, R)$ according to [Dav51]. The second-forbidden beta decay of ${}^{137}\text{Cs}$ uses the shape factor from [BC83].

4.5.2.3 Auger electrons

K-Auger electrons are generated by specifying the intensity of K-shell x-rays I_{Kx} and intensity of Auger emission I_{Aug} . From this, the probability of an Auger given a K-shell vacancy is deduced, $P_{\text{Aug}} = I_{\text{Aug}}/(I_{\text{Aug}} + I_{Kx})$. The number of K-shell vacancies produced by, for example, K conversion electrons, is counted for each decay process, and an Auger electron is produced according to the

emission probability. The energy of the Auger electron is estimated from the K and L electron binding energies. Assuming an L1 electron drops into a K vacancy, producing a γ of energy $E_K - E_{L1}$, which then knocks out an L2 electron, the Auger is given a kinetic energy of $E_K - E_{L1} - E_{L2}$. This energy estimate generally comes sufficiently close (< 1 keV difference) to published Auger energy values (which include fine details of subshell vacancies not present in the simple estimate).

4.6 Track data reduction

The MC physics code simulates and records the detailed energy deposition tracks of particles in the simulated event. This fine-grained track information is then reduced in a post-processing step to integrated quantities, which can be related to detector observables. A simple example of these is the total energy deposition in each part of the geometry (windows, wirechamber gas, scintillator, etc), from integrating over the energy deposition dE in each step of tracks passing through the volume, $E_{\text{dep}} \equiv \int dE$. The sections below describe other quantities of interest reduced from the detailed MC particle track data.

4.6.1 Scintillator quenched energy

As discussed in section 3.2 of [Yua06], scintillators show a nonlinear response between differential energy deposition $\frac{dE}{dx}$ and light produced $\frac{dL}{dx}$. Higher localized energy deposition “quenches” the conversion of deposited energy to light. A common parametrization for the quenching is “Birk’s Law,” which states that the light produced by depositing energy dE along track length dx will be proportional to $\frac{dE}{1+k_B \frac{dE}{dx}}$, where k_B is a constant dependent on the scintillating material. [Yua06] fit NIST ESTAR data for electron energy deposition in scintillators to parametrize the expected relationship between electron energy and energy deposition density:

$$\frac{dE}{dx} \approx aE^b \rho_{\text{scint}} \equiv 116.7(E/\text{keV})^{-0.7287} \rho_{\text{scint}} \frac{\text{MeV} \cdot \text{cm}^2}{\text{g}}, \quad (4.28)$$

where $\rho_{\text{scint}} = 1.032 \text{ g/cm}^3$ is the density of the scintillator. Then, a fit of scintillator light response to an electron gun (and assuming the parametrized ESTAR $\frac{dE}{dx}$) determined a Birk’s Law constant of $k_B = (0.0191 \pm 0.0020) \text{ cm/MeV}$ for the UCNA scintillator [Yua06].

Quenching effects will produce nonlinearity in the scintillator response, resulting in effective undetected “missing energy” increasing at low electron energies. Such a nonlinearity could, in theory, mostly be fit out within the normal linearity calibration procedure. However, accounting for quenching effects as best as possible in advance takes the “strain” off the calibration procedure to remove the effect, and allows nonlinearities not explained by the quenching model to be visible in the linearity calibration. Additionally, quenching has different effects on backscattered electron populations, which escape the scintillator before coming to a stop (thus missing the large quenching effects at high $\frac{dE}{dx}$ just before stopping). Coincidence events between multiple lower-energy electrons versus a single higher-energy one also cannot be correctly described by assuming a simple scintillator nonlinearity curve between total deposited energy and visible light. Thus, the MC model attempts to produce an estimated “quenched energy” scintillator response in addition to the total deposited

energy variable:

$$E_Q \equiv \int \frac{dE}{1 + k_B \frac{dE}{dx}}. \quad (4.29)$$

The above description of quenching works in a “continuous approximation” picture, where a single primary electron is continuously bleeding off energy in the scintillator until it comes to a halt. However, the MC physics model incorporates more of the “microscopic” dynamics of the event, combining continuous energy loss models with discrete production of low-energy, short-range secondary ionization electrons (“delta rays”) knocked free by the main particle. Indiscriminately applying the “continuous” quenching formula to all the low-energy secondary electrons generated by the MC model will result in grossly over-estimating the quenching effect. To properly apply the continuous quenching model to the discrete “microscopic” MC results, the following approach is taken. When an electron first enters the scintillator volume, it is marked as the “primary” particle. At each tracking step in the MC code, the primary particle can both deposit some energy dE_0 , and create secondary electrons that carry away and eventually re-deposit energy of their own. All secondaries generated from the primary particle are tagged, and their total energy deposition in the scintillator E_{dep} is tallied along with the primary electron’s deposited energy dE_0 for the tracking step where the secondaries were initially generated. Rather than calculating $\frac{dE}{dx}$ for quenching from the MC variables for dE and dx along each tracking segment (which will have large fluctuations from discrete delta-ray events, inconsistent with the “continuous” formalism), $\frac{dE}{dx}$ is estimated using the primary electron’s E in the step in the parametrization of Equation 4.28. Thus, the “quenched energy” produced by each primary electron in the scintillator is estimated, summing over primary particle tracking steps, to be:

$$E_Q \approx \sum_{\text{steps}} \frac{dE_0 + \sum_{\text{secondaries}} E_{\text{dep}}}{1 + k_B a E^b \rho_{\text{scint}}}. \quad (4.30)$$

The (simulated) effects of quenching are demonstrated in Figure 4.9, using a ^{207}Bi calibration source as an example. The plot shows the amount of effective missing energy $E_{\text{dep}} - E_Q$ due to quenching versus the deposited energy. ^{207}Bi has two main conversion electron peaks, at ~ 0.5 MeV and 1 MeV, each with a smaller splitting between K and L-shell lines. The main line running from $(E_{\text{dep}}, E_{\text{dep}} - E_Q) = (0, 0)$ through $(500, 30)$ keV and $(1000, 40)$ keV shows the quenching effect for a single electron terminating in the scintillator. The lines of lower quenching are backscatters terminating in the other scintillator. Higher quenching above the main line comes from coincidence events between two electrons. The strongest concentration of these are at $\sim (1500, 70)$ keV from combining the ~ 0.5 MeV and 1 MeV conversion electrons.

Residual errors in this quenching approximation versus actual scintillator response will be fit out, or at least constrained by, the scintillator calibration procedure. Thus, uncertainty in the accuracy of the above quenching estimate is not directly counted towards the final energy calibration uncertainty of the system.

4.6.2 Detector hit positions

Event positions in the wirechamber and scintillator are determined by an energy-deposition-weighted position average. In addition, a “width” variable in the x , y , and z directions can be determined by

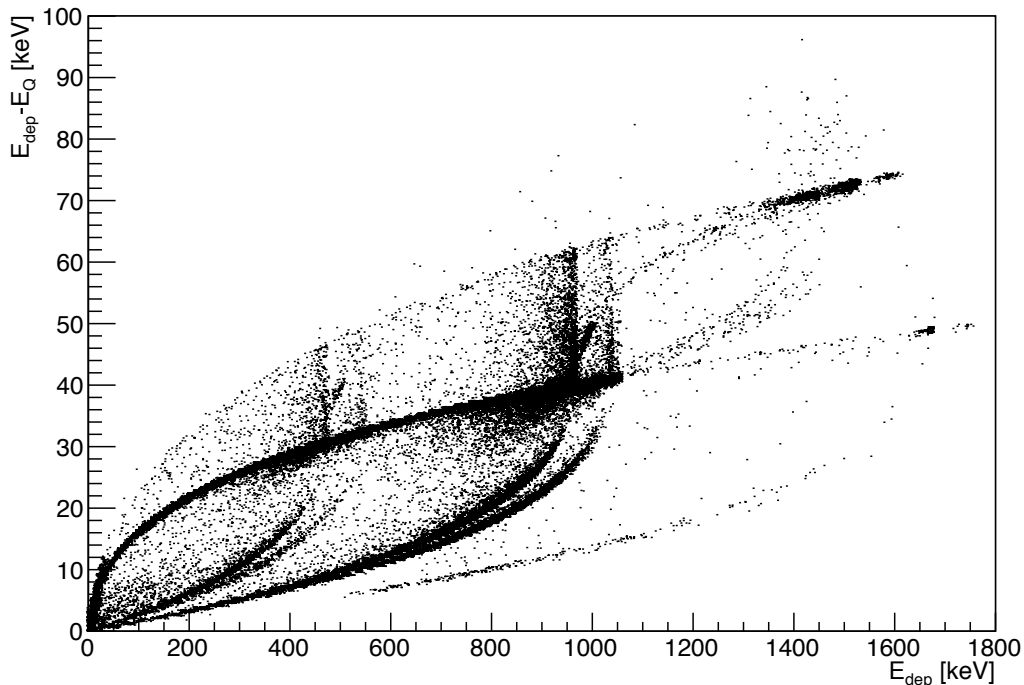
^{207}Bi MC Quenching

Figure 4.9: MC of effective missing energy due to quenching versus scintillator deposited energy for ^{207}Bi calibration source.

also recording $\langle x^2 \rangle$, etc.:

$$\langle x \rangle \equiv \frac{\int x dE}{\int dE}; \quad \langle x^2 \rangle \equiv \frac{\int x^2 dE}{\int dE}; \quad \langle \sigma_x \rangle \equiv \sqrt{\langle x^2 \rangle - \langle x \rangle^2}. \quad (4.31)$$

A slight refinement would be to weight the scintillator position according to quenched rather than deposited energy, but is likely to be of no consequence.

4.6.3 Entry/exit variables

A “hit time” variable is generated for each scintillator by recording the time (relative to the initial vertex event) when energy is first deposited in the scintillator volume. For backscatter and coincidence events resulting in energy deposition in both scintillators, the timing difference between the two sides is an observable in the data.

Also, when an electron enters or leaves the decay trap windows, wirechamber, and scintillators, its pitch angle is recorded. These pitch angles are not directly observable in the data, but are useful for checking “physics intuition” interpretations of the MC results, and can be indirectly approximated by, for example, timing between detectors in backscatter events.

4.7 MC Tuning

Ideally, the MC code would reproduce the observed data “out of the box” with no intervention beyond correctly specifying the detector geometry and initial particle conditions. Over the course of the UCNA experiment, the GEANT4 MC has come closer to this ideal. Improvements in the available low-energy electromagnetic physics models for GEANT4, such as the “Livermore” physics lists, have considerably reduced the amount of “non-physics” MC parameter tweaking necessary to reasonably reproduce the data.

4.7.1 Production cuts

GEANT4 requires specification of cuts for how low energy particles will be produced and tracked. The production of secondary particles below these thresholds are absorbed into “continuous” energy loss and scattering approximations. Cuts can be specified both in minimum particle kinetic energy, and minimum expected particle range within a material, with the more stringent cut of the two being given priority. The “Livermore” EM physics package recommends an electron and gamma energy threshold of 250 eV, though it will attempt to carry out physics calculations down to 100 eV if asked. Sufficiently small electron range cuts ($0.5 \mu\text{m}$) were set in detector materials so that the energy threshold was typically the determining factor.

The MC-predicted backscatter fractions are sensitive to the cuts applied, with lower cuts increasing the predicted backscattering. Using the “Livermore” package with range cuts defaulting to 1 keV, the Type I backscatter fraction in neutron beta decay was under-predicted by 9% by the MC. Setting the recommended 250 eV cuts, Type I backscatters are under-predicted by only 3%. Pushing cuts lower than recommended to 100 eV results in over-prediction of Type I backscatters by 6%. The recommended cut of 250 eV was used for analysis of the 2010 data.

4.7.2 Dead layer

Initial assessment of scintillator behavior using the electron gun in [Yua06] simultaneously fit for the Birk’s Law quenching constant k_B and a scintillator dead layer (treated as a distinct surface layer in which zero light would be produced from deposited energy). This analysis indicated a dead layer of $(3.0 \pm 0.3) \mu\text{m}$. The possibility of such a dead layer can be incorporated into the MC. Similarly to quenching effects, the energy response impact of such a dead layer can be fit out and constrained through the scintillator energy calibration procedure. However, fine details of backscattering and detection efficiency for low-energy electrons will not be corrected by “calibrating out” the extra energy loss.

In the full UCNA geometry, there are additional dead material volumes contributing (indistinguishably) to any scintillator dead layer, such as the MWPC exit window and nitrogen gas volume. Using the current GEANT4 model, any amount of added dead layer worsens agreement with the data. This is most evident from the ^{207}Bi calibration source, which includes a strong 56.7 keV Auger electron line at the margin of detectability. The vast majority of Auger electrons will not reach the scintillator at all, being captured in preceding materials. Predicting the detected number of Auger electrons is thus highly sensitive to accurate modeling of low-energy electron behavior in intervening materials, combined with detector trigger response. The number of observed Auger electrons in the

data typically exceeds that predicted by MC by up to a factor of two, without a dead layer in the MC. A large portion of this effect is attributable to trigger correlation details not included in the model (subsection 5.1.2), though the number of Augers reaching the scintillator in simulation before triggering considerations still typically falls short of the data. Since this indicates that the MC is already over-predicting dead layer effects in volumes prior to the scintillator, the scintillator dead layer was set to zero thickness in the GEANT4 simulations for the 2010 data. Fortunately, these effects are confined to a small portion of the event energy spectrum, generally excluded by energy cuts from asymmetry analysis, aside from higher-order effects on categorization of backscatters with marginal scintillator energy deposition.

With the GEANT4 simulations directly modeling some of the “microscopic” dynamics that might contribute to a dead layer, such as the potential “escape” from the scintillator of low energy delta-ray electrons produced near the scintillator surface, a simple “binary” fully-dead-versus-fully-sensitive-layers approach may not be appropriate for future refinements to the MC model. Potentially, future high-resolution studies comparing electron gun data against recent GEANT4 models would allow the quenching and dead layer issues to be revisited in greater detail.

4.8 Simulation and Data

4.8.1 Matching simulations to data

In order to compare simulation against real data, the simulation results for energy deposition are run forward through the subsequent stages of the system response model outlined in section 3.1 (with details of model detector response in the following chapters). With the detector response portions of the system response model applied to produce simulated ADC readouts (incorporating PMT energy resolution effects and detector triggering), the UCNA analysis code provides an interface for feeding simulated events through the exact same code used to analyze real data, assuring consistency of side-by-side comparisons.

4.8.1.1 Asymmetry weighting

For beta decay data, simulated events (from an initially isotropic, uncorrected spectrum) can be given a weighting factor of

$$w = (1 + \Delta S(E))(1 \pm A(E)\beta \cos \theta), \quad (4.32)$$

where $\Delta S(E)$ indicates the corrections to the “plain phase space” unpolarized spectrum shape described in subsection 4.5.2.2, and $A(E) = (1 + \text{R.O.})(1 + \text{R.C.})A_0$ is the asymmetry including recoil-order and radiative corrections (section 7.6). There is no fundamental reason not to include the fully corrected isotropic spectrum in the initial simulation; for the 2010 analysis, this was separated out to allow simulations to be produced while details of corrections were still being researched. For simulating events to match groups of spin flipper on/off runs, statistical sensitivity to the asymmetry can be greatly increased by re-using the same simulation data twice, once with $+A(E)$ weighting and once with $-A(E)$ for the two spin flipper states. Then, when forming asymmetries from the

simulated data, the counting statistics fluctuations are not \sqrt{N} of the total number of counts, but only $\sim \sqrt{\frac{\beta}{2} A_0 N}$ of the asymmetric portion.

Even greater statistical reach for the simulated data could be achieved by changing from event generators that randomly populate the initial E, θ event phase space to ones that more systematically cover the initial parameter space. Such distributions for uniformly filling multidimensional phase spaces are referred to as “quasi-random” or “low discrepancy” sequences in the literature on numerical integration techniques. Implementations of Sobol’ [Sob67] and Niederreiter [Nie88] quasi-random sequences are available in ROOT’s “Mathmore” libraries. Preliminary tests of generating neutron decay simulations with quasi-random initial energy and angle distributions indicate improvements in convergence equivalent to running $\gtrsim 2$ times as many randomly generated events for fitting the beta spectrum endpoint, and $\gtrsim 5$ times as many primaries for measuring the decay asymmetry. For the 2010 data analysis, statistically sufficient simulations using random initial event distributions were employed. However, for future higher precision work, involving larger beta decay datasets and more detailed tracking of detector configuration changes (such as different magnetic field maps), development of even more “efficient” simulations may be worthwhile.

Note that these data duplication methods, while improving statistical sensitivity to A , introduce complicated correlations into the data which defeat estimating, for example, fit uncertainties by normal methods for statistically-distributed counts. The “recycling” of points can be turned off to permit simulation sets that accurately reflect the statistical properties of the data, to allow simulation of expected statistical variation in extracted quantities. The $\sim 5\%$ asymmetry and spectrum shape correction weighting factors still retained are generally negligible in this regard.

4.8.1.2 Octet data “cloning”

The UCNA analysis code provides methods to automate the bookkeeping for “cloning” octet-structured beta decay data, assigning the appropriate detector response parameters and simulating matching event counts for every run (recycling the same points between spin flipper on and off, with weighting factors for the asymmetry and total number of counts in each spin flipper state). The effects of backgrounds and background subtraction are included by inflating histogram error bars as if by background count subtraction, using the background distributions observed in data (averaged over many runs for sufficient statistics, and scaled to the foreground and background run times being simulated). Such intentional degradation of the nominal statistics (without actually adding undesirable counts) assures consistent comparisons between data and MC when using statistically-weighted fits.

4.8.2 MC/data agreement

Agreement between calibration radioisotope simulations and data is indicated in the following chapters on calibrating the detectors. Such agreement is more a matter of detector calibration accuracy than a test of GEANT4’s capabilities. MC predictions for “typical” event energy deposition characteristics are generally highly reliable, and most systematic differences (such as under/over-stating the thickness/density of materials in the geometry) will be “calibrated out” to coerce data and MC into agreement. The more challenging benchmark for MC performance is accurately reproducing the distributions of “atypical” events, such as backscatters, comprising only a few percent of the data.

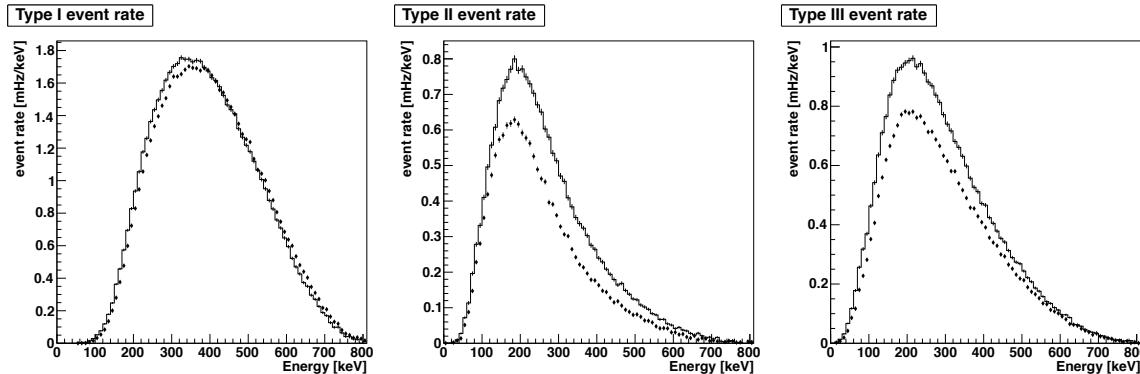


Figure 4.10: GEANT4 predictions of backscatter rates (diamond markers) compared to data (line), for 2010 beta decay data.

Type	I	II	III
data	3.80%	0.75%	1.26%
GEANT4	3.87%	0.50%	1.10%
% diff.	+1.9%	-33.2%	-12.6%

Table 4.3: Backscatter fractions (as % of Type 0 events) in beta decay, GEANT4 MC versus data, for events in the 2010 analysis cuts $r < 50$ mm, $220 < E < 670$ keV.

Comparison of backscatter fractions against the beta decay data provides a test of MC accuracy “where it matters.” Calibration radioisotopes also provide assessment of MC detail accuracy, not from the main peaks (which calibration forces to agree with simulation), but in the distribution of high-energy-loss events in the tails below.

The small difference between the overall asymmetry extracted from data and MC (using A_0 from PDG values as an input parameter to the MC) cannot be used as a check of MC accuracy, as it is effectively the experimental result itself. However, the asymmetries observed and predicted for small specialized subsets of the data (such as backscatter events) are strongly modified by angle/energy-dependent detector efficiencies far larger than tiny differences in the underlying A_0 . Comparison between data and MC predictions for asymmetries in the various backscatter classes indicates the level of confidence which can be placed on the MC’s ability to provide corrections for such effects. This topic is further discussed in subsection 7.3.6.1, in the context of MC corrections.

4.8.2.1 Beta decay backscatter spectra

Figure 4.10 compares GEANT4 simulation predictions for backscatter rates in neutron beta decay with those observed in the data. For events in the 2010 analysis window, the backscatter fractions (as % of Type 0 events) are given in Table 4.3. This improves over discrepancies in previous analyses of $\sim -10\%$ for Type I, and $\sim -30-60\%$ for II and III. The better agreement comes from a combination of improved electron transport physics models available in GEANT4 and incremental improvements to understanding detector response to deposited energy. The largest improvement in understanding detector response is to not treat the wirechamber neopentane volume outside the cathode planes as “dead,” but rather assume sensitivity to ionization in the region (see subsection 6.1.1).

Chapter 5

Scintillator calibration

5.1 PMT readout electronics calibration

5.1.1 PMT pedestals

5.1.1.1 Data selection

A subset of events — selected to be unlikely to contain non-pedestal events — is used to form an ADC spectra for the pedestal of each PMT. A list is collected of the event time and ADC readout for each selected “pedestal” event in the run.

Events are selected using the DAQ “SIS00” trigger bits, which record the subsystem triggers forming the global trigger for the event. Events triggered by the UCN monitors, or by a 2-of-4 PMT trigger on the opposite side of the detector, are used. For beta decay runs, the UCN monitor triggers will dominate. However, these are not produced (above a small noise rate) in many calibration runs without neutrons. For future data collection, a “random sample” trigger source uncorrelated with data events would be a useful addition to the system.

5.1.1.2 Data processing

The pedestal data is subdivided into smaller subsets containing an equal number of points, such that each subset contains at least 3000 events, and on average will be at least 60 seconds long (so, at pedestal event rates above $3000 / 60 = 50$ Hz, the 60 second time binning will determine the division, while at lower rates longer time bins will be used to assure sufficient statistics in each bin). In general beta decay and calibration running, the 60 second bin time was the limiting factor, with ~ 5000 events per bin.

The mean value of the ADC for the points in each bin is calculated, then re-calculated excluding points outside ± 50 ADC channels from the mean to remove influence from extreme outliers that likely correspond to non-pedestal signals in the PMT. This mean value is recorded as the “pedestal center” for the group of events. The RMS spread of ADC values around the mean is also recorded, along with the mean value of the event timestamp for the data points. These averages for the pedestal in ~ 1 minute bins are uploaded to the Calibration DB for each run.

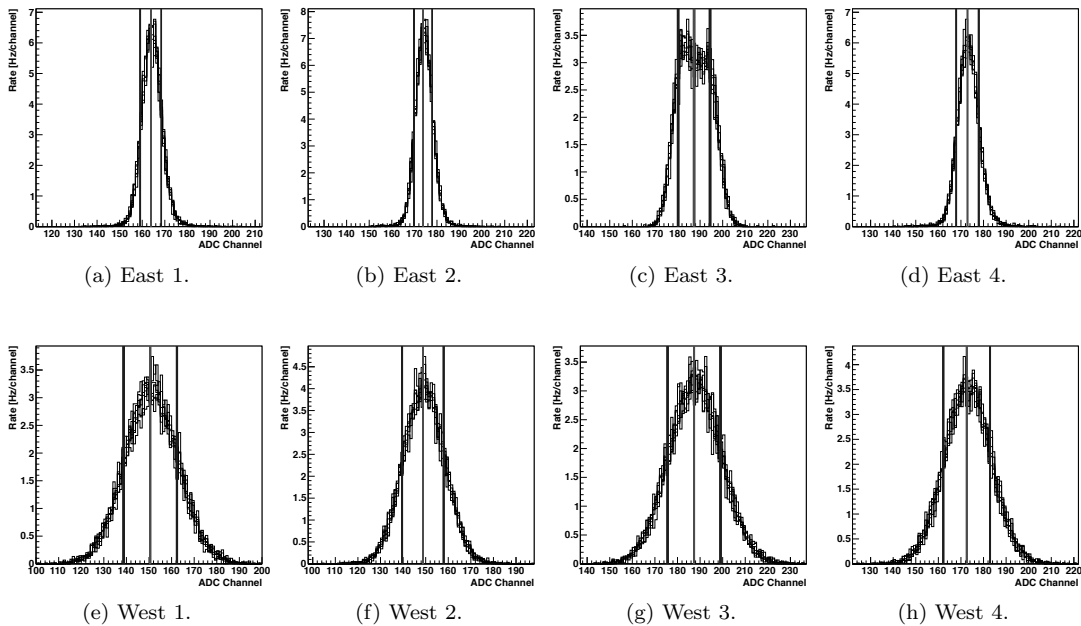


Figure 5.1: Typical PMT pedestal distributions for each PMT. Vertical lines indicate mean and RMS spread.

5.1.1.3 Results

Figure 5.1 shows typical PMT pedestal distributions, which remain more or less identical throughout the year. Figure 5.2 shows the time history of the pedestals over the 2010 run. Note that the y axis scale of all plots is identical, except for East 1, which requires $10\times$ the range to display. PMT pedestal means drift on the order of $\sim \pm 1$ channel over time scales of 1 day ($\sim \pm 20$ channels for East 1), so typical 1 minute time resolution is far more than sufficient to account for all changes.

5.1.1.4 Response model pedestal terms

In the detector response model, the pedestal value p is treated as a continuously varying function of time $p(t)$, linearly interpolated from between the measured points extracted above. The pedestal noise $\pm\Delta p$ is modeled as a Gaussian distribution with the RMS width interpolated as a function of time from the observed pedestal RMS data stored in the Calibration DB. A correlation of $c = +0.2$ between the four PMT pedestals on one side is included (subsubsection 5.5.4.3, Appendix C).

5.1.2 Scintillator event trigger

Each individual PMT is attached to a discriminator. An isolated PMT trigger will increment a scaler for the PMT trigger rate, and start a TDC counting for the single PMT. A coincidence between any two of the four single-PMT triggers on one side generates a ‘2-fold’ DAQ event trigger, causing all DAQ ADC channels to be read out, and a ‘stop’ signal to be sent to all TDCs (operating in common-stop mode).

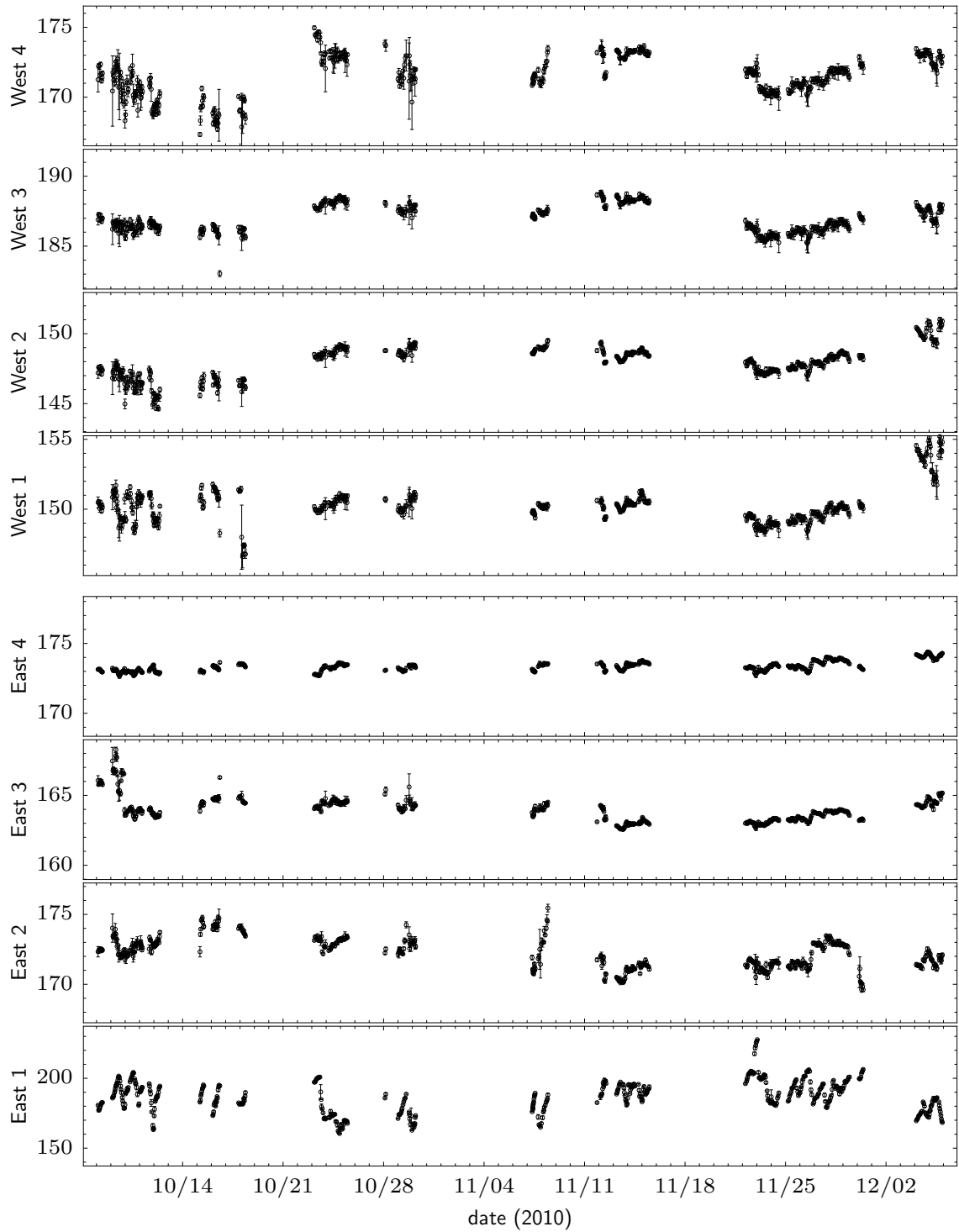


Figure 5.2: PMT pedestal values over all 2010 asymmetry data runs. Errorbars indicate RMS spread of pedestal measurements within one run.

5.1.2.1 Independent trigger model

A simple model for triggering is to assume that the four individual PMT discriminators act independently on the signals produced by the four PMTs (which are also recorded by corresponding ADCs). The individual PMT discriminator response curves (probability of triggering versus observed ADC signal) can be mapped out, and the 2-fold trigger probability deduced from the individual PMT probabilities for an event. As will be discussed below, the assumption of independence in discriminator operation turns out to be incorrect, but forms a starting point for approximating the trigger response.

Suppose an event produces ADC signals Q_1, Q_2, Q_3, Q_4 in the four PMTs. Assuming the probability of each single PMT triggering is independently a function $p_i(Q_i)$, then the probability of forming a coincidence trigger is:

$$\begin{aligned}
 p(\text{2-fold}) &= p(\#1 \text{ triggers})p(\geq 1 \text{ of } \#2,3,4 \text{ trigger}) + p(\#1 \text{ doesn't trigger})p(\geq 2 \text{ of } \#2,3,4 \text{ trigger}) \\
 &= p_1 \cdot [1 - (1 - p_2)(1 - p_3)(1 - p_4)] + (1 - p_1) \cdot [p_2p_3 + p_3p_4 + p_4p_2 - 2p_2p_3p_4] \\
 &= 3p_1p_2p_3p_4 - 2(p_2p_3p_4 + p_1p_3p_4 + p_1p_2p_4 + p_1p_2p_3) + \sum_{i<j=1}^4 p_i p_j.
 \end{aligned} \tag{5.1}$$

5.1.2.2 Single PMT average trigger probability

For each run, an average trigger probability curve as a function of ADC channels above pedestal was extracted from the data and parametrized by a fit curve (saved to the Calibration DB). In order to determine the trigger probability for each PMT, an un-biased sample of events is needed, which would have been collected whether or not the PMT in question triggered. For each PMT, a sample was taken consisting of events where either three or more PMTs had triggered on the PMT's scintillator, or a 2-fold trigger occurred on the opposite scintillator. Events from LED triggers or within the prompt beam burst time cuts were excluded, so sampled events come from "beta-decay-like" data.

The ratio of events in which the PMT fired to total events in the sample, as a function of pedestal-subtracted PMT ADC, produces the trigger efficiency function. The asymmetrical sigmoid shape of the trigger efficiency function is fit by a three-parameter family of curves, whose form is physically motivated by a hand-waving model for discriminator function described as follows.

For a fixed single-PMT ADC signal Q , there will be some distribution in heights of the signal peak which must exceed a fixed discriminator threshold level to produce a trigger. Suppose this distribution has cumulative density function $\text{CDF}(x; Q)$. With a discriminator threshold x , the trigger probability will be the proportion of events above the threshold, $1 - \text{CDF}(x; Q)$. The height of the signal peak corresponds to some number of charge units arriving within some time window, and hence is likely to have a Poisson-like distribution. Thus, we take the CDF to be a continuous variant of the CDF of a Poisson distribution (notation as per Abramowitz and Stegun 6.5, 26.4 [AS64]),

$$\text{CDF}(x; Q) = \frac{\Gamma(x + 1, \lambda(Q))}{\Gamma(x + 1)} = 1 - P(x + 1, \lambda(Q)), \tag{5.2}$$

which is the CDF for the Poisson distribution with mean $\lambda(Q)$ for integer x , smoothly extended to non-integer values of x . P is the normalized lower incomplete gamma function (available as

`TMath::Gamma(a, x)` in ROOT), very closely related to the Chi-Square probability function:

$$P(a, x) = P(\chi^2 = 2x | \nu = 2a) \equiv \frac{1}{\Gamma(a)} \int_0^x t^{a-1} e^{-t} dt. \quad (5.3)$$

At a fixed threshold x , the dependence of $\lambda(Q)$ on Q only matters in the “transition region” between highly probable ($\text{CDF}(x, \lambda) \ll 1$) and highly improbable ($1 - \text{CDF}(x, \lambda) \ll 1$) triggers. Thus, we expand λ linearly around the 50% trigger probability point Q_{50} , noting that the characteristic width of the region will be $\sim \sqrt{\lambda}$:

$$\lambda(Q) \approx \lambda_{50} + \frac{Q - Q_{50}}{w} \sqrt{\lambda_{50}}, \quad (5.4)$$

where λ_{50} is the mean “number of charge units” at the 50% trigger probability point Q_{50} , and w indicates the width of the transition region in ADC channels. The discriminator threshold x is related to the 50% point λ_{50} such that $1 - P(x+1, \lambda_{50}) = \frac{1}{2}$. This can be done approximately using a large- λ approximation for the inverse of P (which turns out to be sufficiently accurate even at $\lambda \sim 1$), based on Abramowitz and Stegun 26.4.17 [AS64],¹

$$P(a, \lambda_{50}) = \frac{1}{2} \Rightarrow \lambda_{50} \approx \left(1 - \frac{1}{9a}\right)^3 a \Rightarrow a \approx \lambda_{50} + \frac{1}{3} - \frac{1}{27\lambda_{50}} + O\left(\frac{0.02}{\lambda_{50}^2}\right). \quad (5.5)$$

Putting everything together, and including an extra asymptotic efficiency parameter η_0 which should be 1 unless something has gone wrong, produces a four-parameter fitting function for the observed trigger efficiency curves:

$$\eta(Q; Q_{50}, w, \lambda_{50}, \eta_0) = \eta_0 \cdot P\left(\lambda_{50} + \frac{1}{3} - \frac{1}{54\lambda_{50}}, \lambda_{50} + \frac{Q - Q_{50}}{w} \sqrt{\lambda_{50}}\right). \quad (5.6)$$

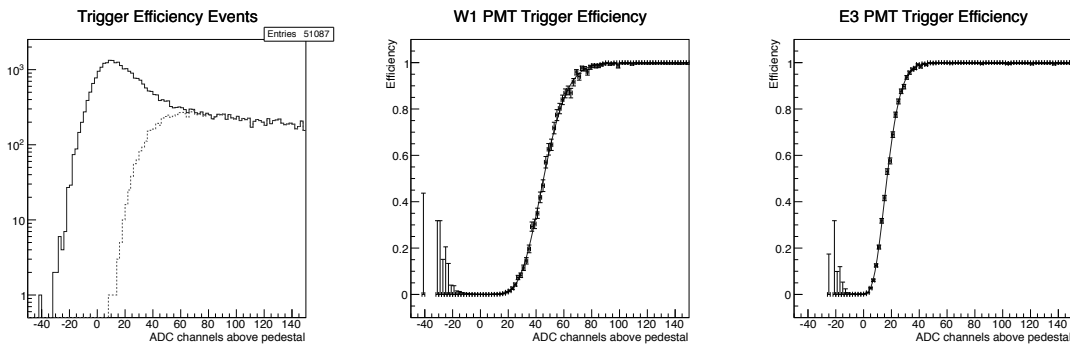
The family of curves produced by this expression appear to provide good fits for observed data, closely following the range of sigmoid shapes seen, from more symmetric (higher- λ_{50}) to asymmetric (low- λ_{50}) instances. That this family of curves fits so well, using only 3 parameters (plus $\eta_0 \approx 1$, which is mainly a check against severe problems), indicates that the hand-waving physics motivation may be reasonable. Figure 5.3 shows an example of trigger efficiency curves extracted from a beta decay run.

5.1.2.3 Shortcomings of independent trigger model

The discussion above has included the assumption that, regardless of how the four PMT ADC values may be correlated, the probability of an individual PMT producing a trigger at some signal Q_i is independent of what the other PMTs are doing. Such an assumption would be enforced if the DAQ ADCs and discriminators for each PMT were separated systems with no way to “communicate.” However, analysis (described below) indicates that the discriminators, which are physically housed in a single module, were not acting independently, but were influenced by the signals on other PMTs.

To test for PMT trigger independence, one can compare the observed 2-fold trigger efficiency to the efficiency predicted by independent combination of the four single-PMT trigger efficiencies (Equation 5.1). Doing this requires a data set from which the 2-fold trigger efficiency can be

¹An even better approximation appears to be obtained by replacing $-\frac{1}{27\lambda}$ by $-\frac{1}{54\lambda}$, for reasons I cannot ascertain.



(a) Trigger efficiency input data: all events in sample (solid line), and subset in which the PMT triggered (dashed). (b) Trigger efficiency curve from ratio of preceding histograms, with parametrization fit (solid line); $\lambda_{50} \approx 21$. (c) Trigger efficiency curve from another PMT, with more asymmetric turn-on, corresponding to a lower $\lambda_{50} \approx 8.5$.

Figure 5.3: Single-PMT trigger efficiency determination, typical example histograms from a beta decay run.

determined, *i.e.* events not recorded because they already had a 2-fold trigger. Data from LED scans is one source, providing LED events captured regardless of the 2-fold trigger (though the 2-fold trigger status is still recorded). Another potential source is events where a 2-fold trigger was generated on the opposite detector side, using backscatters as a source of low-signal events.

With such a data set, events can be binned by “predicted” trigger efficiency based on the independent PMT trigger probabilities for the observed event ADC values. The actual 2-fold trigger efficiency as a function of predicted efficiency is determined from the data. Deviation from a 1:1 correspondence between the predictions of the independent model and the observed efficiency indicates violation of the assumptions of independence. Figure 5.4 shows the result of such analysis using LED data from beta decay runs near the end of the 2010 data set. Both detector sides show significant deviation from trigger independence, with 2-fold trigger probability significantly increased from expected (indicating a strong positive correlation between single-PMT trigger probabilities). One note is that triggering behavior is still “as expected” for the overwhelming majority of events, which have expected and observed trigger probabilities very near 0 or 1. Only a small fraction of events lying in a narrow transition region are affected, the general impact of which is to shift the “edge” of the trigger turn-on to lower energy by up to 10 keV (on the worst-case West side), compared to the independent model. Extracting the individual PMT trigger curves as above still has utility, as it correctly indicates the ADC ranges for near-zero and near-unity trigger probability, though 2-fold efficiency in the transition range is inaccurately described.

For the 2010 data analysis, the independent model was assumed throughout. Discrepancy between data and model expectations for the low-energy trigger threshold was noted, but left unresolved. The energy threshold is well below the asymmetry analysis energy fiducial range, and discrepancies in backscatter detection between data and MC (which could be influenced by detector thresholds) were considered covered by the associated systematic error estimate.

More attention to this detail of trigger efficiency would be useful in future analysis, especially in conjunction with new calibration sources probing lower energy regions than the 2010 set. The trigger efficiency would need to be mapped out not in four “independent” PMT curves, but as a

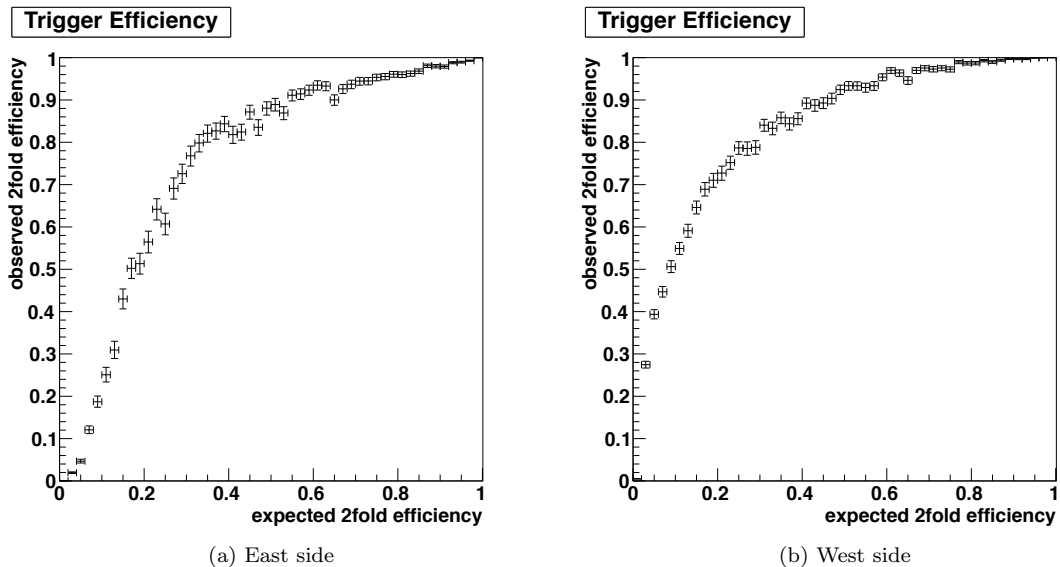


Figure 5.4: Observed 2-fold trigger efficiency as a function of predictions from independent PMT trigger model, indicating violation of assumptions of independence.

function of all four PMT ADCs simultaneously. As noted previously, using events triggered by a 2-fold in the opposite detector (relying on backscatters to provide the range of low-signal events) would provide a good data set for such analysis, appropriately covering the range of signals of interest for beta decay data. However, the smaller statistics of the backscatter dataset, along with larger four-dimensional space to map, precludes fine-grained run-by-run trigger efficiency extraction as is available for individual PMT curves. A more ideal solution for future data is to reconfigure the DAQ electronics to assure discriminator independence.

5.2 PMT gain stability

The gain factor g in Equation 3.1 is determined relative to some time t_0 , with the “absolute” gain factor absorbed into the definition of the linearity curve f . The choice of t_0 is entirely arbitrary, making no difference to results so long as used consistently through the calibration process. Indeed, a constant fictitious set of t_0 values, unrelated to any actual data, could be used. However, t_0 is typically chosen to be the start of one of the source calibration runs used to generate the corresponding linearity curve f , so that comparison to the t_0 values indicates physically meaningful changes.

The basic principle for measuring the gain factor is to measure PMT response $Q_{\text{ref}}(t)$ to some (stable) reference feature as a function of time, and form the ratio to the value at t_0 :

$$g \equiv \frac{Q_{\text{ref}}(t)}{Q_{\text{ref}}(t_0)}. \quad (5.7)$$

This principle may be compounded on multiple time scales, using one “reference feature” that can be quickly and frequently measured but may exhibit slow drift, and correcting the longer-term gain variation using a second more stable (but not as rapidly measurable) feature. The ^{207}Bi “pulser”

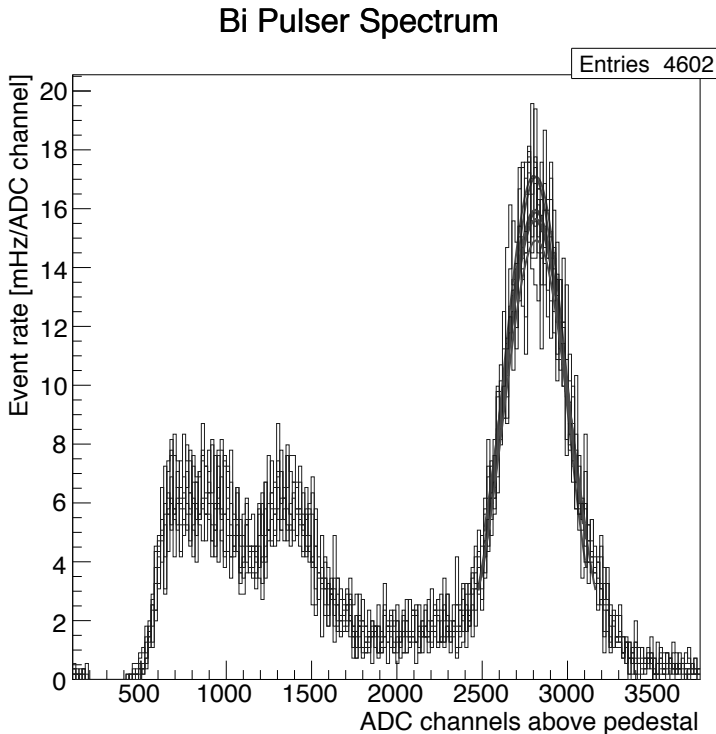


Figure 5.5: Typical ^{207}Bi pulser spectra collected from a beta decay run (eight spectra overlaid), with Gaussian fits to spectrum peak.

attached to each PMT provides the “reference feature” for timescales from minutes to hours, while longer-term gain corrections are made using the beta decay spectrum endpoint.

5.2.1 ^{207}Bi pulser

5.2.1.1 Method

Each run is divided into roughly five-minute-long segments (runs over five minutes long are divided into $\lfloor \text{run length}/300 \text{ s} \rfloor$ equal-time segments), with a pulser spectrum accumulated for each segment. Figure 5.5 shows typical spectra collected from a 40-minute-long Beta run. The main peak in the spectrum is the $\sim 1 \text{ MeV}$ conversion electron line from ^{207}Bi decay, producing $\sim 5 \text{ Hz}$ of events. The edge at ~ 600 ADC channels is due to the high-threshold single-PMT trigger discriminator. The $\sim 500 \text{ keV}$ line from ^{207}Bi is marginally visible at ~ 1400 ADC channels, buried in the rising spectrum of events from decay gamma rays.

A Gaussian fit is made to determine the peak center, used as the “reference feature” $Q_{\text{ref}}(t)$. The fit is performed three times iteratively to determine the fitting window $c \pm 1.5\sigma$, where the center c and width σ are taken from the previous iteration of the fit. Such iteration removes dependence on the initial choice of fit window. Statistics are sufficient to allow the peak location (and thus the gain) to be determined to $\lesssim \pm 0.2\%$ in each 5-minute segment, which will further improve by $1/\sqrt{n}$ when averaged over n segments in many runs. These fit results are recorded to the Calibrations DB, for later reference in gain stabilizing the run.

5.2.1.2 Results

Figure 5.6 shows the time history of the ^{207}Bi peak position relative to the reference run for the 2010 asymmetry data runs. The gain typically varies by $\sim 1\%$ over daily temperature cycles, with the exception of East 4, which shows $\sim 5\times$ the magnitude of gain variation. Based on the observed beta decay endpoint position, the ^{207}Bi gain stabilization is highly successful at removing the $\sim 1\%$ daily fluctuations cycle.

However, some longer-term gain instability was apparent — beta decay endpoint discrepancies of a few percent when corrected relative to calibration reference runs a week or two away. During the 2011 data taking period, PMT W2 demonstrated severe ^{207}Bi pulser instability, with the ^{207}Bi spectrum peak plummeting downward in signal to below trigger threshold over the course of a couple of days, despite no change in PMT response to regular scintillator signals. The PMT pulser signal demonstrated strong sensitivity to the PMT magnetic field bucking coil current. Possibly, the pulser light signal — entering from a different location than the scintillator light guide — is illuminating an edge portion of the PMT photocathode with its own additional gain sensitivity, different from the photocathode region receiving light from the main scintillator. Thus, while the pulser signal (when not plummeting below usable range) is generally useful for stabilizing short-term drifts up to the daily temperature cycle variations, longer-term gain stability requires independent assessment and correction.

5.2.2 Beta endpoint stabilization

To address the longer-term stability issues with the ^{207}Bi pulser, indicated by drift in the observed beta decay endpoint, the beta spectrum endpoint itself can be used for gain correction (on top of the ^{207}Bi pulser corrections for shorter timescale variations). In order to avoid potentially introducing spin-dependent gain changes, which would produce large errors in the asymmetry, beta spectrum based stabilization should not be performed for spin flipper on and off runs individually. However, spectra averaged over combinations of spin flipper on and off runs — from single pulse pairs to entire octet groups — can be used to correct the gain for groups of runs. For the 2010 data analysis, PMT gain was adjusted for each beta decay octet based on the spectrum accumulated over the whole octet. The method for calculating the necessary amount of gain correction, given observed data and expected spectra from simulation, is described below.

5.2.2.1 Beta spectrum endpoint fitting for energy scale comparison

The simplest approximation for the beta spectrum shape (written in the “natural units” of subsection 4.5.2.2) is the phase-space factor ²

$$S_0(W; W_0) \equiv pW(W_0 - W)^2; \quad p \equiv \sqrt{W^2 - 1}. \quad (5.8)$$

²This can be refined for heavier nuclei than the neutron by including an additional factor for the Fermi function $\approx (1 - e^{-2\pi\alpha ZW/p})^{-1}$. However, for the purposes of comparing the energy scale of spectra, rather than accurately ascertaining an endpoint, such further details are irrelevant.

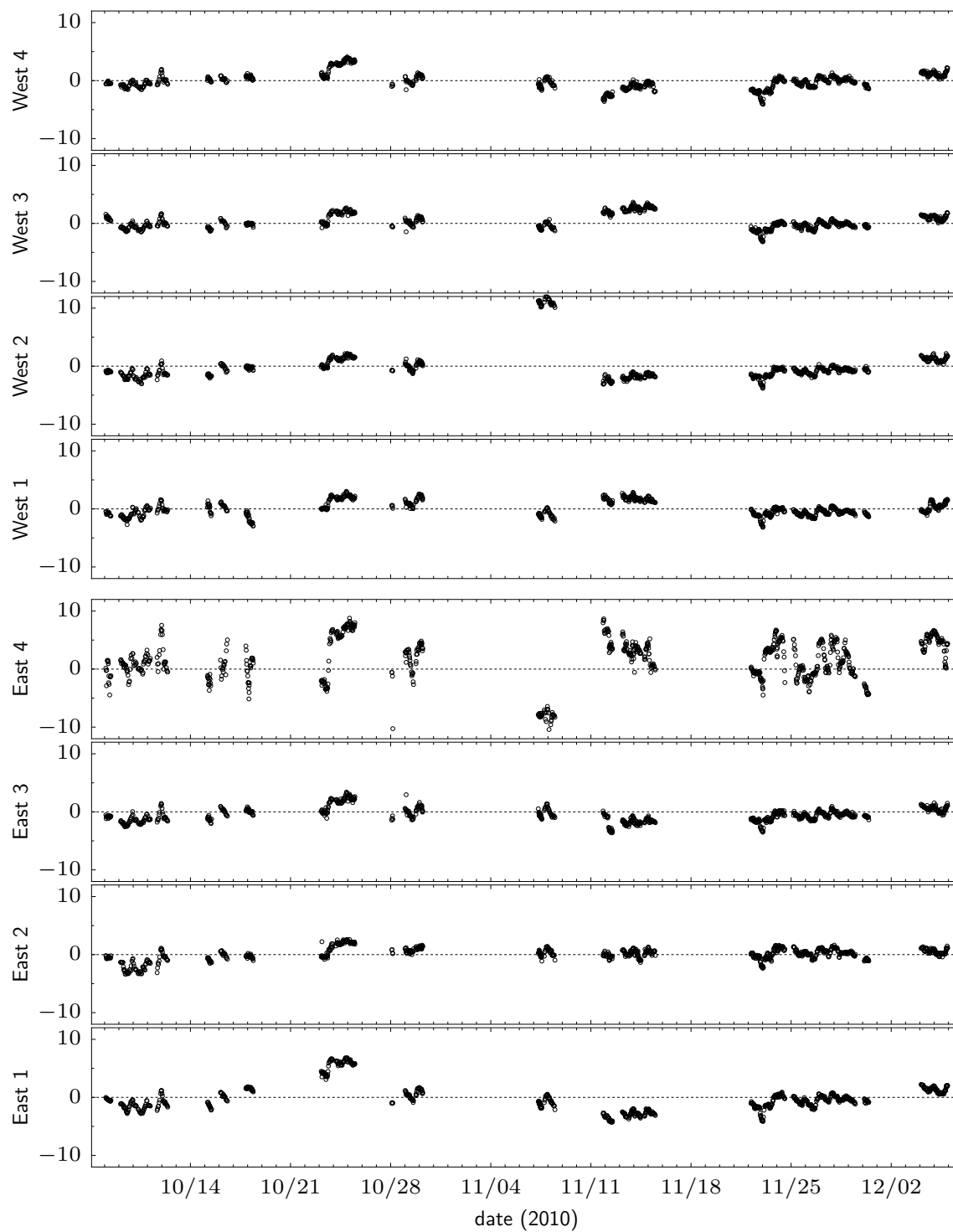


Figure 5.6: PMT ^{207}Bi pulser gain monitor history, % difference from reference run.

Thus, given an observed beta spectrum $S(W)$, one can make the “Kurie plot” [KRP36]

$$K(W) \equiv \sqrt{\frac{S(W)}{pW}} \approx W_0 - W, \quad (5.9)$$

producing a straight line pointing approximately to the endpoint W_0 .

Suppose we have a beta spectrum $S(x)$ measured against some parameter x , which is proportional to kinetic energy, but perhaps with an unknown proportionality factor. Let α be an estimate for this proportionality factor, so $W \approx 1 + \alpha x$. Forming the Kurie plot

$$K(W; \alpha) \equiv \sqrt{\frac{S\left(\frac{W-1}{\alpha}\right)}{pW}}, \quad (5.10)$$

an approximate endpoint $W'_0(\alpha)$ is extracted by a straight line fit over some predetermined range in W . Some value of α will satisfy the condition $W'_0(\alpha) = W_0$. This value can be found by iterative adjustment:

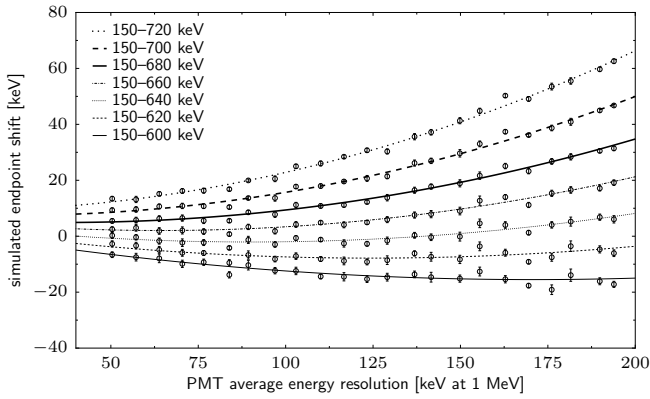
$$\alpha_{\text{new}} \equiv \frac{W_0 - 1}{W'_0(\alpha) - 1} \alpha, \quad (5.11)$$

which converges to the self-consistent point where $W'_0(\alpha) = W_0$. Equivalently, this indicates the approximate location of the endpoint W_0 on the x scale, $x_0 \equiv (W_0 - 1)/\alpha$.

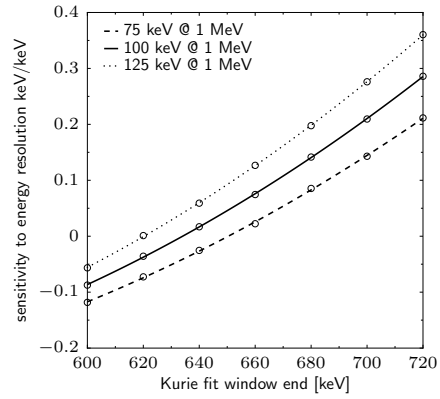
In the case where $S(x)$ is an “idealized” beta spectrum, shaped exactly like the phase space factor, the α determined by this procedure will be the exact scaling factor between x and kinetic energy. For actual observed spectra modified by the impacts of energy loss and detector resolution (along with theory deviations of the underlying spectrum shape from the simple phase space factor), α will not indicate an exact calibration factor. However, α allows relative comparison between two spectra that differ only in axis scale: for example, data with an unknown gain factor versus a simulation, including all the detector response effects, from which a value $\alpha^{\text{sim}} \approx 1$ can be extracted. To the extent that the simulation accurately captures detector effects on the spectrum, the factor $\alpha' \equiv \alpha^{\text{data}}/\alpha^{\text{sim}}$ will place the data onto a correct energy scale.

5.2.2.2 Fit sensitivity to energy resolution

Potential errors in this method stem from inaccurate modeling of detector effects in the simulated comparison. The sensitivity of endpoint extraction to errors in model parameters can be determined from simulations with intentionally varied parameters. The most significant modification to spectrum shape comes from PMT energy resolution. Figure 5.7 shows the simulated result of varying PMT energy resolution on the extracted endpoint of the simulation spectrum for various choices of fitting window for the Kurie plot. Energy resolution indicated is based on photoelectrons per MeV averaged over the fiducial volume, using measured light transport maps. Observed PMT average energy resolutions fall in the ~ 70 keV to 130 keV @ 1 MeV range. The Kurie plots were made using the simulated E_{vis} variable, which includes both the effects of energy loss and scintillator quenching. Thus, while a nominal value of 782.3 keV was used for the endpoint in the Kurie fitting procedure, the endpoint of the simulated E_{vis} spectrum falls at ~ 710 keV, which was used as the (arbitrary) reference point for “0 keV endpoint shift” in the plots. By selection of an appropriate fit window, the Kurie fit results can be made highly insensitive to differences in PMT energy resolution. Figure 5.8

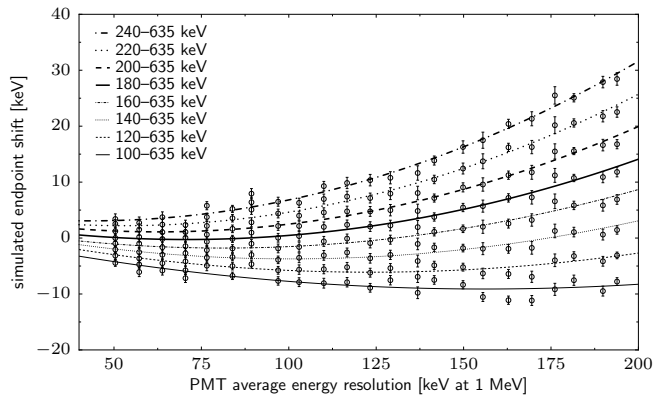


(a) variation in Kurie fit endpoint position as a function of energy resolution and fit window.

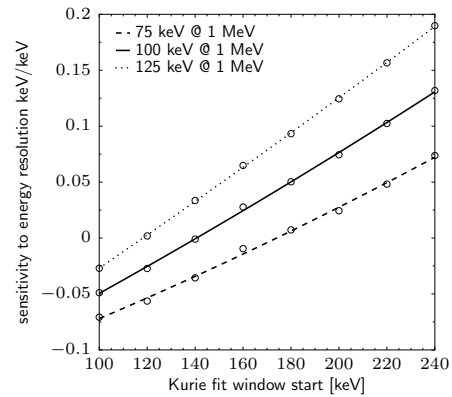


(b) endpoint sensitivity to error in energy resolution relative to nominal, as a function of fit window upper end.

Figure 5.7: Simulated sensitivity of Kurie fit result to single-PMT energy resolution and fit range upper end.



(a) variation in Kurie fit endpoint position as a function of energy resolution and fit window.



(b) endpoint sensitivity to error in energy resolution relative to nominal, as a function of fit window lower end.

Figure 5.8: Simulated sensitivity of Kurie fit result to single-PMT energy resolution and fit window lower end.

repeats the analysis, but now varying the lower edge of the Kurie fit window.

Sensitivity to errors in the energy resolution at 1 MeV can thus be reduced to < 0.1 keV/keV by adoption of a 150 keV to 635 keV Kurie fit window, and to the 0.01 keV/keV level by careful choice of window on an individual PMT basis. The 150 keV to 700 keV window used for the 2010 data analysis introduces a sensitivity of ~ 0.25 keV/keV to errors in modeled PMT energy resolution at 1 MeV, which is known to better than ± 4 keV at 1 MeV (subsection 5.4.4).

5.2.2.3 Analytical approximation for spectrum smearing

As an aside, the following analytical approximations provide guidance in estimating the effect of resolution smearing on the portion of the spectrum near the endpoint.

Consider the situation where the energy resolution at the endpoint is $\sigma \ll W_0$, which is reasonable for the UCNA PMTs ($\sigma \sim 0.1W_0$). In the region around the endpoint, the resolution can be considered approximately Gaussian convolution with some constant width σ . Treating the pW term as approximately constant over the resolution width, it is pulled out of the convolution integral; at and beyond the endpoint, the endpoint value p_0W_0 can be used ($p_0 \equiv \sqrt{W_0^2 - 1}$). Then, the detector resolution convolved spectrum near the endpoint ($x = 0$) will be

$$\frac{S_\sigma(x)}{pW} \equiv \int_{-\infty}^0 \frac{t^2}{\sqrt{2\pi}\sigma} e^{-(x-t)^2/2\sigma^2} dt = \frac{1}{2}(x^2 + \sigma^2) \left(1 - \operatorname{erf}\left(\frac{x}{\sqrt{2}\sigma}\right) \right) - \frac{\sigma x}{\sqrt{2\pi}} e^{-x^2/2\sigma^2}. \quad (5.12)$$

Moving away from the endpoint towards the bulk of the spectrum,

$$\frac{1}{pW} S_\sigma(W_0 \gg -x \gg \sigma) \approx x^2 + \sigma^2 \Rightarrow \sqrt{\frac{S_\sigma(x)}{pW}} \approx - \left(1 + \frac{\sigma^2}{2x^2} \right) x, \quad (5.13)$$

so, the Kurie plot line, which is $\sim -x$ in the un-smearred case, is raised by a factor of $1 + \frac{\sigma^2}{2x^2}$ as the endpoint is approached. In other approximation regimes, the spectrum behavior in the immediate vicinity of the endpoint is:

$$S_\sigma(|x| \ll \sigma) \approx \left(\frac{\sigma^2}{2} - \sqrt{\frac{2}{\pi}} \sigma x \right) p_0 W_0, \quad (5.14)$$

and the tail falling off past the endpoint will be:

$$S_\sigma(x \gg \sigma) \approx \frac{p_0 W_0}{\sqrt{2\pi}} \frac{\sigma^3}{x} e^{-x^2/2\sigma^2}. \quad (5.15)$$

For comparison, the total number of counts in the spectrum is

$$\int_1^{W_0} pW(W_0 - W)^2 dW = \frac{1}{60} [15W_0 \ln(p_0 + W_0) + (2W_0^4 - 9W_0^2 - 8)p_0], \quad (5.16)$$

which, for neutron $W_0 \approx 2.53$ ($\Rightarrow p_0 \approx 2.33$, $p_0W_0 \approx 5.88$) comes out to ≈ 1.63 . The maximum height of the spectrum is ≈ 1.78 at $W \approx 1.48$.³

³An analytical formula for this is possible, but unenlighteningly messy, being a solution to the cubic equation $(W_0 - 3W)(W^2 - 1) + (W_0 - W)W^2 = 0$.

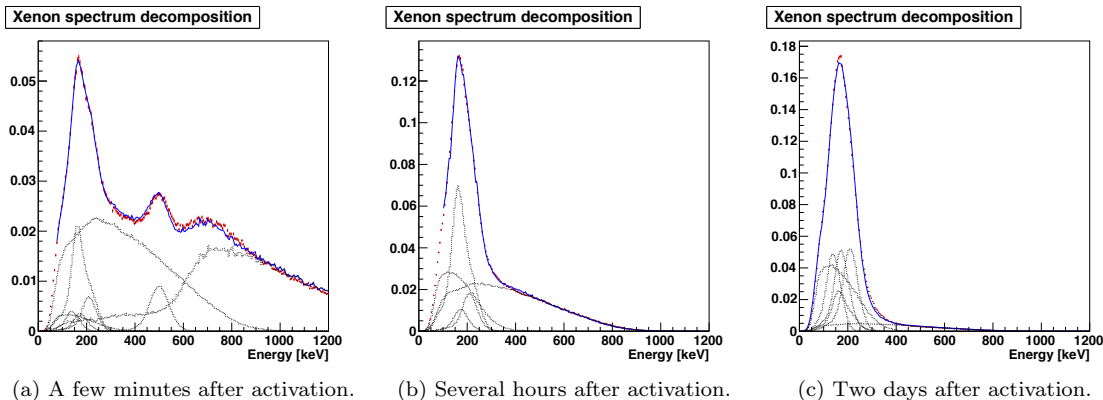


Figure 5.9: Decomposition of observed Xe spectra into isotope components. Dotted lines are simulated components, summed to form solid line, overlaid on data points.

5.3 Scintillator light transport

The basic plan for mapping the scintillator’s light transport efficiency to each PMT as a function of position is to provide a “standard candle” source of identical event distributions at all positions in the detector, and compare the relative scaling between the observed spectra as a function of position. A mono-energetic line source would be ideal, but none has been available. Prior to the 2010 data analysis, the neutron beta spectrum itself was used for this purpose. In the 2010 data and beyond, the system for activating xenon by neutron capture was developed and deployed, providing an independent (and higher statistics) fiducial-volume-filling decay source.

5.3.1 Mapping with activated xenon

The medley of xenon isotopes produced by neutron activation contains many components, decaying away with half lives from four minutes to over a month (subsection 3.4.2). The composition can be estimated by fitting a linear combination of simulated energy spectra for each individual isotope to the observed energy spectrum. Figure 5.9 shows an example of this for xenon at various ages after activation. Short-lived components are $^{137}\text{Xe } \frac{7}{2}^-$, a 4 MeV endpoint beta decay with 4 minute half life, and $^{135}\text{Xe } \frac{11}{2}^-$, a 500 keV conversion electron line with 15 minute half-life. Once these have died away, the xenon spectrum takes a characteristic shape: a broad peak at ~ 200 keV, coming from a large variety of isotopes, and the 915 keV endpoint beta decay of $^{135}\text{Xe } \frac{3}{2}^+$ (9 hour half life).

Of the two distinctive features of the xenon spectrum, the ~ 200 keV peak was considered unsuitable for position mapping in the 2010 setup, as, from locations with lower light transport efficiency, the peak is significantly modified by the detector trigger efficiency edge. For future runs with better-characterized low-energy threshold behavior, this peak could provide an alternative check of the light transport map. Though a beta spectrum endpoint is more finicky to measure than a peak (more counts required for similar statistical accuracy, and much less independent of detector energy resolution), the 915 keV beta endpoint served as the “standard candle” for mapping the light transport in the 2010 data. Because of the effects of detector resolution — which varies $\sim 2 : 1$ for individual PMTs as a function of position due to $\sim 4 : 1$ variations in light transport — on measuring a beta

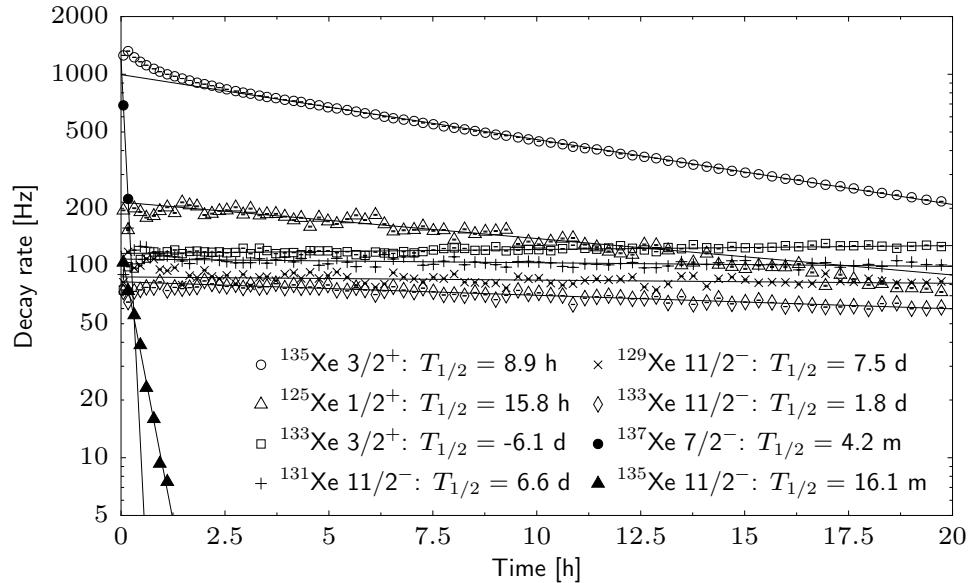


Figure 5.10: Xenon spectrum composition determined by spectrum fits for each of a time series of xenon runs, and fits to apparent half-life of each component (compare to expected values in Table 3.5). Degeneracy between the similar shapes of the longer-lived isotopes impairs the accuracy of the composition fits, as evidenced by the apparent negative half life $^{133}\text{Xe } \frac{3}{2}^+$.

spectrum endpoint, the “standard candle” is not quite as constant as one might hope, and requires correction from comparison against simulated spectra incorporating the resolution effects.

5.3.1.1 Spectrum composition

For the purpose of relative light transport position mapping, a precise determination of the underlying spectrum shape (and the corresponding time-evolving isotopic composition of the source) is wholly unnecessary. So long as the incident spectrum is identical throughout the volume, it matters fairly little precisely what it is. A rough estimate, capturing the approximate size of the low peak versus the 915 keV endpoint spectrum, is useful for inclusion in the resolution smearing simulation to assure any encroachment of the resolution-broadened low peak on the beta spectrum is accounted for. Since the spectra of the various isotopes contributing to the overall peak are similar when viewed at the detectors’ energy resolution, the isotopic proportions derived from the fit are uncertain and sensitive to changes in, for instance, the fit range, though the overall shape of the peak is well described by the combination. Plotting the extracted composition versus time for a series of xenon runs (Figure 5.10) gives some indication of the accuracy of the fit procedure — the apparent lifetime of major components aligns reasonably well with expectations, though with muddled results for the long-lived low-energy peak components. A fitting procedure taking the time-varying structure of the spectrum over multiple runs into account would likely identify the isotopic composition with better accuracy.

5.3.1.2 Mapping method

The light transport efficiency is assumed to be a reasonably smoothly varying function of position, which can be represented to sufficient accuracy by interpolation between a set of points over the

circular acceptance of the detector. The detector area is divided into 351 small sectors, approximately $(4.7\text{ mm})^2$, by the scheme described in section D.1, and the light transport map is taken to be defined by the value at the center point of each sector, and interpolation between by cubic splines as described in section D.2. Using a previous approximate position map $\eta^{\text{old}}(x, y)$ to reconstruct the visible energy for each PMT, the observed visible energy spectrum in each sector is recorded. The spectrum is fit by the Kurie endpoint fitting procedure described in subsection 5.2.2.1, using a nominal endpoint of 915 keV and a fit range of 450 keV to 750 keV, producing an observed location for the endpoint E_i^{obs} in each sector i . This restricted fit range is intended to minimize interference from the potentially resolution-broadened lower energy peak. A simulated spectrum is fit by the same procedure for comparison, producing E_i^{sim} for each sector. A new light transport position map can then be produced by tweaking the old one for the discrepancy between observed and expected signal, defining new values for the center (x_i, y_i) of each sector,

$$\eta^{\text{new}}(x_i, y_i) = \frac{E_i^{\text{sim}}}{E_i^{\text{obs}}} \eta^{\text{old}}(x_i, y_i). \quad (5.17)$$

Figure 5.11 shows an example of the results, indicating the relative light transport determined in each sector for the four PMTs on each detector side.

5.3.2 Associated uncertainties

Uncertainties in the light transport measurement are mostly local — they affect the vicinity of one sector in the position map, and shift energy reconstruction of localized events, while averaging out over the entire detector volume (adding some additional spread but no systematic shift).

5.3.2.1 Statistics

The primary source of uncertainty in the position map is the statistical uncertainty of the fit line in the Kurie procedure.

For the 450 keV to 750 keV range used, simulation indicates a statistical sensitivity of $\pm \frac{102}{\sqrt{N}}\%$, where N is the number of events in the 450 keV to 750 keV fit range. The two xenon maps used for the 2010 data came from an East + West total of 60 million and 100 million xenon events, of which 5.4% and 10.5% were in the fit region (the second dataset being collected from “fresher” activated xenon with a higher proportion of $^{135}\text{Xe } \frac{3}{2}^+$). Dividing this into 351 position bins ($n = 11$ rings) on each side indicates a statistical error in each bin of $\pm 1.4\%$ for the first map, and $\pm 0.8\%$ for the second.

5.3.2.2 Smearing correction

One component of the position mapping procedure which may introduce systematic effects is the correction for energy resolution smearing carried out by comparison to simulation. This resolution correction varies over an $\lesssim 3\%$ range, from high to low light-transport regions. Since the detector response model appears to accurately re-create energy resolution effects for localized sealed calibration source spectra, there is no reason to suspect this correction to introduce errors above the $\pm 0.1\%$ level.

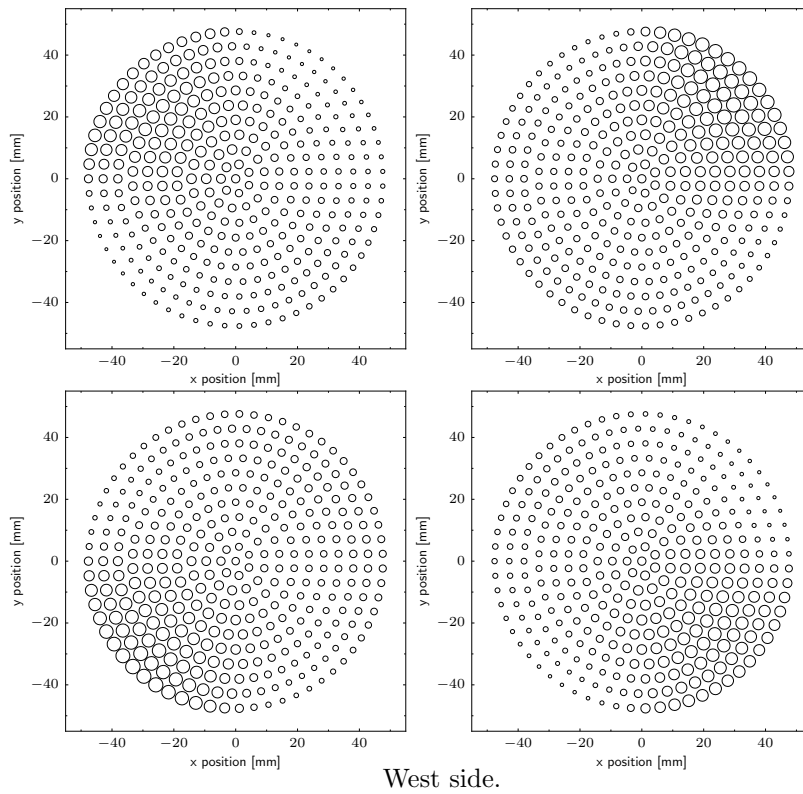
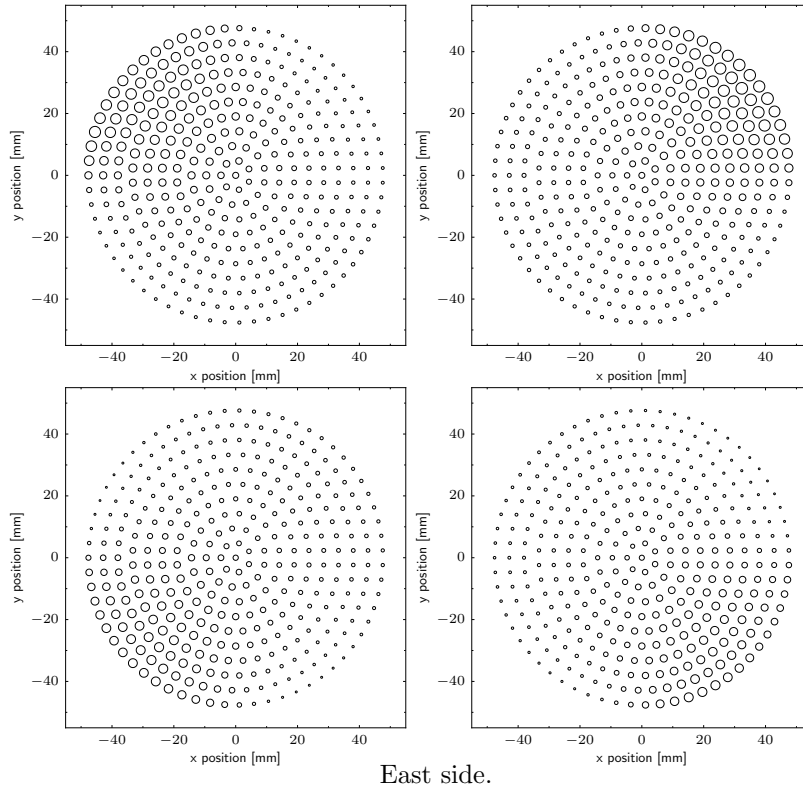


Figure 5.11: Relative light transport to four PMTs on each side, measured by xenon endpoint (circle diameter proportional to light transport).

5.3.2.3 Energy dependent position reconstruction

As detailed in subsection 6.3.4.2, wirechamber position reconstruction is slightly energy-dependent, resulting in higher- and lower-energy events piling up at slightly different average locations, prior to an energy-dependent wirechamber uniformity correction. Uncorrected, this nonuniformity results in up to a $\sim \pm 5\%$ event density difference between low and high energies at particular points in the wirechamber. The impact of this on the xenon 915 keV endpoint extraction can be estimated via simulation, fitting a spectrum modified by shifting the proportion of events. Adding an energy-dependent weighting factor linearly transitioning from $1 - \delta$ at 0 keV to $1 + \delta$ at 1 MeV shifts the fitted endpoint by $95 \cdot \delta$ keV. For an uncorrected wirechamber $\delta \sim \pm 0.025$, resulting in a $\sim \pm 0.3\%$ xenon endpoint variation. Wirechamber uniformity corrections should push this effect to well below the 0.1% level.

5.3.2.4 Interpolation error

After measurement in each position bin, the light transport map is interpolated by a cubic spline as described in section D.2. Deviation of the interpolated light transport map from the true shape of the light transport function will introduce local errors. A rough estimated upper limit on errors induced by interpolation can be produced by comparing to known lower-quality interpolation schemes. Applying linear interpolation in place of the cubic spline will generally follow an underlying curve much more poorly; one can expect cubic interpolation to follow significantly closer to the underlying sampled function than linear interpolation is to the function or the cubic interpolation. Thus, the typical difference between linear and cubic interpolation will be substantially larger than the difference between cubic interpolation and the true function. For the individual PMT position maps, the RMS difference over the detector face between linear and cubic interpolation is 0.6%; for the smoother four PMT combined light transport, the RMS error is 0.3%. Interpolation error from the cubic spline scheme employed can safely be assumed to be significantly less than this.

5.3.2.5 Coupling to wirechamber accuracy

For individual events, there is additional uncertainty from the coupling between varying position response and errors in the wirechamber reconstructed position relative to the position of energy deposition in the scintillator. If the position of an event is reconstructed at position $\vec{\delta}$ away from its true position, then the η determined for the event will be in error by

$$\Delta\eta = \vec{\delta} \cdot \nabla\eta = |\vec{\delta}| |\nabla\eta| \cos\theta, \quad (5.18)$$

where θ is the angle between the position error vector and $\nabla\eta$. The distribution of $\vec{\delta}$ over many events will be isotropic in θ and independent of $\nabla\eta$,⁴ so the RMS relative error will be

$$\sqrt{\langle (\Delta\eta/\eta)^2 \rangle} = \sqrt{\langle |\vec{\delta}|^2 \rangle \langle |\nabla\eta|^2 / \eta^2 \rangle \langle \cos^2\theta \rangle} = \sqrt{\langle |\vec{\delta}|^2 \rangle} \sqrt{\frac{1}{2} \langle |\nabla\eta|^2 / \eta^2 \rangle}. \quad (5.19)$$

⁴ Since the position efficiency map $\eta_i(x, y)$ is generated using the same position reconstruction algorithm used to locate events on the map, systematic errors in position reconstruction away from the true physical location of events are inconsequential. Only event-to-event fluctuations about the mean matter, which will be approximately isotropic despite any systematic shifts.

Averaged over the fiducial volume, $\sqrt{\frac{1}{2} \langle |\nabla \eta_i|^2 / \eta_i^2 \rangle}$ ranges from 0.013/mm to 0.020/mm for the individual PMT position maps; local gradients $|\nabla \eta_i| / \eta_i$ reach up to $\sim 0.10/\text{mm}$. In the four-PMT combined energy, the position dependence is smoother, corresponding to a $\sqrt{\frac{1}{2} \langle |\nabla \eta|^2 / \eta^2 \rangle}$ of 0.007/mm. The positioning error $\vec{\delta}$ can come both from scatter in wirechamber event position reconstruction, and from the fact that a particle, traveling along its helical trajectory in the magnetic field through the wirechamber and into the scintillator, may deposit energy at different average x, y positions in the wirechamber and scintillator. Based on the wirechamber's ability to cleanly reconstruct the event locations from highly localized low energy (low Larmor radius) sources, the latter effect can generally be taken to dominate over the former.

This effect is accounted for in simulations by recording the mean position of energy deposition for each event separately in the wirechambers and scintillators. Using the scintillator mean position for the simulated light transport to the PMTs, but reconstructing the energy based on the wirechamber position, should reproduce the event-to-event energy broadening from the effect.

5.4 PMT linearity and energy resolution

The primary tool for calibrating PMT energy response, in conjunction with the xenon-based light transport maps, is sealed source calibrations, using the radioisotopes described in subsection 3.4.1 and Appendix A. The 2010 calibrations used ^{139}Ce , ^{113}Sn , and ^{207}Bi , in a three-source holder moved across the center of the decay trap. Typically, calibrations consisted of 12 \sim 5 minute runs, moving the source holder in ~ 0.5 inch increments across the detector (see Figure 5.13a for a typical example). With source events outnumbering background counts on the order of $10^4 : 1$ within position cuts around each source, background runs for source measurements are superfluous. In post-2010 data sets, additional sources in a second three-source holder are added to the calibration routine.

Source positions are identified first by a 2-dimensional peak search on event position histograms (using ROOT's `TSpectrum2::SearchHighRes`), then Gaussian fits to the x and y event position profile in the vicinity of identified peaks to refine the position (and spread) of source events. With typically $\sqrt{N} > 100$ points measuring a peak with standard deviation $\sigma \lesssim 5$ mm, statistical precision of the source location is $< \pm 0.05$ mm, considerably better than uncertainty in the physical distribution of radioisotopes on the sealed source (assumed to be a uniform 3 mm diameter disc). A position cut with a radius $4\times$ the observed RMS position spread of the source points is applied to identify events from the source. A matching simulation of the appropriate source for comparison is run through the detector response model, centered at the same x, y location as the measured position, and subjected to the same position cuts. Comparison of fit values between data and simulation calibrates PMT linearity f and energy resolution ΔL terms in the response model.

5.4.1 Data/simulation comparison principle

Since the events from a calibration source are extended over a range of positions (varying η), some care must be taken in defining precisely what averaged quantities to compare. Schematically, the

process for generating calibration data points is:

$$\begin{aligned}
 \text{ADC}^{\text{obs}} &\xrightarrow{f^{-1}} \eta E_{\text{vis}}^{\text{obs}} \xrightarrow{1/\eta} E_{\text{vis}}^{\text{obs}} \xrightarrow{\text{fit}} \overline{E}_{\text{vis}}^{\text{obs}} \xrightarrow{\eta_0} \eta_0 \overline{E}_{\text{vis}}^{\text{obs}} \xrightarrow{f} \overline{\text{ADC}}^{\text{obs}} \\
 &\quad \text{resolution, } \downarrow \text{ accuracy} \quad \swarrow \text{new } f^{-1} \\
 \eta E_Q^{\text{sim}} \pm \Delta L^{\text{sim}} &\xrightarrow{f} \text{ADC}^{\text{sim}} \xrightarrow{f^{-1}} \eta E_{\text{vis}}^{\text{sim}} \xrightarrow{1/\eta} E_{\text{vis}}^{\text{sim}} \xrightarrow{\text{fit}} \overline{E}_{\text{vis}}^{\text{sim}} \xrightarrow{\eta_0} \eta_0 \overline{E}_{\text{vis}}^{\text{sim}}.
 \end{aligned} \tag{5.20}$$

Here, ADC^{obs} is a collection of observed PMT signals in (pedestal subtracted, gain corrected) ADC channels, each with its own associated position. Using a prior calibration curve f (or, its inverse f^{-1}), and the light transport map $\eta(x, y)$ for each event, an observed calibrated energy spectrum $E_{\text{vis}}^{\text{obs}}$ is constructed from the events. A fit locates the observed energy of some spectrum feature (such as a peak center) at $\overline{E}_{\text{vis}}^{\text{obs}}$. $\eta_0 \equiv \eta(x_0, y_0)$ is the light transport at the nominal center position x_0, y_0 of the source events. Using η_0 and f produces an ADC value $\overline{\text{ADC}}^{\text{obs}}$ corresponding to the feature energy being deposited at x_0, y_0 .

Correspondingly, simulated events for the source are run forward through the response model to produce a simulated set of ADC readouts, ADC^{sim} . These are calibrated and fit for the feature location $\overline{E}_{\text{vis}}^{\text{sim}}$ identically to the data.

Note that the original f used matters little, as it is canceled out by its inverse f^{-1} , so long as $\overline{\text{ADC}}^{\text{obs}} \approx \text{ADC}^{\text{obs}}$. The purpose of incorporating the previous f estimate is to allow the feature positions to be measured on an energy axis un-distorted by PMT nonlinearity, which is of vanishing importance to the extent the range of ADC values contributing to the measurement is small enough to sample a locally linear portion of f (while providing an approximate correction to the extent this is violated). Also, the position x_0, y_0 and corresponding η_0 is not highly critical: to the extent that f is linear, it cancels out entirely. Since data and simulation are fit in the same manner, it does not matter how the feature position identified by the fit corresponds to any ‘‘true’’ feature energy. However, the feature ought to be measurable from a small local neighborhood around $\overline{E}_{\text{vis}}$ (*i.e.*, a distinct peak rather than a beta spectrum endpoint), in order to keep $\text{ADC}^{\text{obs}} \approx \overline{\text{ADC}}^{\text{obs}}$ so far as variation in η allows.

Fitting $\eta_0 \overline{E}_{\text{vis}}^{\text{sim}}$ versus $\overline{\text{ADC}}^{\text{obs}}$ produces a new (inverse) calibration curve f^{-1} . Comparison between the peak widths seen by the visible energy fits provides information for adjusting the model energy resolution. The accuracy of the energy reconstruction process is evaluated by comparing $\overline{E}_{\text{vis}}^{\text{obs}}$ and $\overline{E}_{\text{vis}}^{\text{sim}}$, which will be identical when all model parameters are correctly calibrated.

5.4.2 Spectrum feature fitting

Energy spectrum peaks are fit by an iterated Gaussian fit procedure, similar to that used for the ^{207}Bi ‘‘pulser’’ gain monitor, where the fit center and range is adjusted according to the results of the previous iteration in order to erase bias from initial guess choice of fit window. For the ^{207}Bi spectrum, the two peaks are fit simultaneously by a sum of Gaussians, as, from sufficiently low light transport positions, the two peaks are not entirely outside each others’ range of influence. Spectrum peaks are fit over a range of $\pm\alpha$ standard deviations, where α is selected according to the spectrum type so that fit data will primarily come from the region where the peak being measured dominates the spectrum over other components. In general, $\alpha = 2$, though this is reduced to $\alpha = 1.5$ for ^{207}Bi to avoid the significant ‘‘tails’’ between the peaks, and to $\alpha = 1$ for the peak in ^{137}Cs sitting

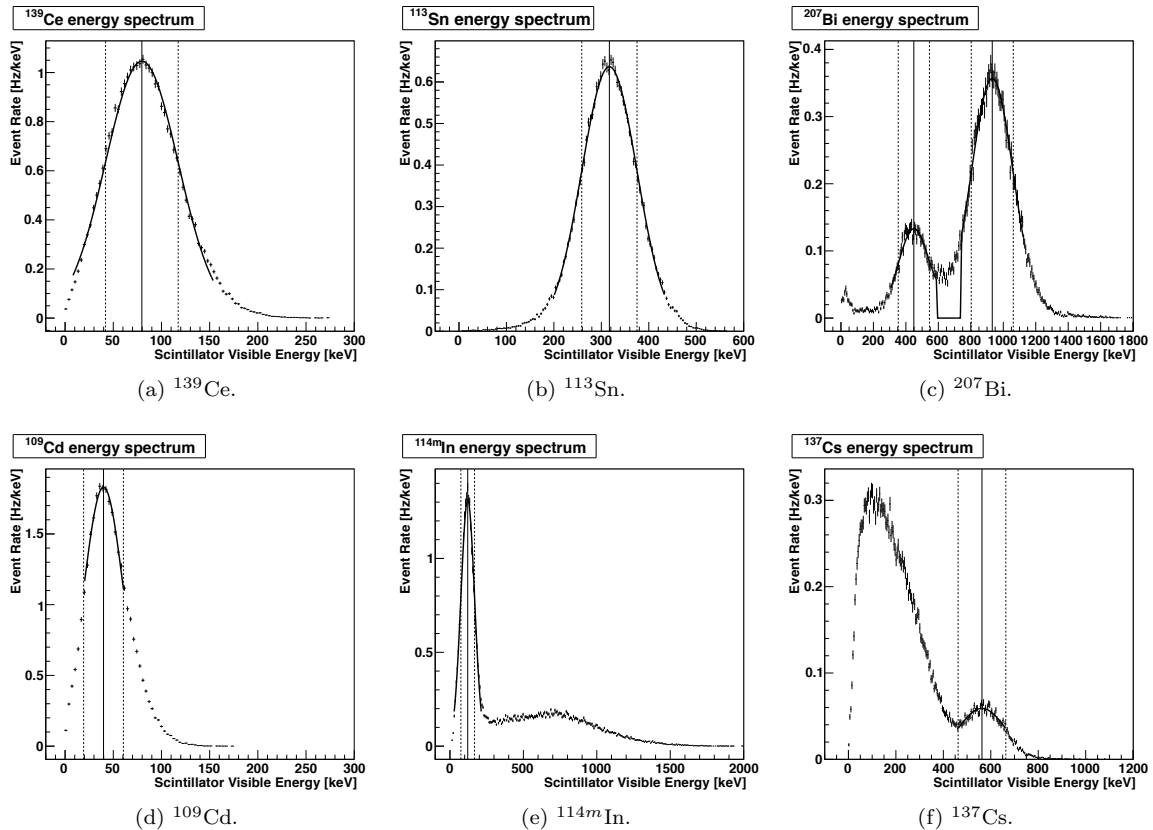


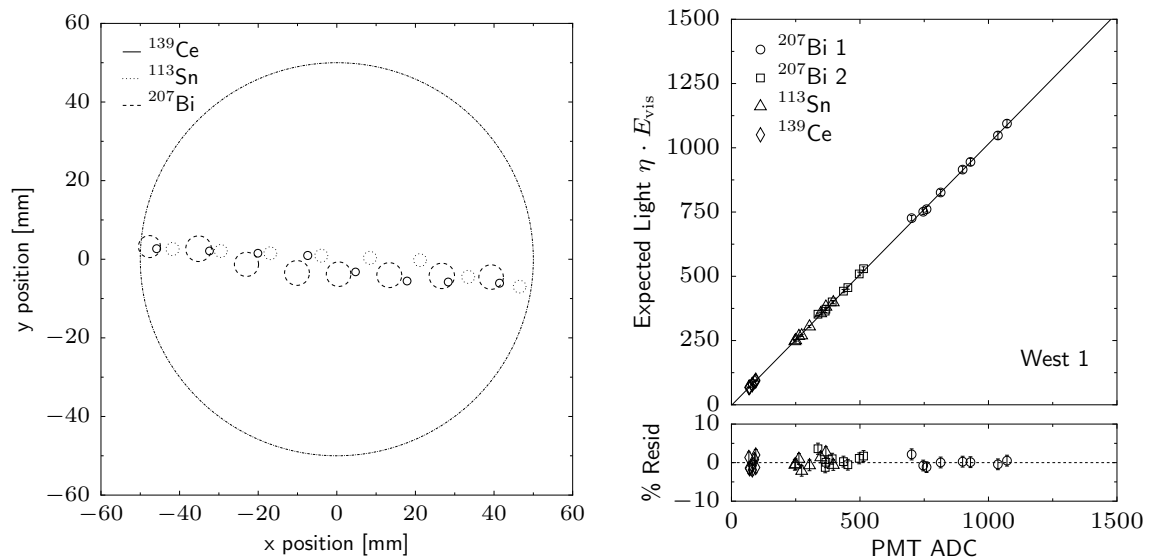
Figure 5.12: Example single-PMT energy spectra fits for various isotopes. Vertical lines indicate center and $\pm 1\sigma$ for peak fits.

atop two beta decay spectra, and for ^{109}Cd to keep somewhat away from the trigger threshold edge. Figure 5.12 shows example fit spectra.

Fit statistics for the peak locations, available from a typical 5 minute run, are generally small compared to other sources of uncertainty; $< \pm 0.5$ keV is usual. The exception to this is ^{137}Cs , where the small peak on the edge of the beta spectrum provides $\sim \pm 2$ keV statistics in a typical source run, which could be improved by a higher-activity source (though, at $\sim \pm 0.3\%$ relative uncertainty, this is already of little concern).

5.4.3 2010 linearity curves

Figure 5.13 shows a typical source scan and PMT linearity curve f^{-1} fit from the 2010 data. The 2010 data set included seven Sn/Bi/Ce source calibration scans, at approximately weekly intervals. The first of these, from the very start of the run, did not correspond to a time period when useful beta decay data was being taken. The fifth of these was bungled by inserting the source holder rotated nearly 90° from its correct orientation, occluding nearly all the source events and producing severely distorted spectra; this set was excluded from the analysis. The five source calibration sets remaining were used for calibrating the detector for the one- to two-week periods surrounding each.



(a) Calibration source positions from source calibration scan (circles; radius is RMS position spread). Large circle indicates 50 mm radius detector acceptance. (b) Linearity calibration curve fit to expected light from simulation versus observed source peak ADCs. Error bars from $\sim \pm 1.4\%$ uncertainty on η .

Figure 5.13: Example of one 2010 data source calibration scan, with PMT linearity curve.

To within the energy calibration uncertainty used for the 2010 data analysis, fitting the linearity curves with a simple $f^{-1}(x) = a + bx$ was sufficient. Analyses of later data sets, with more calibration sources available, might introduce additional terms for nonlinear behavior. Statistics from the source peaks data, primarily limited by the position map uncertainties, typically produced an uncertainty of ± 0.5 keV on a , and $\pm 0.5\%$ on b (anticorrelated with $c = -0.7$).

5.4.3.1 Energy calibration uncertainty envelope

The resulting quality of the linearity and energy calibration procedure can be judged by the accuracy with which reconstructed energy spectra agree between data and simulation. Figure 5.14 shows the energy reconstruction error over the five calibration scans used to calibrate the data. The RMS spread around each point is generally consistent with statistical uncertainty in the light transport map. The mean values hint at some additional nonlinearity not captured by the $f^{-1}(x) = a + bx$ calibration curves. However, with only four energy points (from three calibration sources) available in the 2010 data, a cautious approach indicates against over-interpreting and over-fitting sparse data to achieve a deceptively accurate result. Later calibration data, with additional sources filling intermediate energy points, would provide more sufficient information for determining how to fit out the residual nonlinearity. For the 2010 data analysis, the apparent residual nonlinearity was treated by adopting an energy reconstruction uncertainty (corresponding to a systematic uncertainty in the extracted asymmetry A) — indicated by the dashed lines in Figure 5.14 — which generously covers any potential mean energy reconstruction errors lurking in the observed calibration source data.

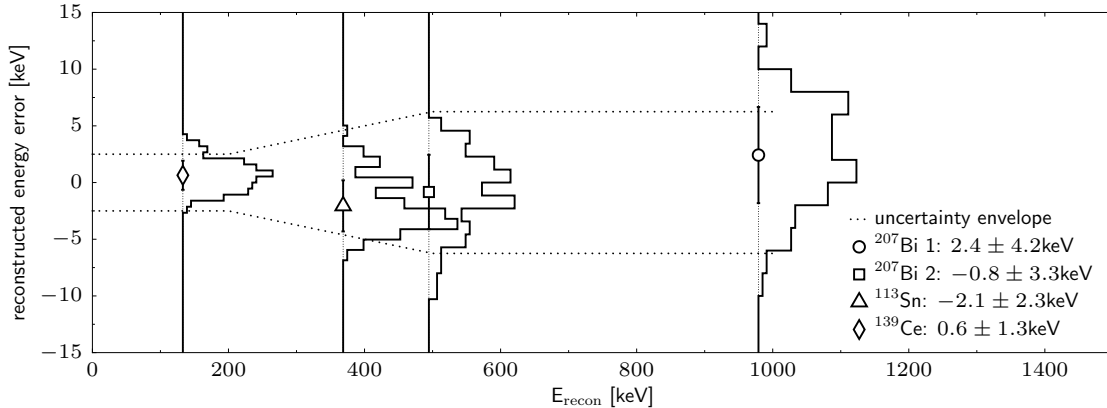


Figure 5.14: Calibration source energy reconstruction errors over all 2010 calibration data points. Sideways histograms indicate distribution of data-simulation discrepancies for each energy peak, with mean and RMS deviation indicated by markers. Dashed lines indicates adopted energy reconstruction uncertainty.

5.4.4 Energy resolution

Accurate determination of detector resolution is unnecessary for the extraction of the asymmetry, which, according to simulation, varies negligibly were the detector to exhibit half or twice its present energy resolution. However, energy resolution plays a second-order role in several calibration processes — fitting beta spectrum endpoints or source peaks, low-energy trigger efficiency, etc.

5.4.4.1 Energy resolution model

The assumed model is that detector resolution response is dominated by photoelectron counting statistics, following a Poisson distribution in the mean number of photoelectrons $nPE \propto \eta E_Q$ produced for a given light production and transport from the scintillator. Following the production of some discrete number of photoelectrons from an event, the amplifying cascade of electrons produced on each successive PMT dynode adds its own counting statistics (dominated by the small number in the first stage), which smooths out the discrete photoelectron counts.

Let k denote the constant of proportionality $nPE = k\eta E_Q$, and g_d denote the electron multiplying gain of the first dynode. Then, the PMT's stochastic effect, adding $\pm\Delta L$ light fluctuations, is modeled by the double Poisson process

$$\eta E_Q \rightarrow \frac{1}{kg_d} \text{Pois}(g_d \text{Pois}(k\eta E_Q)) \equiv \eta E_Q \pm \Delta L, \quad (5.21)$$

where $\text{Pois}(\lambda)$ denotes a random variable produced from a Poisson distribution with mean λ . In this model, the precise value of g_d is not critical. A large value of g_d would allow single-PE peaks to be visible in energy spectra from the data, which they are not. Too small a value for g_d introduces excessive broadening for low energy (low-nPE) peaks. A value of $g_d = 16$ lies between these two extremes, suitable for smoothing out single-PE counting spikes without excessively broadening ^{109}Cd peaks compared to observation.

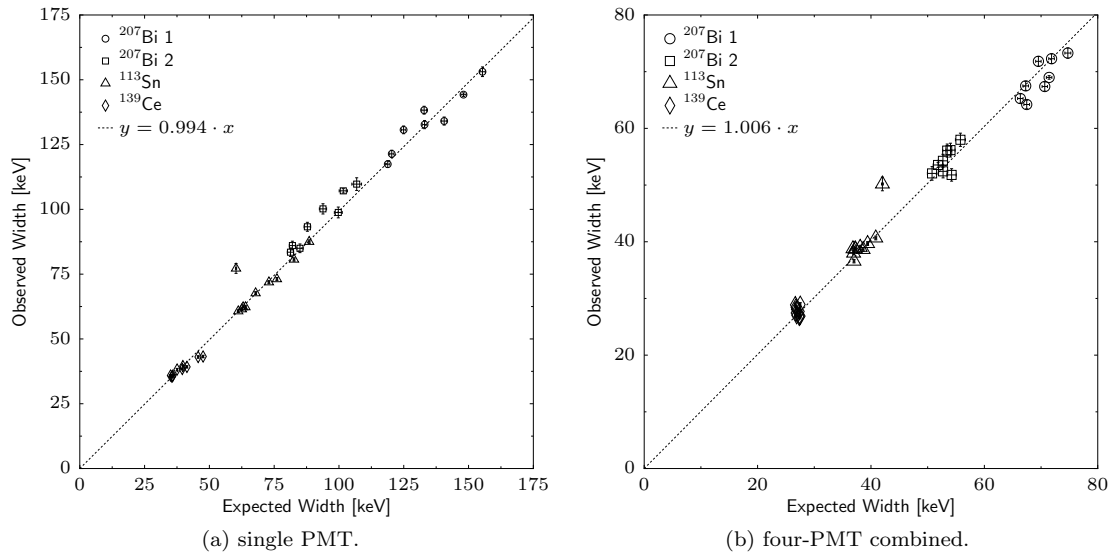


Figure 5.15: Example calibration source energy peak widths, observed versus simulation expected, from a 2010 calibration source scan.

5.4.4.2 Energy resolution from calibration source peak data

PMT energy resolution is determined by comparing simulated and observed peak widths in the calibration source spectrum fits used for the linearity calibration. The observed peak width is broadened by additional mechanisms besides photoelectron counting around a fixed mean, including the underlying width of the E_Q distribution and variations in η over calibration source event positions. Thus, deriving the number of photoelectrons directly by $nPE = \left(\frac{E}{\Delta E}\right)^2$ for an energy spread ΔE at energy E only provides a rough lower bound. However, the simulated spectrum incorporates the relationship between observed $\left(\frac{E}{\Delta E}\right)^2$ and the true number of photoelectrons used by the simulation. Starting with a prior estimated photoelectron proportionality factor k in the simulation, one can adjust the proportionality based on the average discrepancy between observed and simulated widths to produce an improved proportionality factor k' :

$$k' = \left\langle \frac{\text{simulated width}}{\text{observed width}} \right\rangle^2 k. \quad (5.22)$$

The average simulated/observed ratio can be determined by fitting $y(x) = \alpha x$ to a plot comparing simulated and observed source peak widths, as shown in Figure 5.15.

5.4.4.3 Four-PMT crosstalk correlation

Energy resolution is calibrated for the four PMTs on each side individually. With the model consistently reproducing individual PMT resolutions to $\pm 0.5\%$, treating the PMT noise as independent between the four PMTs resulted in a systematic $\sim 3\%$ under-prediction of four-PMT combined signal peak widths. This excess broadening of the four-PMT signal indicates a slight positive correlation between the individual PMTs.

Any correlation in the mean between PMTs is already accounted for by (and indistinguishable from) the light transport maps η for each PMT. Incorporating an assumption that the ΔL PMT fluctuations include 1% “crosstalk” between the fluctuations about the mean of each individual PMTs results in correct reproduction of four-PMT combined energy resolutions from calibrated individual PMTs.

5.4.4.4 Energy resolution accuracy

As with the energy reconstruction, the accuracy of the width model can be assessed by comparing predicted and observed widths across all calibration data points. Figure 5.16 shows this for the 2010 data. Based on the upper Bi peak, energy resolution is reliably reproduced to $< \pm 4$ keV at 1 MeV for individual PMTs, and $< \pm 2$ keV for the four-PMT combined. This is for localized sources sampling a small portion of the position map. For an extended source (like a volume-filling beta spectrum), statistical fluctuations in the position map will add their own contribution to the width. However, adding a $\pm 1\%$ fluctuation to signal with ± 100 keV width at 1 MeV only changes the width of the signal to $\pm\sqrt{100^2 + 10^2} = \pm 100.5$ keV.

5.5 PMT signal correlations

As hinted by the four-PMT combined resolution, the ADC signals from the four PMTs may include correlations between PMTs. Correlations may be introduced by a variety of mechanisms. Fortunately, the existing calibrations process will generally produce the correct results regardless of correlations. The fine details of signal correlations might potentially matter for very low-energy events, where correlations will interact with trigger probabilities. However, even this is generally a small effect (large correlations can be added to the simulation with nearly no impact on outcomes).

5.5.1 Underlying physics correlation

The foremost correlation seen in the data is that the four PMTs are viewing the same physics process: one expects that, for varying energy deposition input, the four PMTs will display a nearly 100% correlated output (with correlation less than unity due to fluctuations in each PMTs response). In certain limits this could also lead to a signal anti-correlation: if each PMT is counting photons from a small “pool” so that detecting a photon in one PMT significantly decreases the chances of detecting it in another. However, this effect is generally trivial. PMT quantum efficiency on the order of 0.1, compounded with splitting the light four ways and additional light transport losses, means that the initial “pool” of photons is quite large compared to the number counted by each PMT. Thus, this effect is likely to result in an anticorrelation of order smaller than $\sim 1\%$ for the smallest signals (single PE expected per PMT), and proportionally smaller (below the 0.01% level) for typical energies.

5.5.2 Extracting correlation from the data

Because of the strong underlying physics correlation, measuring additional, smaller correlations is challenging. However, if a “repeatable” source of physics is available with little intrinsic scatter,

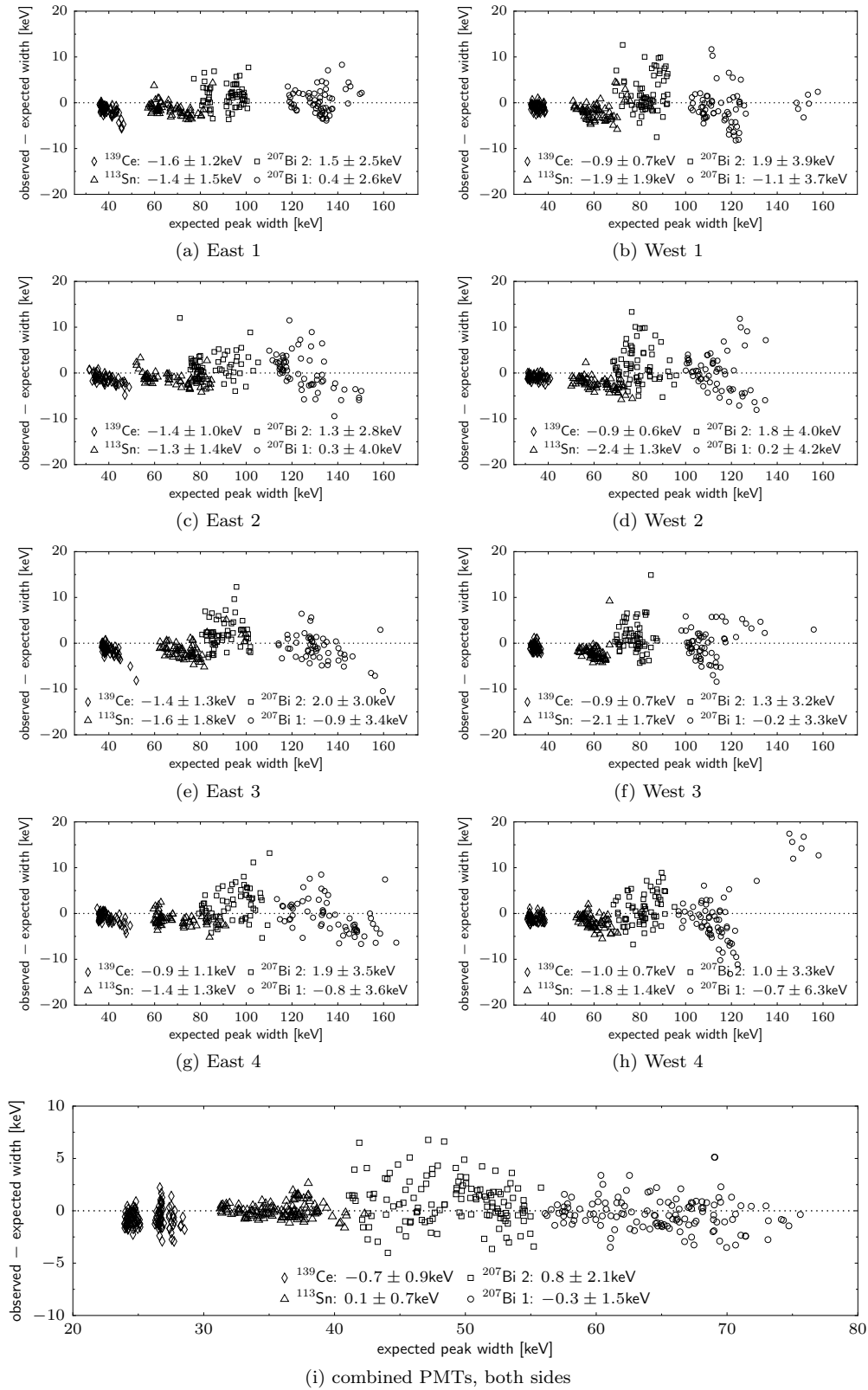


Figure 5.16: Errors in source peak widths for individual PMTs and combined energy, over all 2010 sealed source calibrations. Plot legends indicates average and RMS spread for each peak.

then additional correlations might be observable in the data. Supposing such a stable input signal was available, then, one could observe the variance $\sigma^2(i)$ of the signal produced by the i^{th} PMT. Similarly, one could sum together the signals of PMTs i and j to produce a new “summed” signal, which would have its own variance $\sigma^2(i+j)$. A correlation of c between the PMTs i and j means that the individual and summed signal variances are related by

$$\begin{aligned}\sigma^2(i+j) &= \sigma^2(i) + \sigma^2(j) + 2c\sigma(i)\sigma(j) \\ \Rightarrow c &= \frac{\sigma^2(i+j) - \sigma^2(i) - \sigma^2(j)}{2\sigma(i)\sigma(j)},\end{aligned}\tag{5.23}$$

allowing the correlation c between PMTs i and j to be extracted from the data.

5.5.3 Correlation contributions model

A simple model of correlated noise contributions is to consider the possibility of correlations from two mechanisms:

1. constant-amplitude correlated electronic noise, added to any signal, as is visible “on its own” in the spread of the pedestal distribution, and
2. “crosstalk” between channels, in which each ADC channel includes a small contribution proportional to other channels, thus growing in amplitude proportional to the noise amplitude in other channels.

One can characterize the individual PMT noise for these two potentially correlated processes from available data:

1. the pedestal electronic noise level at zero signal $\sigma_0(i)$, and
2. the proportionality factor between input signal S_i and counting-statistics spread in the signal, $k_i \equiv \sigma_{\text{PE}}^2(i, S_i)/S_i$.

In the two-component model, the total individual PMT variance for signal S would be a combination of these two,

$$\sigma^2(i) = \sigma_0^2(i) + k_i S_i.\tag{5.24}$$

One can also form the PMT sum variables for each pair (i, j) of PMTs, and measure its variance. The variance of the sum variable includes cross-terms from the correlation c_0 between pedestal noise, and from crosstalk correlation c_c between the PE contributions, which together produce a total effective correlation c_{tot} between the signals,

$$\begin{aligned}\sigma^2(i+j) &= \sigma^2(i) + \sigma^2(j) + 2c_{\text{tot}}\sigma(i)\sigma(j) \\ &= \sigma_0^2(i) + k_i S_i + \sigma_0^2(j) + k_j S_j + 2c_0\sigma_0(i)\sigma_0(j) + 2c_c\sqrt{k_i S_i}\sqrt{k_j S_j} \\ \Rightarrow c_{\text{tot}} &= \frac{c_0\sigma_0(i)\sigma_0(j) + c_c\sqrt{k_i S_i k_j S_j}}{\sqrt{(\sigma_0^2(i) + k_i S_i)(\sigma_0^2(j) + k_j S_j)}}.\end{aligned}\tag{5.25}$$

Note that in the large signal limit where PE counting dominates ($k_i S_i, k_j S_j \gg \sigma_0^2(i), \sigma_0^2(j)$), $c_{\text{tot}} \rightarrow c_c$. Similarly, in the small-signal limit $k_i S_i, k_j S_j \rightarrow 0$, the pedestal noise correlation dominates, and $c_{\text{tot}} \rightarrow c_0$.

5.5.4 Measurement with LED data

Any process based on electron energy deposition in the scintillator will have a noticeable intrinsic spread due to energy losses in non-scintillator materials, backscattering, etc. The LED pulser system provides the possibility of a more repeatable signal, with a narrower pulse-to-pulse spread. In addition, the independent LED trigger allows measurements of small-signal effects to be disentangled from 2-fold trigger efficiency. The suitability of the LED system for such measurements, based on LED data acquired towards the end of the 2010 run, is discussed below.

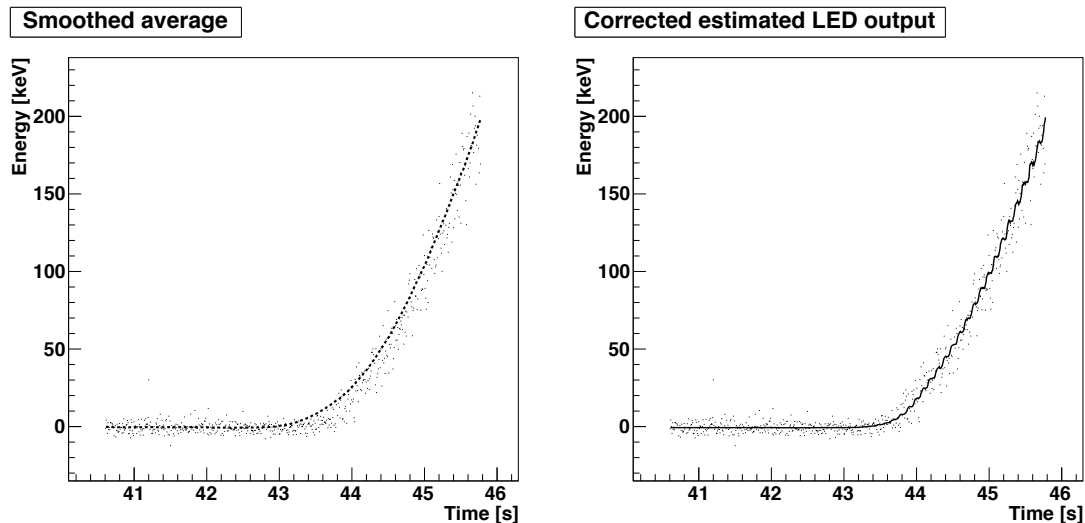
5.5.4.1 LED mean output estimation

To make best use of LED data, it is helpful to know what the nominal LED output is for each data point. The state of the LED controller is not stored in the data, and thus must be inferred from the detectors. Consider a data set in which the LED is set to ramp periodically, from zero to some full output level. Each sweep follows the same pattern. One analysis approach is to directly identify the timing of each sweep, in order to time-align all sweeps together.

Here is an alternate approach to effectively align the the data without requiring identification of the timing structure of the sweeps. All that is assumed is that the sweeps are identical and roughly monotonic. Some observable related to the LED output is selected; the lower the noise/scatter, the better. For the 2010 data, a good choice of variable is an 8-PMT averaged effective energy, $E_8 \equiv \frac{1}{2}(E_{\text{vis}}^E + E_{\text{vis}}^W)$, where $E_{\text{vis}}^{E,W}$ is the visible energy reconstructed from PMT outputs on each side, as if for a beta event hitting the center of the detector. For later datasets with a photodiode monitor of the LED, this would provide a good low-noise variable. A rolling window average \overline{E}_8^* is calculated for each data point, as an average of n points before and n points after (excluding the data point itself, to avoid bias). At the beginning and end of each sweep (identified by an abrupt change from high to low signal), the averaging window can be truncated down to a half-window at the edges to avoid including vastly different points belonging to another sweep. This produces a “smoothed” version of the data, with scatter about the mean reduced by a factor of $\sqrt{2n}$ compared to the raw data.

As n is increased, the smoothing becomes greater. However, when the averaging window becomes large compared to second-derivative changes in the signal, an error is introduced between the smoothed curve and the true underlying average, about which the observed signal is varying. Reducing n will decrease this error, but at the cost of greater noise in the averaged variable.

However, assuming each sweep is identical, the over-smoothed signal will have identical values at identical points in each sweep. Thus, points can be binned by \overline{E}_8^* to overlay all sweeps together without requiring determination of time alignment. With the whole dataset plotted as a function of \overline{E}_8^* rather than time, a fine-grained average of E_8 can now be made $\overline{E}_8(\overline{E}_8^*)$. Now, every point in the dataset can be associated with an LED output averaged over all sweeps via \overline{E}_8 . Figure 5.17 shows an example of this procedure applied to part of a sweep from real data: the smoothed \overline{E}_8^* , and the associated average \overline{E}_8 calculated from 755 sweeps aligned by \overline{E}_8^* . Note how the \overline{E}_8^* curve is a bit high going up the “knee” of the sweep, while the \overline{E}_8 curve not only follows the nonlinear ramp, but even resolves the discrete steps in LED output.



(a) E_8 for points in one sweep of an LED scan, overlaid with $n = 100$ windowed average \bar{E}_8^* . (b) Points overlaid with averaged response $\bar{E}_8(\bar{E}_8^*)$, determined from 755 sweeps. Note that steps in LED output are clearly resolved.

Figure 5.17: Multi-sweep determination of LED averaged output applied to one sweep.

5.5.4.2 LED output width

The LED output itself may have some fluctuation width about the mean value determined by the method above. This will add a constant width² component to all measures of LED output, including both single-PMT and combined E_8 , 100% correlated between all such measures. Using the sweep averaging method described above, the fluctuations in E_8 about \bar{E}_8 as a function of \bar{E}_8 are shown in Figure 5.18. Substantial deviations are visible from a simple width² = $w_0^2 + kE_8$ model for pedestal fluctuations w_0^2 plus counting statistics $\propto E_8$. In the ~ 5 keV to 30 keV region just above pedestal, there is an excess of signal fluctuation. This could be attributed to the LED having a “turn-on bump,” adding $\sim (5 \text{ keV})^2$ of fluctuation when switched on at low levels. In the higher energy range, additional deviation from linearity is apparent.

If these features of the total observed width are due to LED output fluctuations adding to PMT mechanisms, then they will also appear equally in the width² distributions of each individual PMT’s energy measurement, 100% correlated between PMTs. Including an LED width contribution $\sigma^2(\text{LED})$ in Equation 5.23 indicates

$$\sigma^2(i+j) - \sigma^2(i) - \sigma^2(j) = 2c\sigma(i)\sigma(j) + 2\sigma^2(\text{LED}). \quad (5.26)$$

Extracting individual PMT and PMT-pair energy widths from the data, $\frac{1}{2}(\sigma^2(i+j) - \sigma^2(i) - \sigma^2(j))$ follows a roughly similar pattern for each of the 28 pairs of PMTs. The average value of this quantity over all 28 PMT pairs, as a function of \bar{E}_8 , is shown in Figure 5.19a. This average also includes the averaged correlated component between PMTs, $c\sigma(i)\sigma(j)$. However, the total amount (equivalent to correlations of several percent between PMTs) is significantly larger than PMT correlations indicated by conversion electron peak widths (subsection 5.4.4.3). Thus, this correlated term can primarily

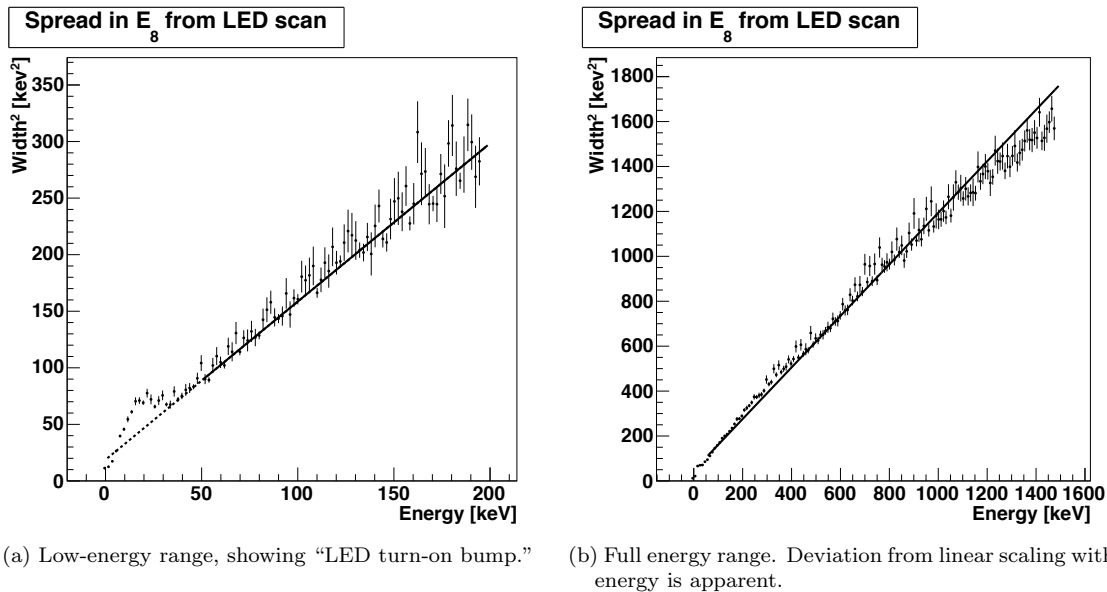


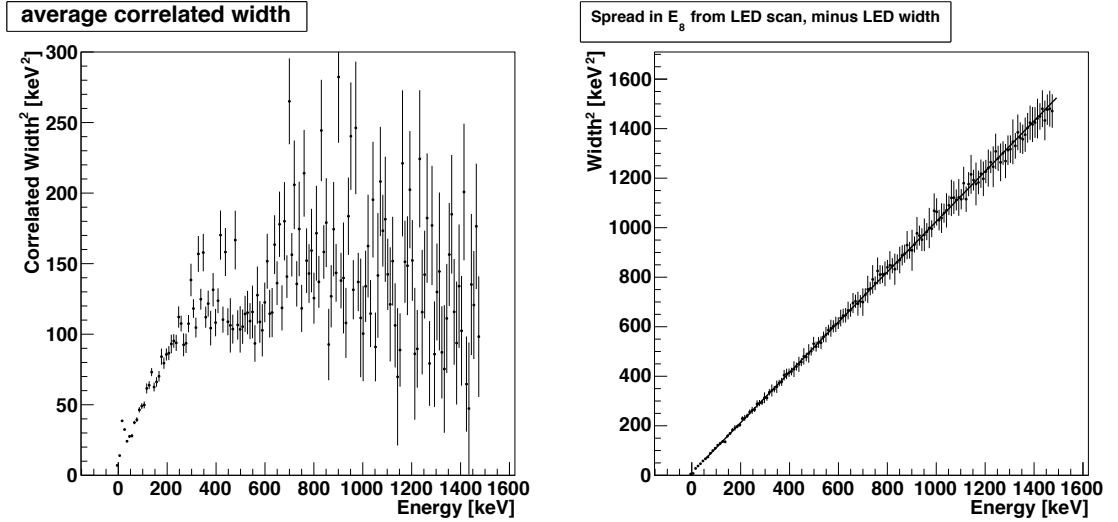
Figure 5.18: Observed scatter in 8-PMT combined effective energy $\langle (E_8 - \bar{E}_8)^2 \rangle$ from LED sweep data.

be attributed to the LED itself. Subtracting this average correlated width component from the E_8 width² distribution removes the anomalous deviations from a simple linear model (Figure 5.19b).

Ideally, an independent high-resolution measurement of the LED output and fluctuation width (such as the photodiode added in later runs) would allow the LED width contribution to be cleanly separated out from PMT correlations. Additionally, improvements in the LED driver circuitry might improve pulse-to-pulse stability, which currently appears to be only $\sim \pm 1\%$ at 1 MeV-equivalent light output.

5.5.4.3 Pedestal correlations

While LED output fluctuations muddle correlation measurements above pedestal, for portions of the LED sweep the LED is fully off, adding no additional spread to the pedestal events sampled by the LED trigger. Taking events selected in a narrow region around $\bar{E}_8 = 0$, which are abundant, pedestal fluctuation correlations between PMT DAQ channels can be calculated via Equation 5.23. Table 5.1 shows the pedestal correlation between each of the 28 pairs of the 8 PMTs. Correlations between PMTs on the same side, along with typically smaller correlations across the two sides, are observed. Because pedestal fluctuations are already quite small compared to the photoelectron statistics resolution, observed data is insensitive to the fine details of pedestal fluctuation. For completeness, a “typical” correlation of $c = 0.2$ between PMTs on the same side is included in the detector response model implementation of pedestal fluctuations $\pm \Delta p$, with the correlated random variables generated as described in Appendix C.



(a) Correlated width $\frac{1}{2}(\sigma^2(i+j) - \sigma^2(i) - \sigma^2(j))$, averaged over each pair i, j of the 8 PMTs, presumably mainly from LED output fluctuations.

(b) Scatter in observed E_8 minus average PMT-pair correlated width, which fixes the anomalies seen in Figure 5.18.

Figure 5.19: Estimated LED output fluctuation contribution to total observed E_8 fluctuations.

c	#1	#2	#3	#4
#1	-	.10	.10	.08
#2	.09	-	.39	.28
#3	.05	.06	-	.36
#4	.10	.09	.06	-

(a) PMT pairs on same side: East pairs upper right; West lower left.

c	E1	E2	E3	E4
W1	.02	.07	.09	.08
W2	.03	.14	.16	.10
W3	.01	.04	.07	.05
W4	.01	.06	.10	.08

(b) PMT pairs across sides.

Table 5.1: Correlation in fluctuations around zero signal between each pair of PMTs, calculated as per Equation 5.23 using zero-average-signal portions of LED sweep data.

Chapter 6

Wirechamber calibration

6.1 Wirechamber energy calibration

6.1.1 MC expectations

GEANT4 Monte Carlo simulations predict that energy deposited in the wirechamber will vary as a function of scintillator deposited energy for the same event, with lower-energy events (higher $\frac{dE}{dx}$) generally depositing more energy in the wirechamber. For events at a particular scintillator deposited energy, wirechamber energy deposition will approximately follow a Landau distribution (with a larger high-energy tail). The GEANT4 model used to predict energy deposition from the beta is not designed to model the fine details of the ionization charge cloud evolution as it is drifted towards the anode and cathode planes at energy scales (tens to hundreds of eV) well below GEANT’s “low energy” physics. Detailed modeling of the wirechamber charge cloud is a project remaining for future researchers. For this analysis, the simplifying assumption is made that initial energy deposition is linearly converted to ionization charge, eventually collected by the anode (with some electron multiplication gain in the strong electric field very near the anode wires). Both cathodes will see a proportional “mirror charge” effect from the negative charge cloud built up around the anode, even if initial ionization only occurs on one side of the anode.

Prior to analysis of the 2010 data, an assumption was made that the wirechamber would only sense charge deposited in the “active” region enclosed between the two cathode planes, and that the external neopentane volume between the cathodes and windows would be an insensitive “dead” region. The system was designed to permit the cathodes to be biased up to a couple hundred volts above the grounded enclosing volume. This biased operation mode was only employed for a short test in December 2008 (using sealed calibration sources), during which no apparent increase in wirechamber sensitivity was observed. However, observed backscatter counts in the 2010 dataset — higher than expected under the dead volume assumption — were more consistent with a hypothesis that ionization in the external region was being collected even without cathode biasing (boosting sensitivity to backscatters not reaching far into the inner region). Subsequent wirechamber electric field models by Syed Hasan using the Garfield drift chamber simulation package support the hypothesis that the wire cathode plane is “porous,” with sufficient leakage fields to pull in ionization from the external region. Consequently, the current working hypothesis is that ionization in the

entire neopentane volume between the (aluminized, grounded) wirechamber windows contributes to the observable wirechamber signals.

6.1.2 Calibrations plan

Calibration of wirechamber PADC readouts to wirechamber energy deposition is important for the detection and categorization of backscattering events, along with validation of Monte Carlo predictions. The relationship between energy deposited by a transiting particle and quantity of ionization may vary both as a function of position in the wirechamber (due to wirechamber geometry and electric fields), and as a function of time (varying gas content with temperature and gain drifts in the readout electronics). The position variations appear to be relatively stable over time; for the 2010 data analysis, a single position correction map sufficed for the entire dataset. The general calibration scheme is to first remove the position dependence, producing a position-uniform signal proportional to energy deposition. Then, on an octet-by-octet basis, a conversion factor is calculated between this uniformized signal and deposited energy, stabilizing any gain drifts on ~ 8 hour time scales. Putting everything together, the master equation for an event's MWPC deposited energy E^{MWPC} is

$$E^{\text{MWPC}} = \frac{\eta^{\text{MWPC}}(0, 0)}{\eta^{\text{MWPC}}(x, y)} g_i Q, \quad (6.1)$$

where (x, y) is the event's reconstructed position (section 6.3), Q is the observed wirechamber charge signal (subsection 6.1.4), η^{MWPC} is the position dependence of the wirechamber's charge response (subsection 6.1.5), and g_i is a gain calibration factor (for a run or group of runs, subsection 6.1.6).

6.1.3 Pedestals

Pedestal subtraction for the anode and cathode signals follows a similar mechanism to that used for the PMT signals (subsection 5.1.1). Pedestals are measured from the following theoretically wirechamber-activity-free events:

- LED pulser triggers,
- UCN monitor triggers, and
- Bi GMS pulser triggers not triggering any PMTs on the wirechamber's side.

This event selection provides a considerably larger number of pedestal events than PMT pedestal events, providing abundant statistics for finely time-resolved pedestal tracking. Figure 6.1 shows typical examples of cathode and anode pedestals. Since extreme precision in wirechamber calibration is not needed, the “0” point for pedestal subtraction is simply taken as the mean of the pedestal distribution, disregarding minor complicating details suggested by the asymmetric skew of the pedestal distributions. Switching the West Anode preamplifier from the PA3300 module to the external charge preamplifier added complexly structured noise to the pedestal, likely similarly degrading the signal. Fortunately, even this additional “messy” spread is small compared to the rough accuracy needed from the anode signal.

The time history of two example cathode pedestals over the 2010 run is shown in Figure 6.2. All cathode pedestals appeared to follow the same general drift pattern, except scaled by (apparently

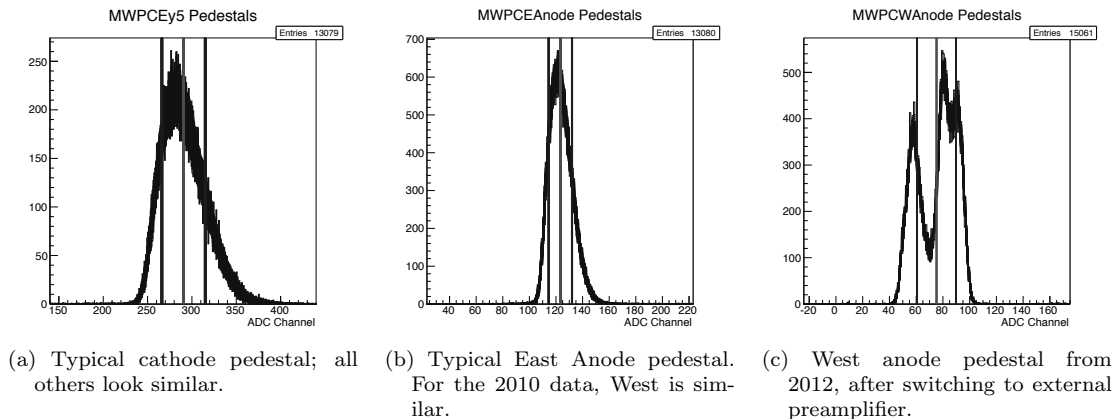


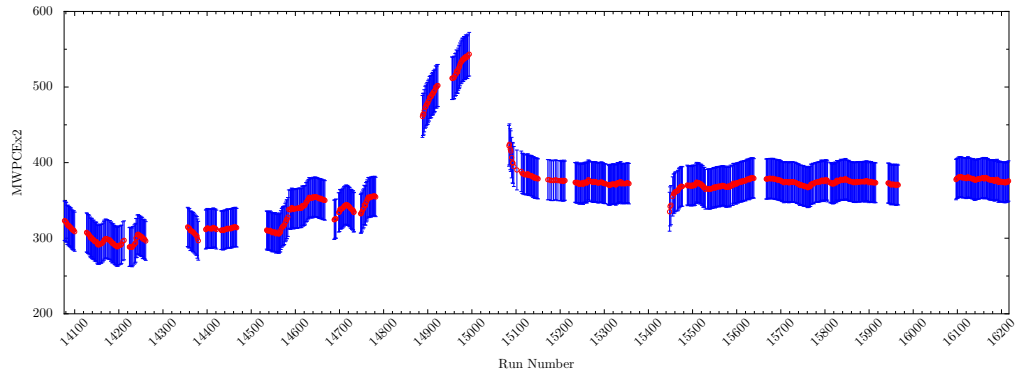
Figure 6.1: Examples of wirechamber pedestals. Vertical lines mark mean and RMS deviation.

randomly assorted) factors of differing sign and magnitude. This drift pattern includes both wiggles on the timescale of diurnal temperature variations, and larger long drifts over multiple days. The anode pedestals are more constant, showing primarily the diurnal zigzags without the longer-term drift structure. This suggests that the cathode pedestal offset circuitry, which is the main difference between the anode and cathode signal chains, is responsible for the longer term varying-scale pedestal drifts.

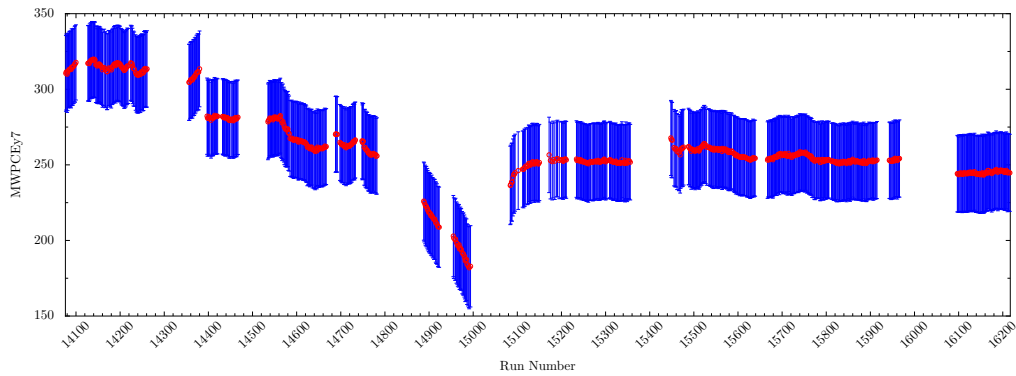
6.1.4 Total charge signal

The anode signal, when available, provides a straightforward measure of the charge deposited. Anode signals from both wirechambers were available throughout the 2010 dataset. An alternative, for cases where the anode readout is unavailable, is the sum of (gain normalized) cathode signals, which bears a nearly 1:1 correspondence with the anode when all cathode segments are accounted for. However, because the signal chain for the individual cathodes has higher gain than the anode signal, events can exceed the ADC range of their nearest cathode at lower signal levels than exceed the anode ADC range (though for a sufficiently small portion of events that it is unlikely to be a major problem). In addition, for cases where the readout on one cathode segment is disabled, the cathode sum no longer reflects the magnitude of the charge cloud for events in the vicinity of the malfunctioning segment.

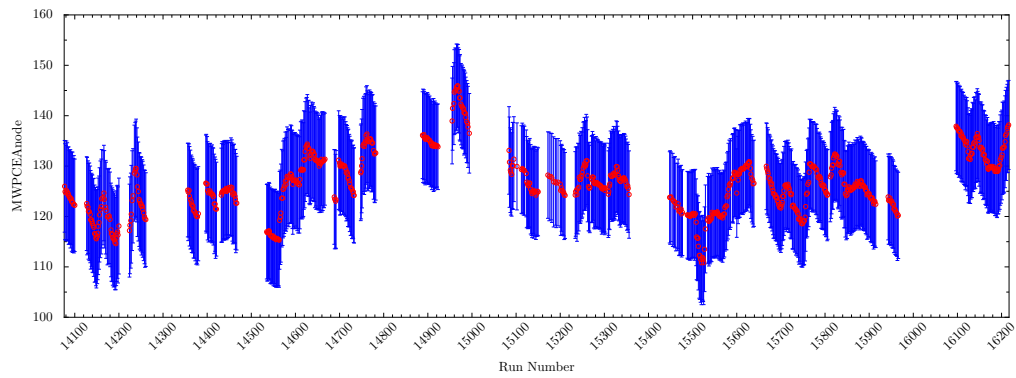
An approximated integral charge value from the shape of the center-locating function fit to the cathode data (as in subsection 6.3.3.2) provides a third option, which is both more robust against cathode clipping, and deals with missing cathode segments. Figure 6.3 shows the relationship between the reconstructed charge cloud side and the anode signal. For the bulk of events, the two bear a near perfectly linear relationship. Above ~ 2000 anode ADC channels, the cathode segment nearest the event center typically clips at its maximum ADC readout, so the charge cloud shape is determined using segments farther out in the tails of the event. Combined with deviations from the simplified Gaussian-shaped charge cloud model, this causes the cathode-based charge cloud size to deviate from perfect linearity relative to the anode readout. However, the readout is still reasonably proportional to the anode, and even extends to measure high-charge-deposition events exceeding the clipping range of the anode readout. All discussion below related to quantities derived from the



(a) Cathode East X 2, one of the more strongly varying cathodes pedestals.



(b) Cathode East Y 7, following the drift pattern of East X 2 above, but with smaller opposite magnitude.



(c) East anode, primarily reflecting daily temperature cycle wiggles.

Figure 6.2: Pedestal histories for two cathodes and an anode over the 2010 run. Bars indicate RMS width of pedestal distribution.

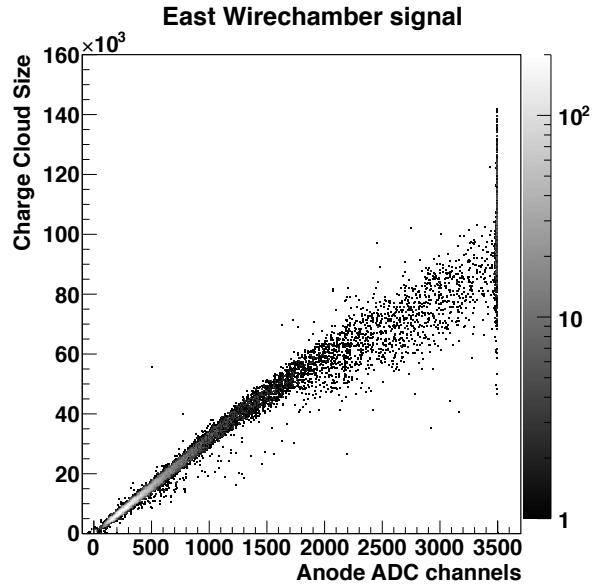


Figure 6.3: Charge cloud size extracted from cathode data, versus measurement by anode. From a 2010 beta run. Note anode ADC clipping at large signals, avoided by cathode-based charge cloud estimation.

charge signal is based on anode data for the 2010 analysis; however, the cathode-based charge cloud size could be used in the same manner.

6.1.5 Charge signal position dependence

The magnitude of the charge signal produced for a given energy deposition varies as a function of event position in the wirechamber. The form of the variation appears to be unique to each wirechamber, but reasonably stable and repeatable over time (even after breaking and rebuilding the wirechamber). The cause of this non-uniformity is unknown. However, it can be mapped out (similarly to the scintillator position dependence) by analyzing wirechamber gain as a function of position.

Either beta decay data or xenon data provides a useful signal for this application. Xenon datasets provide the most abundant statistics, allowing for precise checks whenever the wirechambers may have changed. One concern is that overall wirechamber gain appears to change significantly when subjected to the high event rates of Xenon decay runs. However, the relative position dependence extracted from Xenon and beta decay data sets are consistent, up to a scaling factor which is fixed by the energy calibration factor described in the following section.

The relative position response is determined by binning Type 0 events by position according to the same scheme employed for the light transport position dependence. The events in each position bin are further subdivided in 25 keV scintillator energy deposition bins, which produces a more clearly Landau-shaped distribution for the charge spectrum of events in each energy bin, allows comparison against the MC expected dependence of wirechamber charge on event energy, and disentangles possible effects from position-varying energy-dependent trigger efficiencies. In each energy bin, the observed charge spectrum of the events is fit with a Landau distribution, an example

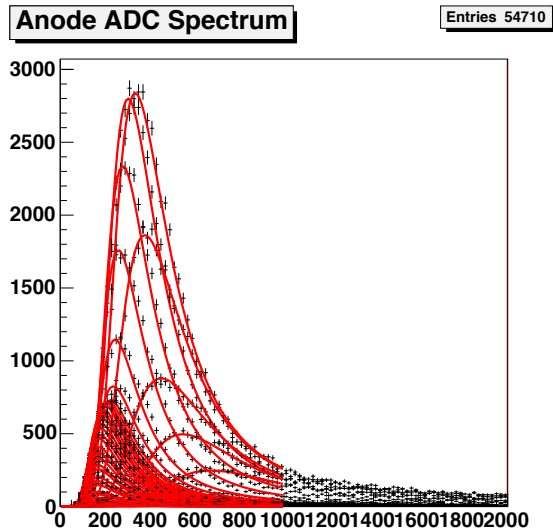


Figure 6.4: Anode ADC spectra in one position bin, divided into 25 keV scintillator energy bins and fit with Landau distributions. From a 2010 Xenon dataset.

of which is shown in Figure 6.4. Figure 6.5 shows the extracted Landau MPV of the ADC spectra as a function of energy, for all position bins in the West detector. Monte Carlo provides expected wirechamber energy deposition spectra, binned by scintillator energy and fit with a Landau function in the same manner as the anode ADC data. A scaling factor to match the ADC MPV to the energy deposition MPV is determined for each position bin, mapping the position dependence of the wirechamber charge signal. Figure 6.6 shows the anode ADC MPV curves of Figure 6.5 after scaling to match expected energy deposition. The measured position dependence of the charge signal is shown for the wirechambers on both sides in Figure 6.7, based on a 2010 Xenon data set. There is approximately a factor of 2 variation over the wirechamber, in an irregular pattern whose cause is unknown, but which has remained approximately stable through many rebuildings of the wirechambers.

6.1.6 Gain calibration

Were the wirechambers' gain response constant, the position-dependent scaling factor from anode ADC to MC expected energy determined by the above procedure would suffice for calibration. However, the gain does change over time, including a significant reduction in gain observed during high-rate Xenon runs. Thus, an additional overall gain factor is applied to calibrated sets of runs, extracted by a similar procedure as the position dependence described above. Following the usual iterated calibration procedure (subsection 3.2.2), a prior rough calibration factor allows the wirechamber data to be calibrated and MC expected energy deposition to be compared on the same scale. The observed wirechamber energy spectrum for Type 0 events, in 100 keV bins as a function of scintillator energy, is fit by a Landau function to determine the MPV. Comparison against MC simulations analyzed in the same manner allows correction of the gain calibration factor to best match data to MC. Figure 6.8 shows a typical data/MC comparison for Type 0 events extracted from one beta decay octet. Also shown is the same comparison using Type I backscatter events;

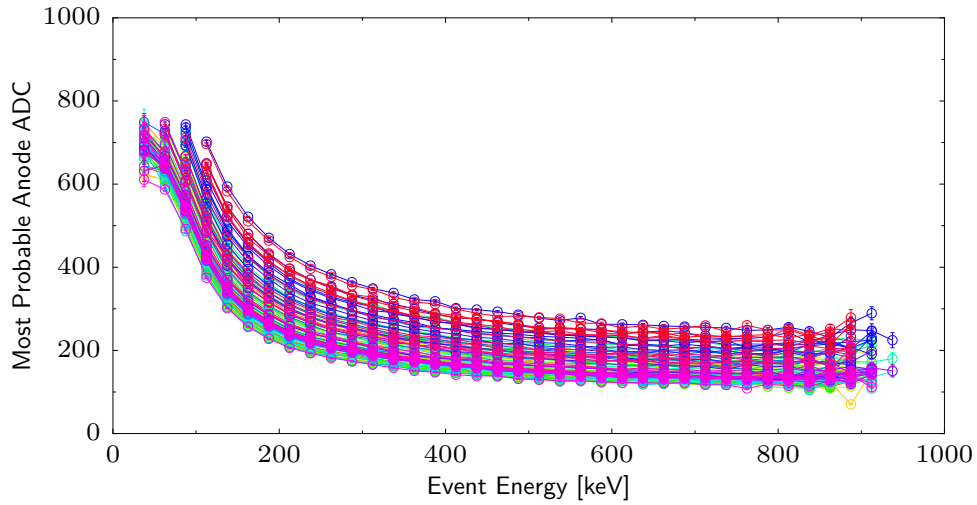


Figure 6.5: Most Probable Value for anode ADC spectra extracted as a function of scintillator energy for each position bin (lines connect points from same position bin); East detector from a Xenon data set.

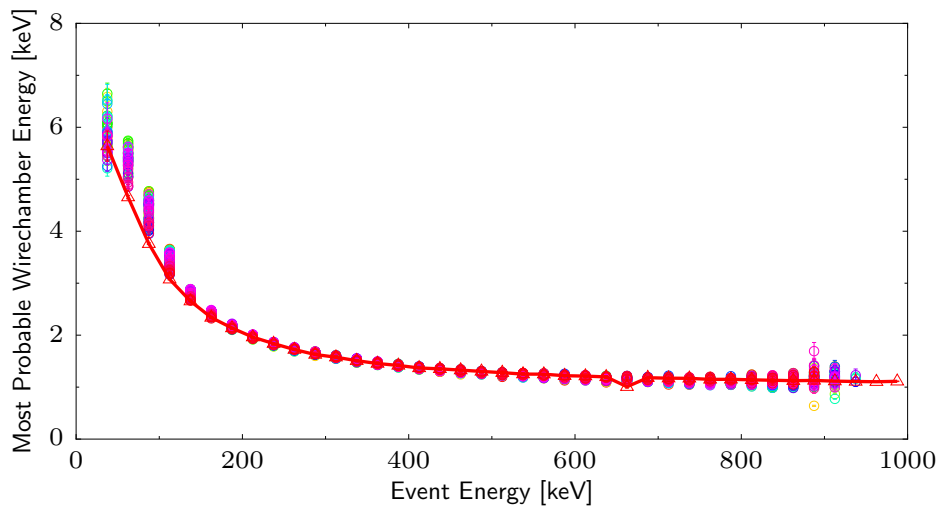


Figure 6.6: Most Probable Value for wirechamber energy deposition, as a function of scintillator energy. Thick line and triangles indicate MC expected values. Circles are anode ADC MPV data from each position bin, multiplied by a scaling factor to match the MC expected energy on average over the 300 keV to 700 keV range.

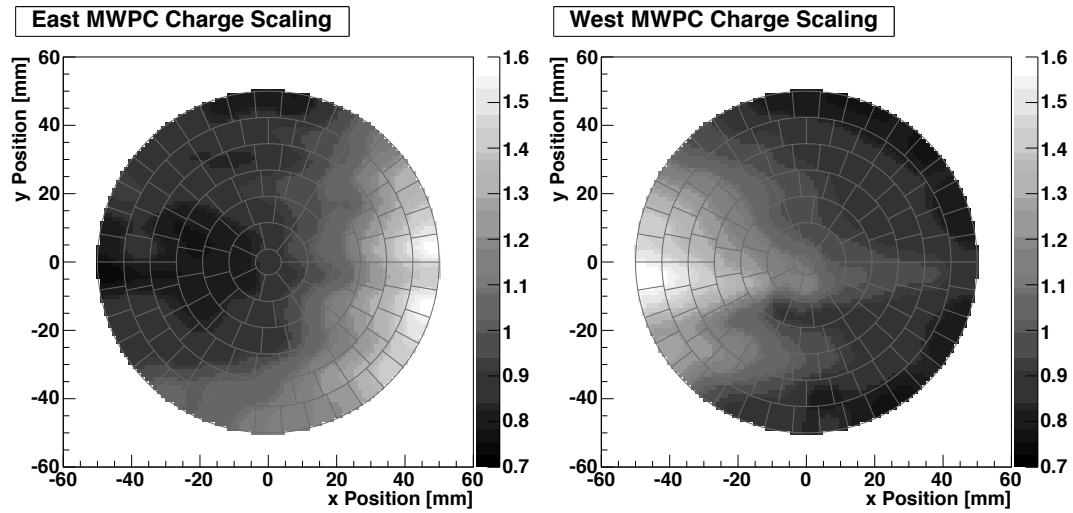
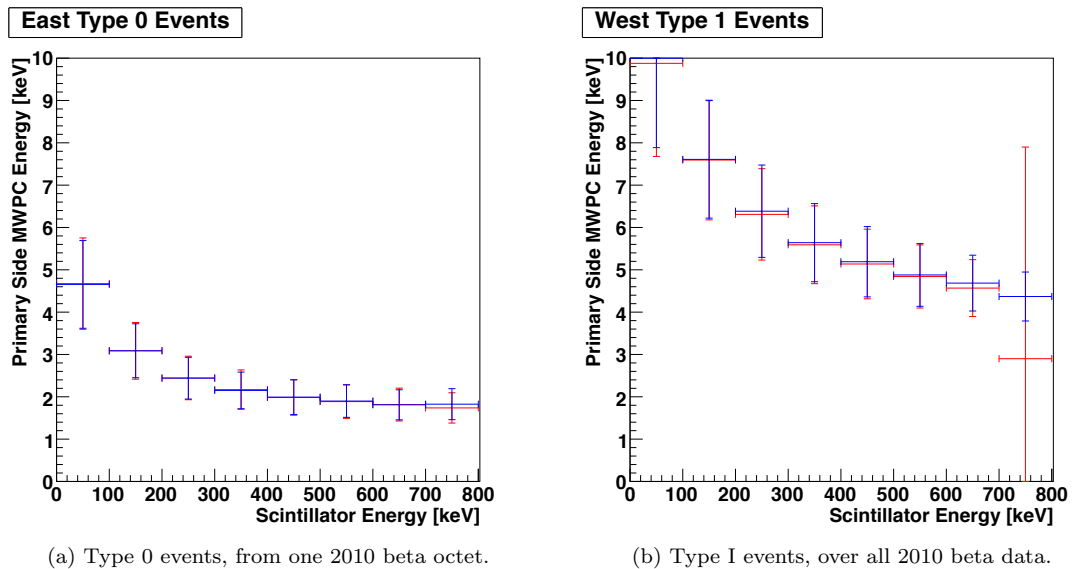


Figure 6.7: Position dependence of wirechamber charge signal magnitude, normalized to position-averaged value of 1.



(a) Type 0 events, from one 2010 beta octet.

(b) Type I events, over all 2010 beta data.

Figure 6.8: Wirechamber energy deposition, most probable value and width (indicated by bars) from Landau fit as a function of scintillator energy. Calibrated data and MC shown together.

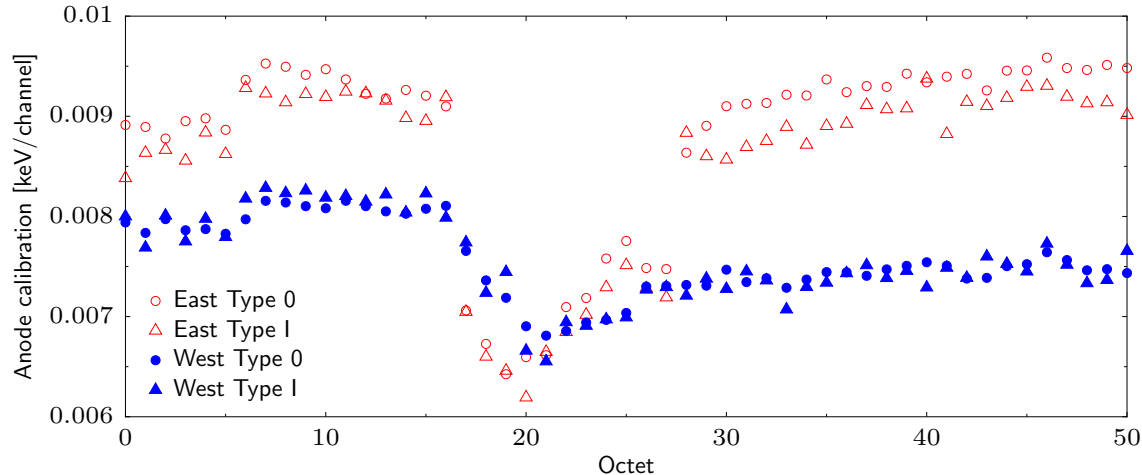


Figure 6.9: Anode gain calibration factor for each beta decay octet, as determined using Type 0 and Type I events.

comfortingly, calibration to Type 0 events also correctly reproduces the expected Type I wirechamber spectra. The gain calibration factor g_i extracted for each 2010 beta decay octet is shown in Figure 6.9, alongside the gain correction factor extracted using Type I events instead of Type 0 in the analysis.

6.2 Software wirechamber trigger

6.2.1 Trigger cut possibilities

For event type classification, a binary distinction about whether or not a wirechamber was “hit” in an event is useful. There are multiple cuts on which such a classification could be based:

- cut on the anode signal;
- cut on the sum of cathode signals;
- cut on the lesser of the maximum cathode signals in the X and Y planes; and
- cut on the sum of the maximum cathode signal in the X and Y plane.

The optimum cut uses the variable that maximizes the separation between pedestal events and the distribution of energy-depositing events. The anode signal, typically with low signal gain relative to the pedestal width, is simple but sub-optimal. Summing all the cathode signals adds noise from all the “irrelevant” cathodes far from the charge cloud location.

The final two options, using only the maximum cathode signals, avoid summing in this extra noise. Choosing the minimum of the two cathode plane maximums helps assure that the event position can be reconstructed in both directions (both planes have a signal above pedestal). Summing the cathode max signals admits the possibility that position reconstruction might be poor in one plane, but with overall better efficiency for separating small-signal events from background.

For the 2010 data analysis, a summed cathode maximum cut was set (by eye) at the typical position of the minimum in the dip between the pedestal and signal portions of the summed cathode maximum spectrum. A more detailed study of cut position effects will be important for future analysis efforts. Because there is imperfect separation between the pedestal and real events (which include a tail going down to 0 wirechamber energy deposition), there is no cut position that completely avoids both false-positive and false-negative categorizations. The effects of both missing real wirechamber events and adding noise events must be evaluated.

6.2.2 False negative effects

The primary effect of placing the cut too high is reducing efficiency for identifying low-wirechamber-deposition Type 0 events, which will instead be miscategorized as gamma (scintillator only) triggers. This preferentially removes more forward-directed beta electrons (especially at higher energies) from the data, diluting the observed asymmetry. In beta decay data, this process will produce an excess “gamma” background that persists after background subtraction, indistinguishable from any neutron-generated gamma backgrounds that might also be studied. Using calibration sources (with well-known actual gamma backgrounds), the rate of spurious “gamma” events can be measured to estimate the wirechamber inefficiency; a procedure carried out for the 2010 data analysis.

Secondary effects of too high cuts include misclassifying Type II and III backscatters with low wirechamber energy deposition opposite the primary scintillator side. These events will be misclassified as Type 0, which results in asymmetry-diluting side misidentification for real Type II’s.

The impact of wirechamber inefficiency on the asymmetry is discussed in subsection 7.3.5.

6.2.3 False positive effects

Placing the cut too low spuriously tags Type 0 events as Type II/III backscatters (due to noise “triggering” the opposite side wirechamber). These events will primarily be labeled as Type II (resulting in asymmetry dilution), since Type 0 primary-side wirechamber energy deposition generally coincides with the lower range identified as Type II. The frequency of false-positive wirechamber triggers can be evaluated by counting wirechamber triggers concurrent with LED or UCN monitor triggers. Incorporating a model of wirechamber “noise” events into the Monte Carlo for generating associated corrections was not done for the 2010 data analysis, but is recommended for future efforts.

6.3 Position reconstruction

6.3.1 Overview

The position of tracks passing through the wirechamber is determined from the observed distribution of charge over the cathode planes. The two orthogonally oriented cathode planes are treated independently, each reconstructing one dimension of the position. The wirechambers operate in a regime that precludes simple yet accurate analytical physics-motivated models for the expected charge distribution shapes. The spacing between wire planes (determining the characteristic width of the charge distribution on the cathodes in response to localized anode charge), typical event

Larmor diameters (further smearing out the charge distribution), and the width of the cathode segments sampling the charge distribution are all on the same size scale. Thus, rather than attempt a first-principles position reconstruction algorithm, an empirical approach is taken, starting from the very basic assumption that the charge distribution will peak at and fall monotonically from the center of the event.

An *acceptable* position reconstruction algorithm provides the following two characteristics:

Locality: Reconstructed positions are guaranteed to be reasonably near to the true event position.

Monotonicity: Two events differing only in position with true positions $x_1 < x_2$ should have reconstructed positions $x'_1 < x'_2$. On account of the presence of noise in the observed cathode signals, this requirement is relaxed to apply only to the average reconstructed positions of many events.

A “pseudo position” produced with such characteristics, despite any deviations from true event locations, is fully suitable for every purpose in calibrations when used consistently through the calibrations process. The distortion of reconstructed event positions from true will primarily be visible as unevenness in plots of nominally uniform event position distributions.

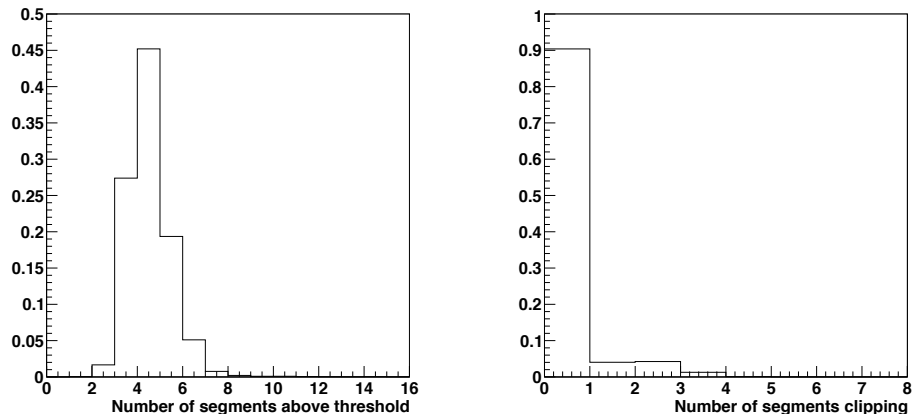
Achieving locality is straightforward, by assuring that the mathematics of the position reconstruction algorithm will never “fling” an event location far from the position of the highest signal cathode (the crudest approximation for event position). For events producing the same underlying charge distribution shape, only translated by the difference in position (and perhaps scaled by an overall factor), monotonicity is likewise straightforward to achieve by mathematical construction (assuming no more than that the cathode signal decreases with distance from the center).

However, differences in underlying charge distribution shapes — especially as a function of event energy (and associated typical Larmor radius) — complicate matters. Energy-dependent non-uniformity is troublesome for one particular application: determining the position-dependent light transport factor by measuring a beta spectrum endpoint, which is distorted if higher energy events tend towards one position and the lower energies towards another. Hence, an additional step in position reconstruction (subsection 6.3.4) is taken to smooth out energy dependent positioning distortion, assuring that nominally uniform events are reconstructed to a uniform position distribution for every scintillator energy.

6.3.2 Input data

The data available for position reconstruction is the signal, presumably proportional to charge collected, from each of the 16 cathode segments in each plane. The charge cloud for a typical event spans a smaller portion of the wirechamber; signals notably above background noise have a most probable span of 4 cathode segments (see Figure 6.10a). Only the data from the cathode segment with the highest signal (henceforward named the “maximum segment”) and its two neighbors is taken into consideration for reconstruction; little information is lost by excluding more distant segments, while the influence of noise is suppressed.

For a few intervals of data taking in 2009, the readout electronics for some of the cathode segments was failing and no signal was available for certain cathode segments. These “dead” segments are easily identified in the data (sporadic or no signal above background), and are ignored in the



(a) Multiplicity of cathode segments with signal more than 70 channels above background. (b) Multiplicity of cathode segments with signal clipping; 9.6% of these events are clipped.

Figure 6.10: Cathode segment data available for a typical beta decay run.

position reconstruction process, relying on the width of the charge cloud to provide sufficient signal in neighboring segments. In several percent of events (see Figure 6.10b), the signal in one or more cathode segments exceeds the dynamic range of the cathode ADC, producing a “clipped” value at the maximum $2^{12} - 1$ channels. A clipped signal provides no information about event position finer than its general proximity to the segment. When the charge cloud is strong enough to produce clipping in one or more segments, there is also abundant signal in neighboring segments below the clipping threshold. Clipped segments are ignored for position reconstruction, just like dead segments.

6.3.3 Initial position estimate

6.3.3.1 Parabola center

Suppose the maximum segment is at position p_0 with signal s_0 , and its neighbors to either side are at positions $p_- < p_0 < p_+$ with signals $s_-, s_+ < s_0$. For a simple approximation, the shape of the charge distribution around its maximum can be taken as roughly parabolic. The three points (p_i, s_i) provide a system of three equations in three unknowns for a parabola passing through them,

$$s_i = Ap_i^2 + Bp_i + C \equiv h_p - \frac{1}{2} \left(\frac{p_i - c_p}{w_p} \right)^2 \quad (6.2)$$

$$c_p = -\frac{B}{2A}, \quad w_p = \frac{1}{\sqrt{-2A}}, \quad h_p = C - \frac{B^2}{4A} = C + \frac{c_p^2}{2w_p^2}.$$

Solving the linear system of equations in A, B, C allows determination of the parabola center, width, and maximum height

$$c_p \equiv \frac{p_+^2 \cdot (s_0 - s_-) - p_0^2 \cdot (s_+ - s_-) - p_-^2 \cdot (s_0 - s_+)}{2[p_+ \cdot (s_0 - s_-) - p_0 \cdot (s_+ - s_-) - p_- \cdot (s_0 - s_+)]} \in \left(\frac{p_- + p_0}{2}, \frac{p_0 + p_+}{2} \right) \quad (6.3)$$

$$w_p \equiv \sqrt{\frac{(p_0 - p_-)(p_+ - p_0)(p_+ - p_-)}{2[p_+ \cdot (s_0 - s_-) - p_0 \cdot (s_+ - s_-) - p_- \cdot (s_0 - s_+)]}} \quad (6.4)$$

$$h_p \equiv \frac{(p_0 - p_-)p_-p_0s_+ - (p_+ - p_-)p_+p_-s_0 + (p_+ - p_0)p_+p_0s_-}{(p_0 - p_-)(p_+ - p_-)(p_+ - p_0)} + \frac{c_p^2}{2w_p^2}. \quad (6.5)$$

In the most common case without clipping or dead segments, the cathode segments are evenly spaced. Taking $p_-, p_0, p_+ = -1, 0, +1$, the parabola's center relative to the maximum segment in units of the wire spacing and its associated width are

$$c_p \equiv \frac{s_+ - s_-}{4s_0 - 2s_+ - 2s_-} \in \left(-\frac{1}{2}, \frac{1}{2}\right); \quad w_p \equiv \sqrt{\frac{1}{2s_0 - s_- - s_+}}; \quad h_p = s_0 + \frac{(s_+ - s_-)^2}{8(2s_0 - s_+ - s_-)}. \quad (6.6)$$

This ‘‘parabola center’’ positioning algorithm provides locality and monotonicity for any charge distribution shape that itself monotonically decreases away from a central maximum. The uniformity of the parabola center reconstruction, however, leaves much to be desired, as deviations of the actual charge cloud shape from the oversimplified parabola model bias the reconstructed positions.

6.3.3.2 Adjusted Gaussian center

An improvement over the parabola model is to assume that the charge cloud shape can be better described by a Gaussian of width σ . For such a Gaussian centered at position c_g , the extracted ‘‘parabola center’’ in the uniformly spaced segments case would be

$$c_p = \frac{e^{-(1-c_g)^2/2\sigma^2} - e^{-(-1-c_g)^2/2\sigma^2}}{4e^{-c_g^2/2\sigma^2} - 2e^{-(1-c_g)^2/2\sigma^2} - 2e^{-(-1-c_g)^2/2\sigma^2}} = \frac{e^{2c_g/\sigma^2} - 1}{4e^{c_g/\sigma^2}e^{1/2\sigma^2} - 2e^{2c_g/\sigma^2} - 2} \quad (6.7)$$

$$\Rightarrow (2c_p + 1) \left[e^{c_g/\sigma^2} \right]^2 - 4c_p e^{1/2\sigma^2} e^{c_g/\sigma^2} + 2c_p - 1 = 0$$

$$\Rightarrow c_g = \sigma^2 \ln \frac{2e^{1/2\sigma^2} c_p + \sqrt{1 + 4(e^{1/2\sigma^2} - 1)c_p^2}}{1 + 2c_p} \in \left(-\frac{1}{2}, \frac{1}{2}\right), \quad (6.8)$$

providing a formula for an ‘‘improved’’ center c_g from the parabola center c_p and characteristic charge cloud spread σ . The parameter σ can be extracted from the data by fitting the cumulative distribution of observed c_p by $c_g(c_p; \sigma) + \frac{1}{2}$, producing a σ that renders the most uniform distribution for c_g . The adjusted Gaussian center c_g preserves the desirable locality and monotonicity of the parabola center, while improving the uniformity.

Note that the derivation of the analytical expression for $c_g(c_p; \sigma)$ relies on the wires being uniformly spaced; without this assumption, the relationship between parabola and Gaussian center becomes analytically intractable.

6.3.3.3 Direct Gaussian center

A Gaussian center can also be determined directly without passing through the parabola center calculation. Noting that the log of Gaussian is a parabola, the above formula for the parabola center can be applied with $\ln s_-, \ln s_0, \ln s_+$ replacing s_-, s_0, s_+ . The characteristic width of the parabola becomes the σ of the Gaussian.

While this approach is capable of producing a Gaussian center for nonuniformly spaced wires, it has two drawbacks compared to the preceding parabola to Gaussian center conversion method. First, for events with small wirechamber signals, $\ln(\text{small signal} + \text{noise})$ becomes problematic, especially with the possibility of $\text{small signal} + \text{noise} \leq 0$; the parabola center, on the other hand, remains more numerically stable towards small-signal fluctuations. Second, allowing the σ of the Gaussian to be determined from the data precludes tuning σ to a fixed value to minimize non-uniformity. Nevertheless, direct calculation of the Gaussian center is useful when discarding clipped cathode segments requires position reconstruction from non-uniformly spaced segments; the signal on the remaining cathodes is sufficiently large to avoid concerns about noise fluctuations.

6.3.3.4 Pair and edge wires

For events where the maximum segment is the edge wire of the plane, or any other case where only two wire signals are available, there is insufficient data to apply the methods above. Assuming the charge cloud has the same shape as a “typical” event, a Gaussian with width σ as in the adjusted Gaussian center procedure above, the position is deduced from the two cathode segments nearest the edge. If these wires are positioned at p_-, p_+ with signals s_-, s_+ , then the Gaussian charge cloud that would produce this has center and height

$$c_e \equiv \frac{p_- + p_+}{2} + \frac{\sigma^2}{p_+ - p_-} \ln \frac{s_+}{s_-} \quad (6.9)$$

$$\ln h_e \equiv \frac{p_+ \ln s_- - p_- \ln s_+}{p_+ - p_-} + \frac{c_e^2 - p_+ p_-}{2\sigma^2}. \quad (6.10)$$

Scaling coordinates as necessary, so that $p_{\pm} = \pm \frac{1}{2}$, this reads

$$c_e = \sigma^2 \ln \frac{s_+}{s_-}; \quad \ln h_e = \frac{1}{2} \left(\ln \frac{s_+}{s_-} \right)^2 \sigma^2 + \ln \sqrt{s_+ s_-} + \frac{1}{8\sigma^2}. \quad (6.11)$$

In the small signal case where the second-to-edge wire has a negative signal, the position is ill-determined; assigning the position of the edge wire and height of the edge wire signal in this case seems as good as any other choice.

6.3.4 Uniformity correction

Although the adjusted Gaussian center procedure ameliorates the non-uniformity over the straight parabola center construction, a readily apparent level of nonuniformity remains, even varying with event energy. An empirical correction to iron out the observed nonuniformity in the data completes the position construction.

6.3.4.1 Cathode relative gain normalization

Since position reconstruction begins with identifying the highest-signal cathode for an event, and then identifying the position within the local zone around the segment, a cathode segment with higher or lower response than its neighbors will gain or lose counts from within its zone. A cathode gain correction is carried out to “share” points uniformly between neighboring segments.

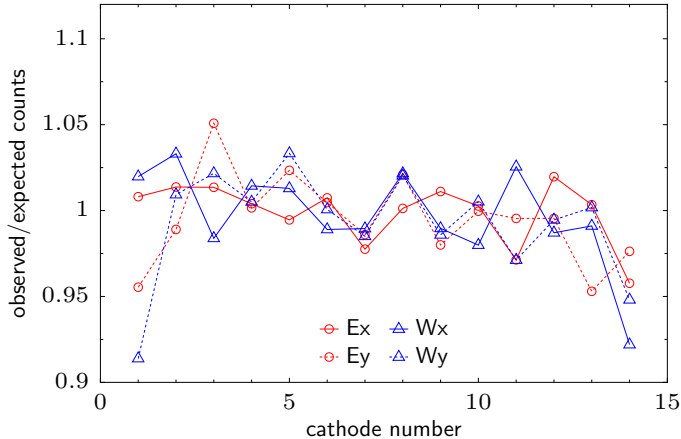


Figure 6.11: Cathode segment event counts, observed versus expected, for 2010 beta decay data, prior to cathode gain adjustment.

Compared against MC expectations, there is a few percent variation in the number of events assigned to each cathode segment without applying gain corrections (Figure 6.11). This variation includes both local nonuniformity between adjacent cathode segments, and larger-scale systematic deviations. The overall trend of the y deviation, dropping by $\sim 5\%$ from the decay trap bottom to top, is consistent with the scale expected for gravitational impact on UCN density, not included in the simulation: $(10\text{ cm}) \cdot m_n g \approx 10\text{ neV}$, so density at the top of the decay trap for $\sim 200\text{ neV}$ kinetic energy neutrons should be $\sim e^{-10/200} \approx 0.95$ of the density at the bottom. The extreme edge cathode segments are excluded from such considerations, as they are entirely outside the fiducial determined by the wirechamber entrance window. Using the observed behavior of the cathode signal for events in the “crossover regions” midway between cathode segments, the response of the system to small cathode gain changes can be estimated, and a corresponding set of gain adjustments generated to reduce the counts discrepancy.

Since the cathode sum signal scales approximately proportionally to the anode signal, we can produce a “normalized cathode” signal for each event $s_i^* \equiv s_i/a$, where s_i is the signal from the i^{th} cathode segment, and a is the anode charge. The anode charge could be substituted with another total charge estimate, such as the cathode sum. This normalized variable “unifies” all wirechamber events onto the same amplitude scale, regardless of total charge. For each cathode, histogramming s_i^* versus reconstructed hit distance from cathode center (Figure 6.12a) gives the average charge distribution shape over all events, convolved by the cathode segment width. To the extent that all events share a common charge distribution shape (varying only by an overall scale factor divided out by the anode normalization), the histogram of s_i^* versus position will fall on a sharply defined curve, with spread around the curve indicating the extent of shape variation in event signals. This curve is not exactly the true charge distribution in the wirechamber, as the position axis incorporates distortion from incorrect position reconstruction — nevertheless, it is quite close. Curves for all cathode segments are visually quite similar.

These cathode signal shape curves provide the necessary information to estimate how gain changes will affect position reconstruction. By definition of the position reconstruction algorithm, curves from adjacent cathode segments will cross over at equal signal at normalized positions ± 0.5 .

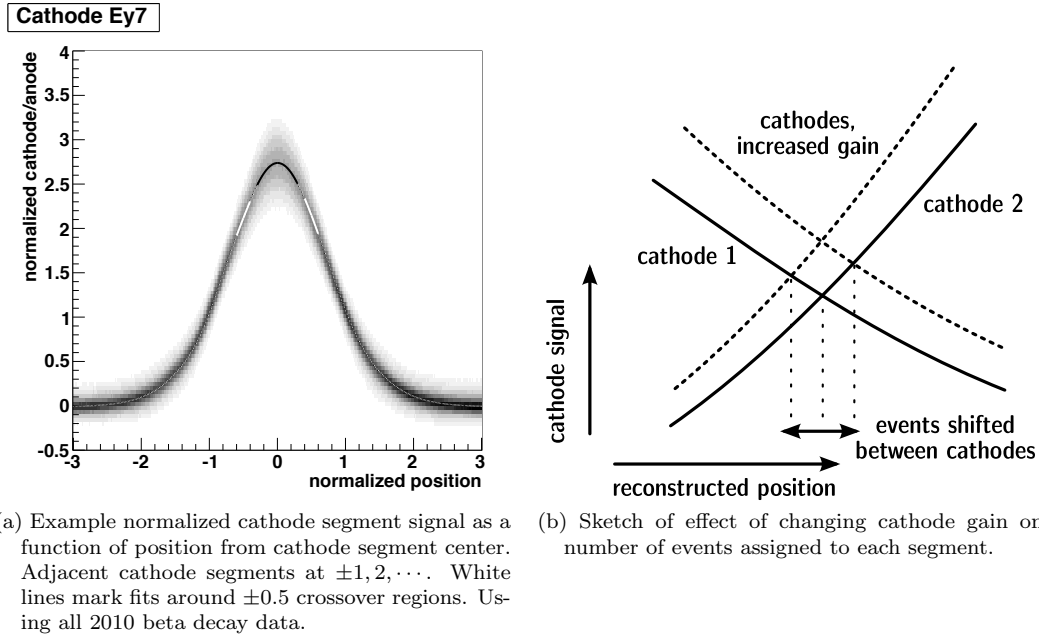


Figure 6.12: Normalized cathode signal distribution, and sketch of effect of cathode gain changes.

Figure 6.12b sketches the consequent effect of changing one of the cathode gains, which shifts the crossover point, moving events from one side to the other of the dividing line midway between cathodes. To lowest order, the shift dx of the midpoint between cathodes i and $i + 1$ caused by multiplying cathode signal s_i by a gain factor $1 + dg_i$ will be

$$\frac{dx}{dg_i} = \frac{s^*}{\frac{ds_{i+1}^*}{dx} - \frac{ds_i^*}{dx}}, \quad (6.12)$$

where s^* is the normalized cathode signal at the crossover point, and $\frac{ds_i^*}{dx}$ are the derivatives of the cathode signals at the crossover point for cathodes i and $i + 1$ (all of which can be determined from a fitting the corresponding crossover regions of the cathode signal shape curves).

Using the observed number of events observed as a function of position, we can determine the event density $\frac{dN_i}{dx}$ at each crossover point between cathodes i and $i + 1$, which indicates the relationship between small gain changes and the number of events shifted between segments i and $i + 1$,

$$\frac{dN_i}{dg_i} = \frac{dN_i}{dx} \frac{dx}{dg_i}, \quad \frac{dN_{i+1}}{dg_i} = -\frac{dN_i}{dg_i}. \quad (6.13)$$

Putting together the effects from gain changes in cathode i and its neighbors,

$$dN_i = -\frac{dN_{i-1}}{dg_{i-1}} dg_{i-1} + \left(\frac{dN_{i-1}}{dg_{i-1}} + \frac{dN_i}{dg_i} \right) dg_i - \frac{dN_i}{dg_i} dg_{i+1}. \quad (6.14)$$

To counter the observed discrepancies between observed counts N_i^{obs} and expected N_i^{exp} , one would set the gain adjustments dg_i such that

$$dN_i = N_i^{\text{exp}} - N_i^{\text{obs}} \quad (6.15)$$

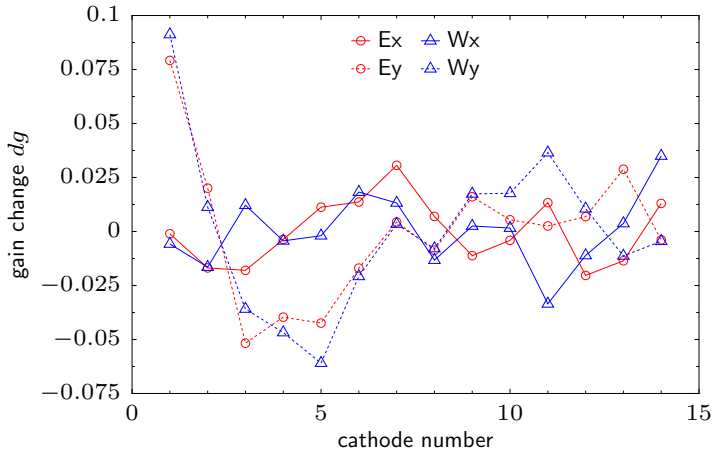


Figure 6.13: Cathode gain adjustment produced to correct deviations in Figure 6.11.

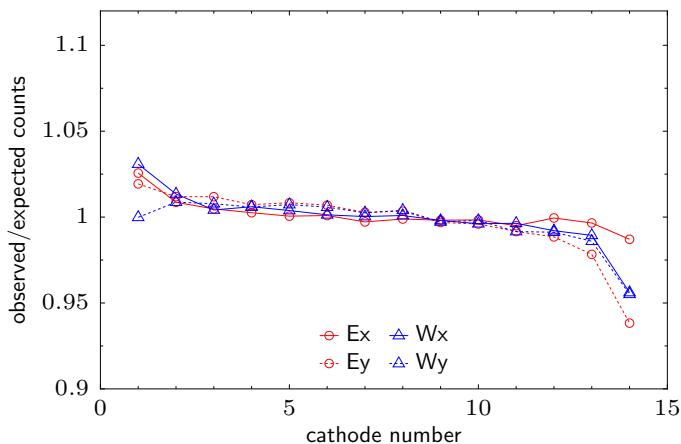


Figure 6.14: Cathode segment event counts after cathode gain correction (compare to Figure 6.11).

defining a linear system of equations for the dg_i . Because of conservation of total events $\sum_i dN_i = 0$, this system is singular (one constraint short of the number of variables). Furthermore, attempting to adjust the gains to correct the overall global count discrepancies results in very large changes, attempting to move events all the way across the detector to resolve, for example, the gravitational effect. For a more useful set of constraints, this can be transformed into a set of equations to suppress *local* imbalances between adjacent cathodes,

$$dN_{i+1} - dN_i = (N_{i+1}^{\text{exp}} - N_{i+1}^{\text{obs}}) - (N_i^{\text{exp}} - N_i^{\text{obs}}), \quad (6.16)$$

and we can add additional constraints of the form $\alpha dg_i = 0$, solving the system in the least-squares sense. The coefficient α dictates the general scale of corrections allowed. Choosing $\alpha \approx 0.02 \sum_i N_i$ makes the system well-behaved, allowing few-percent gain corrections to smooth out unevenness between adjacent cathodes without going crazy attempting to resolve large-scale discrepancies. Figure 6.13 shows the gain corrections produced by this procedure, and Figure 6.14 the more uniform segment-to-segment event counts produced using the gain corrections.

6.3.4.2 Cathode segment uniformity

Let $N(p \in (-\frac{1}{2}, \frac{1}{2}))$ denote the (uncorrected) observed distribution of events at position p around a cathode segment at $p = 0$ (with neighboring segments at $p = \pm 1$). By local symmetry of construction of the wirechamber around $p = 0$, we expect $N(p)$ to be an even and periodic (under translation by one segment spacing $\Delta p = 1$) function of p . Thus, we can generally express $N(p)$ by the Fourier series

$$N\left(p \in \left(-\frac{1}{2}, \frac{1}{2}\right)\right) = 1 + \sum_{n=1}^{\infty} c_n \cos(2\pi np). \quad (6.17)$$

For the most general case (allowing breaking of expected symmetry), additional antisymmetric terms $\sum_{n=1}^{\infty} s_n \sin(2\pi np)$ can be included to describe any observed distribution.

Assuming the true event distribution should be uniform, we can recover a uniform distribution by using the cumulative distribution of $N(p)$,

$$C(p' \leq p) = \frac{1}{2} + p + \sum_{n=1}^{\infty} \frac{c_n \sin(2\pi np)}{2\pi n} \quad (6.18)$$

to correct observed position p to corrected position $p_{\text{true}} \equiv C(p' \leq p) - \frac{1}{2}$.

Note that this indicates that a relatively small systematic position offset can produce a large visible nonuniformity: the lowest-order sinusoidal shift of $\pm \frac{c}{2\pi}$ of the segment spacing produces a nonuniformity of $\pm c$. Thus, observed positioning nonuniformities on order of $\pm 10\%$ indicate systematic shifts on the order of ± 0.01 mm.

The position distribution $N(p)$ can be observed from the data, and fit with a few terms of a Fourier series to provide the coefficients c_n for a position-correcting function. Note that $N(p)$, for events uniformly populating the detector, should not actually be uniform, due to the circular aperture of the detector. A corresponding MC simulation can provide the expected distribution $N_{\text{sim}}(p)$ (including all energy-dependent edge effects), and the ratio $N(p)/N_{\text{sim}}(p)$ fit for deviations from uniformity.

The nonuniformity observed in the data varies as a function of event (scintillator) energy. Using xenon data for high statistics across a wide range of energies, the uniformity coefficients can be extracted for each cathode segment (excepting the extreme two on each edge, with few events falling in their zone), as a function of energy. The individual cathode segments show approximately the same overall pattern of distortion. Distortion coefficients extracted from xenon data, averaged over the 12 central cathode segments in each of the four wireplanes, are shown in Figure 6.15. The lowest-order symmetric $\cos(2\pi x)$ term dominates, with a positive sign corresponding to bunching up around wire positions. Some cathodes show a little antisymmetric $\sin(2\pi x)$. Next higher order terms $\cos(4\pi x)$ appear only at low energies with opposite sign. High energy events tend towards a uniform distribution without further correction. The distinctive double-peaked structure of the correction coefficients at ~ 200 keV will provide an interesting benchmark for any future attempts to produce a detailed physical model for wirechamber response.

Figure 6.16 and Figure 6.17 show examples with beta decay data. The raw positions are the product of the adjusted Gaussian center procedure described above; corrected positions apply the distortion correction determined for each cathode segment from the xenon data. No distortion correction is applied to edge segments (which are never the central segment for events in the fiducial

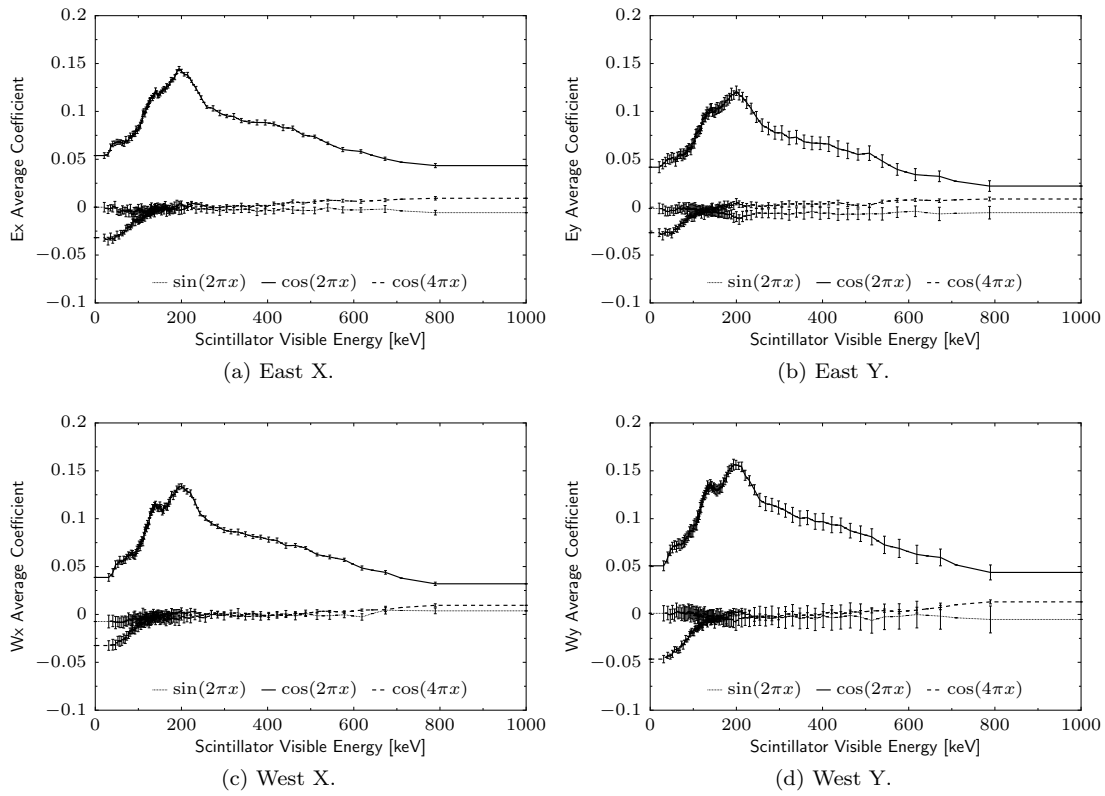


Figure 6.15: Average position correction coefficients for each wireplane as a function of scintillator energy. Error bars indicate standard deviation of individual cathode segment position corrections.

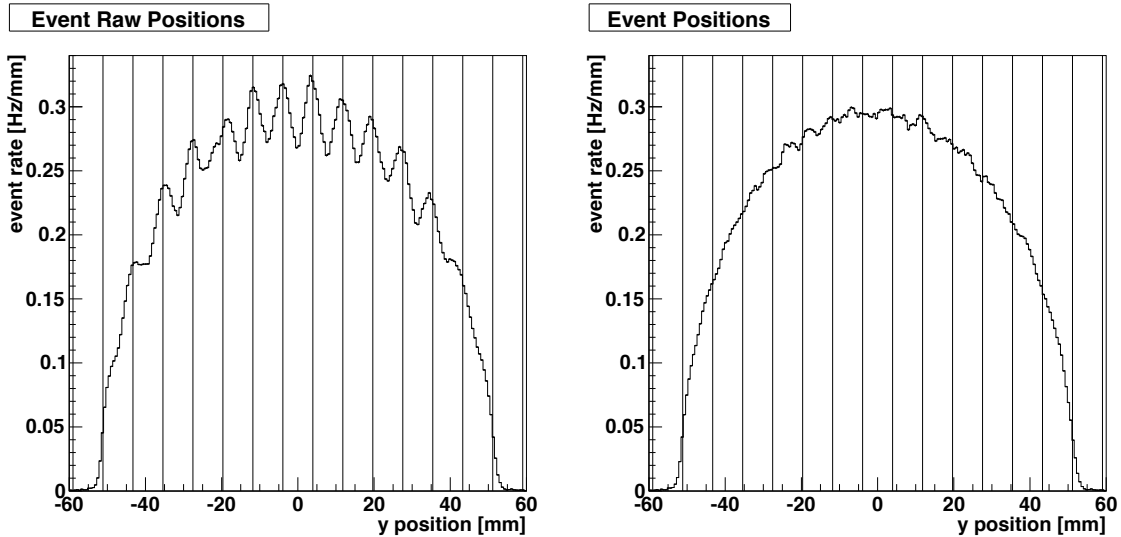


Figure 6.16: Wirechamber beta decay event positions, before and after uniformity correction. Vertical lines mark cathode segment centers. East Y profile for all 2010 beta decay events.

region), and the average distortion correction from the central 12 segments is applied to second-to-edge segments.

6.3.5 Localized position reconstruction quality

While average large-scale position reconstruction is corrected and assessed by the uniformity corrections described above, the quality of localized position reconstruction can be tested by observing the reconstructed position distribution of events from sealed source calibration radioisotopes. Figure 6.18 shows two examples. For low-energy sources with expected narrow position distributions, wirechamber positioning precision exceeds uncertainties in the physical dimensions of the spot from which decays are originating: assumed to be 3 mm diameter in simulation, but apparently smaller based on wirechamber reconstruction. The intrinsic resolution of wirechamber positioning can be taken as negligible compared to the physical width of available real-world event sources.

6.3.6 Towards a first-principles wirechamber response model

The approach above does not require understanding the physics details of actual wirechamber charge distributions, relying instead on empirical uniformity corrections to simplistic shape assumptions. A more physical model of the charge distribution will rapidly become analytically intractable, since the wirechamber functions in a regime where few approximations can be made. The cathode segment width, spacing between cathode and anode planes, and typical Larmor radius of particles are all on the same size scale. A numerical approach, using a pre-calculated look up table for position as a function of cathode segment response based on charge cloud simulation, would likely be necessary. Implementation of an accurate cathode response model would permit more thorough analysis of wirechamber trigger efficiency systematics.

A comprehensive review of wirechamber charge distribution theory is given in [Mat91]. For a wirechamber with an anode plane between two cathode planes at distance h away, the simplest

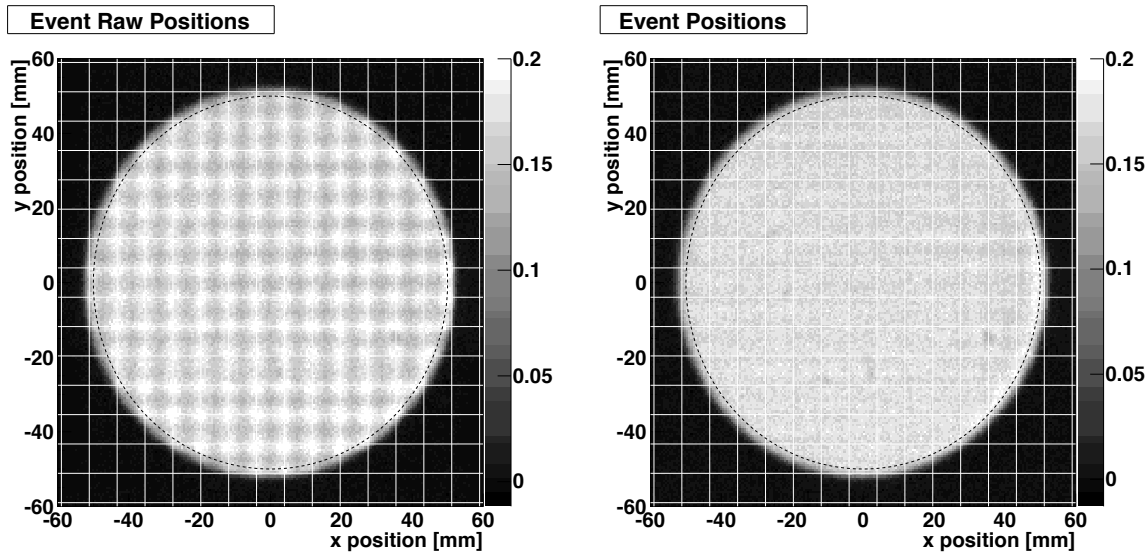
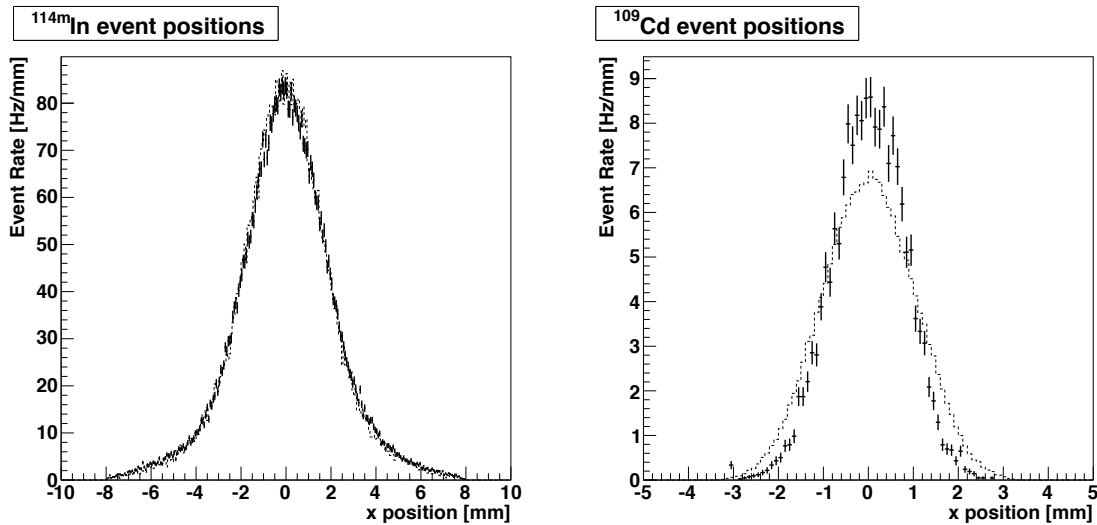


Figure 6.17: Wirechamber beta decay event positions, before and after uniformity correction, 2D distribution for Type 0 beta decays. East side, 2010 data. Lines mark cathode segment centers; dashed circles at 50mm radius. Z axis units are Hz/cm².



(a) ^{114m}In , combining a narrower spot from the 175 keV conversion electron peak with a broad distribution from the 1989 keV beta decay.

(b) ^{109}Cd , 75 keV conversion electron peak. Excess width in simulation from assuming nominal 3 mm diameter source spot.

Figure 6.18: Example position reconstructions of localized event distributions from sealed sources. Points from data, dotted line from simulation.

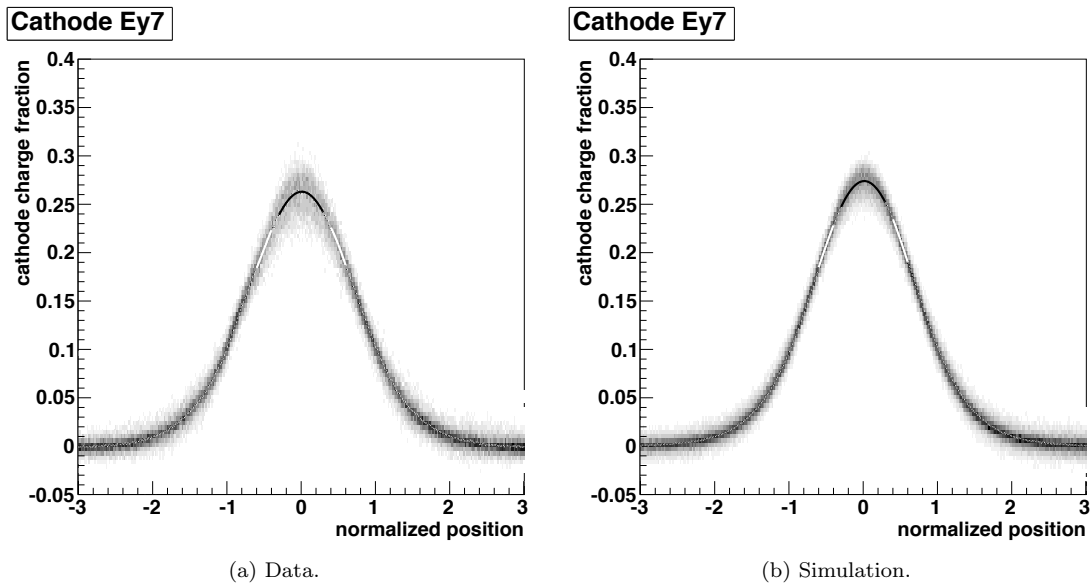


Figure 6.19: Cathode charge signal distribution from beta decay data and matching simulation.

approximation ([Mat91] Eq. 5.40) for the ratio of cathode charge density to anode charge (integrated along an infinite narrow strip at distance $\lambda \equiv x/h$ from the charge and width $d\lambda$) is

$$\Gamma(\lambda)d\lambda = \frac{\pi}{8} \operatorname{sech}^2\left(\frac{\pi\lambda}{2}\right) d\lambda. \quad (6.19)$$

An improved empirical approximation accounting for anode wire radius effects is ([Mat91] Eqs. 5.41–5.43):

$$\Gamma(\lambda) = K_1 \frac{1 - \tanh^2 K_2 \lambda}{1 + K_3 \tanh^2 K_2 \lambda}; \quad K_1 = \frac{K_2 \sqrt{K_3}}{4 \tan^{-1} \sqrt{K_3}}; \quad K_2 = \frac{\pi}{2} \left(1 - \frac{1}{2} \sqrt{K_3}\right), \quad (6.20)$$

where K_3 is a parameter determined from the wirechamber geometry, which may be read off [Mat91] Figure 5.2. For the UCNA wirechambers with anode spacing s : $h/s = 3.94$ and anode radius r_a : $r_a/s = 0.002$, $K_3 \approx 0.18$. The FWHM of the resulting distribution is ([Mat91] Eq. 5.44):

$$\text{FWHM} = \frac{4 \tanh^{-1} 1/\sqrt{2+K_3}}{\pi} \frac{1}{1 - \sqrt{K_3}/2} h \approx 1.33h \quad (6.21)$$

(note that, in the limiting case for a dense anode plane, $h/s \rightarrow \infty$, $K_3 = 0$ and $\text{FWHM} \approx 1.12h$). This point-charge response must be further convolved by the charge spread over the circle of the Larmor spiral, summed over the four-wire-group cathode segments, and combined with a stochastic noise contribution to match the observed cathode pedestal spread in the data. Charge distributions produced by this method are visually in good agreement with the data, as shown in Figure 6.19.

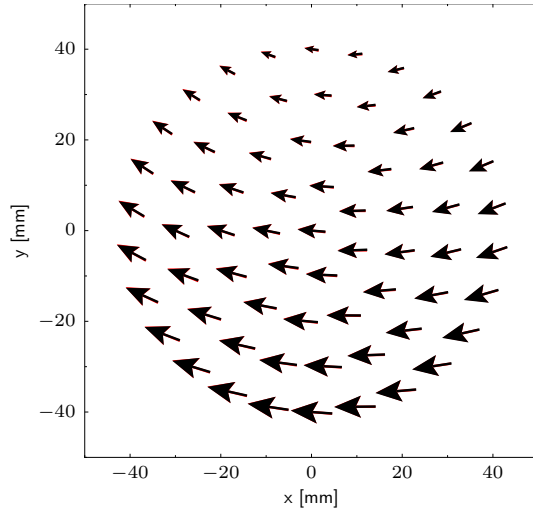
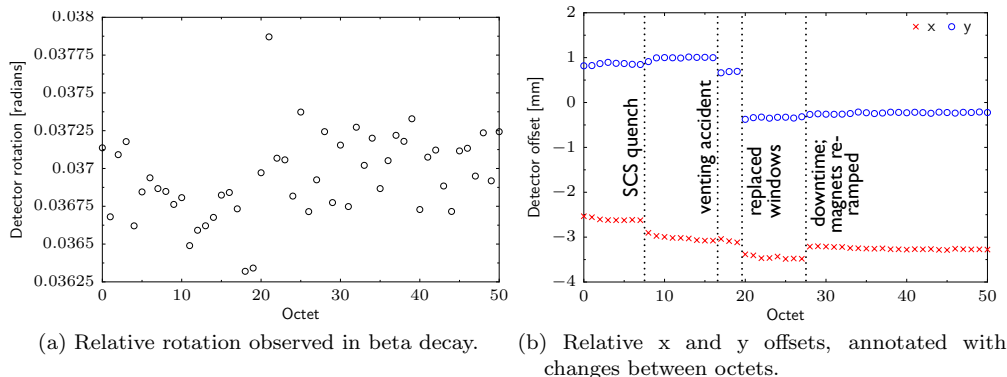


Figure 6.20: E-W wirechamber position relative differences, averaged over 2010 beta octets.



(a) Relative rotation observed in beta decay. (b) Relative x and y offsets, annotated with changes between octets.

Figure 6.21: E-W wirechamber position relative differences by beta decay octet.

6.4 East-West position offsets

Wirechamber position reconstruction, as discussed above, provides event positioning relative to the cathode plane wires in each detector. The entire detector units, however, might be imperfectly aligned with the spectrometer axis.

6.4.1 Offset measurement

Type I backscatter events can be used to map relative displacement between the two detectors. Using the 2010 beta decay data, Figure 6.20 shows the relative displacement mapped out as a function of position using the Type I backscatter data. The displacement can be parametrized, to ~ 0.1 mm precision, by a simple rotation and shift between detectors.

There are easily sufficient backscatter statistics to map out this offset for each beta decay octet. Figure 6.21 shows the rotation and shift components extracted for each 2010 octet. The rotation appears constant within measurement fluctuations; this is likely determined by the rotationally rigid mounting of the detectors. The x and y offsets, however, are inclined to shift by up to 1 mm when

changes are made to the detectors. The y offset is somewhat of a free parameter when installing the detectors, which are aligned with flange bolt-holes using a vertical lift, which is unlikely to result in < 1 mm repeatability in results. The x offset appears to vary less with detector installation changes; this is more rigidly mechanically constrained, though there is conceivably fractional-millimeter variation possible in the installation of new cathode planes. However, the x offset (and, to a lesser extent, the y offset) also changes when the spectrometer magnetic field is re-ramped. Variations in field uniformity between field ramps may be distorting the field line paths between the two detector faces.

6.4.2 Offset effects

Detector offsets impact the fiducial volume of observable events.

Offsets relative to the decay trap might include more events involving interaction with the decay trap walls and collimator. Slight misalignments relative to the decay trap will be hard to diagnose from the data. Gross misalignments, however, would be evidenced by the position distribution of Type 0 events being cut off along one edge. As this is not seen in the data, the level of misalignment with the decay trap is small; an event radius cut that excludes events in the region cut off by the wirechamber entrance window's own collimation will also exclude regions where decay trap collimation may be interfering.

Relative offsets between the detectors will impact the fiducial volume for backscatter events, restricting them to a smaller “almond-shaped” region where coverage of the two detectors overlaps, with backscatters in the non-overlapping crescents being seen as Type 0. The “almond shaped” distribution of observed backscatter events is readily seen in the data. One approach to dealing with this effect would be to restrict data analysis to the reduced fiducial region in the overlap between the detectors — which also discards the statistics of all potentially useful non-backscatter events outside the overlap region. Alternatively, the measured detector offset can be incorporated into the Monte Carlo geometry for simulating beta decay, folding the fiducial effect into the other Monte Carlo backscatter corrections. This was the approach taken for the 2010 data. With only the relative offset between the detectors known, the detectors in the MC model were rotated/offset in opposite directions from their nominal positions to evenly “split the difference” of the total offset.

Chapter 7

Asymmetry extraction and uncertainties

Having calibrated the detectors, attention may be turned to measuring some quantity of greater interest with them. This chapter describes the analysis of collected neutron beta decay data to extract the beta decay asymmetry A_0 , for the 2010 UCNA dataset. While extracting some value for the asymmetry from the data is quite straightforward, producing a value with high precision and accuracy takes more care; the bulk of analysis effort consists in determining corrections and uncertainties to the extracted value. Table 7.1 shows corrections and uncertainties from the published analysis of the UCNA 2010 dataset [Men+13], providing a framework for the major topics of discussion in the following sections.

7.1 Asymmetry calculation from data

7.1.1 Super-ratio asymmetry

The simplest measurement of the asymmetry would be to count the number of decays N_E , N_W observed on the two sides of the detector from polarized neutrons, and form the “bonehead asymmetry”

$$A_{\text{BH}} = \frac{N_E - N_W}{N_E + N_W}. \quad (7.1)$$

Were we to have flawless detectors with perfect efficiency, this approach would be satisfactory, and this thesis far shorter. Since perfect detectors are unavailable, a more robust approach that minimizes sensitivity to detector idiosyncrasies is necessary. By measuring the decay asymmetry separately for neutrons in both polarization states (denoted “off” and “on” according to the state of the neutron spin flipper), while keeping the detectors (presumably) the same, a “super ratio asymmetry” can be formed:

$$R \equiv \frac{N_E^- N_W^+}{N_W^- N_E^+}, \quad A_{\text{SR}} \equiv \frac{1 - \sqrt{R}}{1 + \sqrt{R}}. \quad (7.2)$$

The super-ratio R perfectly cancels out any factors of the counts N_s^\pm , which are common to both detectors (such as individual detector efficiencies), and any factors which are common to both spin states.

Systematic	corr. (%)	unc. (%)	details in
Polarization	+0.67	±0.56	7.2
$\Delta_{\text{backscattering}}$	+1.36	±0.34	7.3.2
Δ_{angle}	-1.21	±0.30	7.3.3
Energy reconstruction		±0.31	7.4.1.3
Gain fluctuation		±0.18	7.4.2.1
Field non-uniformity	+0.06	±0.10	7.3.4
ϵ_{MWPC}	+0.12	±0.08	7.3.5
Muon veto efficiency		±0.03	7.5.5.1
UCN-induced background	+0.01	±0.02	7.5.6
$\sigma_{\text{statistics}}$		±0.46	
Theory contributions			
Recoil order	-1.71	±0.03	7.6.1
Radiative	-0.10	±0.05	7.6.2

Table 7.1: UCNA 2010 asymmetry corrections and uncertainties (as fractions of A_0) as published in [Men+13], with cross-reference to relevant sections of this work.

The differential observed counts for decay beta electrons emitted at kinetic energy E into solid angle Ω will be

$$dN_s^\pm(E, \Omega) = c^\pm \eta_s(E, \Omega) S^\pm(E, \Omega) dE d\Omega, \quad (7.3)$$

where $\eta_s(E, \Omega)$ is each detector's efficiency for counting decay beta electrons produced at E, Ω , c^\pm is an overall factor for the total number of decays produced in each spin flipper state (which cancels out in R), and $S^\pm(E, \Omega) dE d\Omega$ is the physics differential decay rate for neutrons polarized by the \pm spin flipper states:

$$S^\pm(E, \Omega) = S(E)(1 + \langle P^\pm \rangle \beta A(E) \cos \theta), \quad (7.4)$$

where $S(E)$ is the unpolarized beta decay spectrum, $\langle P^\pm \rangle$ is the average polarization in each spin flipper state, and β is the electron's relative velocity $\beta = v/c$.

The utility of the super-ratio becomes apparent in the limit of three simplifying approximations:

- the detector can (perfectly) determine the energy of each event,
- the detector efficiency $\eta_s(E, \Omega)$ is 0 for electrons initially heading away from the detector, and $\eta_s(E)$ for electrons initially heading towards the detector, and
- the two polarizations are the same aside from a sign flip, $\langle P^\pm \rangle = \pm \langle P \rangle$.

In this simplified scheme, we may integrate out solid angle Ω to get

$$dN_s^\pm(E) \approx 4\pi c^\pm \eta_s(E) S(E) \left[1 \pm_s \frac{\pm \langle P \rangle}{2} \beta A(E) \right] dE, \quad (7.5)$$

where \pm_s is + for $s = \text{East}$, $-$ for West . Figure 7.1 shows a simulation for the expected form of $\eta_s(E)$. Let

$$S_s(E) \equiv \eta_s(E) S(E), \quad S_s^\pm(E) \equiv S_s(E) \left[1 \pm_s \frac{\pm \langle P \rangle}{2} \beta A(E) \right] \quad (7.6)$$

denote the unpolarized and polarized energy spectrum seen by each detector, including efficiency effects. Then, forming the super-ratio as a function of energy, $S_s(E)$ cancels out, eliminating the

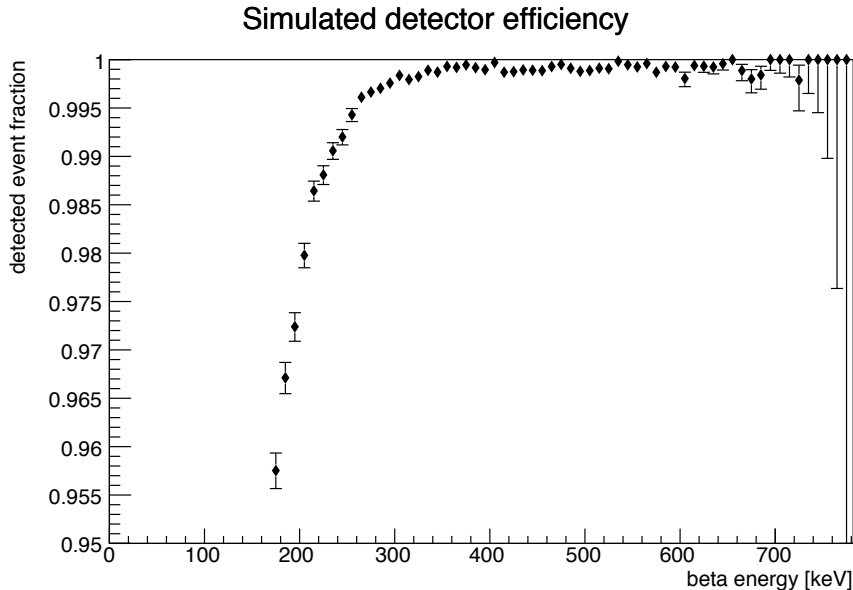


Figure 7.1: Simulated detector efficiency $\eta_s(E)$, showing the probability for neutron decay events to produce observed “beta-like” events in the UCNA detectors.

effects of detector efficiency:

$$R(E) \approx \frac{\left[1 - \frac{1}{2} \langle P \rangle \beta A(E)\right]^2}{\left[1 + \frac{1}{2} \langle P \rangle \beta A(E)\right]^2} \Rightarrow A_{\text{SR}}(E) \approx \frac{1}{2} \langle P \rangle \beta A(E). \quad (7.7)$$

Deviations from the simplifying assumptions are treated as corrections (or uncertainties) to the super-ratio asymmetry, as described in the following sections.

Note that a related construction proposed by Kevin Hickerson [Hic12] for analysis of unpolarized spectrum shapes is the “super-sum”

$$\Sigma \equiv \sqrt{N_E^- N_W^+} + \sqrt{N_W^- N_E^+}, \quad (7.8)$$

which results in cancellation of asymmetric contributions. This provides a useful method for combining the four detector side and spin flipper state distributions, for any observable variable, when the asymmetric component is not of interest.

7.1.1.1 Incorporation of backscatter data

In the calibrated dataset, events have been tagged by estimated backscatter topology (Type 0 “correct” events, and Type I, II, and III backscatters, as described in subsection 3.3.2). The straightforward approach is to use this information to assign each event to its most likely initial detector side when forming the energy spectra N_s^\pm entering the super ratio, coming closest to the “perfect detectors” limit requiring the least correction. That is, all events but Type II are assigned to the energy spectrum for the side of their primary scintillator, while Type II backscatters are swapped to the opposite detector side; this is indeed the approach taken for producing the final result. However, making alternate choices for the handling of backscatter data provides a test of the quality of

(primarily Montecarlo-based) corrections. Ideally, no matter how the events are assigned, the subsequent corrections procedure will account for the differences and arrive at the same answer (modulo statistical fluctuations).

Thus, as a test of corrections consistency (requiring the corrections to properly deal with the differing event populations comprising each identified event class), asymmetries can be formed for a variety of “analysis choices” for the data, typically named by letters in UCNA Collaboration internal notes:

- A:** All event types used; Type II+III events left unseparated and assigned to their primary scintillator side.
- B:** Only Type 0 and I events are used (assigned to primary trigger side), discarding II/III.
- C:** All event types used; Type II/III events separated and assigned to most likely sides.
- D:** Type 0 events alone are used, discarding all backscatters.
- F:** Type I backscatters only.
- G:** Type II/III backscatters only, unseparated, on primary scintillator side.
- H:** Type II/III backscatters only, separated and assigned to most likely detector side.
- J:** Type II backscatters only.
- K:** Type III backscatters only.

Choices **E** and **I** have been used in prior analyses to refer to the use of a “likelihood” assignment of II/III events fractionally to both sides. However, this method increases the likelihood of misidentifying initial directions over the usual binary II/III cut, and is of little independent value to the analysis (falling somewhere between the separated and unseparated II/III analysis choices). Choice **C**, which uses all recorded events with the most likely correct initial direction identification, is used for the final answer.

7.1.2 Extracting A_0 from A_{SR}

Having formed the super-ratio $A_{\text{SR}}(E)$ from the observed beta decay energy spectra for each detector and spin flipper state, we now wish to extract the model parameter A_0 . To do so, we apply whatever corrections $\Delta_1, \Delta_2, \dots$ should be needed to convert A_{SR} into the “idealized” form $\frac{1}{2}A_0\beta$:

$$A_{\text{SR}}^{\text{corr}}(E) \equiv (1 + \Delta_1 + \Delta_2 + \dots)A_{\text{SR}}(E) \approx \frac{1}{2}A_0\beta. \quad (7.9)$$

Then, dividing out the factor $\frac{\beta}{2}$, a statistically weighted average of the results extracts the desired measured parameter A_0^{meas} .

7.1.2.1 Statistical weighting and energy window

The most general scheme for determining optimal weighting would be to apply the formalism of Appendix B, treating each energy bin of $\frac{2}{\beta}A_{\text{SR}}^{\text{corr}}$ as a measurement of A_0 , with uncorrelated statistical and fully correlated systematic errors. This would “naturally” de-weight results from the extreme ends of the spectrum, with small statistics and large systematic uncertainties.

However, for clarity, a simpler weighting scheme is adopted, using data only from within a predetermined energy range window. Although systematic errors (correlated across all energies) may outweigh combined statistical uncertainty over the energy window, over smaller sections of the data (such as an individual 10 keV-wide energy bin), a reasonable approximation is that the statistical uncertainty will overwhelmingly predominate. Thus, a near-optimal weighting scheme will be $1/\sigma_{\text{stat}}^2$ for the results from each energy bin.

The analysis energy window is selected (before unblinding) by minimizing the combined statistical and systematic error as a function of the lower and upper bounds, assuming $1/\sigma_{\text{stat}}^2$ weighting will be applied to each data point. For the 2010 dataset, an analysis window of 220 keV to 670 keV was selected.

7.1.2.2 Extracted A_0 , corrections, and uncertainties

In actual practice, σ_{stat}^2 can be taken from the observed data; but, to good approximation everywhere but near $E = 0$ or the decay endpoint, the statistical uncertainty on $A_{\text{SR}}^{\text{corr}}(E)$ will be proportional to \sqrt{N} statistics of an ideal unpolarized beta spectrum, $1/\sigma_{\text{SR}}^2 \propto S(E)$. So, after dividing out $\frac{\beta}{2}$, approximately optimal weights will be $\frac{\beta^2}{4}S(E)$. So, averaging $\frac{2}{\beta}A_{\text{SR}}^{\text{corr}}$ over an energy window E_0 to E_1 ,

$$A_0 \approx A_0^{\text{meas}} \equiv \frac{\int_{E_0}^{E_1} \frac{\beta}{2} S(E) A_{\text{SR}}^{\text{corr}}(E) dE}{\int_{E_0}^{E_1} \frac{\beta^2}{4} S(E) dE} \quad (7.10)$$

$$\langle \Delta_i \rangle \equiv \frac{\int_{E_0}^{E_1} \frac{\beta}{2} S(E) \Delta_i(E) A_{\text{SR}}(E) dE}{A_0^{\text{meas}} \int_{E_0}^{E_1} \frac{\beta^2}{4} S(E) dE} \approx \frac{\int_{E_0}^{E_1} \beta^2 S(E) \Delta_i(E) dE}{\int_{E_0}^{E_1} \beta^2 S(E) dE},$$

where $\langle \Delta_i \rangle$ indicates the contribution of Δ_i averaged over the energy window. Total averaged uncertainties may be calculated in the same way as the correction contributions $\langle \Delta_i \rangle$.

7.1.2.3 Statistical sensitivity approximation

An analytical approximation for the statistical sensitivity of A_0 measurements provides guidance on how measured beta decay counts translate into statistical sensitivity. Consider a measurement in which the number of events measured in some energy bin dE for each detector side and spin flipper state is

$$N_s^\pm(E) dE \approx \left(1 \pm_s \frac{\pm\beta}{2} A_0 \right) \frac{N^\pm}{2} S(E) dE; \quad \int_0^{E_0} S(E) dE \equiv 1, \quad (7.11)$$

where $S(E)$ is the (normalized) unpolarized beta decay spectrum shape, so there are N^\pm total events on both sides of the detector for the two spin flipper states. The exact form is given by replacing $\frac{\beta}{2}A_0$ and $S(E)$ by versions incorporating all modifications from theory and detector effects. Propagating

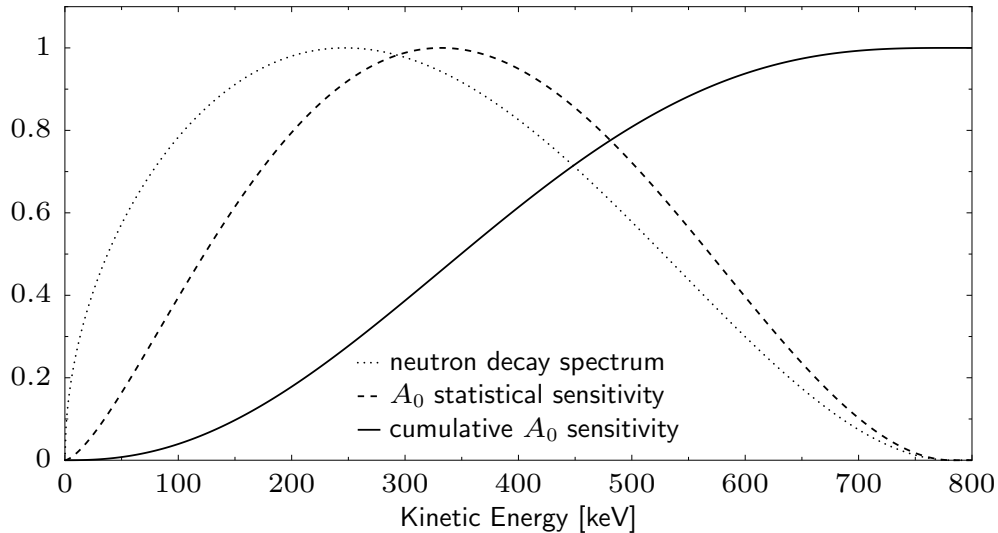


Figure 7.2: Neutron beta decay statistical sensitivity for extracting asymmetry A_0 . Beta decay spectrum $S(E)$, A_0 sensitivity-weighted spectrum $\beta^2 S$, and cumulative sensitivity $\int_0^E \beta^2 S dE$ shown, all normalized to maximum of 1.

the corresponding $dN_s^\pm = \pm\sqrt{N_s^\pm}$ counting statistics uncertainties through the procedure, the uncertainty on A_0^{meas} for that energy bin will be

$$\begin{aligned} \frac{\partial R}{\partial N_s^\pm} &= \pm_s \frac{\mp R}{N_s^\pm} \Rightarrow dR \approx \pm R \sqrt{\sum_{s,\pm} \frac{1}{N_s^\pm}} \approx \pm 2 \sqrt{\frac{1}{S(E)} \sum_{\pm} \frac{1}{N^\pm}} \\ R &\approx 1 - 2\beta A_0^{\text{meas}} \Rightarrow dA_0^{\text{meas}} \approx -\frac{1}{2\beta} dR \approx \pm \frac{1}{\beta} \sqrt{\frac{1}{S(E)} \sum_{\pm} \frac{1}{N^\pm}}. \end{aligned} \quad (7.12)$$

Note that since the the statistical uncertainty should not depend on the sign of A_0 , this expression is good to order A_0^2 , though terms of order A_0 were disregarded in its derivation. Combining energy bins with $\frac{1}{\sigma^2}$ weights, the total statistical uncertainty on A_0^{meas} will be

$$\sigma_{\text{stat}} = \pm \left[\int \frac{1}{\sigma^2} \right]^{-1/2} \approx \pm \left[\int \beta^2 S(E) dE \right]^{-1/2} \sqrt{\sum_{\pm} \frac{1}{N^\pm}} \approx \pm 1.34 \sqrt{\sum_{\pm} \frac{1}{N^\pm}} \quad (7.13)$$

(where the coefficient 1.34 comes from integrating over the whole spectrum; for 220 keV to 670 keV, this becomes 1.53). Counts from the beta decay spectrum $S(E)$ contribute to the measurement of A_0 with a weighting factor of β^2 . Figure 7.2 shows the beta spectrum and its β^2 -weighted sensitivity to measuring A_0 . Figure 7.3 shows the counts N^\pm accumulated during the 2010 run period.

7.2 Polarization

The details of polarization analysis are a dissertation on their own [Hol12; Hol+12; Hol12]; only a brief summary will be given here. Polarization is measured by a combination of “*in situ*” measurement runs intended to count wrong-polarization neutrons present during asymmetry data collection,

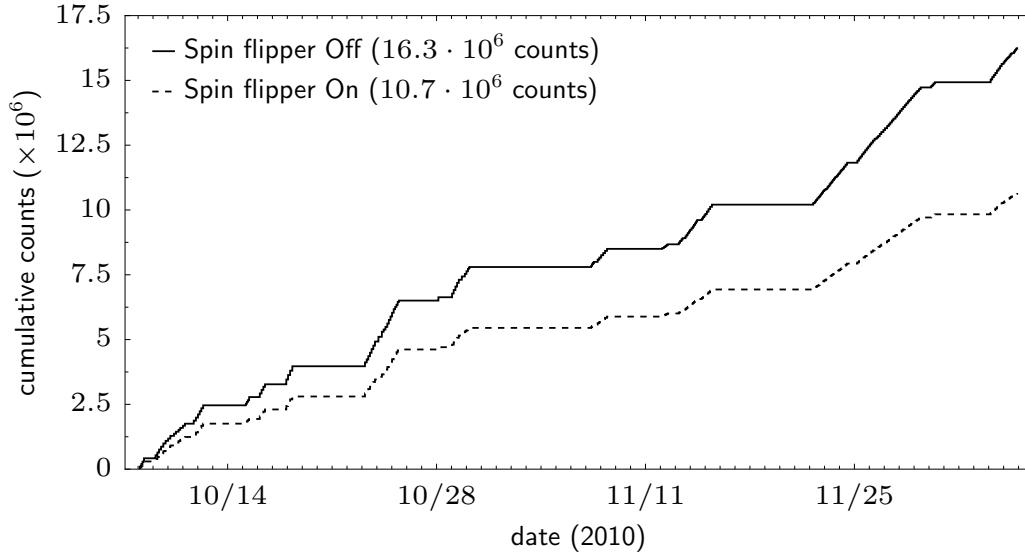


Figure 7.3: Cumulative neutron decays collected as a function of time in the 2010 dataset (background-subtracted counts for all energies).

and “*ex situ*” runs providing additional details about neutron transport necessary to interpret the *in situ* results.

7.2.1 Measurement procedure

An *in situ* depolarization run was taken immediately after each beta decay foreground run, proceeding as follows. The influx of new UCN is stopped by turning off the proton beam and closing the gate valve leading to the SD₂ UCN source. At the same time, the UCN guide path is changed at the “switcher” to dump neutrons into a UCN detector. Correctly-polarized neutrons from the decay trap are able to transit the AFP to the switcher detector, providing a measure of the decay trap neutron population. Depolarized neutrons in the decay trap, however, are blocked by the AFP 7 T field region. After ~ 25 s, the spin flipper state is reversed, allowing previously-trapped depolarized neutrons to be counted at the switcher detector.

Interpretation of the event counts observed in each *in situ* depolarization measurement requires additional information to understand factors such as the transport efficiency of UCN from decay trap to switcher detector, the loss rate of depolarized neutrons during the ~ 25 s correct-polarization unloading, and counts from correct-polarization UCN mixed with the depolarized UCN after the flipper is toggled. A variety of specially-designed *ex situ* runs provide this information, including “reload” runs where the spin flipper is toggled for a few seconds to intentionally inject wrong-polarization neutrons into the system.

7.2.2 2010 polarimetry results

For the 2010 dataset polarization analysis, the runs were broken up into two groups denoted 2010_I and 2010_{II}, before and after the wirechamber damage in the venting accident, which may have changed UCN polarization and transport parameters by depositing hydrocarbon gunk on the guides. Table 7.2 shows the polarizations extracted for each group of runs and spin flipper state. Some of

Data Set	Polarization
2010 _I spin flipper off	1.0013(16) _{stat} (54) _{sys}
2010 _I spin flipper on	0.9900(12) _{stat} (53) _{sys}
⇒ 2010 _I $\langle P \rangle$	0.9957(10) _{stat} (54) _{sys}
2010 _{II} spin flipper off	0.9920(52) _{stat} (78) _{sys}
2010 _{II} flipper on	0.9884(37) _{stat} (31) _{sys}
⇒ 2010 _{II} $\langle P \rangle$	0.9902(32) _{stat} (55) _{sys}

Table 7.2: Polarizations determined for the two portions of the 2010 dataset [Hol12]; individual spin flipper states, and average polarizations $\langle P \rangle$ over both spin flipper states.

the “reload” runs were shared between the final 2009 UCNA geometry and nominally identical 2010_I, since an insufficient number of such runs had been taken during the 2010_I period. Systematic uncertainties are treated as 100% correlated between the measurements.

7.2.3 Impact on asymmetry

Note that in cases where the polarization differs by more than a sign flip between spin flipper states, we may write $\langle P^\pm \rangle \equiv \pm(\langle P \rangle \pm \delta)$. Then, the dependence of the super ratio on the polarization goes as

$$R \approx \frac{[1 - \frac{1}{2}(\langle P \rangle + \delta)\beta A][1 - \frac{1}{2}(\langle P \rangle - \delta)\beta A]}{[1 + \frac{1}{2}(\langle P \rangle - \delta)\beta A][1 + \frac{1}{2}(\langle P \rangle + \delta)\beta A]} = \frac{[1 - \frac{1}{2}\langle P \rangle \beta A]^2}{[1 + \frac{1}{2}\langle P \rangle \beta A]^2} + O\left[\left(\frac{\beta}{2}A\delta\right)^4\right]. \quad (7.14)$$

Thus, the single mean polarization between the two spin flipper states may be generally used in place of separate spin flipper polarization factors, as the contribution from the on/off difference is very small. Then the correction to the measured A_{SR} for imperfect polarization is a constant factor of $1/\langle P \rangle$.

7.3 Montecarlo Corrections

Corrections for modifications to the observed decay spectra from missed backscatters, energy losses in electron transport, and entirely lost events (and the interaction of these terms with detector response) are made via Montecarlo simulations, processed through the detector response model developed in calibrations and analyzed identically to the data (with additional ability to track important but unobservable quantities). The most straightforward MC correction would be to divide out the super-ratio MC asymmetry:

$$A_0^{\text{meas}}(E) = A_{\text{SR}}^{\text{meas}}(E) \cdot A_0^{\text{PDG}}/A_{\text{SR}}^{\text{sim}}(E), \quad (7.15)$$

where A_0^{PDG} is the PDG value for the asymmetry incorporated into the MC simulation. This procedure is simple and effective, and will correct for all affects (accurately) included in the MC. However, in this approach, the MC remains an opaque “black box” correction, yielding little physical insight into the cause for correction. Thus, the UCNA collaboration has adopted a scheme of subdividing the MC correction into pieces attributed to various physical causes [Pat+09; LMH+10; Pla+12; Men+13] (which add up to the same total effect of the simple MC correction). These individual

portions then allow the possibility of separately tweaking one aspect of the MC correction (multiplying by a non-unity factor) to account for observed deficiencies of the Montecarlo in particular areas (such as systematic under-prediction of backscattering).

The two main divisions of the MC correction are “backscattering” (subsection 7.3.2) and “angle/energy acceptance” (or “ $\langle\beta \cos \theta\rangle$ ”, subsection 7.3.3). The first corrects for missed backscatters in the observed data; ideally, correcting the result to what would be seen if every recorded event was assigned to the side of its true initial direction. The second accounts for how events are moved around in the energy spectrum, or lost from the data entirely, by (pitch-angle-dependent) energy losses. A third small MC correction accounts for the deflection of high-pitch-angle electrons by nonuniformities in the spectrometer magnetic field.

7.3.1 Extraction of MC corrections

For the 2010 analysis, a slightly modified approach for determining corrections was adopted, incorporating observed data spectra where possible in the corrections extraction, while using MC spectra as necessary for all “hidden” parameters not observable in the data. This generally results in minute differences versus using MC spectra throughout, as most of the resulting correction still comes from the MC “hidden contributions” with the particular shape of the incorporated data spectra contributing small higher-order alterations. The primary effect is to automatically scale corrections associated with particular backscatter event types with observed event type fractions rather than fractions predicted by MC.

The general scheme is as follows. We begin with observed energy spectra $N_{s,i}^{\pm}(E)$ for each detector side, spin flipper state, and observed event type $i \in \{0, 1, 2, 3\}$. Summing these together into a total event spectrum of all event types (according to a particular backscatter analysis choice) $N_s^{\pm}(E)$, the uncorrected super-ratio $A_{\text{SR}}^{\text{dat}}$ is calculated. MC predictions are then applied to correct some particular “deficiency” of the data, such as the fraction of misidentified events in a particular event type, producing corrected data spectra $N_{s,i}^{\pm'}$. Using the corrected spectra, a new super-ratio $A_{\text{SR}}^{\text{dat}'}$ is calculated; then, the amount of correction Δ' is identified from the difference between corrected and uncorrected super-ratios,

$$1 + \Delta' \equiv \frac{A_{\text{SR}}^{\text{dat}'}}{A_{\text{SR}}^{\text{dat}}}. \quad (7.16)$$

This procedure is then repeated to correct the next “deficiency” on top of the previous, producing spectra $N_{s,i}^{\pm''}$ and asymmetry $A_{\text{SR}}^{\text{dat}''}$, and corresponding correction factor $(1 + \Delta'')$ from $A_{\text{SR}}^{\text{dat}'}$ to $A_{\text{SR}}^{\text{dat}''}$, etc. The process is continued until all correction procedures that would be necessary to bring the MC super-ratio into “ideal” form $A_{\text{SR}}^{\text{sim}''''} = \frac{\beta}{2} A_0$ have been performed on the data spectra.

7.3.2 Backscattering

The backscatter correction, labeled Δ_2 or $\Delta_{\text{backscattering}}$ in UCNA Collaboration publications, corrects the observed asymmetry for missed backscattering in observed counts. Δ_2 is further subdivided for the missed backscatter contributions from each identified event type, $\Delta_{2,i}$ for $i \in \{0, 1, 2, 3\}$ for Type 0,I,II,III events.

For each spin flipper state and event type (suppressing the associated super/sub-scripts \pm, i for notational compactness), the MC predicts the total number N_s^{MC} of events detected on each detector

side s , and the subset of these \tilde{N}_s^{MC} which were initially heading towards the opposite detector side. This indicates the misidentified event fraction on each detector side $m_s \equiv \tilde{N}_s^{\text{MC}}/N_s^{\text{MC}}$, which is then used to “unscramble” the observed event counts N_s in the data to recover the count of observed events $N'_E = N_E - \tilde{N}_E + \tilde{N}_W$ which *should have been* assigned to the East side (likewise for West), assuming the data events are mixed up by the same amount as the MC:

$$N'_E \equiv (1 - m_E)N_E + m_W N_W; \quad N'_W \equiv (1 - m_W)N_W + m_E N_E. \quad (7.17)$$

Applying this correction sequentially for each individual event type $i \in \{0, 1, 2, 3\}$, and noting the differential changes in the super-ratio asymmetry, produces the chain of backscattering corrections $(1 + \Delta_2) = (1 + \Delta_{2,3})(1 + \Delta_{2,2})(1 + \Delta_{2,1})(1 + \Delta_{2,0})$.

The Δ_2 corrections used for the 2010 data analysis are shown in Figure 7.4. Unsurprisingly, the most common events in the data (Type 0) contribute the majority of the correction for missed backscatters. Lower energy events, requiring correspondingly less momentum transfer to get turned around, require a greater correction for the resulting dilution of the asymmetry from missed backscatters. Type I backscatters contribute little to the correction — on their way to reaching the first scintillator, they are similarly likely to surreptitiously backscatter as Type 0 events; their overall smaller number produces a correspondingly tiny correction. Type II/III events, however, because of their significant probability of misidentification with each other, contribute more significantly to the correction.

7.3.2.1 Comparison to prior analyses

Note that the 2010 analysis Δ_2 of +1.36% is somewhat increased over the +1.09% value used for previous analysis of the 2009 data in the same detector configuration [LMH+10; Pla+12]. Some of this is due to different choice of analysis window — the 2009 data was analyzed over 275 keV to 625 keV; over this range, the 2010 analysis correction would be $\Delta_2 = +1.24\%$. The remainder of the difference comes from updates to the MC simulation, which improved agreement with observed backscatter fractions compared to 2009.

UCNA Collaboration analyses prior to the 2010 dataset partially compensated for GEANT4’s systematic under-prediction of backscatter rates, by applying a scaling factor $f_{\text{thin}} = 1.6$ to the MC prediction of Type 0 missed backscatters entering Δ_2 [Pla+12], based on observed discrepancies in predicting Type II/III backscatter rates off the “thin” wirechamber gas. Note that the small-angle scattering producing missed backscatters from the decay trap foils comes from a somewhat different regime of the MC physics model than large-angle observable backscattering of more forward-directed events at the detectors, so the observable backscatter discrepancy is an imperfect guide to missed backscattering from the decay trap foils. With the decreased data/MC backscatter discrepancy observed in the present analysis (subsubsection 4.8.2.1), these correction factors are no longer applied.

7.3.3 Angle and energy acceptance

Having nominally corrected the spectra to only contain “proper” events for each detector side via the Δ_2 correction, the other main component of MC correction is accounting for the fact that events tallied in a particular energy bin neither necessarily originated at that energy, nor uniformly sample

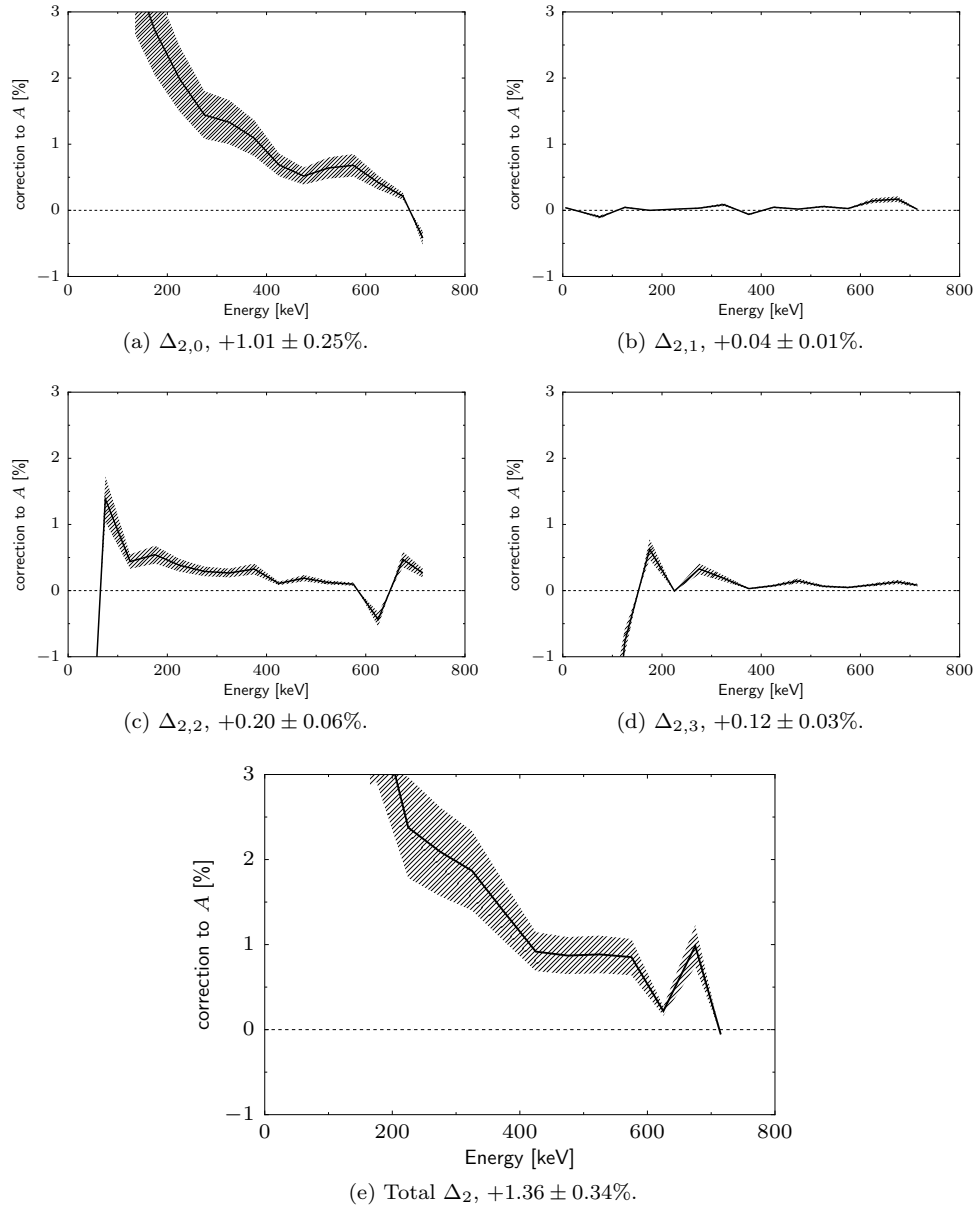


Figure 7.4: MC Backscattering corrections for 2010 geometry; captions indicate statistics-weighted contribution over 220 keV to 670 keV analysis window.

the space of initial pitch angle θ . As a result, the events will not follow a distribution proportional to $1 \pm \frac{\beta}{2} A_0$. The Δ_3 correction (as it is called in UCNA Collaboration papers) is intended to correct for this effect.

Each E_{recon} bin will have some efficiency $\eta(E_{\text{true}}, \theta)$ for counting events. Treating each energy bin i as a separate “detector” with its own efficiency $\eta_s^i(E, \Omega)$, the actual counts in each spin flipper state will be (from Equation 7.3 and Equation 7.4):

$$N_{s,i}^{\pm} = c^{\pm} \iint \eta_s^i(E, \Omega) S(E) (1 + \langle P^{\pm} \rangle \beta A(E) \cos \theta) dE d\Omega. \quad (7.18)$$

Since the factor of c^{\pm} cancels out in the super-ratio between the detector sides in the same spin flipper state, along with any normalization factor included for both spin flipper states, this is equivalent to forming the super ratio from normalized counts

$$\bar{N}_{s,i}^{\pm} \equiv 1 + \langle P^{\pm} \rangle \frac{\iint \eta_s^i(E, \Omega) S(E) \beta A(E) \cos \theta dE d\Omega}{\iint \eta_s^i(E, \Omega) S(E) dE d\Omega} \equiv 1 + \langle P^{\pm} \rangle \langle \beta A(E) \cos \theta \rangle_{s,i}. \quad (7.19)$$

The quantity $\langle \beta A(E) \cos \theta \rangle_{s,i}$ for each energy bin is extracted from simulation by taking the average value of $\beta A(E) \cos \theta$ (using the true energy and angle available from simulation) over all events from unpolarized neutron decay simulated to be detected in that particular reconstructed energy bin, *including* re-assignment to their correct true side, since Δ_2 has already corrected the counts to reflect this. Since the usual MC procedure is to throw an unpolarized beta spectrum and include the asymmetry in the weighting factor for each event, this averaged quantity is calculated over the normal course of simulations using the same events except without the asymmetry weighting.

Now, correcting the counts in each bin of the Δ_2 -corrected data spectra to

$$N_{s,i}^{\pm \prime} \equiv \frac{1 \pm \frac{\pm_s \beta}{2} A(E)}{1 \pm \langle \beta A(E) \cos \theta \rangle_{s,i}} N_{s,i}^{\pm} \quad (7.20)$$

and computing the resulting change in super-ratio asymmetry A'_{SR} gives the correction $1 + \Delta_3 \equiv \frac{A'_{\text{SR}}}{A_{\text{SR}}}$. Note that the denominator substitutes ± 1 as an approximation for $\langle P^{\pm} \rangle$; this leaves polarization effects uncorrected by Δ_3 . At this point, the corrections procedure should have adjusted the asymmetry into the form

$$(1 + \Delta_3)(1 + \Delta_2) A_{\text{SR}} \approx \langle P \rangle \frac{\beta}{2} A(E), \quad (7.21)$$

modulo any remaining smaller corrections such as for magnetic field uniformity and wirechamber efficiency, below.

Figure 7.5 shows Δ_3 for 2010, and the combined $\Delta_2 + \Delta_3$. The overall impact of energy/angle acceptance effects is to increase the measured asymmetry (requiring a negative correction of -1.21 ± 0.30 over the analysis energy window). At the middle to high energy side of the spectrum, high-pitch-angle (low asymmetry) events are more likely to be lost (entirely, or shifted down to low energies). At low energies, the asymmetry is further increased by the high-energy-loss tails of events originating at higher energy (thus higher typical βA).

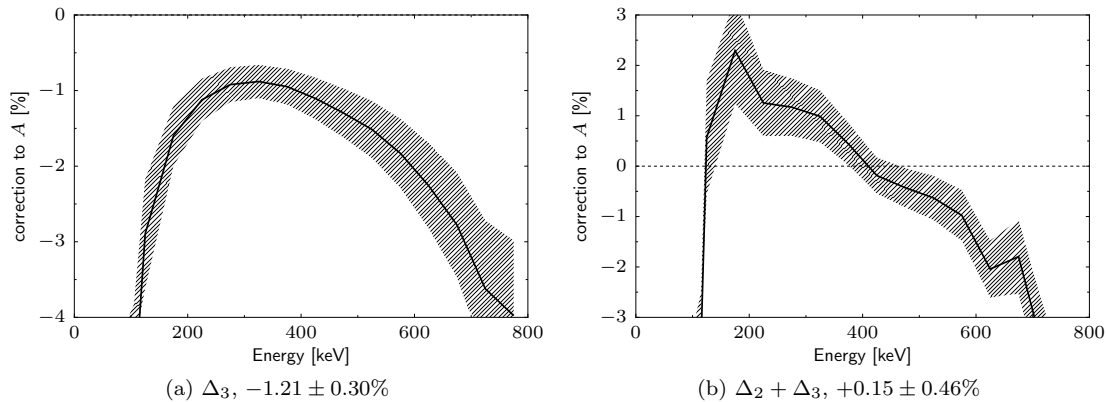


Figure 7.5: MC acceptance correction Δ_3 and combined $\Delta_2 + \Delta_3$ for 2010 geometry; captions indicate statistics-weighted contribution over 220 keV to 670 keV analysis window.

7.3.4 Magnetic field

As discussed in subsection 4.2.1, charged particles starting in field B_0 will be mirrored by a higher field B_M , depending only on their initial pitch angle

$$\frac{B_M - B_0}{B_0} = \left(\frac{p_{\parallel}}{p_{\perp}} \right)^2 \approx \cos^2 \theta. \quad (7.22)$$

Thus, high-pitch-angle events formed in a field dip will be trapped, until scattering out with the help of residual gas in the vacuum, with their initial direction now randomized. Similarly, the highest point B_{\max} in the field will reflect high-pitch-angle events coming from either side; this can create an apparent East-West instrumental asymmetry when there is a larger initial decay volume on one side versus the other. For initially isotropic events, the proportion whose direction will be changed by the field nonuniformity is

$$p_{\text{refl}} \approx \left\langle \sqrt{\frac{B_{\max}}{B} - 1} \right\rangle, \quad (7.23)$$

averaged over the decay trap. Fortunately, as far as measuring the asymmetry goes, high-pitch-angle events carry little information about the asymmetry in the first place — scrambling the directions of already isotropic events makes no difference. Zeroing out the asymmetry of events up to $|\cos \theta| < x$ reduces the asymmetry to $A' \approx (1 - x^2)A$. Thus, a quick estimate for the correction for field uniformity is

$$\Delta_{\text{mag}} = \left\langle \frac{B_{\max}}{B} - 1 \right\rangle. \quad (7.24)$$

However, the actual impact of small magnetic field wiggles must be left to simulation, to determine the interaction between pitch-angle modification and detector efficiency $\eta(E, \Omega)$. For example, to the extent that backscattering already spoils the detectors' sensitivity to the initial direction of high-pitch-angle events, no difference is made by further randomizing the already randomized events.

Incorporation of measured magnetic field nonuniformity into the MC simulation is described in subsection 4.2.3. The two magnetic field profiles shown in Figure 4.6 correspond to reflected fractions p_{refl} of 3.3% and 3.6%, and analytically estimated Δ_{mag} of +0.13% and +0.16%.

Recall from subsection 4.2.3 that this magnetic field nonuniformity is not incorporated into the main beta decay MC used to determine the Δ_2 and Δ_3 corrections; otherwise, its effects would already be folded into those preceding corrections. Rather, separate simulations with the spectrometer residual gas pressure increased from 10^{-5} torr to 10^{-3} torr, with and without the nonuniform magnetic field map, are produced. These secondary, lower-statistics simulation runs are sufficient to determine the total average correction over the analysis energy window, but not so well suited as the high-statistics main simulation for revealing finer energy-dependent details.

To separate the effects of simulating with added residual gas from those of magnetic trapping, the asymmetry $A_{\text{sr}}^{\text{mag}}$ from the 10^{-3} -torr simulation with nonuniform magnetic field is compared against the asymmetry $A_{\text{sr}}^{\text{mtorr}}$ from a 10^{-3} -torr simulation with a uniform field, rather than directly against $A_{\text{SR}}^{\text{sim}}$ from the 10^{-5} -torr simulation. The magnetic field effects correction is then taken to be $1 + \Delta_{\text{mag}} \equiv A_{\text{sr}}^{\text{mtorr}}/A_{\text{sr}}^{\text{mag}}$. Using the 2010 representative field map, the correction is $\Delta_{\text{mag}} = +0.06 \pm 0.10\%$ (consistent with the analytical estimates), with the uncertainty mainly limited by statistics of 10^7 simulated decays in the nonuniform field.

7.3.5 Wirechamber efficiency

Wirechamber efficiency — the probability of registering a signal above the maximum cathode cut used to separate “gamma-like” events from beta electrons — can influence the asymmetry by selectively lowering detector sensitivity to higher energy, more forward-directed events (with lower typical wirechamber energy deposition). Unlike magnetic field trapping, which interferes with events carrying little asymmetry information, wirechamber inefficiency preferentially cuts events with maximal asymmetry. The worst case of losing precisely the top $n\%$ most forward-directed events in a given energy bin would reduce the asymmetry by $\sim 2n\%$. The wirechambers are not so selective — simulation of imposing a wirechamber energy threshold for triggering indicates a typical scaling of $\sim 0.5n\%$ loss in measured asymmetry per $n\%$ loss in events in a given energy bin.

Collaborator Bryan Zeck analyzed events in calibration source runs, to identify event counts generating scintillator triggers (in the appropriate source energy range) but not passing wirechamber cuts [Zec12]. This method indicated typical inefficiencies of 0.12(03)% on the East detector side and 0.00(01)% on the West at the ^{113}Sn source energy. Setting a wirechamber energy threshold in simulation sufficient to match this observed inefficiency produced the $+0.12 \pm 0.08\%$ wirechamber efficiency correction applied to the 2010 data analysis.

7.3.6 Estimation of MC uncertainties

Uncertainties on the MC corrections are difficult to precisely assess. Agreement between data and MC for things that can be observed — such as backscatter fractions (subsubsection 4.8.2.1), the asymmetry associated with backscatter events, and energy distributions from calibration sources — provide a sense of the general level of consistency between MC predictions and actual physics. Allowing some additional margin for caution, the assumption is made that unobservable effects from similar physical processes have a similar level of discrepancy between simulation and reality. Prior to the 2010 dataset analysis, a uniform uncertainty of $\pm 30\%$ had been adopted for all MC corrections. For the 2010 analysis, with advances in available electron transport MC physics models producing better agreement with backscatter observables, this uncertainty was lowered to $\pm 25\%$.

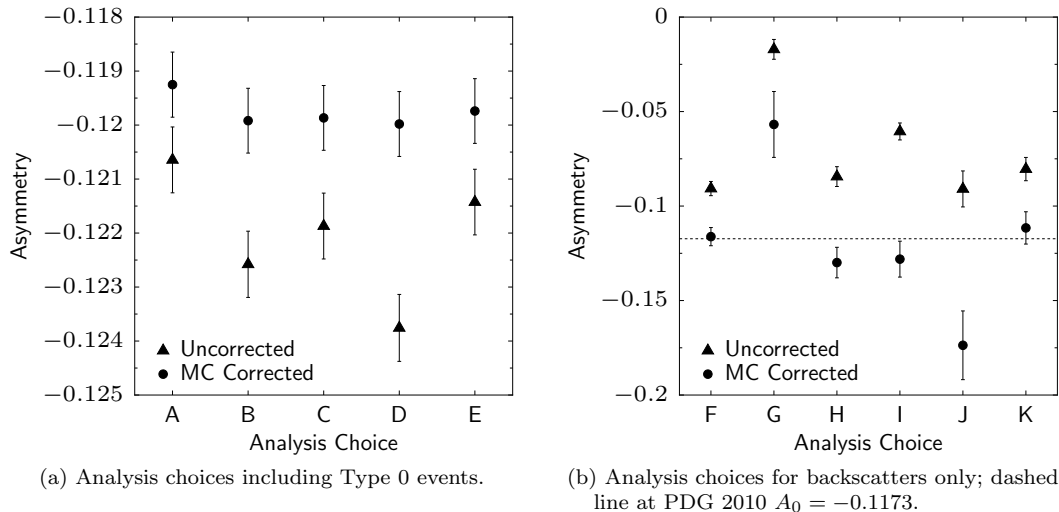


Figure 7.6: Extracted asymmetries for various analysis choices (subsubsection 7.1.1.1), with and without MC correction. Errorbars are statistical.

Note that the subdivision of MC corrections into components adds an extra level of caution in assessing MC uncertainties. The two major correction components appear with opposite signs, canceling to a smaller overall correction. However, the corrections probe somewhat different portions of the MC physics model — momentum-changing elastic scattering(s) turning around particle direction, versus the loss of kinetic energy through ionization. The $\pm 25\%$ uncertainty is applied to each correction individually, capturing uncertainty on the total amount of meddling with electron trajectories that the MC predicts is occurring in the spectrometer before fortuitous cancellations between component effects. These two errors are then treated as independent (added in quadrature), resulting in a significantly more cautious error estimate than treating the canceling components as correlated.

7.3.6.1 Comparison of analysis choices

One test of the MC corrections procedure is its ability to consistently correct the asymmetry for different backscatter type event populations. Figure 7.6 shows raw and MC-corrected asymmetries extracted from the “analysis choice” combinations of events defined in subsubsection 7.1.1.1. Analysis choices **A–F** are dominated by the asymmetry for Type 0 events (with **D** being only Type 0 events). The differences come from the asymmetry contributions of the backscatter populations, isolated in **F–K**. Type I backscatters (**F**), III alone (**K**), and II/III separated and assigned to best-guess sides (**H**) are corrected by the MC to within statistical fluctuations of the expected asymmetry (resulting in a total spread of $< 0.25\%$ between analysis choices **B–E** where these are used). Taking Type II alone (**J**), or leaving them unseparated from III and assigned to the wrong side (**G**) results in larger discrepancies, where the MC has overpredicted the asymmetry dilution in Type II events. This results in a “worst case” situation for **A**, where Type II are unseparated from III (thus generally assigned to the wrong side), requiring the largest MC correction for the backscatter class most poorly predicted by the MC. Note, however, that even this “worst case” produces only a 1σ shift for the uncertainty $\sigma \approx 0.45\%$ assigned to the MC corrections.

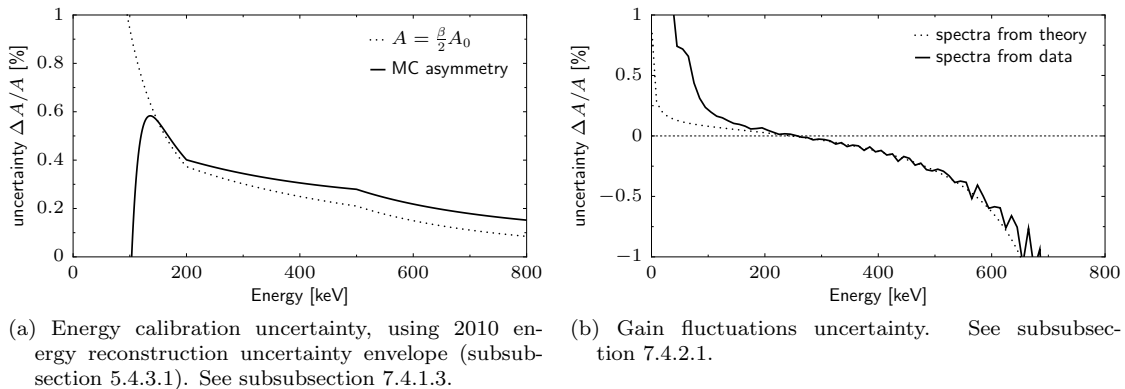


Figure 7.7: Energy calibration related uncertainties on A in 2010 data analysis, using simplistic spectrum shape models (dotted lines) and spectra modified by detector effects (solid lines).

7.4 Energy Calibration Systematics

Energy calibration errors may generally be divided into two categories: those that remain the same for both spin flipper states, and those that vary with spin flipper state. Effects that are the same for both spin flipper states are suppressed by a factor of $\sim A$, coupling to $\frac{d}{dE}A_{\text{SR}}(E)$, compared to energy calibration changes which vary with spin flipper state and couple to the overall spectrum shape $\frac{d}{dE}S(E)$. While there is no known (or suspected) systematic variation of energy calibration with spin flipper state, such may occur by chance due to fluctuating errors such as gain variation. The subsections below treat each of these kinds of errors.

7.4.1 Constant energy distortions

Suppose energy reconstruction on detector side s assigned an incorrect energy $E'_s(E) = E + \delta_s(E)$ to events of true energy E . In place of the “correct” (efficiency-modified) energy spectrum of events $S_s^\pm(E)$, we would observe a distorted spectrum

$$S_s^{\pm'}(E'_s) = \frac{dE}{dE'_s} S_s^\pm(E) = \frac{dE}{dE'_s} S_s^\pm(E'_s - \delta_s). \quad (7.25)$$

Forming the super-ratio $R'(E'_s = E')$ using the distorted spectra, the Jacobian terms $\frac{dE}{dE'_s}$ cancel out, leaving

$$R'(E') = \frac{S_E^-(E' - \delta_E) S_W^+(E' - \delta_W)}{S_W^-(E' - \delta_W) S_E^+(E' - \delta_E)}. \quad (7.26)$$

7.4.1.1 Common mode errors

First, consider a “common mode” distortion, where the energy error is identical on both sides, $\delta_E = \delta_W \equiv \delta$. Then, the super ratio and super ratio asymmetry become

$$R'(E') = R(E' - \delta) = R(E) \Rightarrow A'_{\text{SR}}(E') \equiv \frac{1 - \sqrt{R'(E')}}{1 + \sqrt{R'(E')}} = A_{\text{SR}}(E), \quad (7.27)$$

i.e., the energy distorted asymmetry is simply the correct asymmetry plotted against the wrong E' energy scale. Expanding for small energy error δ , the impact on the extracted asymmetry is

$$A'_{\text{SR}}(E') \approx \left(1 - \delta \frac{d}{dE'} A_{\text{SR}}(E')\right) A_{\text{SR}}(E') \approx \left(1 - \frac{\delta}{2} \frac{d\beta}{dE'} A_0\right) A_{\text{SR}}(E'), \quad (7.28)$$

noting that the approximation $\frac{d}{dE'} A_{\text{SR}}(E') \approx \frac{1}{2} \frac{d\beta}{dE'} A_0$ ignores additional modifications to the simple $\frac{\beta}{2} A_0$ energy dependence of the asymmetry by both radiative corrections and detector effects.

7.4.1.2 Differential mode errors

On the other hand, consider a “differential mode” distortion, where the energy error goes in opposite directions on the two detector sides, $E'_s = E \pm_s \delta$. Then, forming the super-ratio using the erroneous energy,

$$R'(E') = \frac{S_E^-(E' - \delta) S_W^+(E' + \delta)}{S_W^-(E' + \delta) S_E^+(E' - \delta)}. \quad (7.29)$$

For small δ , we can approximate this by expanding

$$S_s^\pm(E' \mp_s \delta) \approx S_s^\pm(E') \mp_s \delta \frac{dS_s^\pm}{dE'}. \quad (7.30)$$

In the absence of differences in efficiency between the two detector sides, $S_E^+ = S_W^-$ and $S_W^+ = S_E^-$, so the oppositely-signed cross terms will cancel out:

$$\left[S_E^+(E') - \delta \frac{dS_E^+}{dE'} \right] \left[S_W^-(E') + \delta \frac{dS_W^-}{dE'} \right] = S_E^+(E') S_W^-(E') - \delta^2 \frac{dS_E^+}{dE'} \frac{dS_W^-}{dE'}, \quad (7.31)$$

and there will even be approximate cancellation, to order A , between the remaining small $\delta^2 \left(\frac{dS}{dE}\right)^2$ terms in the numerator and denominator. Thus, for differential mode energy distortions, the opposite shifts nearly cancel in the super ratio, leaving the observed asymmetry unchanged

$$R'(E') \approx R(E') \Rightarrow A'(E') \approx A(E'), \quad (7.32)$$

so long as there are no significant differences in detector efficiency between the two sides and $\delta \frac{dS}{dE} \ll S$, which is only violated near the trigger threshold or the endpoint.

7.4.1.3 2010 energy calibration uncertainty

The energy calibration uncertainty for the 2010 result comes from taking the “worst-case scenario” that fits within the (already conservative) energy calibration error envelope (subsubsection 5.4.3.1), which would be a common mode energy offset following the boundary of the envelope. Figure 7.7a shows the resulting uncertainty on A , both assuming a simple $A_{\text{SR}} = \frac{\beta}{2} A_0$ form, and the shape of A_{SR} expected from Montecarlo simulation. In a statistics-weighted average over the 220 keV to 670 keV energy window, the $\frac{\beta}{2} A_0$ form corresponds to a $\pm 0.25\%$ uncertainty on A_0 , while the MC asymmetry expectation gives $\pm 0.31\%$, which was adopted for the published result. Roughly a quarter of the difference comes from the radiative corrections to the asymmetry from theory.

Note that the MC curve was produced from an empirical fit to the shape of $A_{\text{SR}}^{\text{sim}}$, necessary to smooth statistical fluctuations interfering with calculating $\frac{d}{dE}A_{\text{SR}}^{\text{sim}}$, of the form

$$A_{\text{SR}}^{\text{sim}}(E) \approx \frac{1}{2}\beta(E)A_0^{\text{PDG}} \cdot p_1 \cdot (1 + p_2E) \cdot \left[1 + \frac{p_3}{1 + e^{(E-p_4)/p_5}}\right] \quad (7.33)$$

$$p_2 \approx 0.000117/\text{keV}, \quad p_3 \approx 2.19, \quad p_4 \approx 56.6 \text{ keV}, \quad p_5 \approx 12.9$$

in which the p_2 term captures the additional energy dependence on top of $\beta(E)$. The p_3, \dots, p_5 portion describes the abrupt distortion of the asymmetry near the low energy trigger threshold, where events brought down from higher initial true energy (thus typically higher asymmetry) by energy losses outnumber observed true low-energy events. This results in an abrupt sign reversal of $\frac{d}{dE}A_{\text{SR}}$. See section 7.7 for plots of this effect in simulation and data.

7.4.2 Variable energy distortions

Along with energy reconstruction errors which are constant between spin flipper on and off runs, there can also be faster varying changes in detector behavior that shift energy reconstruction errors between the different spin flipper state parts of the measurement. The distortion to the super-ratio from meddling with the energy reconstruction $E \rightarrow E + \delta_s$ only for “on” runs would be

$$R'(E) = \frac{S_E^-(E)S_W^+(E + \delta_W)}{S_W^-(E)S_E^+(E + \delta_E)} \frac{1 + \frac{d\delta_W}{dE}}{1 + \frac{d\delta_E}{dE}}. \quad (7.34)$$

In the case of common-mode energy errors $\delta_E = \delta_W$ between the two sides, the Jacobian terms $1 + \frac{d\delta_E}{dE} = 1 + \frac{d\delta_W}{dE}$ cancel out, and there is cancellation to order A between the energy-offset spectra. For differential changes $\delta_E \neq \delta_W$ between the two sides, there is no cancellation of either the Jacobian terms or the spectrum shape contributions. The effects can be especially strong towards the low and high energy ends of the spectrum, where small energy changes result in large fractional changes in the spectrum. Generally, the effect will have opposite signs on the high and low energy ends of the spectrum (corresponding to the rising and falling slope of the overall decay spectrum shape), possibly creating small partial cancellations depending on the energy window used.

7.4.2.1 2010 gain fluctuation uncertainty

Suppose we have an anticorrelated, spin flipper-dependent gain change producing a shift of ΔE to the beta decay endpoint between spin flipper on and off runs, in opposite directions for the two sides. Given beta decay endpoint measurements for each detector side and spin flipper state E_s^\pm , this component can be extracted by

$$\Delta E = \frac{1}{2} [(E_E^+ - E_E^-) - (E_W^+ - E_W^-)]. \quad (7.35)$$

Note that one expects $E_s^+ \neq E_s^-$, even in the absence of gain fluctuations, due to interaction between the Kurie endpoint fitting procedure and the change in polarized spectrum shape from the asymmetry. Based on MC, the difference between the on/off extracted endpoints is ~ 3 keV, varying by a further ~ 0.2 keV between the two detector sides due to fine detector response differences. Thus, the mean ΔE extracted in this manner includes a systematic offset of 3.1 keV not indicative of a

systematic energy shift, which agrees within error bars between data and MC. Gain fluctuations will contribute to the observed spread of ΔE values about the mean over many runs.

Treating the data as $N \approx 200$ pulse pairs, or combining into half-octets or octets, the average fluctuation in ΔE about the mean over the whole 2010 dataset is $\sigma/\sqrt{N} = 0.19$ keV. Matching simulations with statistical variation alone shows $\sigma_{\text{stat}}/\sqrt{N} = 0.16$ keV, leaving $\sigma_{\Delta E}/\sqrt{N} = \sqrt{0.19^2 - 0.16^2} = 0.10$ keV of endpoint fluctuation not explained by statistics. This indicates gain fluctuations of ± 1.4 keV change in endpoint between the East and West detectors between spin flipper on and off segments of each pulse pair, corresponding to $\sim 0.25\%$ -level residual run-to-run gain fluctuations uncorrected by the ^{207}Bi pulser system.

Figure 7.7b shows the uncertainty in A produced by this level of gain fluctuations averaged over the 2010 dataset. The uncertainty can be calculated using simplified “ideal” spectra, or applying the gain error to observed spectra with all detector effects; there is little difference except near the trigger threshold and endpoint, where detector effects significantly modify the spectrum shape. Over the 220 keV to 670 keV analysis window, this produces a $\pm 0.18\%$ uncertainty on A .

7.4.2.2 Pedestal fluctuation uncertainty

The effects of pedestal fluctuations are expected to be very small. Assuming a ± 2 keV anticorrelated offset between the two halves of each pulse pair, approximately the drift rate of the fastest-drifting PMT pedestal if left entirely uncorrected, would produce $\sim \pm 0.5\%$ uncertainties on A averaged over the 200 pulse pairs. However, not only do all the other PMTs show an order of magnitude lower pedestal drift, but this drift is finely tracked and corrected by routine pedestal subtraction. Thus, the associated uncertainty on A may be conservatively put at $\ll \pm 0.05\%$.

7.5 Backgrounds

7.5.1 Background effects on A

Following the notation of Equation 7.11, the most general case of adding (or subtracting) spurious counts to the asymmetry can be written as

$$dN_s^\pm(E) \equiv [B_s(E) \pm \tilde{B}_s(E)]t_\pm, \quad (7.36)$$

where t_\pm is the time taken for \pm spin flipper runs, and the spectrum of spurious events on each detector side has been decomposed into a spin flipper-independent component B_s and spin flipper-varying change \tilde{B}_s . Recall that the influence of adding counts $N_s^\pm \rightarrow N_s^\pm + dN_s^\pm$ is

$$\frac{\partial}{\partial N_s^\pm} A_0^{\text{meas}} = -\frac{1}{2\beta} \frac{\partial R}{\partial N_s^\pm} = \frac{\pm_s 1 \pm R}{2\beta N_s^\pm}. \quad (7.37)$$

Considering only the contributions from the spin flipper-independent component B_s ,

$$\begin{aligned} dA_0^{\text{meas}} &= -\frac{1}{2\beta} \left[\left(\frac{t_-}{N_E^-} - \frac{t_+}{N_E^+} \right) B_E - \left(\frac{t_-}{N_W^-} - \frac{t_+}{N_W^+} \right) B_W \right] \\ &\approx -\frac{1}{\beta S} \left[\left(\frac{t_-}{N^-} + \frac{t_+}{N^+} \right) (B_E + B_W) \frac{\beta}{2} A_0 + \left(\frac{t_-}{N^-} - \frac{t_+}{N^+} \right) (B_E - B_W) \right], \end{aligned} \quad (7.38)$$

where the term not suppressed by the factor of A_0 vanishes for equal contributions on each detector side $B_E = B_W$, and is generally reduced to the extent of similarity in spin flipper on/off total decay rates $\frac{N^-}{t_-} \approx \frac{N^+}{t_+}$. For the spin flipper-dependent component \tilde{B}_s ,

$$\begin{aligned} dA_0^{\text{meas}} &= -\frac{1}{2\beta} \left[\left(\frac{-t_-}{N_E^-} - \frac{t_+}{N_E^+} \right) \tilde{B}_E - \left(\frac{-t_-}{N_W^-} - \frac{t_+}{N_W^+} \right) \tilde{B}_W \right] \\ &\approx \frac{1}{\beta S} \left[\left(\frac{t_-}{N^-} - \frac{t_+}{N^+} \right) (\tilde{B}_E + \tilde{B}_W) \frac{\beta}{2} A_0 + \left(\frac{t_-}{N^-} + \frac{t_+}{N^+} \right) (\tilde{B}_E - \tilde{B}_W) \right], \end{aligned} \quad (7.39)$$

so the most “dangerous” form of spurious background is one that mimics the asymmetry, having opposite signs on each detector side and flipping sign with the spin flipper.

7.5.2 Avoiding background contributions

Detector backgrounds are dealt with in three ways:

- Suppression by detector design. Gammas are unlikely to produce noticeable ionization in the wirechambers; requirement of an above-threshold wirechamber signal greatly reduces sensitivity to gamma rays.
- Veto by coincidence with muon detectors surrounding the detector suppresses most cosmic ray events.
- Subtraction of remaining backgrounds by dedicated background runs.

Note that the third method, subtraction of background runs, serves as a catch-all method for eliminating the effect of any background components leaking past the first two checks. Thus, for most detector backgrounds, fluctuation in sensitivity to background is of greater concern than absolute efficiency of background rejection by the first two methods. The exception to this is any background associated specifically with the presence of neutrons in the decay trap, which will not appear in the neutron-free background runs.

7.5.3 Ambient gamma ray background

Gamma events are primarily rejected by requiring a wirechamber coincidence trigger. Figure 7.8 shows the scintillator reconstructed energy spectra for gamma(-like) events, which produce a 2-fold scintillator PMT trigger but do not pass wirechamber trigger cuts.

The broad “bump” on the East side around 500 keV comes from ^{207}Bi gain stabilization pulser events leaking enough light to other PMTs to form a 2-fold coincidence. An event identification cut looking for events with very large signal in one PMT and very low signals in the other three (statistically impossible from main scintillator events) properly assigns Bi pulser events above this energy range. The West side, with its higher single-PMT trigger thresholds, is less sensitive to ^{207}Bi pulser light leakage. Since these events are already excluded from the beta decay data by wirechamber cuts, there is no impact on the asymmetry data from confusion between gamma and ^{207}Bi pulser events. The East side is also closer to the accelerator beamline shielding stack, thus subjected to a slightly higher room gamma background.

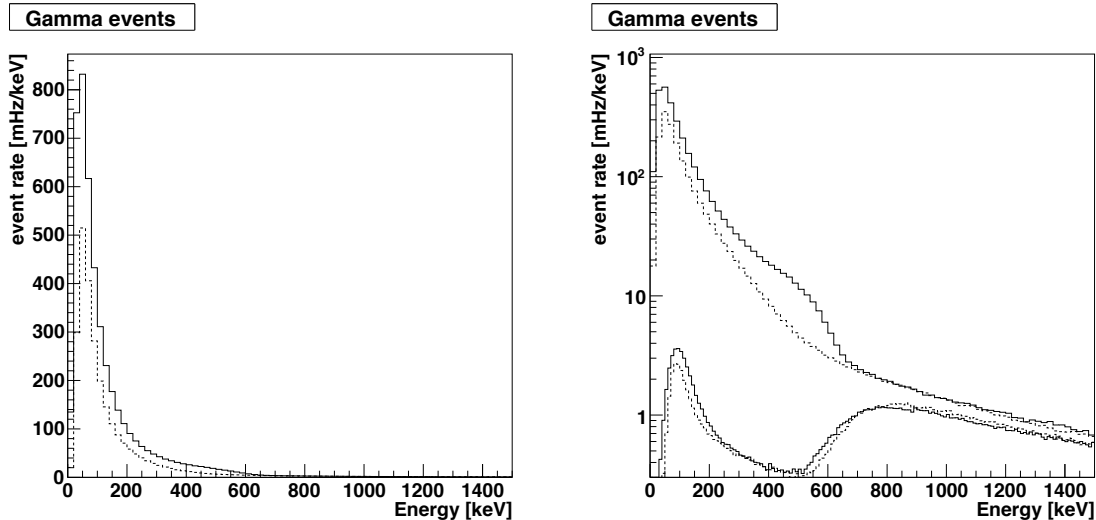


Figure 7.8: Gamma events spectra (2-fold scintillator triggers without wirechamber trigger); same plot on linear and log scales. Solid lines for East detector, dashed for West. Lower curves on log plot show the background rate (gamma rays and muons) that *passes* the wirechamber cut, indicating $> 99\%$ suppression of the ambient gamma background.

By comparison with the rate of wirechamber-triggering events in background runs, the wirechamber coincidence requirement suppresses $> 99\%$ of PMT gamma event triggers. Since background subtraction makes up for residual gamma rays not eliminated by the wirechamber cut, uncertainties associated with the gamma background are folded into considerations of the subtracted background.

7.5.4 Cosmic ray muon background

Cosmic ray muon backgrounds (or, in general, any ionizing radiation originating from outside the spectrometer) are suppressed by a coincidence veto between 2-fold beta scintillator triggers and various veto detectors surrounding the spectrometer. Directly behind each beta scintillator is a 25 mm-thick “muon backing veto” scintillator disk, connected through a (narrow and inefficient) light guide to a single PMT. A large scintillator panel connected to three PMTs covers the top of the East side of the spectrometer. Gas drift tubes [Rio+11] cover the East sides, and the West top and sides.

Figure 7.9 shows the coincidence timing spectra with 2-fold beta scintillator triggers produced by each system, used to tag muon events. For the scintillator-based vetoes (backing and East top), an associated ADC signal is available, shown in Figure 7.10. The drift tubes produce accidental coincidences with $\sim 0.3\%$ of events, including beta decays. Because the accidental coincidences are a uniform random sampling of events, this has no impact on observed event spectra (besides a small uniform rate decrease).

Figure 7.11 shows the energy spectra of muon-tagged events, for all systems combined and the backing vetoes alone. The backing vetoes detect roughly half the muons, with the top and side vetoes covering the rest. The gas drift tubes add moderate sensitivity to gamma rays in addition to muons.

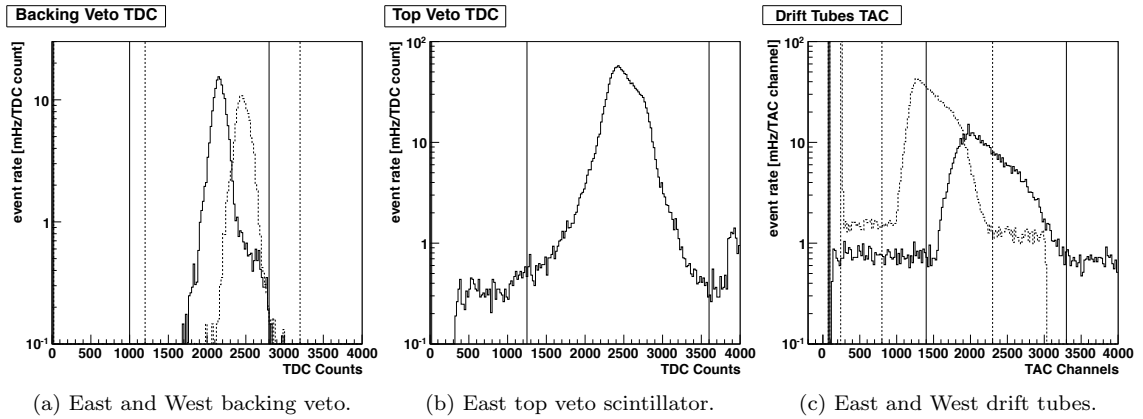


Figure 7.9: Timing coincidence spectra from muon veto detectors, example from a 2010 beta decay run. Solid lines for East detector, dashed for West; vertical lines mark coincidence cut ranges.

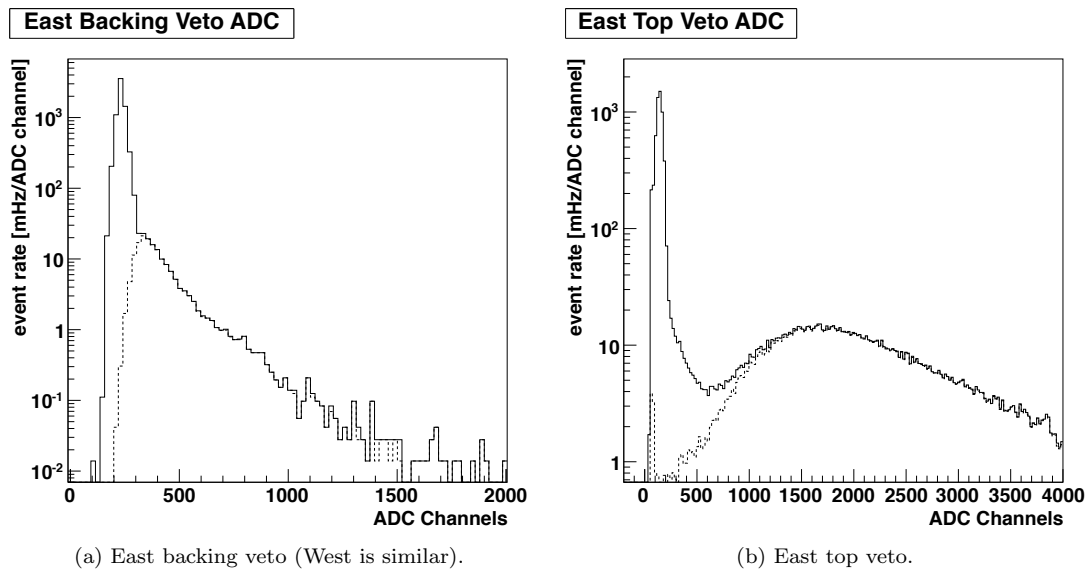


Figure 7.10: Muon veto scintillator event spectra from example 2010 beta decay run. Solid lines for all events, dashed line for events in coincidence timing cut.

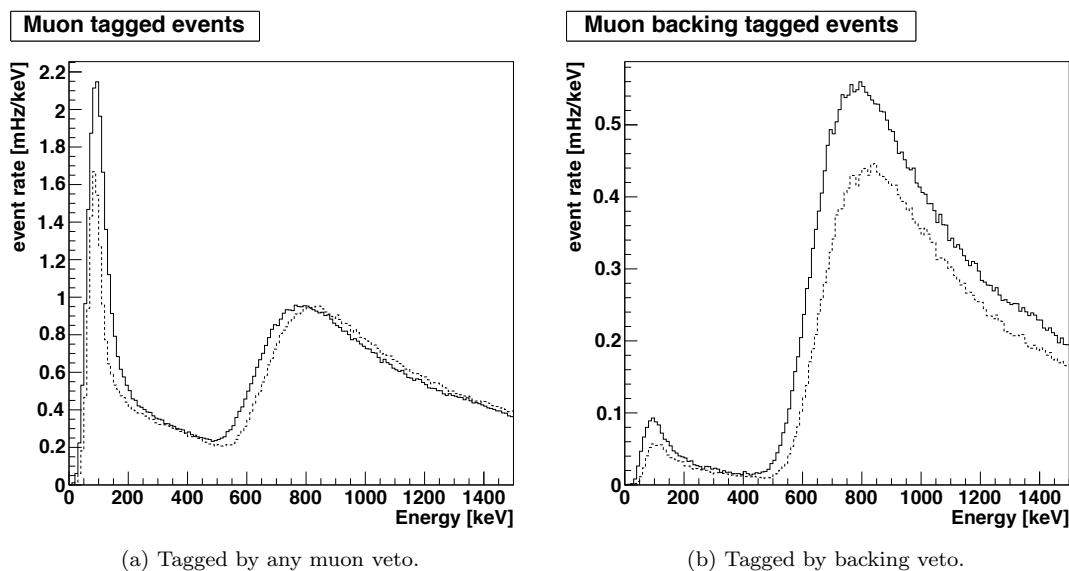


Figure 7.11: Muon-tagged events passing beta decay position cuts from 2010 dataset beta runs. Solid lines for East detector, dashed for West.

Figure 7.12 shows the muon-tagged event rate otherwise falling within analysis cuts as a function of time (half-octet number) for the 2010 dataset. Rates are taken from background runs, rather than higher-statistics beta runs, to avoid the addition of accidental coincidences with beta decay, which are on the same scale as actual muon events over the analysis window. The rates are statistically distributed, indicating no large-scale fluctuations in muon flux or detection efficiency. As expected, there is no statistically significant difference between spin flipper on and off rates.

7.5.5 Subtracting residual background

After removing as many non-beta-decay events as possible via detector coincidence requirements, the remainder of background events are removed by subtracting off backgrounds observed in background

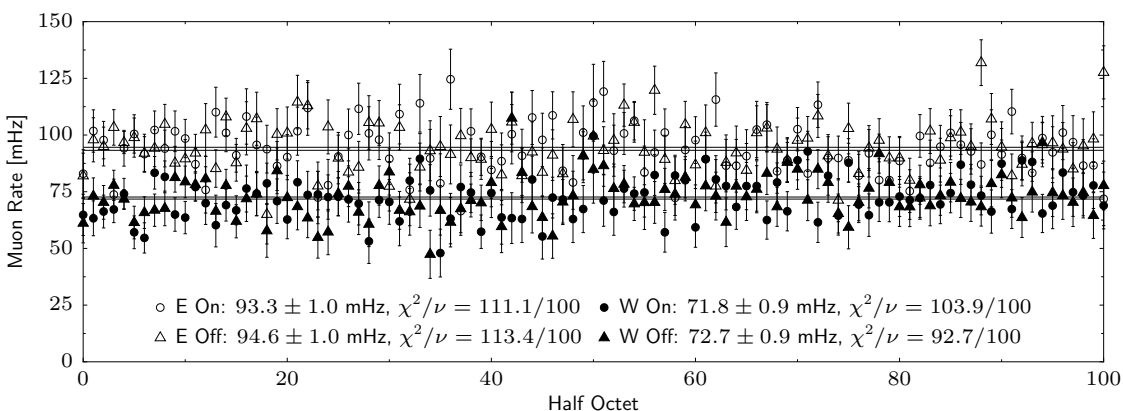


Figure 7.12: Muon-tagged event rate in 50mm beta decay position cut and 220 keV to 670 keV energy analysis range, from background runs over all 2010 beta decay half-octets.

runs matched to each beta decay run. Background runs are typically $\sim 1/6$ the length of decay runs, with their counts scaled up for subtraction according to the actual time ratio (accounting for all time cuts).

Since individual background runs often produce statistics with few or no counts in a particular energy bin, counting statistics errorbars for low-statistics ($N < 25$) bins in background subtraction are estimated from the average background distribution over all runs, scaled down to the total number of counts in the individual background histogram. This procedure produces correct errorbar estimates under the assumption that the background distributions are constant over time (so the higher-statistics average accurately represents the event distribution from which each shorter run is sampled), which is consistent with the observed data. Incorporating the background counting statistics (appropriately scaled up by the foreground:background run time ratios) into background-subtracted histogram statistical errorbars automatically includes the statistical impact of backgrounds in the final result.

Figure 7.13 shows the energy spectra observed in background runs, for events otherwise passing all cuts qualifying for inclusion in the beta decay asymmetry measurement spectra. Type 0 backgrounds show a mixture of gamma rays and residual muon peak not suppressed by other mechanisms. Backscatter-type events, requiring a coincidence between detectors on both sides, are primarily due to Compton-scattered electrons from within the scintillator (or wirechamber) that manage to traverse the spectrometer to the opposite side. Higher-energy events typically reach both scintillators, producing the high-energy Type I background distribution, while lower-energy events are distributed between Type II and III.

Figure 7.14 shows the position distributions for backscatter events. Type 0 events are uniform over the detector, plus a ring at the edge of the acceptance, likely from Compton scatters off the edges of the aluminum detector entrance bore. Backscatter backgrounds uniformly cover the smaller circular portion of the acceptance visible to both sides of the detector.

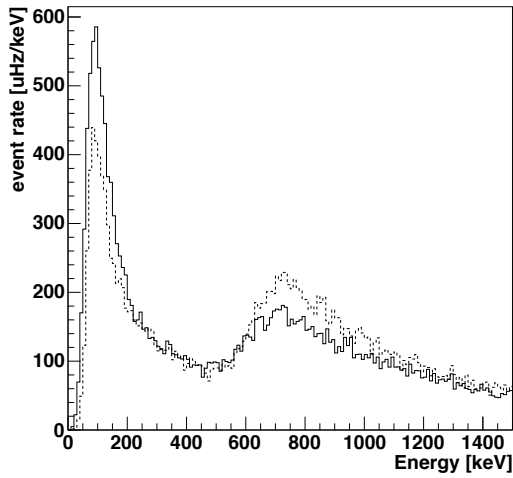
Figure 7.15 shows the history of the subtracted background rate over the 2010 dataset. Background rates are statistically distributed with the exception of one group of runs around half-octet 60, where an anomalously increased background rate is sustained across four background runs (which appear otherwise normal from closer inspection of the data).

7.5.5.1 Systematic uncertainty from background subtraction

The muon veto efficiency systematic of $\pm 0.03\%$ on A_0 published for the 2010 data analysis is intended to cover the extent of background subtraction errors beyond statistical fluctuations. Concern over muon veto efficiency (as a contributor to erroneous backgrounds) is a carryover from the 2008–2009 data analysis [LMH+10; Pla+12], when the newly-developed drift tube veto was operating erratically (showing much larger than statistical fluctuations). Consistency of the 2010 muon vetoed event rate fluctuations with counting statistics indicates that large additional instrumental fluctuations are no longer of great concern. An estimated scale for potential remaining non-statistical muon detection efficiency fluctuations (and, by extension, general errors in the subtracted background, which is of the same scale as muon-tagged event rates) was made by assuming that efficiency fluctuations were “hiding” at the magnitude of observed counting statistics.

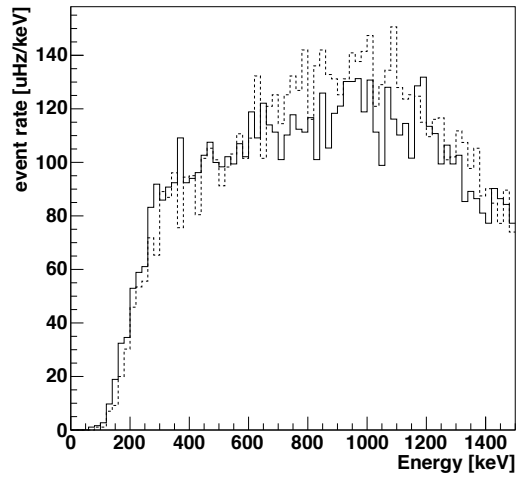
Taking the observed tagged-muon spectrum $M_s^\pm(E)$ for each detector side and spin flipper state, the change in extracted asymmetry was calculated for $dN_s^\pm = \pm_s \frac{\pm\delta}{2\sqrt{N}} M_s^\pm(E)$ (the spin flipper- and

Type 0 events background



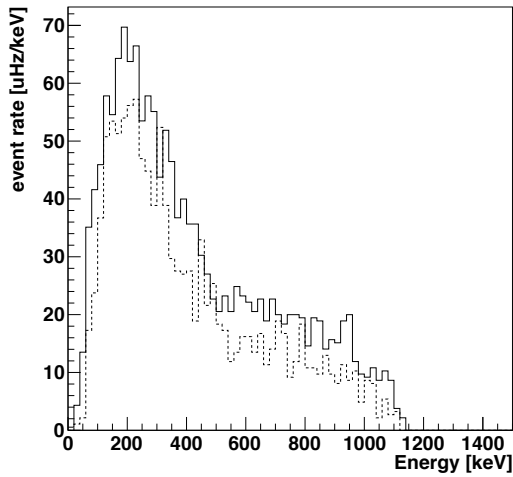
(a) Type 0.

Type I events background



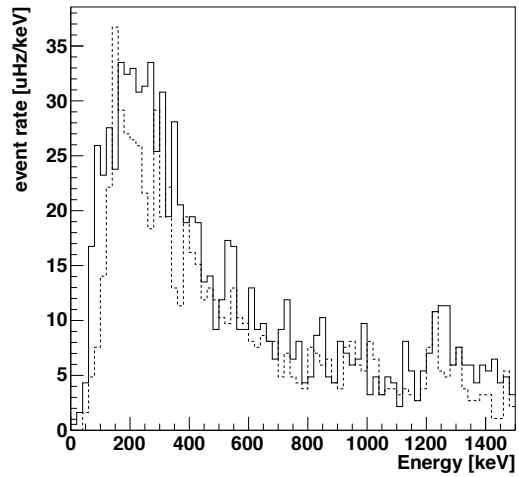
(b) Type I.

Type II events background



(c) Type II.

Type III events background



(d) Type III.

Figure 7.13: Subtracted background reconstructed energy spectra by identified event type, summed over all background runs from 2010 dataset. Solid lines for East detector, dashed for West.

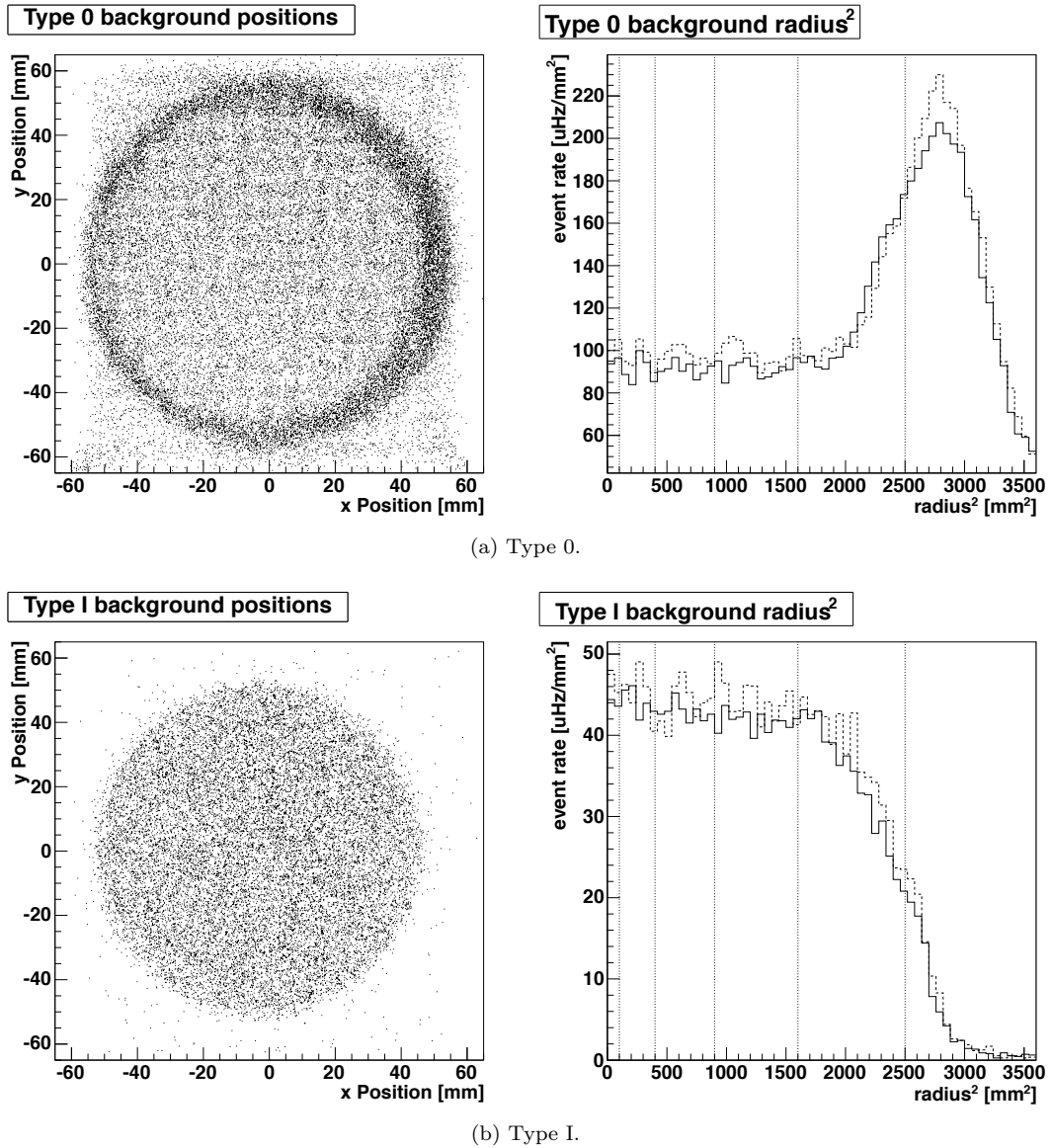


Figure 7.14: Background runs event positions, from the 2010 dataset. East side shown in 2D plots (West is similar “mirror image”). Radius plots show East (solid) and West (dashed) positions, with dotted verticals marking 1 cm intervals from center. Solid lines for East detector, dashed for West.

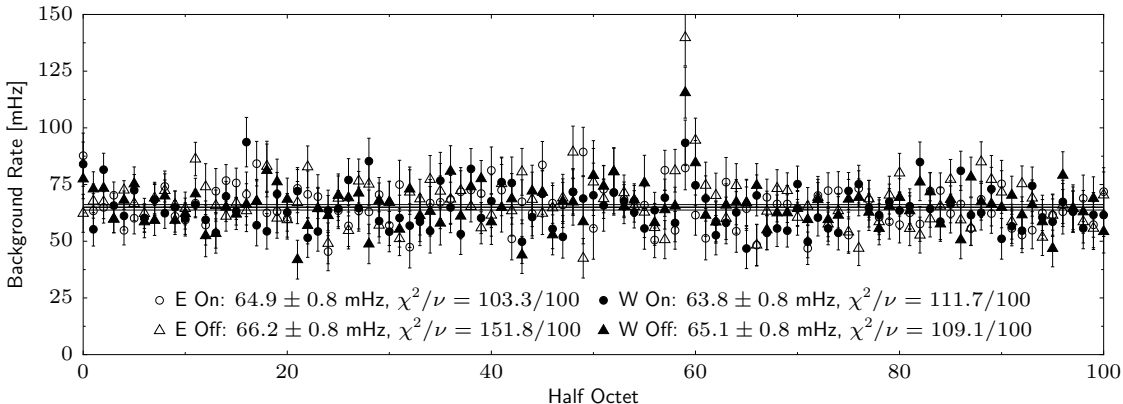


Figure 7.15: Subtracted background event rate within beta decay analysis cuts, from background runs over all 2010 beta decay half-octets.

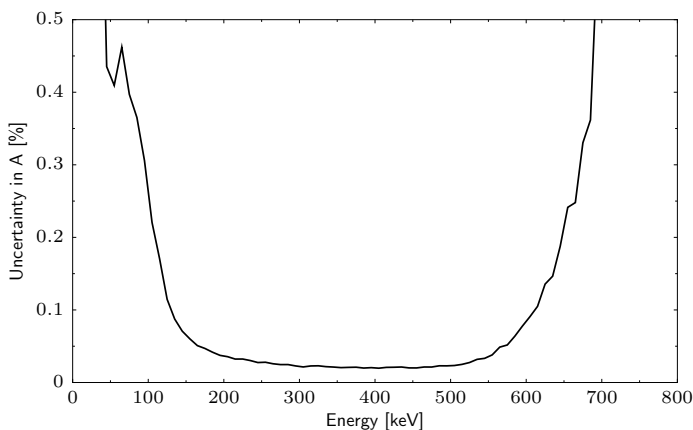


Figure 7.16: Muon veto efficiency fluctuation uncertainty for 2010 data.

detector-side-anticorrelated “worst case” component of potential fluctuations). Here, $\delta/\sqrt{N} = 0.2\%$ represents a conservative estimate for the scale of efficiency fluctuations, based on observed statistical variation of tagged muon counts (without imposing beta analysis position and energy cuts, to improve statistics). Note that this corresponds to $\pm 4\%$ detector efficiency changes over hour time scales for the $N \sim 400$ beta runs taken; there is no reason to assume actual detector efficiency would be fluctuating so much so fast.

The impact of detector efficiency fluctuations is inflated by background subtraction, where fluctuations between beta and background runs are multiplied by the $\sim 6 : 1$ run length ratio. Note, however, that the mean time between beta and paired background runs is about half that between beta runs in each spin flipper state, which would reduce the level of relevant random detector efficiency changes by $\sim 1/\sqrt{2}$. Thus, this veto efficiency fluctuation estimate corresponds to $\sim \pm 1\%$ efficiency changes over the average half-hour intervals between beta and background runs. Figure 7.16 shows the resulting uncertainty, which explodes at the extremes of the beta spectrum where background counts are large compared to neutron beta electrons, but contributes $\pm 0.033\%$ uncertainty on A_0 when statistics-weighted over the 220 keV to 670 keV analysis window. This uncertainty can be interpreted as a placeholder for the general scale of potential background subtraction errors, from the

muon vetoes or beta detector efficiency changes, corresponding to $\lesssim \pm 1\%$ background event rate fluctuations between beta and background runs (with no long-term spin flipper state correlation).

7.5.6 Neutron-generated background

Neutron-generated backgrounds are one potential source of background events that will evade background subtraction. Analysis for the 2009 dataset [LMH+10; Pat12; Pla+12] estimated neutron generated background contributions by two methods: first, looking for increased gamma event rates (scintillator triggers without wirechamber triggers) during beta decay runs, and, second, by a dedicated set of “beta blocker” runs in which a plastic sheet blocked direct beta electrons from the decay trap. These methods indicated an uncertainty on A_0 of $\pm 0.02\%$.

While no dedicated neutron background runs were performed in the 2010 detector geometry, the increased beta decay statistics of the 2010 dataset allow a more in-depth consideration of neutron-generated backgrounds within the data. Signatures of neutron-generated backgrounds include an excess of gamma events after background subtraction, along with beta events past the neutron beta decay endpoint. Excess counts were observed in background-subtracted data, both gamma rays and past-endpoint beta electrons (see Table 7.3).

A set of Montecarlo simulations was used to explore the effects of various neutron-generated background scenarios. Because of detector geometry, no plausible scenarios were found for neutron interactions in the decay trap producing the observed excess events. Simple geometrical suppression from the distance between decay trap and detectors massively reduces sensitivity to any gamma rays resulting from neutron interactions in the decay trap; beta electrons are largely blocked by the decay trap collimators; any passing are restricted to the outermost detectable radii.

However, a much smaller number of neutrons outside the decay trap, interacting near the detectors, could produce the observed signal. Given typical decay trap storage lifetimes of ~ 60 seconds, compared to the neutron lifetime of ~ 900 seconds, every neutron decay observed corresponds to ~ 15 neutrons lost by some mechanism from the decay trap — upscattering, capture, or escape into the spectrometer magnet bore through gaps in the trap walls. While the spectrometer bore is not designed specifically to be UCN-friendly, the majority of surface area within the bore is stainless steel, aluminum, or copper; all reasonably capable of bottling much of the UCN spectrum.

Two plausible neutron capture scenarios were modeled: $n + {}^{27}\text{Al} \rightarrow {}^{28}\text{Al}$ on the aluminum surfaces of the wirechamber entrance and exit window frames, and $n + {}^1\text{H} \rightarrow {}^2\text{D}$ on hydrogen within the scintillator. By capture cross-section and abundance in the geometry, these are the most likely sites for neutron capture. The wirechamber itself should be fairly transparent to UCN — “thin” compared to expected capture mean free paths. Neutron capture on ${}^{27}\text{Al}$ results in a varied selection of gamma rays up to ~ 7 MeV; ${}^{28}\text{Al}$ has a 134 s half life before beta decay (2863 keV endpoint) to an excited state of ${}^{28}\text{Si}$, which promptly converts to the ground state via a 1779 keV gamma. Neutron capture on hydrogen results in a 2223 keV gamma.

Table 7.3 shows the excess counts in various categories, from data and simulation, for each detector side and spin flipper state. Counts from background runs in each category are provided for comparison. Columns for Type 0, I, and II/III indicate excess events after background subtraction within a 50mm radius at >1 MeV. Excess beta electrons at all positions are listed for 1 MeV to 2.2 MeV and >2.2 MeV. Gammas are likewise listed by energy range. Note that the

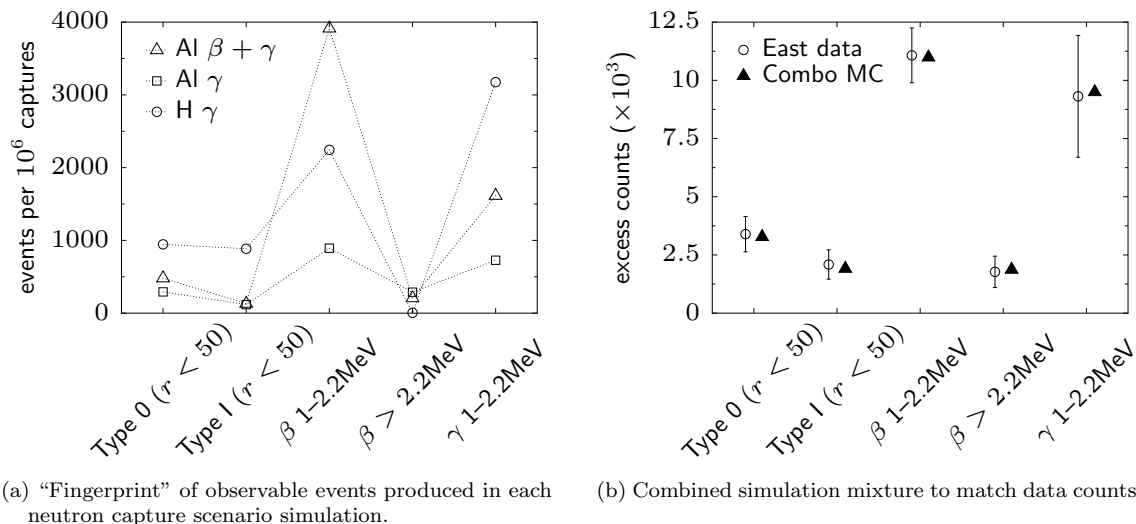


Figure 7.17: Neutron generated backgrounds simulation.

0.2 MeV to 1 MeV gamma range may also contain beta electrons missed by wirechamber trigger inefficiency. The β 1–2.2 MeV count provides the best statistics for an unambiguous signature of neutron backgrounds. There is a distinct asymmetry between the two sides. The total β excess spin flipper Off:On ratio of 1.68 ± 0.26 is statistically consistent with the Off:On ratio of observed decays of ~ 1.54 .

The lower half of the table shows results from simulation of neutron capture products. The “Trap Cu” and “H” lines are from $2.5 \cdot 10^8$ neutrons captured on copper and hydrogen near the decay trap collimator, the most likely location in the decay trap for producing detectable gamma rays and Compton scatters. Despite representing on order of half the total number of neutrons lost by all mechanisms, these decay trap capture scenarios are unable to reproduce observed excess rates.

The first three simulations in the table are for 10^6 events each of neutron captures near the detectors. “Al $\beta + \gamma$ ” is captured on the inner diameter of the aluminum wirechamber window frames, producing prompt gamma rays and the delayed ^{28}Al beta decay. To simulate neutrons capturing on nearby aluminum surfaces with no plausible path for beta electrons to reach the scintillator (such as the inner walls of the wirechamber box), the “Al γ ” simulation is for the initial ^{27}Al capture gamma without the delayed beta (and gamma). “Scint. H” is the gamma from neutron capture on Hydrogen over the scintillator face. Based on capture cross sections, approximate penetration depths for 3 m/s neutrons of $\lambda = 1.0$ mm for aluminum and 0.8 mm for scintillator were used to generate initial event positions embedded into the material surfaces to depth $-\lambda \ln(\text{rand}(0, 1))$.

Each capture scenario produces a distinctive “fingerprint” of excess events, plotted in Figure 7.17a. Capture gamma rays on scintillator hydrogen provide Type 0 and I Compton-scatters within the 50mm detector fiducial, along with gamma events. Delayed aluminum beta electrons provide an abundance of larger-radius beta events. Comptons from the higher-energy aluminum gamma rays contribute to beta electrons above what the 2.2 MeV hydrogen gamma can produce. A linear combination of these three is fit to match the East On+Off counts in the categories shown in Figure 7.17b, producing an 0.7:5.9:1.3 (Al $\beta + \gamma$):(Al γ):(H γ) “Combined” simulation. This

	Type 0	Type I	Type II/III	β 1-2.2 MeV	$\beta > 2.2$ MeV	γ 0.2-1 MeV	γ 1-2.2 MeV	$\gamma > 2.2$ MeV
Background-subtracted data and background run counts								
E Off	2517 \pm 503	1213 \pm 454	82 \pm 110	7435 \pm 781	1318 \pm 478	81184 \pm 13873	3522 \pm 1767	429 \pm 1136
BG	5429	4138	261	12075	4559	3817390	62426	25785
E On	1237 \pm 567	876 \pm 435	-50 \pm 113	3636 \pm 879	456 \pm 476	93873 \pm 15018	5971 \pm 1930	1040 \pm 1129
BG	5559	4181	272	12252	4614	3823090	62076	25917
W Off	416 \pm 553	331 \pm 463	189 \pm 100	3216 \pm 837	635 \pm 515	38861 \pm 10482	2278 \pm 1758	-540 \pm 1180
BG	6626	4514	206	13841	5250	2181760	61723	27752
W On	604 \pm 617	907 \pm 456	177 \pm 97	2584 \pm 1003	812 \pm 514	8905 \pm 11285	1057 \pm 1930	-2037 \pm 1310
BG	6678	4390	198	13786	5300	2190600	61890	28196
Montecarlo simulations								
Al $\beta + \gamma$	522 \pm 7	138 \pm 3	9 \pm 0	3888 \pm 19	208 \pm 4	9081 \pm 30	2198 \pm 14	38 \pm 1
Al γ	299 \pm 5	120 \pm 3	6 \pm 0	892 \pm 9	285 \pm 5	4449 \pm 21	877 \pm 9	71 \pm 2
Scint. H	951 \pm 9	892 \pm 9	51 \pm 2	2227 \pm 14	5 \pm 0	9204 \pm 30	3772 \pm 19	1 \pm 0
Combined	3371 \pm 35	1945 \pm 24	112 \pm 5	10967 \pm 60	1858 \pm 31	44741 \pm 133	11578 \pm 61	446 \pm 15
Trap Cu γ	600 \pm 44	62 \pm 14	9 \pm 5	761 \pm 27	136 \pm 11	10625 \pm 103	162 \pm 12	3 \pm 1
Trap H γ	61 \pm 7	12 \pm 3	2 \pm 1	289 \pm 17	0 \pm 0	7894 \pm 88	453 \pm 21	0 \pm 0

Table 7.3: Data counts indicating neutron generated backgrounds, and MC simulations of possible background sources. See text.

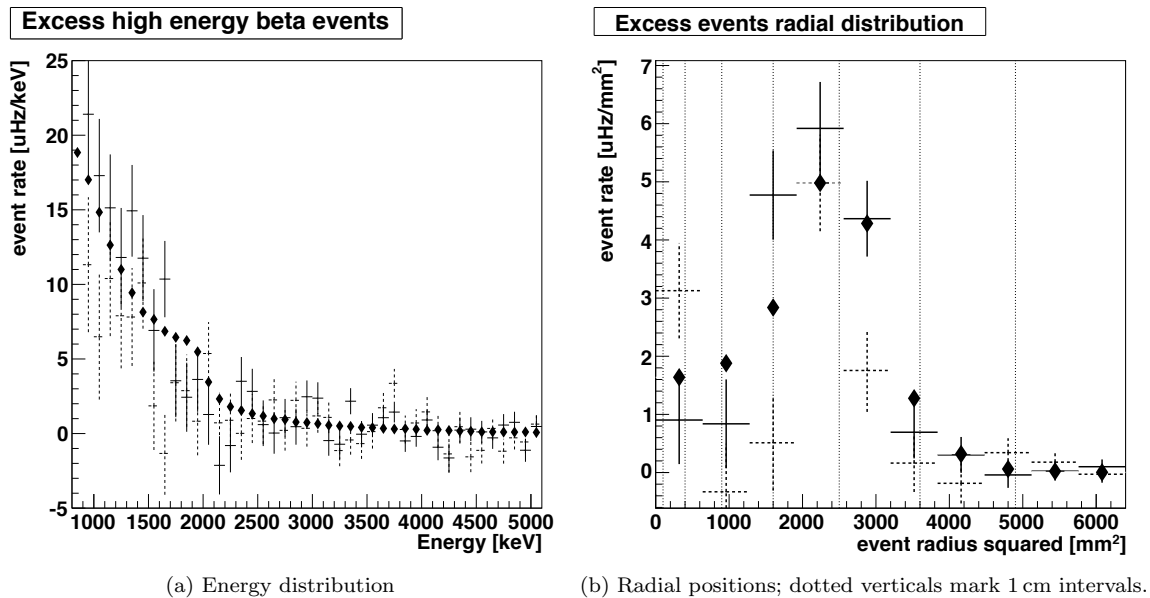


Figure 7.18: Data/MC comparison for high energy excess beta events after background subtraction. Solid lines: East data; dashed: West; diamond markers: MC.

“Combined” simulation then provides an estimate for the background contributions hidden under the beta decay spectrum. Figure 7.18 shows the “Combined” simulation energy and event positions compared to the high-energy excess events in the data.

An estimate for the neutron background impact on the asymmetry can be made by subtracting these MC-predicted spectra out of the observed data, scaled to match the observed excess On+Off counts, allowing for an additional $\pm 10\%$ variation in the overall scaling factor for each detector side and $\pm 25\%$ variation from scaling with the observed spin flipper on/off decay rates. The result of such analysis is shown in Figure 7.19, indicating an overall uncertainty at below the 0.01% level, similar to past assessments of neutron generated background impacts, but perhaps with increased understanding of the mechanism behind observed neutron-generated counts.

7.6 Theory contributions

Neutron decay parameters like A_0 , τ_n , etc., as canonically defined in the literature, pertain to the decay of neutrons into infinitely massive, neutrally charged, point-like protons. Since neutrons available in the lab tend to decay into somewhat more complex physical protons, we rely on theorists to provide the corrections necessary to translate between parameters observed in physical neutron decay and their “spherical cow model” counterparts.

Modifications to the shape of the unpolarized decay spectrum primarily cancel out in the super-ratio, leaving only tiny corrections to corrections. Corrections to the unpolarized spectrum shape, as discussed in subsection 4.5.2.2, are included in the MC, so their infinitesimal effects are accounted for in the corrections procedure (primarily Δ_3).

Theory indicates two main modifications to the asymmetry. A recoil order correction accounts for the proton’s finite mass, along with the Weak Magnetism coupling in the transition. Radiative

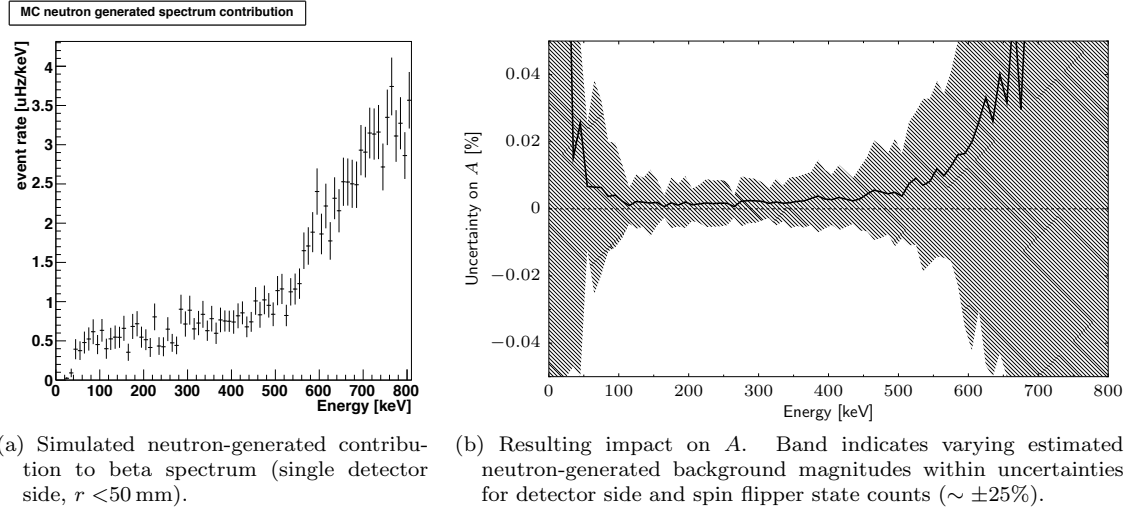


Figure 7.19: MC estimated neutron generated background.

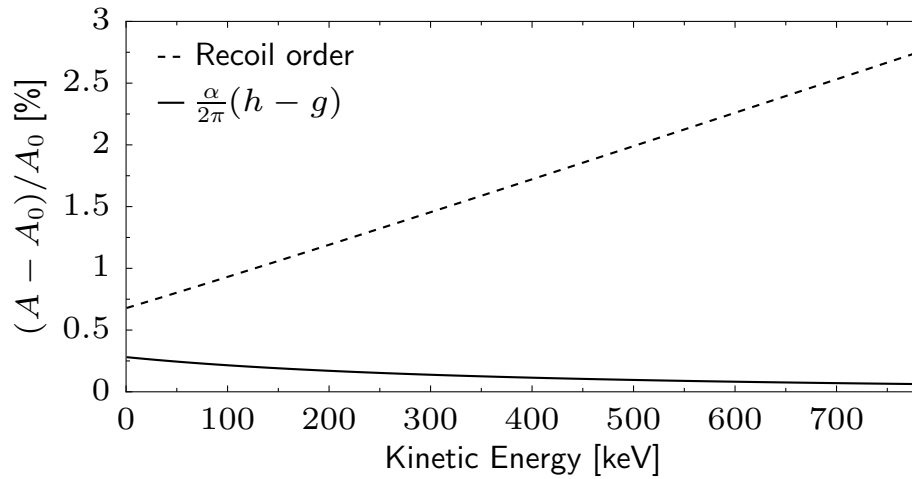


Figure 7.20: Recoil order and radiative theory modifications to observed asymmetry.

corrections account for the proton and electron's charge. Together, these produce the observed asymmetry $A(E) = (1 + \text{RO})(1 + \frac{\alpha}{2\pi}(h - g))A_0$. Since the Δ_2 , Δ_3 corrections have already nominally corrected the asymmetry to the form $\frac{\beta}{2}A(E)$, correction for these effects consists of simply dividing out the terms from theory (and calculating the resulting statistics-weighted asymmetry change over the analysis window, as for all other corrections). Figure 7.20 shows a plot of the two corrections, which are further described below.

7.6.1 Recoil order effects

The first calculation of recoil order effects (recoil and Weak magnetism) was from Bilen'kiĭ *et al.* [Bil+60], 1960. Bilen'kiĭ's recoil-order-corrected asymmetry is

$$A^{\text{RO}}(E) = A_0 + \frac{2(\lambda + \mu)}{(1 + 3\lambda^2)^2} \frac{1}{M} \left[\left(\lambda^2 + \frac{2}{3}\lambda - \frac{1}{3} \right) E_0 - \left(\lambda^3 + 3\lambda^2 + \frac{5}{3}\lambda - \frac{1}{3} \right) E - 2\lambda^2(\lambda - 1) \frac{m_e^2}{E} \right], \quad (7.40)$$

where M is the neutron mass, E the electron's total energy and E_0 the endpoint energy, $\mu \equiv \mu_p - \mu_n \approx 4.706$, and $\lambda \equiv |g_A/g_V|$. So far as Standard Model terms go, the Bilen'kiĭ *et al.* results for the recoil order correction have remained unchanged in subsequent literature (such as Wilkinson's 1982 review of neutron decay corrections [Wil82]). This formula is used for the $1 + \Delta_{\text{RO}}(E) \equiv A_0/A^{\text{RO}}(E)$ recoil-order theory contribution, which produces a statistics-weighted total contribution $\Delta_{\text{RO}} = -1.71\%$ over the 2010 analysis energy window.

7.6.1.1 Additional BSM terms

A more general approach, retaining form factors even for Standard Model forbidden terms, is carried out in an expansive review of recoil order effects in nuclear beta decays by Holstein in 1974 [Hol74]. Holstein extends the formalism in great detail to a wide variety of decay correlations.

A 2001 paper by Gardner and Zhang [GZ01] conveniently consolidates the theory relevant to A and a measurements, indicating contributions from beyond-Standard-Model second-class currents. They note that their results are consistent with Holstein's, and with Bilen'kiĭ when non-Standard-Model terms are dropped. Gardner and Zhang's notation defines six form factors $f_1(q^2), \dots, g_3(q^2)$ for each term in the generalized model for polarized neutron decay,

$$\langle p | J^\mu(0) | \vec{n} \rangle = \bar{u}_p \left[f_1 \gamma^\mu - i \frac{f_2}{M} \sigma^{\mu\nu} q_\nu + \frac{f_3}{M} q^\mu + g_1 \gamma^\mu \gamma_5 - i \frac{g_2}{M} \sigma^{\mu\nu} \gamma_5 q_\nu + \frac{g_3}{M} \gamma_5 q^\mu \right] u_n, \quad (7.41)$$

so, in terms of traditional coupling constant names,

$$f_1(0) = g_V, \quad g_1(0) = -g_A, \quad f_2 = \frac{g_M - g_V}{2}, \quad g_2 = \frac{g_{II}}{2}, \quad f_3 = \frac{g_S}{2}, \quad g_3 = \frac{g_P}{2}. \quad (7.42)$$

Further notation defines $\tilde{f}_i \equiv f_i(0)/f_1(0)$ (and similar for \tilde{g}_i). In this scheme, the asymmetry is given by

$$A(E) = A_0 + \frac{1}{(1 + 3\lambda^2)^2} \frac{1}{M} \left\{ [4\lambda^2(1 - \lambda)(1 + \lambda + 2\tilde{f}_2) + 4\lambda(1 - \lambda)(\lambda\tilde{g}_2 - \tilde{f}_3)] \frac{m_e^2}{E} + \left[\frac{2}{3}(1 + \lambda + 2\tilde{f}_2)(1 - 5\lambda - 9\lambda^2 - 3\lambda^3) + \frac{4}{3}\tilde{g}_2(1 + \lambda + 3\lambda^2 + 3\lambda^3) \right] E + \left[\frac{2}{3}[1 + \lambda + 2(\tilde{f}_2 + \tilde{g}_2)](3\lambda^2 + 2\lambda - 1) \right] E_0 \right\} + O\left(\frac{E_0^2}{M^2}\right). \quad (7.43)$$

7.6.2 Radiative effects

The radiative correction is the Shann/Sirlin $\frac{\alpha}{2\pi}(h-g)$ [Sir67; Sha71] discussed in subsection 1.1.2.10,

$$h - g = 4 \left(\frac{\tanh^{-1} \beta}{\beta} - 1 \right) \left(1 - \beta^2 + \frac{E_0 - E}{8E} \right) \frac{E_0 - E}{3E\beta^2} + \frac{\tanh^{-1} \beta}{\beta} \left(2 - 2\beta^2 - \frac{(E_0 - E)^2}{6E^2} \right), \quad (7.44)$$

which has been upheld by later theory calculations such as [GT92]. Over the 2010 analysis window, this corresponds to a correction of $\Delta_{\text{rad}} = -0.10\%$.

A newer approach using effective field theory [And+04; GGC06] apparently gives results generally agreeing with Shann to within 0.01% of A [You12].

Note that in both the prior UCNA result [LMH+10] and the PERKEO II result of [Abe+02], this correction was applied with the wrong sign.

7.7 2010 asymmetry extraction

7.7.1 Data selection cuts

Data for inclusion in the analysis is selected from the total dataset after a set of cuts on time and position. These cuts are not critical to the analysis in the sense that the rest of the analysis procedure would correct for their omission — though at the expense of decreased signal-to-noise and increased reliance on MC corrections for electrons interacting with spectrometer walls.

7.7.1.1 Timing cuts

Timing cuts (discarding data within particular time intervals) are applied to the data to improve signal to noise, by removing prompt beam-related backgrounds and any stretches of runs without useful UCN production rates. Such cuts are not strictly necessary, in the sense that there is no systematic effect on the asymmetry by omitting the cuts and letting routine background subtraction handle the difference. All events within 0.05s of a beam pulse (indicated by a scalar counting 1 MHz clock ticks since the arrival of each beam pulse) are removed from the data. Since the accelerator pulse structure sends beam in bursts of 5 pulses at 20 Hz every 5 seconds, this results in 0.25 seconds out of every 5 seconds of running (5%) of run time being cut. Events are also cut from any time period more than 10 seconds after the preceding beam pulse, to remove temporary accelerator dropouts from the data. Similarly, the data is cut whenever the UCN counting monitor immediately upstream of the gate valve falls below 10 Hz rate in a rolling window average over the past 5 s.

Additional timing cuts were added to the beginning of 8 background runs which had been started, outside of the normal run cycle, with neutrons still present in the trap. Brief bursts of unusually noisy wirechamber behavior in three runs(not seen in other runs) were also cut.

7.7.1.2 Position cuts

An $r < 50$ mm radius cut was applied to all events. For Type 0 events, this is right at the edge of where larger-Larmor-radius beta electrons start to hit the wirechamber entrance port wall; the cut removes $\sim 8\%$ of events. Because of the offset between detector sides, backscatters are only fully clear of wall interactions at $r < 45$ mm (or, in a somewhat larger asymmetric region), with the density reduced by $\sim 50\%$ at $r = 50$ mm. However, because this represents a small total portion of events, and wall interactions are accounted for in the Montecarlo (including the detector offset), this is a tiny effect and folded into the MC corrections. Figure 7.21 shows the radial position distributions for each event type, and the MC re-creating the falloff at the wall radius.

7.7.2 Extracted asymmetry

7.7.2.1 Blinding factor removal

Recall from subsection 2.2.3 that a blinding factor was inserted into the run length factors used to form rates entering the super-ratio asymmetry. After the establishment of all analysis procedures, corrections, and uncertainties, the blinding factor is removed by re-compilation of the analysis code to retrieve run timing information without the blinding factor. The UCNA collaboration unblinded the analysis of the 2010 dataset on October 2, 2012, producing the results given below.

7.7.2.2 Octet asymmetries

To check the consistency of the dataset, a lower-statistics asymmetry may be extracted from every data pulse pair (or half-octet and octet combinations of pulse pairs). Figure 7.22 shows these for the 2010 dataset. Distributions are consistent with statistical scatter, with the gain fluctuations systematic uncertainty also covering the slightly (not statistically significantly) high χ^2/ν .

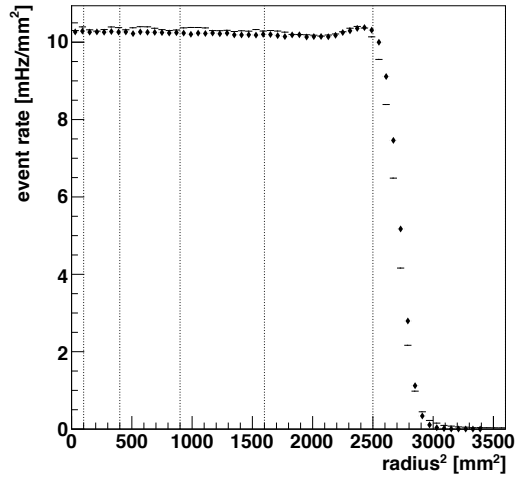
7.7.2.3 Complete dataset

The total combined dataset produces the beta decay spectrum shown in Figure 7.23, and asymmetry curves shown in Figure 7.24. Because of the different polarization corrections for the earlier and later halves of the dataset, the corrected asymmetry is determined for the before- and after-guide-contamination sections separately. The resulting corrected asymmetries before and after, separating out the statistical and systematic polarization uncertainties from other systematics,

$$\begin{aligned} A_0^I &= -0.11851(75)_{\text{stat}}(12)_{\text{stat}}^P(65)_{\text{syst}}^P(72)_{\text{syst}} \\ A_0^{II} &= -0.12100(78)_{\text{stat}}(38)_{\text{stat}}^P(66)_{\text{syst}}^P(72)_{\text{syst}}. \end{aligned} \tag{7.45}$$

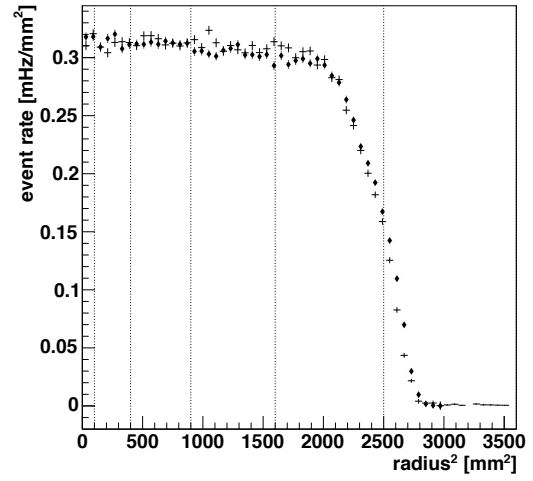
Note that the difference between these two measurements is $A_0^I - A_0^{II} = 0.00249(115)_{\text{stat}}$, a 2.2σ discrepancy on the edge of concern. If the systematic errors are less than completely correlated between the two sections (decreasing the combined uncertainty), the statistical strength of this discrepancy is diminished.

Type 0 events radius distribution



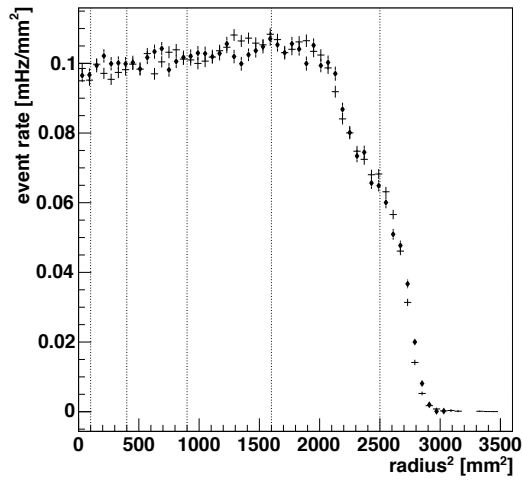
(a) Type 0.

Type I events radius distribution



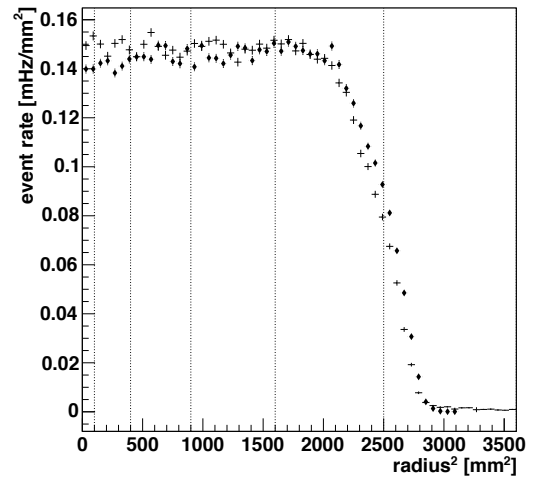
(b) Type I.

Type II events radius distribution



(c) Type II.

Type III events radius distribution



(d) Type III.

Figure 7.21: Event radial distributions for 2010 data (super-sum). Diamond markers are MC simulation, normalized to same total counts. Vertical lines mark 1 cm intervals, including the $r^2 < 2500 \text{ mm}^2$ analysis position cut.

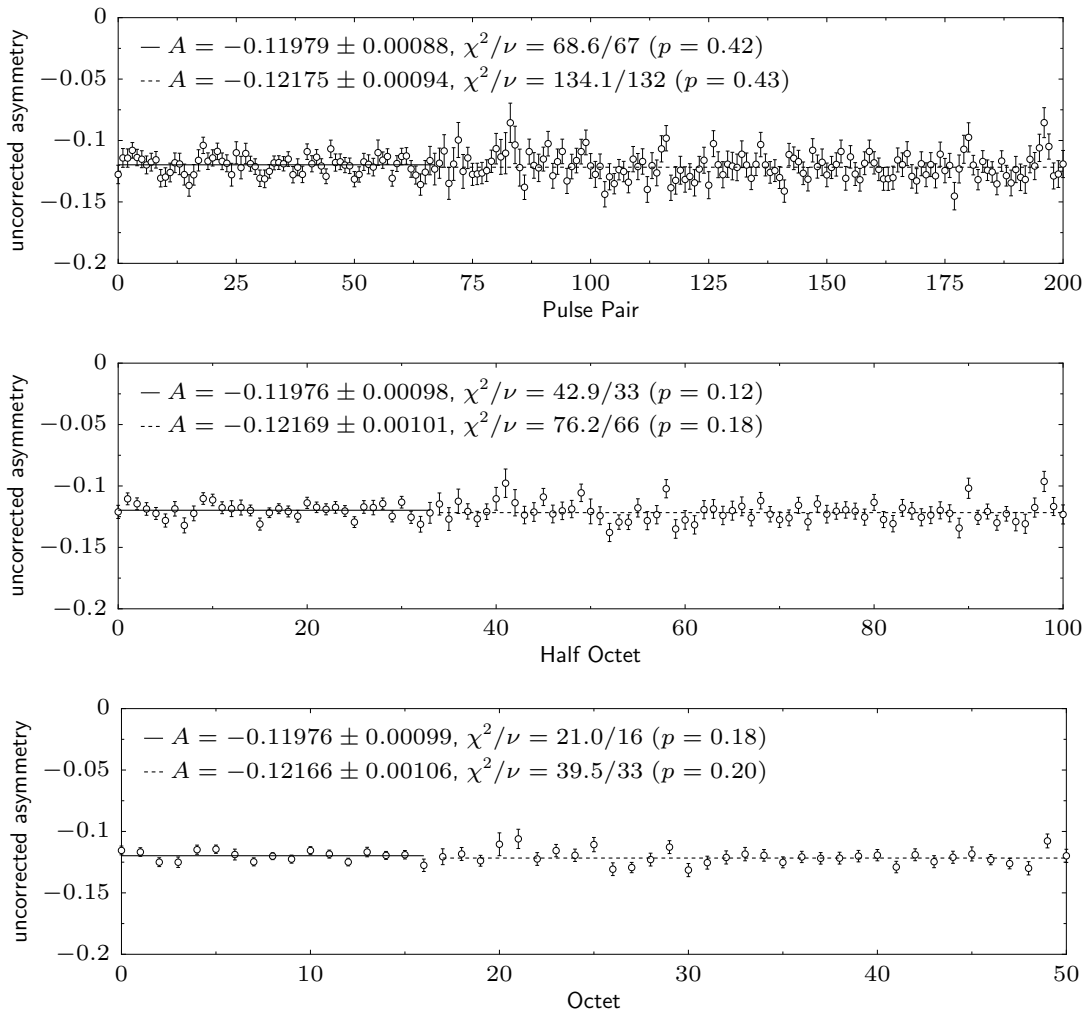


Figure 7.22: Asymmetries (uncorrected) for pulse-pairs, half-octets, and octets in 2010 data. Averages and χ^2/ν given individually for set of runs before and after guide contamination incident, based on statistical errorbars alone.

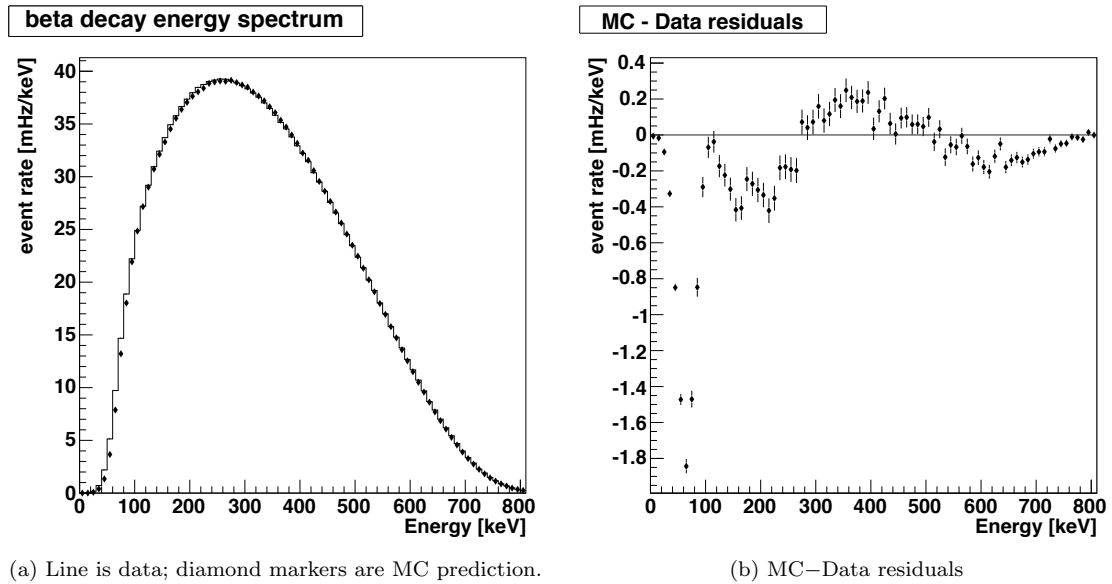


Figure 7.23: Beta decay energy spectrum from 2010 dataset, “super sum” over detector sides and spin flipper states.

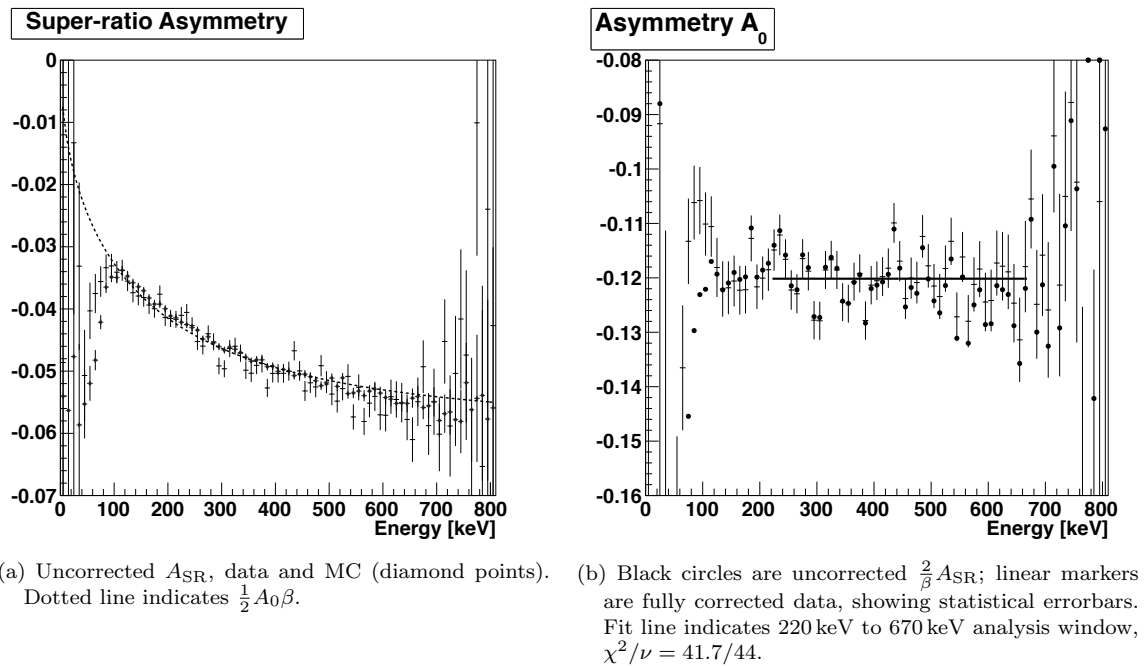


Figure 7.24: Combined asymmetry from 2010 dataset.

7.7.2.4 Combined result

Following the formalism given in Appendix B for optimal statistical combination of correlated measurements (treating the systematic uncertainties in the two sections as 100% correlated across the sections, though uncorrelated with each other), the correlation between the two measurements is $C_{12} = 0.59$, and the optimal weights are $w_I, w_{II} = 0.59, 0.41$. This produces the total UCNA 2010 dataset result

$$A_0 = -0.11954(55)_{\text{stat}}(98)_{\text{syst}} = -0.11954(112) \Rightarrow \lambda = -1.2756(30). \quad (7.46)$$

Expanding the analysis energy window has little impact on the answer, producing $A_0 = -0.11951$ over 150 keV to 750 keV or $A_0 = -0.11938$ over 100 keV to 800 keV.

For combining this measurement with the preceding UCNA result [LMH+10; Pla+12] $A_0 = -0.11966(89)_{-140}^{+123}$, the polarization uncertainties are treated as independent, and other systematics (dominated by energy reconstruction) as correlated between the measurements. This prior measurement should first be corrected by -0.20% , to correct for a sign error on the radiative theory contribution applied ($+0.10\%$ was used in place of -0.10%). Applying the statistical combination formalism of Appendix B using either the upper or lower asymmetric errorbar gives practically the same result (differing only by $\Delta A_0 = 0.00001$), with a total correlation $C_{12} = 0.5$ and optimal weights of 0.8, 0.2 for the newer and older measurement, respectively. This gives a UCN combined result of $A_0 = -0.11952(110)$.

Chapter 8

Conclusion

8.1 Looking behind

Figure 8.1 compares the experimental state of electroweak parameters experiment in 2010, when the primary dataset discussed in this thesis was being collected, and in late 2013, after the analysis was completed and published. The impetus for the UCNA 2010 measurement is indicated by the state of the field at the time — the 2002 PERKEO II measurement [Abe+02] in moderate disagreement with prior PDG average values, followed by the immense 6.5σ discrepancy between Serebrov’s 2005 UCN trap τ_n measurement [Ser+05] with preceding high-precision measurements.

Developments in the interim temporarily appeared to have resolved the discrepancies. Serebrov published a re-analysis [SF10] of the two τ_n experiments dominating the PDG 2010 average. This analysis identified previously uncorrected systematics, shifting the lifetimes down by ~ -6 s towards Serebrov’s experimental value. These conclusions have been accepted by researchers in the field, and incorporated into revised results for the primary lifetime experiments in the present PDG average [Ber12] of (880.0 ± 0.9) s. PERKEO II published a new, higher-precision result [Mun+13], in agreement with their previous result and stronger disagreement with the pre-Serebrov τ_n - V_{ud} intersection. Around the same time, the UCNA result from the 2010 dataset was published [Men+13], providing an independent cross-check with different systematics from the cold neutron beam experiments. Figure 8.2 shows the history of A measurements, from the final Argonne publication in 1975 through the latest results. By mid-2013, the discrepancies of the preceding decade of Weak decay experiments appeared to be resolved to a tidy conclusion.

While the PDG average for τ_n is dominated by experiments using disappearance of bottled UCN, an alternate method for measuring the neutron lifetime had been developed at the NIST Center for Neutron Research (NCNR) by counting decay-product protons in a cold neutron beam. The 2005 beam lifetime result [Nic+05] of $\tau_n = (886.3 \pm 3.4)$ s was primarily limited by systematic uncertainty on the neutron beam absolute fluence. Improved calibration of the beam fluence detector produced a re-analyzed result in late 2013 [Yue+13] of (887.7 ± 2.2) s, a 3.2σ discrepancy with the PDG average.

8.2 Looking ahead

The continued experimental discrepancy in Standard Model Weak interaction parameters indicates the need for further precision measurements using a variety of complementary methods. At the level

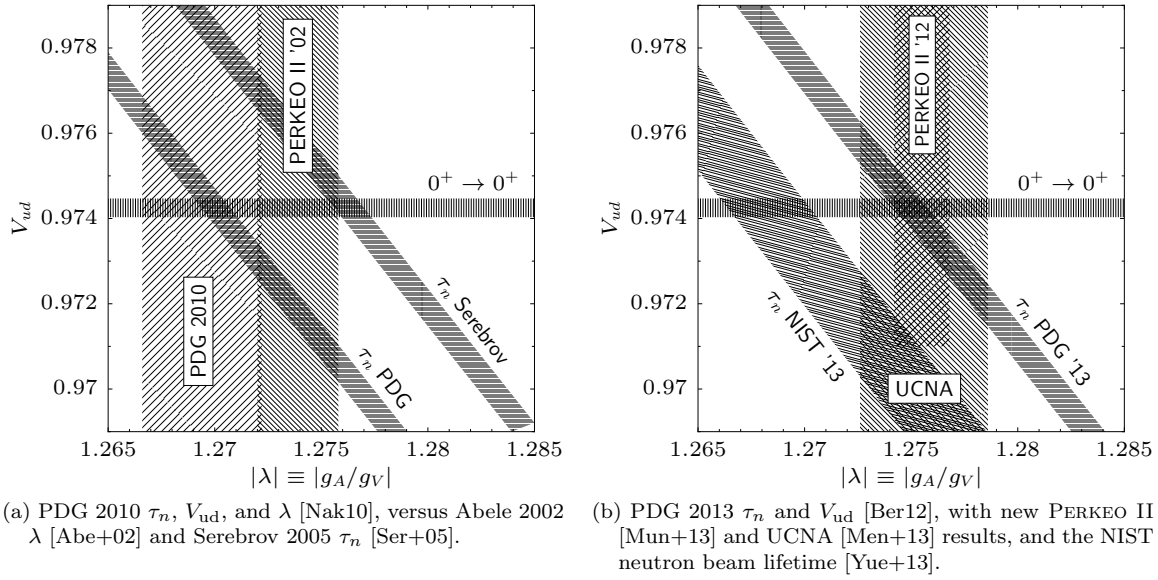


Figure 8.1: Weak decay parameter discrepancies, before and after the UCNA results publication.

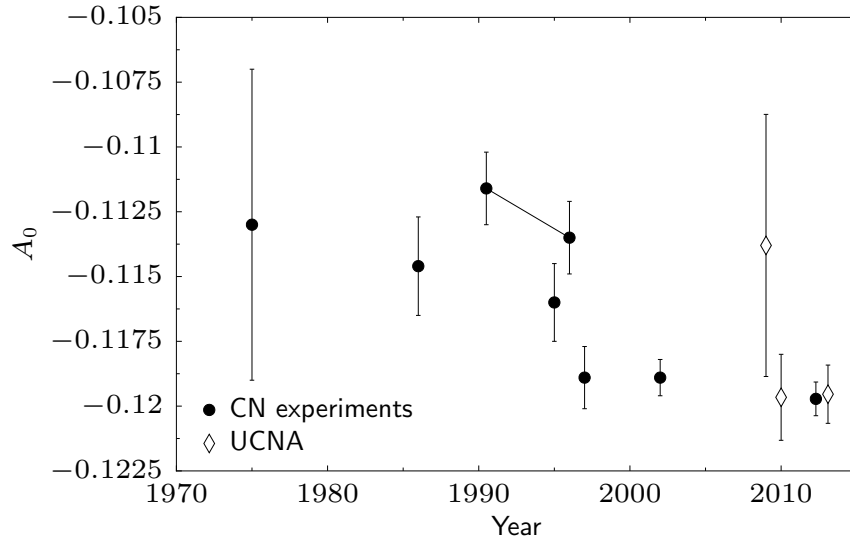


Figure 8.2: History of A_0 experimental results. In time order as shown: [KR75; Bop+86; Ero+90; Sch+95; Yer+97; Abe+97; Abe+02; Pat+09; LMH+10; Mun+13; Men+13].

of precision being reached, experimental methods will also allow more detailed tests of Standard Model assumptions — such as the negligible contribution of second-class currents to beta decay — that have remained basically unchallenged since the development of Weak interactions theory half a century ago. Specifically, details of the energy dependence of the asymmetry become interesting for constraining additional recoil-order couplings beyond the $V - A$ decay form [PHY13]. Expanding trustworthy detector response to a wider energy window (especially on the low end, where statistics are abundant) may be especially helpful. Additionally, precision measurements of other neutron decay correlations can provide sensitivity to novel non-Standard-Model physics.

8.2.1 UCNA 2011-2013 dataset

The UCNA experiment already has a few more years’ data collected since 2010, awaiting detailed analysis. This 2011-2013 dataset contains all the ingredients for a result with significantly lower systematic uncertainty: improved polarimetry data, extra-thin decay trap windows to reduce missed backscatters, and an expanded set of calibration sources to map out energy response (especially the critical low-energy region).

8.2.1.1 Polarimetry improvements

Polarimetry improvements should significantly reduce the largest systematic uncertainty from the 2010 dataset analysis. Starting in 2011, a new UCN shutter was added to the UCNA neutron guide system at the entrance to the SCS. This allows neutrons to be bottled in the decay trap while the upstream guide system is emptied, permitting more “clean” measurements of depolarized neutron counts with reduced neutron-transport-related corrections. In addition, new coated UCN guides replaced guides potentially contaminated with depolarizing material in 2010.

8.2.1.2 Reduction of MC correction uncertainties

Continued incremental improvements in available MC physics codes for electron transport are welcomed, but such progress is largely outside the hands of UCNA collaborators, and reductions in uncertainties remain difficult to assess. The more reliable way to reduce MC uncertainties is to reduce physical causes for the corrections where possible, and, where not possible, to develop new ways to directly measure system parameters.

Based on the research of [Hoe03] on producing strong, thin substrates by spin-coating 6F6F fluorinated polyimide foils, new extra-thin (~ 120 nm to 200 nm 6F6F with ~ 150 nm beryllium coating) decay trap windows were installed in the spectrometer in Fall of 2012. Preliminary simulations indicate a reduction of 30–50% in the Δ_2 correction for missed backscatters (with correspondingly smaller reliance on and uncertainty from the MC correction).

The Δ_3 correction decreases more slowly with decay trap window reduction. Future work may allow direct measurement and characterization of detector angular acceptance, using calibration sources that tag the origin time of electron producing events to allow estimation of pitch angle from time of flight. Work is underway to prototype both a radionuclide decay source using an avalanche photodiode (APD) to time initial events, and a pulsed photocathode electron gun. Direct measurement of pitch-angle-dependent system response may eliminate dependence on MC for this largest correction.

8.2.1.3 Energy calibration

A new set of radioisotope calibration sources were added, starting in 2011, to the ^{139}Ce , ^{113}Sn , and ^{207}Bi set used in 2010. The ^{109}Cd , ^{114m}In , and ^{137}Cs sources incorporated into the calibration routine supply additional independent calibration points, allowing finer mapping of PMT linearity with increased confidence, especially in the lower-energy range that dominates A uncertainties. Multiple sets of activated xenon runs, and an expanded LED pulser system, provide additional inputs for improved characterization of detector response.

8.2.2 Next-generation decay measurements

After completion of system characterization measurements for analysis of the 2011–2013 datasets, the UCNA spectrometer may become home to new correlation experiments presently under development. Replacing the wirechamber and scintillators with segmented silicon detectors, and using an open-ended decay trap, the spectrometer system would be capable of also detecting the recoiling proton (providing a measurements of the a and B correlations alongside A) from UCN beta decay. Though a and B measurements are, relative to A , comparatively insensitive for determining λ , they provide additional sensitivity to non-Standard-Model contributions. A magnetic trap UCN neutron lifetime experiment [Wal+09; Sal+14] is also in preparation to share the LANL UCN source in the UCNA experimental hall.

Complementary cold neutron beam measurements are also underway. A new PERKEO III spectrometer [Mär+09] returns to the original PERKEO design of a neutron beam along the axis of a magnetic field (for a large decay volume), with the field bending out of the beamline towards detectors at the ends. However, a pulsed CN beam allows decays in the field bends to be cut by time-of-flight, avoiding the large magnetic mirroring corrections of the first PERKEO spectrometer.

8.2.3 Future UCN source prospects

At the time of writing, several higher flux next generation UCN sources are under development, along with continued upgrades to existing facilities. The LANL experimental area is being upgraded with multiple UCN beamlines, for simultaneous operation of other experiments (such as the magnetic trap lifetime) alongside the UCNA apparatus. An SD_2 source, using similar operating principles to the LANL source with a larger source volume, has been commissioned at the Paul Scherrer Institut (PSI) [Ang+09; Lau11], and is beginning to provide UCN to experiments. The Spallation Neutron Source (SNS) at Oak Ridge National Laboratory provides the world’s highest pulsed flux of neutrons, from an accelerator-driven spallation target. One of the 24 beamlines at SNS, the Fundamental Neutron Physics Beamline (FNPB), is available for fundamental physics research, and provides a cold neutron port that will feed into a superfluid ^4He (“helium-II”) superthermal UCN source. Another UCN user facility using a spallation target with a helium-II UCN source is under construction at TRIUMF [Mar+08], the particle physics national laboratory in Vancouver, Canada. A large ^4He UCN “supersource” is under development at PNPI [Ser11], slated for operation in 2016.

The commissioning of higher-flux sources for cold and ultracold neutrons will provide high statistics for future precision experiments. The promised future higher statistics will challenge experimentalists to assure matching systematic precision.

Appendix A

Sealed source calibration radioisotopes

I have generally followed the adopted values in Nuclear Data Sheets for modeling radioisotope decays, including conversion electron production coefficients (with details for each calibration source given in the following sections). The Nuclear Data Sheets evaluations (with full details available in ENSDF format [Tul96]) include a mixture of theory and experiment for determining decay parameters. The state-of-the-art for conversion electron theory is encapsulated in the **BrIcc** (Band-Raman Internal conversion coefficients) package [Kib+08], which has been adopted for use in new Nuclear Data Sheets publications, and often exceeds experimental data for accuracy. Table A.1 gives **BrIcc** calculations for the conversion electron sources used in UCNA. The only discrepancy of note between **BrIcc** and the values adopted for the 2010 UCNA data analysis is an 0.5 keV reduction in the average electron energy associated with the 569.7 keV gamma in ^{207}Bi decay (negligible compared to overall calibration uncertainty). Note, for calculating the uncertainty on the average energy of a peak due to shell splittings, that the uncertainty of a weighted average with (uncorrelated) uncertainty on the weights is given by:

$$\frac{\sum_i (w_i \pm dw_i) E_i}{\sum_i w_i \pm dw_i} = \bar{E} \pm \frac{\sqrt{\sum_i [(E_i - \bar{E}) dw_i]^2}}{\sum_i w_i}, \quad \bar{E} \equiv \frac{\sum_i w_i E_i}{\sum_i w_i} \quad (\text{A.1})$$

A.1 2010 conversion electron sources

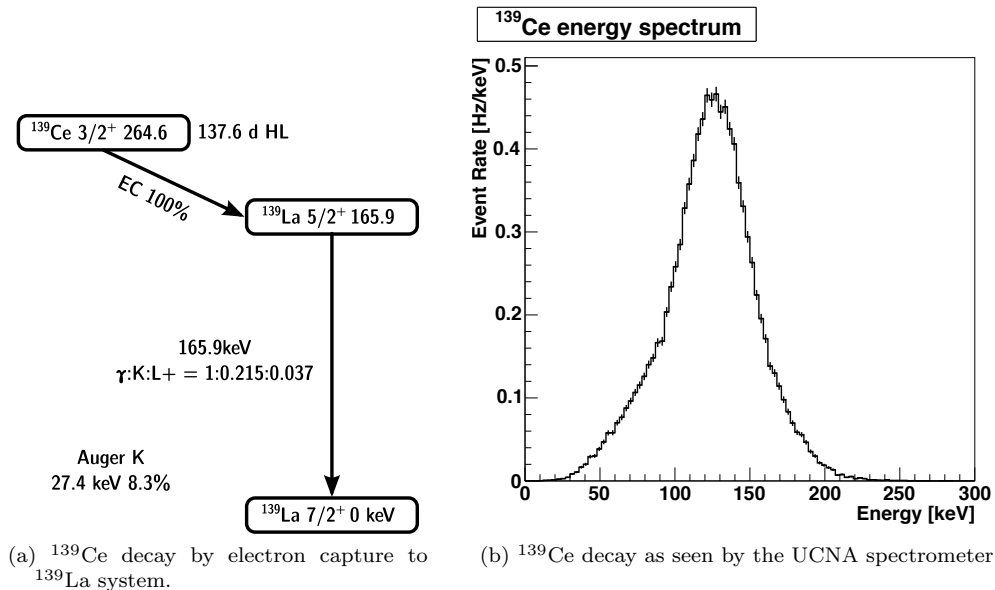
A.1.1 ^{139}Ce

The decay of ^{139}Ce by electron capture to ^{139}La is shown in Figure A.1. ^{139}Ce anchored the low energy end of energy calibrations for 2010. Following the recommendations of [BHS07; Bur01], α_K is taken from the survey of experiments [Han85], and α_L from the experiment [HM76]. L subshell splittings, and α_{M+} based on $K:M+=28(1)$, are from the experiment [Gei+65]. These give conversion electron ratios for the 165.9 keV gamma of:

$$\alpha_K = 0.2146(10), \quad \alpha_L = 0.0289(12) [1 : 0.072(3) : 0.016(1)], \quad \alpha_{M+} = .0077(3) \quad (\text{A.2})$$

Z	47 Ag	57 La	49 In	49 In	82 Pb	56 Ba	82 Pb
E_γ	88.0336(1)	165.8575(11)	190.27(3)	391.698(3)	569.698(2)	661.657(3)	1063.656(3)
type	E3	M1	E4	M4	E2	M4	M4+E5
K	11.41(15)	0.2231(31)	2.56(3)	0.444(6)	0.01583(22)	0.0915(12)	0.0943(13)
L_{tot}	12.06(16)	0.0300(4)	2.031(28)	0.0862(12)	0.00439(6)	0.01648(23)	0.0238(3)
L_2/L_1	5.79(11)	0.0689(13)	4.22(8)	0.1580(31)	0.662(13)	0.1412(27)	0.204(4)
L_3/L_1	6.75(13)	0.01478(29)	3.37(6)	0.208(4)	0.231(4)	0.1160(22)	0.0909(17)
M_{tot}	2.47(3)	0.00622(8)	0.429(6)	0.01750(24)	0.00108(1)	0.00352(4)	0.00589(8)
M_2/M_1	6.44(12)	0.0748(14)	4.69(9)	0.168(3)	0.743(14)	0.1525(30)	0.226(4)
M_3/M_1	7.55(14)	0.0161(3)	3.76(7)	0.226(4)	0.271(5)	0.1291(25)	0.1072(21)
M_4/M_1	0.0685(13)	0.00026	0.0672(13)	0.00201(3)	0.00270(5)	0.00117(2)	0.00171(3)
M_5/M_1	0.0876(17)	0.00022	0.0606(12)	0.00075(1)	0.00172(3)	0.00030	0.00029
N_{tot}	0.386(5)	0.00137(1)	0.0725(10)	0.00315(4)	0.00027	0.00076(1)	0.00151(2)
N_2/N_1	5.80(11)	0.0716(14)	4.30(8)	0.1521(30)	0.736(14)	0.1450(28)	0.222(4)
N_3/N_1	6.76(13)	0.01545(30)	3.42(6)	0.204(4)	0.269(5)	0.1234(24)	0.1064(21)
N_4/N_1	0.0403(7)	0.00024	0.0463(9)	0.00137(2)	0.00293(5)	0.00105(2)	0.00186(3)
N_5/N_1	0.0506(10)	0.00020	0.0414(8)	0.00051(1)	0.00184(3)	0.00027	0.00031
N_6/N_1	—	—	—	—	0.00000	—	0.00000
N_7/N_1	—	—	—	—	0.00000	—	0.00000
O_{tot}	0.00140(1)	0.00022	0.00207(2)	0.00019	0.00005	0.00011	0.00030
O_2/O_1	—	0.0607(12)	2.26(4)	0.0799(15)	0.663(13)	0.1217(24)	0.200(3)
O_3/O_1	—	0.01292(25)	—	—	0.232(4)	0.1008(19)	0.0918(18)
O_4/O_1	—	0.00009	—	—	0.00172(3)	—	0.00109(2)
O_5/O_1	—	—	—	—	0.00106(2)	—	0.00018
P_{tot}	—	0.00002	—	—	0.00000	0.00001	0.00003
P_2/P_1	—	—	—	—	0.395(7)	—	0.1191(23)
α_{tot}	26.3(3)	0.261(3)	5.10(7)	0.551(7)	0.02163(30)	0.1124(15)	0.1257(17)
$\langle E_e \rangle$, keV	75.33(8)	131.82(7)	174.61(9)	368.52(6)	502.00(23)	630.27(8)	994.56(23)

Table A.1: BRICc [Kib+08] (v2.3a 30-Jun-2013) conversion electron predictions from ENSDF input, for conversion electron sources used for UCNA. Electron shell binding energies taken from [BB67] to calculate average conversion electron energy $\langle E_e \rangle$.

Figure A.1: ^{139}Ce decay source.

for an average conversion electron energy of (131.9 ± 0.1) keV.

A.1.2 ^{113}Sn

The decay of ^{113}Sn by electron capture to ^{113}In is shown in Figure A.2. ^{113}Sn offers a relatively “clean and simple” spectrum in the lower-middle energy range, allowing fine details of energy loss to be observed in the tails of the distribution.

Following the recommendations of [Bla10], I take the conversion electrons for the 391.7 keV gamma ($I_\gamma = 64.97(17)\%$) to be

$$\alpha_K = 0.444(7), \alpha_L = 0.0862(12), \alpha_M = 0.01750(25), \alpha_N = 0.00316(5), \alpha_{O+} = 0.000194(3) \quad (\text{A.3})$$

resulting in a conversion electron average energy of 368.1 ± 0.1 keV. For the 255.1 keV gamma ($I_\gamma = 2.11(8)\%$),

$$\alpha_K = 0.039(5), \alpha_L = 0.0054(11), \alpha_M = 0.00105(22), \alpha_N = 0.00019(4), \alpha_{O+} = .0000127(14) \quad (\text{A.4})$$

for a 230.7 keV average conversion electron energy, hidden under the tail of the main peak. Because of the 99.5 min half-life of the 391.7 keV level, these two lines are not seen in coincidence.

A.1.3 ^{207}Bi

The decay of ^{207}Bi by electron capture to ^{207}Pb is shown in Figure A.3, as described in [KL11]. ^{207}Bi offers a two-for-one deal on conversion electron lines, providing mid- and upper-energy peaks at ~ 0.5 MeV and ~ 1 MeV. The internal conversion cascades from electron capture to multiple levels of ^{207}Pb give the ^{207}Bi source a rich structure of coincidences (in same or opposite detectors)

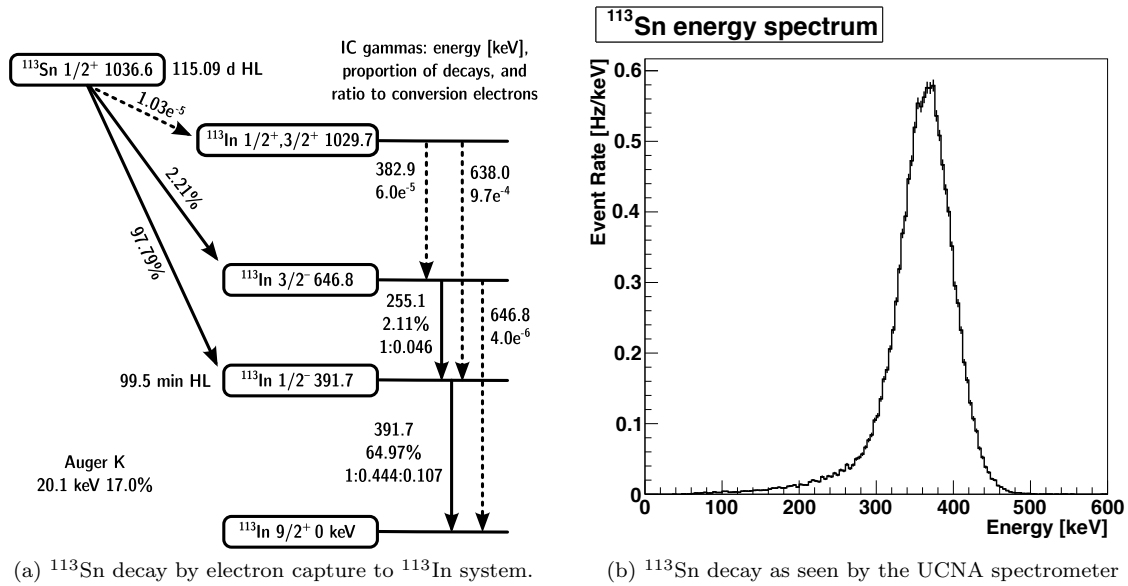


Figure A.2: ^{113}Sn decay source.

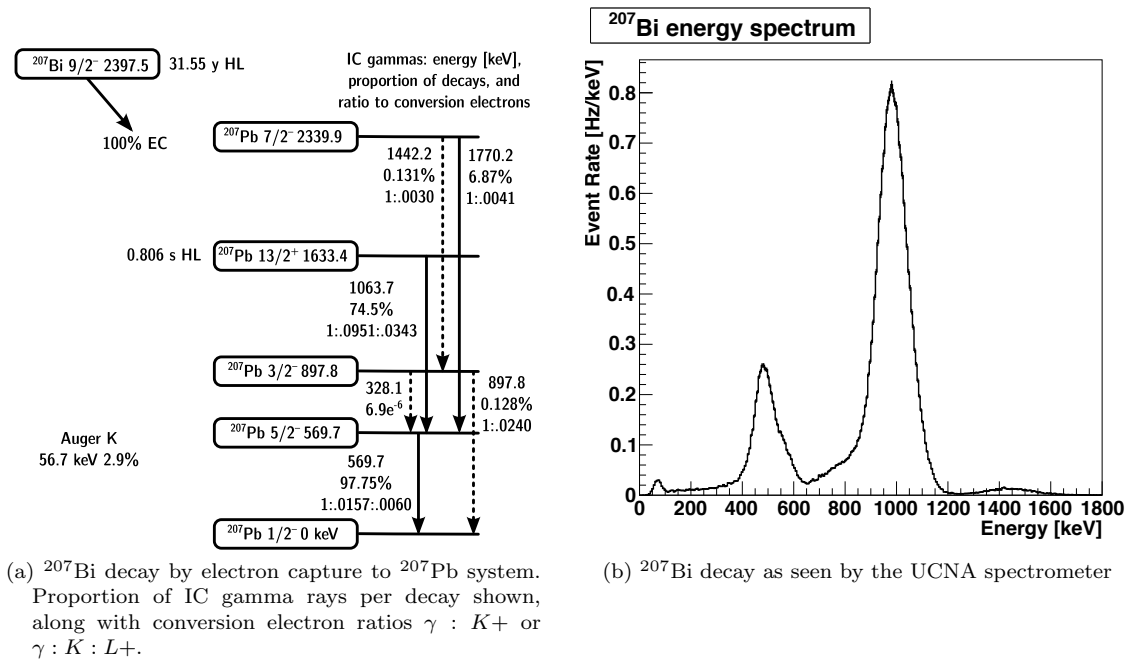


Figure A.3: ^{207}Bi decay source.

between lines. Conversion electrons from the 1770.2 keV gamma will be hidden under coincidences between the ~ 0.5 MeV and ~ 1 MeV lines. ^{207}Bi has a fairly low conversion efficiency, so the source will be accompanied by a high flux of gamma rays (see section A.3 for discussion of associated Compton scattering).

Due to the high-Z nucleus, ^{207}Bi has large binding energies for inner electron shells, and consequently a high energy for Auger K emission at 56.7 keV, which is marginally detectable in the spectrometer after material energy losses. The Auger K peak thus provides a sensitive test of understanding low-energy detector response.

Conversion electron efficiencies are adopted from [KL11], based on experiment. Subshell splittings are taken from the most precise experimental measurement [Fuj+88]. For the 596.7 keV gamma ($I_\gamma = 97.75(3)$),

$$\begin{aligned} \alpha_K &= 0.01572(23), \alpha_L = 0.00452(6) [4.33(15) : 2.84(8) : 1], \\ \alpha_M &= 0.00114(5) [3.70(30) : 3.01(28) : 1], \alpha_{N+} = 0.00029(3) \end{aligned} \quad (\text{A.5})$$

indicating an average line energy of (502.5 ± 0.3) keV. For the 1063.7 keV gamma ($I_\gamma = 74.5(3)$),

$$\begin{aligned} \alpha_K &= 0.0951(23), \alpha_L = 0.0247(6) [10.7(4) : 2.09(8) : 1], \\ \alpha_M &= 0.0059(4) [10.50(53) : 2.10(11) : 1], \alpha_{N+} = 0.00194(12) \end{aligned} \quad (\text{A.6})$$

for an average line energy of (994.8 ± 0.5) keV.

A.2 Post-2010 additional sources

A.2.1 ^{114m}In

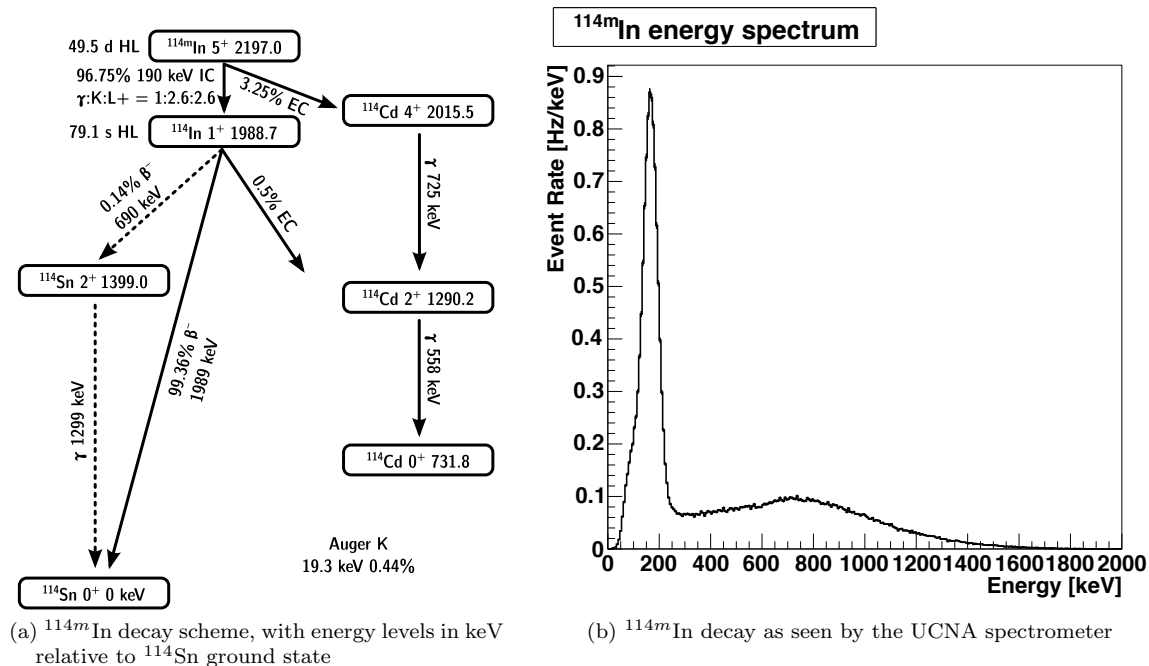
A calibration source using a metastable excited state of ^{114}In was developed for the UCNA experiment, as described in [Wre+11]. A spot of ^{113}In is implanted on a $10\ \mu\text{m}$ -thick aluminum foil (to a depth of ~ 200 nm) by ion beam. The foil is placed in a high neutron flux reactor, resulting in neutron captures to the ^{114m}In 5^+ metastable excited state with a 49.5 day half life. The decay scheme of ^{114m}In is sketched in Figure A.4, as per [Bla12].

96.75% of decays are via internal conversion to the ^{114}In ground state; high conversion efficiency leaves $I_\gamma = 15.56(15)\%$ of all decays for the transition. Conversion electron production is taken from ENSDF theory calculation, which in this case was not provided with uncertainties:

$$\alpha_K = 2.58, \alpha_L = 2.052, \alpha_M = 0.431, \alpha_{N+} = 0.0868 \quad (\text{A.7})$$

Prior best experimental measurement of the conversion efficiency [Red+76] indicates $\alpha_K = 2.00(9)$, 19% lower than theory values. Electron spectra using the UCNA detectors appear consistent with the higher theory predictions, though a precise analysis of this has not been carried out.

The ^{114}In ground state has a 71.9 s half life, beta decaying to ^{114}Sn ((1984 ± 4) keV endpoint) 99.36(6)% of the time. The endpoint of the beta decay is beyond the stopping power of UCNA's 3.5 mm thick scintillator, so, in the observed energy spectrum, higher energy beta electrons that punch through the scintillator show up as a broad distribution in the ~ 800 keV region. Electron

Figure A.4: ^{114m}In decay source.

captures to the ^{114}Cd system are also possible, followed by internal conversions to the stable ^{114}Cd ground state with low conversion efficiency.

A ^{114m}In source was produced and briefly tested in the UCNA spectrometer in 2010, but was not used in the regular calibrations process for the 2010 data. In subsequent years, the ^{114}In implanted foil was re-activated by neutron capture at the beginning of each year's neutron decay season, with the 49.5 day half life sufficing for several months of calibrations.

A.2.2 ^{109}Cd

The decay of ^{109}Cd by electron capture to ^{109}Ag is shown in Figure A.5, as described in [Bla06]. Following the adopted values in [Bla06], $\alpha = 26.0(8) \Rightarrow I_\gamma = 3.70(10)\%$ and shell splittings are taken from theory [HS68] (in reasonable agreement with experiments). L subshell ratios are taken from experiment [Dra+76]. This gives conversion electron coefficients

$$\alpha_K = 11.3(5), \alpha_L = 11.9(5) [0.63(13) : 5.48(18) : 6.11(20)], \alpha_M = 2.41(11), \alpha_{N^+} = 0.43(2) \quad (\text{A.8})$$

for an average energy of (75.3 ± 0.3) keV.

A.2.3 ^{137}Cs

The decay of ^{137}Cs is shown in Figure A.6, as per [BT07]. The isotope features both a first-forbidden beta decay with a (514.03 ± 0.23) keV endpoint in 94.7(2)% of decays, and a second-forbidden decay with an (1176 ± 1) keV endpoint in 5.3(2)% of decays. The shape of these beta decay spectra

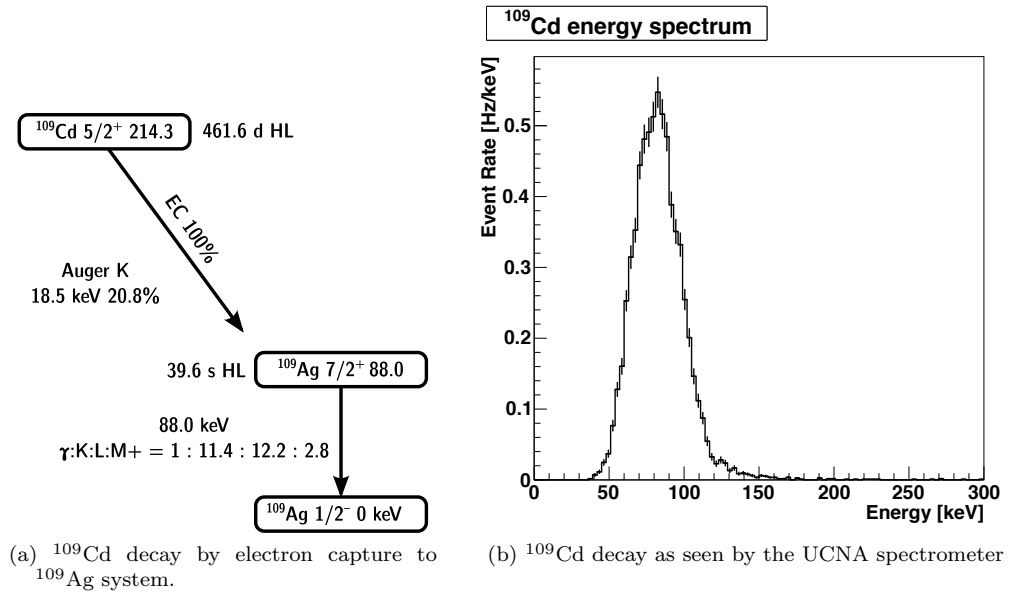


Figure A.5: ^{109}Cd decay source.

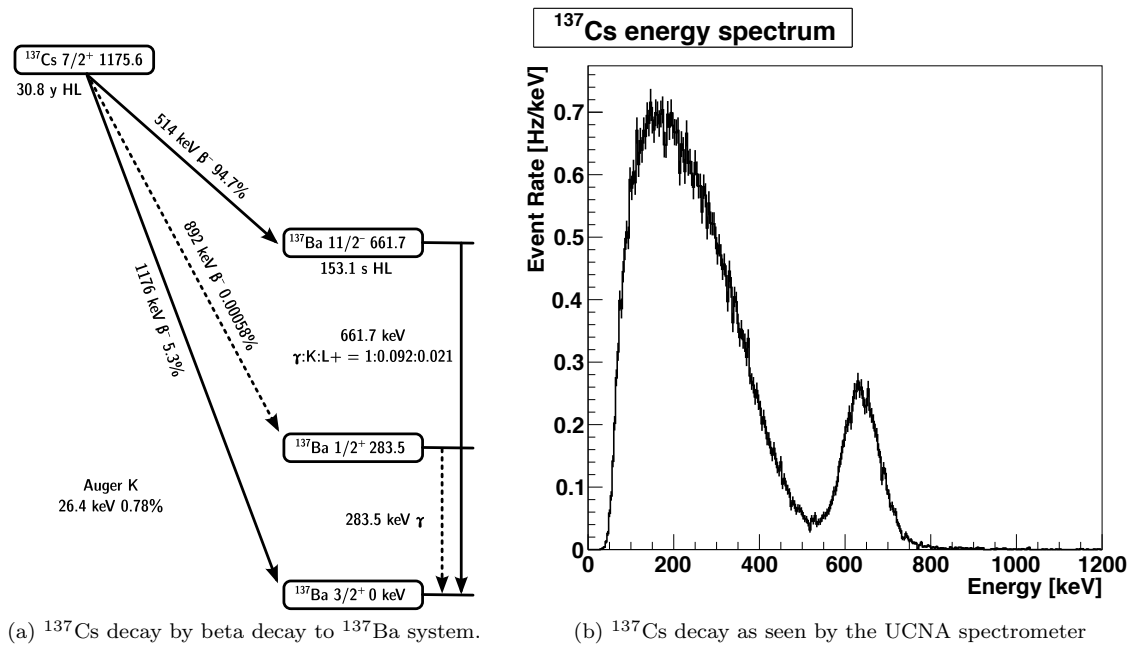


Figure A.6: ^{137}Cs decay source.

are further discussed in subsection 4.5.2.2. A conversion electron line sits just past the lower endpoint, with ENSDF values from theory:

$$\begin{aligned} \alpha_K &= 0.0915(13), \quad \alpha_L = 0.01648(23) [3.41(10) : 1 : 50(3)], \\ \alpha_M &= 0.00352(5), \quad \alpha_N = 0.000759(11), \quad \alpha_{O+} = 0.0001205(17) \end{aligned} \tag{A.9}$$

for an average electron energy of (630.3 ± 0.1) keV. The 153.1 s half-life of the upper ^{137}Ba level means that the beta decays and subsequent conversion electrons are not seen in coincidence. Note, while this line is clearly resolved from the beta spectra at the UCNA detectors' full four-PMT resolution, the spectrum seen by individual PMTs, from positions with lower light transport efficiency to the PMT, may not have sufficient resolution to clearly separate the conversion electron line and beta spectrum.

A.3 Compton scatter electrons

Conversion electron sources often also produce a high flux of gamma rays. The probability of those gamma rays hitting the detectors directly is immensely reduced by geometry, with the detectors far from the decay trap covering a negligibly small portion of the solid angle for gamma rays. However, material close to the decay sources — especially, the sealing foil and holder of the source itself — may produce Compton-scattered electrons, which will reach the detectors.

Figure A.7 shows the positions of detected electrons from simulation of gamma sources (at various energies) in the normal sealed-source holder geometry. See Figure 3.6 for an example with observed data (Comptons plus electrons directly from calibration sources). Figure A.8 shows the Compton production rates predicted by the simulation, for events in the central “spot” of the distribution, which will be mixed in with detected conversion electrons.

For sources with low conversion efficiency, these Comptons may comprise a measurable component of the tail below the main peak. For a somewhat extreme example, consider the 570 keV gamma following ^{207}Bi decay, with $\sim 2.2\%$ conversion efficiency. With $\sim 280 \cdot 10^{-6}$ source foil Comptons per gamma, the line's Compton rate will be $\sim 1.3\%$ of its conversion electron rate. Along with slightly modifying the energy spectrum shape, such Comptons can create back-to-back coincidence events with other conversion electrons, contributing to the observed backscatter distribution from the source.

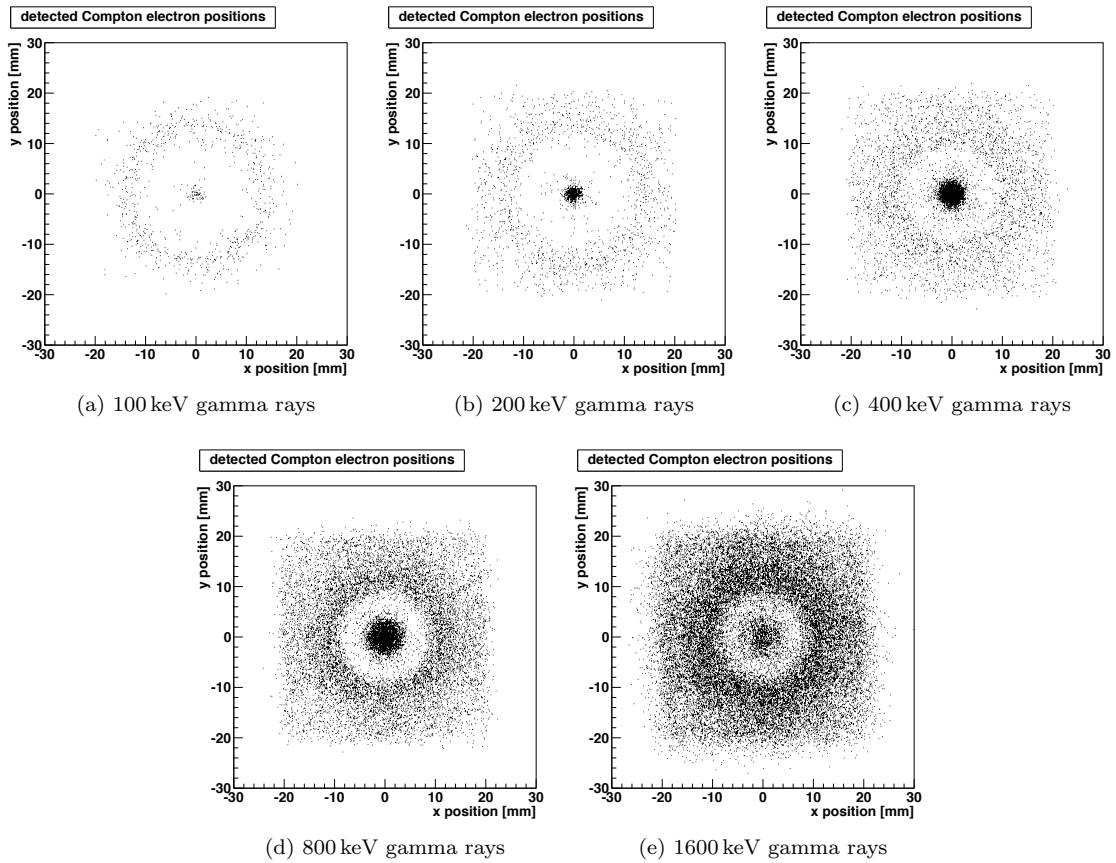


Figure A.7: Simulated positions of detected electrons from gamma rays produced in sealed source holder.

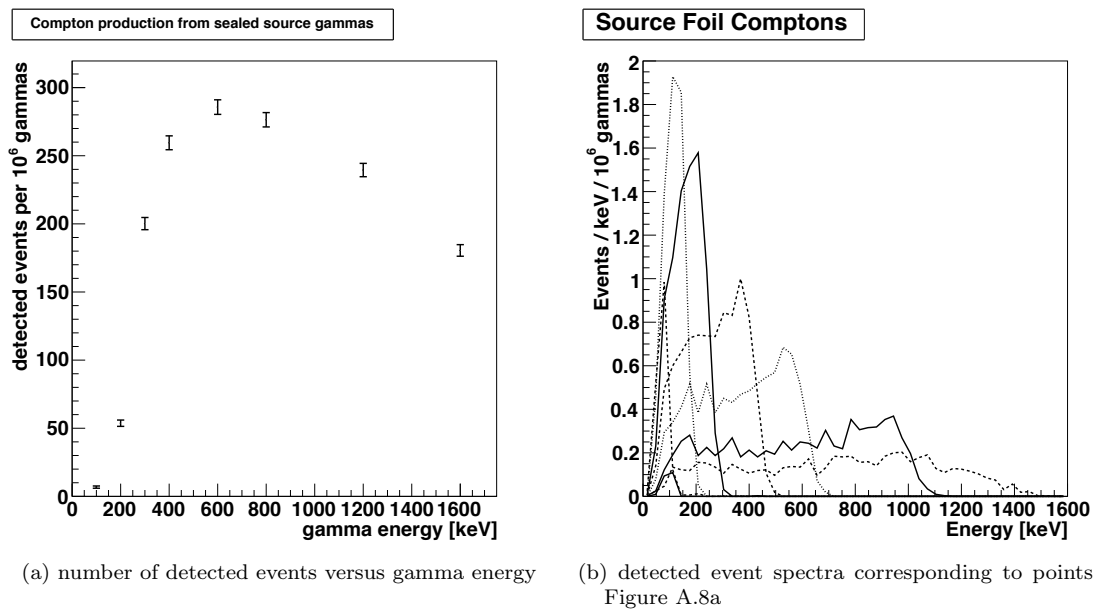


Figure A.8: Simulated Compton electron spectra from gamma rays originating in a sealed source, detected within 7mm radius cut of source.

Appendix B

Combining measurements with correlated errors

Suppose we have several measurements of the form $m_i = A_i \pm \epsilon_1^i \pm \epsilon_2^i \pm \dots$, where A_i is the central value and ϵ_j^i are (possibly correlated) errors. Name the correlations between errors ϵ_j^i and ϵ_l^k by C_{kl}^{ij} , in the special case of wholly uncorrelated errors $C_{kl}^{ij} = 0$, while for fully correlated errors $C_{kl}^{ij} = 1$. By symmetry of correlation, $C_{kl}^{ij} = C_{ij}^{kl}$. Further note that every error is fully correlated with itself, so $C_{ij}^{ij} = 1$.

We can first calculate a ‘‘lump sum’’ error for each measurement m_i by combining all its error components,

$$\epsilon_i \equiv \sqrt{\sum_{j,k} \epsilon_j^i C_{ik}^{ij} \epsilon_k^i}, \quad (\text{B.1})$$

and a ‘‘combined’’ correlation coefficient between measurements m_i and m_j , $C_{ij} = C_{ji}$, so that when we add the lump sum errors between each measurement we get the same result as adding all the individual errors,

$$\begin{aligned} (\pm\epsilon_i \pm \epsilon_j)^2 &= \epsilon_i^2 + \epsilon_j^2 + \epsilon_i C_{ij} \epsilon_j + \epsilon_j C_{ji} \epsilon_i = (\pm\epsilon_1^i \pm \epsilon_2^i \pm \dots \pm \epsilon_1^j \pm \epsilon_2^j \pm \dots)^2 \\ &\Rightarrow C_{ij} = \frac{1}{\epsilon_i \epsilon_j} \sum_{k,l} \epsilon_k^i C_{jl}^{ik} \epsilon_l^j. \end{aligned} \quad (\text{B.2})$$

Note the expected result for the special case self-correlation $i = j$:

$$C_{ii} = \frac{1}{\epsilon_i^2} \sum_{k,l} \epsilon_k^i C_{il}^{ik} \epsilon_l^i = \frac{\epsilon_i^2}{\epsilon_i^2} = 1. \quad (\text{B.3})$$

We now have the simplified problem of combining measurements $m_i = A_i \pm \epsilon_i$ with correlations C_{ij} . We wish to determine a set of weights w_i such that the combined result

$$m \equiv \frac{\sum_i w_i m_i}{\sum_i w_i} \quad (\text{B.4})$$

has the minimum uncertainty, subject to the constraint $w \equiv \sum_i w_i = 1$. The total uncertainty of this weighted sum is

$$\epsilon^2 \equiv \sum_{i,j} \epsilon_i w_i C_{ij} w_j \epsilon_j. \quad (\text{B.5})$$

Applying the method of Lagrange Multipliers to minimize ϵ subject to the constraint $w = 1$ gives the series of equations

$$\frac{\partial \epsilon^2}{\partial w_i} + \lambda \frac{\partial w}{\partial w_i} = 0 = 2 \sum_j \epsilon_i C_{ij} w_j \epsilon_j + \lambda, \quad (\text{B.6})$$

a simple matrix equation for the optimal weights w_i with solution

$$\mathbf{w} = -\frac{\lambda}{2} \mathbf{M}^{-1} \mathbf{1}; M_{ij} \equiv \epsilon_i C_{ij} \epsilon_j. \quad (\text{B.7})$$

Note that we recover the expected case for completely uncorrelated errors:

$$C_{ij} = \delta_{ij} \Rightarrow 0 = 2\epsilon_i^2 w_i + \lambda \Rightarrow w_i \propto \frac{1}{\epsilon_i^2}. \quad (\text{B.8})$$

Example: Suppose we have two measurements of A. Each measurement has an $\pm 0.6\%$ statistical and $\pm 0.3\%$ energy uncertainty, with $\pm 0.2\%$ depolarization on the first and $\pm 0.6\%$ on the second. Energy and depol errors are entirely correlated between the two, but uncorrelated with each other and statistics. Calculating the lump sum errors,

$$\epsilon_1^2 = 0.6^2 + 0.3^2 + 0.2^2 = 0.7^2; \quad \epsilon_2^2 = 0.6^2 + 0.3^2 + 0.6^2 = 0.9^2, \quad (\text{B.9})$$

and the correlations are

$$C_{11} = C_{22} = 1; \quad C_{12} = C_{21} = \frac{1}{0.7 \cdot 0.9} (0.3^2 + 0.2 \cdot 0.6) = \frac{1}{3}. \quad (\text{B.10})$$

Hence we calculate the optimal weights, and normalize to 1 total:

$$\mathbf{w} \propto \begin{bmatrix} 0.7^2 & 0.7 \cdot 0.9/3 \\ 0.7 \cdot 0.9/3 & 0.9^2 \end{bmatrix}^{-1} \begin{pmatrix} 1 \\ 1 \end{pmatrix} = \begin{pmatrix} 1.70 \\ 0.79 \end{pmatrix}, \Rightarrow \mathbf{w} = \begin{pmatrix} 0.68 \\ 0.32 \end{pmatrix} \quad (\text{B.11})$$

and extract the combined uncertainty

$$\epsilon^2 = 0.7^2 \cdot 0.68^2 + 2 \cdot 0.7 \cdot 0.68 \cdot \frac{1}{3} \cdot 0.32 \cdot 0.9 + 0.9^2 \cdot 0.32^2 = 0.63^2$$

Appendix C

Generation of correlated random fluctuations

Suppose one wishes to generate a vector of random variables \mathbf{x} with covariance matrix $\Sigma(\mathbf{x})$. Using a property of covariance that, for any matrix A , $\Sigma(A\mathbf{x}) = A\Sigma(\mathbf{x})A^\top$, we can pick a change-of-variable $A = \Sigma(\mathbf{x})^{-1/2}$ so $\Sigma(A\mathbf{x}) = I$ (so long as $\Sigma(\mathbf{x})$ has an invertible square root). Hence, we can generate uncorrelated random variables (with $\sigma^2 = 1$) for $\tilde{\mathbf{x}} \equiv A\mathbf{x}$, and produce the appropriately correlated variables $\mathbf{x} = A^{-1}\tilde{\mathbf{x}}$.

Consider the special case of wanting n random variables, individually with a mean of 0 and standard deviations $\sigma_1, \dots, \sigma_n$, and the same correlation c between each pair. So, in this case,

$$\Sigma(\mathbf{x}) = \sigma M \sigma; \quad \sigma \equiv \begin{bmatrix} \sigma_1 & & & \\ & \ddots & & \\ & & \ddots & \\ & & & \sigma_n \end{bmatrix}, \quad M \equiv \begin{bmatrix} 1 & c & \cdots & c \\ c & 1 & & \vdots \\ \vdots & & \ddots & c \\ c & \cdots & c & 1 \end{bmatrix}. \quad (\text{C.1})$$

Defining $\mathbf{y} \equiv \sigma^{-1}\mathbf{x} \Rightarrow \mathbf{x} = \sigma\mathbf{y}$, then \mathbf{y} is a random vector with covariance $\Sigma(\mathbf{y}) = M$.

We can find the square root of M by noting that we expect these matrices to be of similar form to M , with one value along the diagonal and another filling all the non-diagonal slots:

$$A^{-1} = M^{1/2} = \begin{bmatrix} a & b & \cdots & b \\ b & a & & \vdots \\ \vdots & & \ddots & b \\ b & \cdots & b & a \end{bmatrix} : \quad a^2 + (n-1)b^2 = 1, \quad 2ab + (n-2)b^2 = c \quad (\text{C.2})$$

$$\begin{aligned} \Rightarrow a &= \frac{1}{n} \sqrt{1 + (n-1)^2 - (n-1)(n-2)c + 2(n-1)\sqrt{(1-c)(1+(n-1)c)}} \\ b &= \frac{2(n-1)c + (n-2)(\sqrt{(1-c)(1+(n-1)c)} - 1)}{n^2 a}. \end{aligned} \quad (\text{C.3})$$

Note that in the limit $nc \ll 1$, this is approximately

$$a \approx 1 - \frac{n-1}{8}c^2, \quad b \approx \frac{c}{2} - \frac{n-2}{8}c^2. \quad (\text{C.4})$$

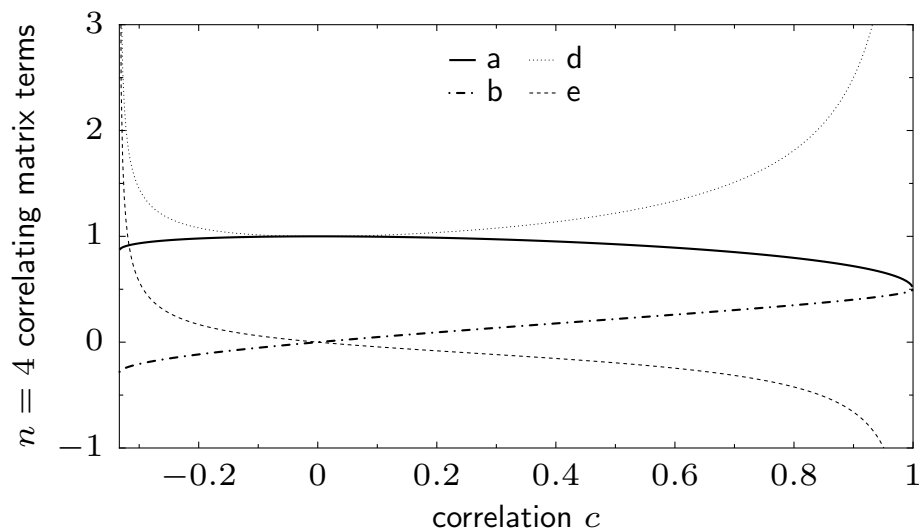


Figure C.1: Elements a, b, d, e in the square root and inverse square root of the special case matrix discussed in the text, for $n = 4$.

The same method applies should we wish to find the inverse $A = M^{-1/2}$, by taking its form to be d on the diagonal and e elsewhere,

$$\begin{aligned} ad + (n-1)be &= 1, & ae + bd + (n-2)be &= 0 \\ \Rightarrow d &= \frac{a + (n-2)b}{(a-b)(a + (n-1)b)}, & e &= \frac{-b}{(a-b)(a + (n-1)b)}, \end{aligned} \quad (\text{C.5})$$

which, in the limit $nb \ll a$, is approximately

$$d \approx \frac{1}{a} + \frac{n-1}{a^3}b^2 \approx 1 + \frac{3n-3}{8}c^2, \quad e \approx -\frac{b}{a^2} + \frac{n-2}{a^3}b^2 \approx -\frac{c}{2} + \frac{3n-6}{8}c^2. \quad (\text{C.6})$$

Figure C.1 shows the terms a, b and d, e calculated for $n = 4$ as a function of c .

Appendix D

Segmenting and Interpolating a Circular Region

D.1 Segmenting

Position-dependent quantities of interest in UCNA calibration are typically measurable over the circular acceptance defined by the entrance to the wirechamber. Imposing a grid of square regions over a circular fiducial leaves many areas within a grid-spacing of the circle edge with marginal statistics from a partially filled volume. The following scheme was adopted for segmenting the circular detector region of interest, and interpolating values measured over segments.

The circle is first divided into $n \geq 1$ rings at equal spacing. For a total radius of r_0 , rings are placed at radii

$$r_i \equiv \frac{i - \frac{1}{2}}{n - \frac{1}{2}} r_0, \quad i \in [1, \dots, n]. \quad (\text{D.1})$$

Each annular region is then divided into n_i^θ equal-angular sectors, where

$$n_1^\theta \equiv 1, \quad n_{i>1}^\theta \equiv \lceil 2\pi(i-1) \rceil, \quad (\text{D.2})$$

and the angular division begins at $\theta = 0$ (along the $+x$ axis). This produces sectors with approximately equal areas for well-balanced statistics, which tend towards squares for large n^θ . Figure D.1 shows an example of this division scheme.

D.2 Interpolating

First, consider one-dimensional interpolation given an evenly-spaced grid of input values. Suppose we have values p_{-1}, p_0, p_1, p_2 at positions $x = -1, 0, 1, 2$, respectively, and wish to interpolate for $x \in [0, 1]$. Then, a reasonable choice is a Catmull-Rom cubic interpolating spline [CR74]:

$$C(x \in [0, 1]) \equiv -\frac{1}{2}(1-x)^2xp_{-1} + (1+x - \frac{3}{2}x^2)(1-x)p_0 \\ + (1+(1-x) - \frac{3}{2}(1-x)^2)xp_1 - \frac{1}{2}(1-x)x^2p_2 \equiv \sum_{i=-1}^2 P_i(x)p_i. \quad (\text{D.3})$$

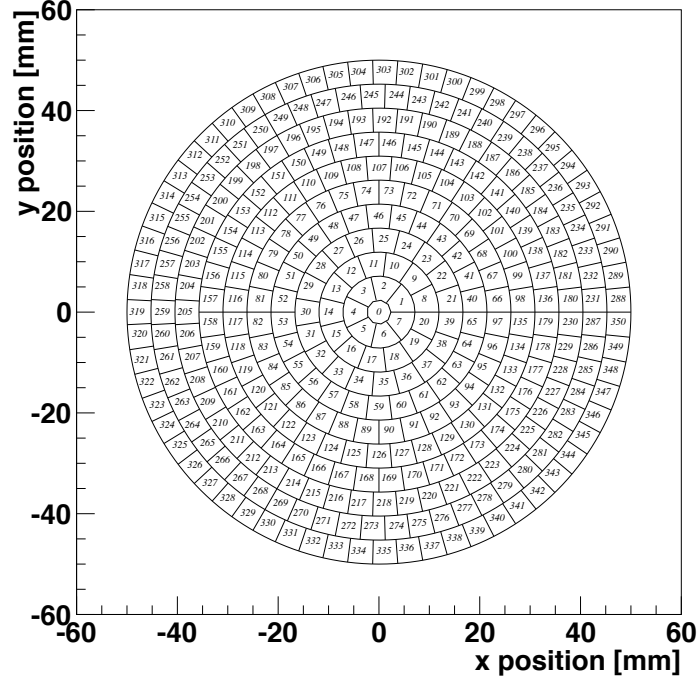


Figure D.1: Example division of circle, $r_0 = 50$ mm with $n = 11$ rings.

Note that $C(0) = p_0$ and $C(1) = p_1$. Furthermore, the derivative is

$$\begin{aligned}
 \frac{d}{dx}C(x) &= -\frac{1}{2}(1-3x)(1-x)p_{-1} + \left(\frac{9}{2}x-5\right)xp_0 \\
 &\quad - \left(\frac{9}{2}(1-x)-5\right)(1-x)p_1 + \frac{1}{2}(1-3(1-x))xp_2 \\
 \Rightarrow \frac{d}{dx}C(0) &= \frac{p_1-p_{-1}}{2}, \quad \frac{d}{dx}C(1) = \frac{p_2-p_0}{2}.
 \end{aligned} \tag{D.4}$$

Extending this interpolation scheme into neighboring regions, *e.g.* $x \in [1, 2]$, the interpolation produced is consequently C^1 continuous. The second derivative, however, is not guaranteed continuous across adjacent regions:

$$\frac{d^2}{dx^2}C(x) = (2-3x)p_{-1} + (9x-5)p_0 + (9(1-x)-5)p_1 + (2-3(1-x))p_2. \tag{D.5}$$

Considering the interpolation curve as a function of the four points $C(x; p_{-1}, p_0, p_1, p_2)$, first note that C is linear on combinations of input values:

$$C(x; p_{-1} + \alpha p'_{-1}, p_0 + \alpha p'_0, p_1 + \alpha p'_1, p_2 + \alpha p'_2) = C(x; p_{-1}, p_0, p_1, p_2) + \alpha C(x; p'_{-1}, p'_0, p'_1, p'_2) \tag{D.6}$$

and has the following additional useful properties:

$$\begin{aligned}
C(x; 1, 1, 1, 1) &= 1 \\
C(x; -1, 0, 1, 2) &= x \\
C(x; 1, 0, 1, 4) &= x^2
\end{aligned}
\tag{D.7}$$

which means the interpolation will perfectly reproduce any quadratic function sampled at the four points $p_i = c_2 i^2 + c_1 i + c_0$. For higher-order cubic components, $C(x; p_i = (i - \frac{1}{2})^3) = 3(x - \frac{1}{2})^3 - \frac{1}{2}(x - \frac{1}{2})$ deviates by at worst $\pm \frac{1}{6\sqrt{3}} \approx \pm 0.10$ from $(x - \frac{1}{2})^3$.

For interpolation of two-dimensional (or higher) datasets, we may apply the interpolation first in one dimension, and then interpolate the values across the other. In the case of data points $p_{i,j}$ on an integer lattice,

$$C(x, y \in [0, 1] \times [0, 1]) \equiv \sum_{i=-1}^2 \sum_{j=-1}^2 P_i(x) P_j(y) p_{i,j}.
\tag{D.8}$$

Note that it does not matter what order the interpolation along the two dimensions is done in.

For the $r - \theta$ data points frequently produced in position maps of the circular UCNA detector acceptance, points on the same “ring” are equally angularly spaced, but at different angular positions from those on other rings. Interpolation control points $p_{r,\theta}$ are taken to be the center (half-way in r and θ) of each sector. Interpolation is first applied to produce four equally-spaced radial points at constant θ (each interpolated from the appropriate four points bracketing the angle θ on their ring), and then interpolated between the four radial points. For radial points near the center or edge of the ring, interpolation input points from outside the dataset (p_{-1} in the innermost ring and p_2 in the outermost) must be synthesized. Approaching the point p_0 at the origin, setting $p_{-1} = p_1$ will make $\frac{\partial}{\partial r} C(r \rightarrow 0, \theta) \rightarrow 0$, which assures the interpolation remains C^1 continuous at the origin. For the outer edge of the circle and beyond, synthesized interpolation points are set equal to the last actual data point.

Bibliography

- [Aba+95] S. Abachi et al. “Search for High Mass Top Quark Production in $p\bar{p}$ Collisions at $\sqrt{s} = 1.8$ TeV.” In: *Physical Review Letters* 74 (13 Mar. 1995), pp. 2422–2426. DOI: 10.1103/PhysRevLett.74.2422.
- [Abe+02] H. Abele et al. “Is the Unitarity of the Quark-Mixing CKM Matrix Violated in Neutron β -Decay?” In: *Physical Review Letters* 88 (21 May 2002), p. 211801. DOI: 10.1103/PhysRevLett.88.211801.
- [Abe+95] F. Abe et al. “Observation of Top Quark Production in $\bar{p}p$ Collisions with the Collider Detector at Fermilab.” In: *Physical Review Letters* 74 (14 Apr. 1995), pp. 2626–2631. DOI: 10.1103/PhysRevLett.74.2626.
- [Abe+97] H. Abele et al. “A measurement of the beta asymmetry A in the decay of free neutrons.” In: *Physics Letters B* 407.3–4 (1997), pp. 212–218. DOI: 10.1016/S0370-2693(97)00739-9.
- [Ago+03] S. Agostinelli et al. “GEANT4 — a simulation toolkit.” In: *Nuclear Instruments and Methods A* 506.3 (2003), pp. 250–303. DOI: 10.1016/S0168-9002(03)01368-8.
- [And+04] S. Ando et al. “Neutron beta-decay in effective field theory.” In: *Physics Letters B* 595.1–4 (2004), pp. 250–259. DOI: 10.1016/j.physletb.2004.06.037.
- [Ang+09] A. Anghel et al. “The PSI ultra-cold neutron source.” In: *Nuclear Instruments and Methods A* 611 (2009), pp. 272–275. DOI: 10.1016/j.nima.2009.07.077.
- [AS64] M. Abramowitz and I. A. Stegun. *Handbook of Mathematical Functions*. National Bureau of Standards, 1964.
- [Aub+74] J. J. Aubert et al. “Experimental Observation of a Heavy Particle J.” In: *Physical Review Letters* 33 (23 Dec. 1974), pp. 1404–1406. DOI: 10.1103/PhysRevLett.33.1404.
- [Aug+74] J.-E. Augustin et al. “Discovery of a Narrow Resonance in e^+e^- Annihilation.” In: *Physical Review Letters* 33 (23 Dec. 1974), pp. 1406–1408. DOI: 10.1103/PhysRevLett.33.1406.
- [BB67] J. A. Bearden and A. F. Burr. “Reevaluation of X-Ray Atomic Energy Levels.” In: *Reviews of Modern Physics* 39.1 (Jan. 1967), pp. 125–142.
- [BC83] H. Behrens and P. Christmas. “The Beta Decay of ^{137}Cs .” In: *Nuclear Physics A* 399 (1983), pp. 131–140.
- [Ber12] J. Beringer et al. (Particle Data Group). “The Review of Particle Physics.” In: *Physical Review D* 86 (2012 and 2013 partial update for the 2014 edition), p. 010001.

- [BG64] B. J. Björken and S. L. Glashow. “Elementary particles and SU(4).” In: *Physics Letters* 11.3 (1964), pp. 255–257. DOI: 10.1016/0031-9163(64)90433-0.
- [Bha+12] Tanmoy Bhattacharya et al. “Probing novel scalar and tensor interactions from (ultra)cold neutrons to the LHC.” In: *Physical Review D* 85 (5 Mar. 2012), p. 054512. DOI: 10.1103/PhysRevD.85.054512.
- [BHS07] M. M. Bé, R. G. Helmer, and E. Schönfeld. ¹³⁹Ce: *comments on evaluation*. Dec. 2007. URL: <http://www.nucleide.org/DDEP\WG/DDEPdata.htm> (visited on 11/15/2013).
- [Bil+60] S. M. Bilen’kiĭ et al. “On the theory of neutron beta decay.” In: *Journal of Experimental and Theoretical Physics* 10 [ZETF 37].6 (June 1960 [1959]), 1241–1244 [1758–1763].
- [Bla06] J. Blachot. “Nuclear Data Sheets for A = 109.” In: *Nuclear Data Sheets* 107 (2006). Data extracted from the ENSDF database, version 200602, pp. 355–506.
- [Bla10] J. Blachot. “Nuclear Data Sheets for A = 113.” In: *Nuclear Data Sheets* 111 (2010). Data extracted from the ENSDF database, version 201006, pp. 1471–1618.
- [Bla12] J. Blachot. “Nuclear Data Sheets for A = 114.” In: *Nuclear Data Sheets* 113 (2012). Data extracted from the ENSDF database, version 201203, pp. 515–714.
- [Bop+86] P. Bopp et al. “Beta-Decay Asymmetry of the Neutron and $\frac{g_A}{g_V}$.” In: *Physical Review Letters* 56 (9 Mar. 1986), pp. 919–922. DOI: 10.1103/PhysRevLett.56.919.
- [BT07] E. Browne and J.K. Tuli. “Nuclear Data Sheets for A = 137.” In: *Nuclear Data Sheets* 108 (2007). Data extracted from the ENSDF database, version 200709, pp. 2173–2318.
- [Bur01] T. W. Burrows. “Nuclear Data Sheets for A = 139.” In: *Nuclear Data Sheets* 92 (2001). Data extracted from the ENSDF database, version 200104, pp. 623–782.
- [Bur+57] M. T. Burgy et al. “Measurement of Beta Asymmetry in the Decay of Polarized Neutrons.” In: *Physical Review* 107 (Sept. 1957), pp. 1731–1733. DOI: 10.1103/PhysRev.107.1731.2.
- [Bur+60] M. T. Burgy et al. “Measurements of Spatial Asymmetries in the Decay of Polarized Neutrons.” In: *Physical Review* 120 (5 Dec. 1960), pp. 1829–1838. DOI: 10.1103/PhysRev.120.1829.
- [Byr82] J. Byrne. “Weak interactions of the neutron.” In: *Reports on Progress in Physics* 45.2 (1982). DOI: 10.1088/0034-4885/45/2/001.
- [Cab63] Nicola Cabibbo. “Unitary Symmetry and Leptonic Decays.” In: *Physical Review Letters* 10 (12 June 1963), pp. 531–533. DOI: 10.1103/PhysRevLett.10.531.
- [Chr+64] J. H. Christenson et al. “Evidence for the 2π Decay of the K_2^0 Meson.” In: *Physical Review Letters* 13 (4 July 1964), pp. 138–140. DOI: 10.1103/PhysRevLett.13.138.
- [CKR70] C. J. Christensen, V. E. Krohn, and G. R. Ringo. “Measurement of Angular Correlations in the Decay of Polarized Neutrons.” In: *Physical Review C* 1 (5 May 1970), pp. 1693–1698. DOI: 10.1103/PhysRevC.1.1693.
- [Col11] GEANT4 Collaboration. *Physics Reference Manual, Version: geant4 9.5.0*. Dec. 2011.
- [CR74] E. Catmull and R. Rom. “A Class of Local Interpolating Splines.” In: *Computer Aided Geometric Design*. Ed. by R. E. Barnhill and R. F. Riesenfeld. Academic Press, 1974.

- [Dav51] J. P. Davidson Jr. “The First Forbidden Shape Factor and the f_{nt} Products for Beta-Decay.” In: *Physical Review* 82.1 (Apr. 1951), pp. 48–51. DOI: 10.1103/PhysRev.82.48.
- [Dra+76] O. Dragoun et al. “Internal Conversion of High-Multipolarity Transitions in ^{109}Ag and ^{113}In .” In: *Zeitschrift für Physik A* 279.1 (Mar. 1976), pp. 107–111.
- [EF57] M. E. Ebel and G. Feldman. “Further remarks on Coulomb corrections in allowed beta transitions.” In: *Nuclear Physics* 4 (1957), pp. 213–214. DOI: 10.1016/0029-5582(87)90020-4.
- [Ero+90] B. G. Erozolimskii et al. “Measurement of the asymmetry of the electron emission with respect to the spin direction of a decaying neutron.” In: *Soviet Journal of Nuclear Physics* 52.6 (Dec. 1990), pp. 999–1005.
- [Ero+91] B. G. Erozolimskii et al. “New measurements of the electron-neutron spin asymmetry in neutron beta-decay.” In: *Physics Letters B* 263.1 (July 1991), pp. 33–38.
- [Fer34] E. Fermi. “Versuch einer Theorie der β -Strahlen. I.” In: *Zeitschrift für Physik* 88 (1934), pp. 161–177. DOI: 10.1007/BF01351864.
- [Fer36] E. Fermi. “Sul moto dei neutroni nelle sostanze idrogenate.” In: *La Ricerca Scientifica* 7 (1936), pp. 13–52.
- [FGM58] R. P. Feynman and M. Gell-Mann. “Theory of the Fermi Interaction.” In: *Physical Review* 109 (1 Jan. 1958), pp. 193–198. DOI: 10.1103/PhysRev.109.193.
- [Fie37] Markus Fierz. “Zur Fermischen Theorie des β -Zerfalls.” In: *Zeitschrift für Physik* 104 (7–8 July 1937), pp. 553–565. DOI: 10.1007/BF01330070.
- [FM47] E. Fermi and L. Marshall. “Interference Phenomena of Slow Neutrons.” In: *Physical Review* 71 (10 May 1947), pp. 666–677. DOI: 10.1103/PhysRev.71.666.
- [Fuj+88] Y. Fujita et al. “Precise intensity measurements of internal conversion lines in the decay of ^{207}Bi and systematic comparison with theoretical predictions.” In: *Nuclear Physics A* 484 (1988), pp. 77–89.
- [FZ46] E. Fermi and W. H. Zinn. “Reflection of Neutrons on Mirrors.” In: *Physical Review* 70 (1946), p. 103.
- [Gei+65] J. S. Geiger et al. “Measurements of M1 and E2 transition probabilities in Te^{125} , I^{127} , Xe^{129} , Cs^{133} , La^{139} and Pr^{141} .” In: *Nuclear Physics* 68.2 (1965), pp. 352–368. DOI: 10.1016/0029-5582(65)90652-8.
- [GGC06] V. Gudkov, G. L. Greene, and J. R. Calarco. “General classification and analysis of neutron β -decay experiments.” In: *Physical Review C* 73 (3 Mar. 2006), p. 035501. DOI: 10.1103/PhysRevC.73.035501.
- [GIM70] S. L. Glashow, J. Iliopoulos, and L. Maiani. “Weak Interactions with Lepton-Hadron Symmetry.” In: *Physical Review D* 2 (7 Oct. 1970), pp. 1285–1292. DOI: 10.1103/PhysRevD.2.1285.
- [GM58] M. Gell-Mann. “Test of the Nature of the Vector Interaction in β Decay.” In: *Physical Review* 111 (1 July 1958), pp. 362–365. DOI: 10.1103/PhysRev.111.362.

- [GM62] M. Gell-Mann. “Symmetries of Baryons and Mesons.” In: *Physical Review* 125 (3 Feb. 1962), pp. 1067–1084. DOI: 10.1103/PhysRev.125.1067.
- [GM64] M. Gell-Mann. “A schematic model of baryons and mesons.” In: *Physics Letters* 8.3 (1964), pp. 214–215. DOI: 10.1016/S0031-9163(64)92001-3.
- [GP75] R. Golub and J. M. Pendlebury. “Super-thermal sources of ultra-cold neutrons.” In: *Physics Letters A* 53.2 (1975), pp. 133–135. DOI: 10.1016/0375-9601(75)90500-9.
- [GRL91] R. Golub, D. Richardson, and S. K. Lamoreaux. *Ultra-Cold Neutrons*. Adam Hilger, 1991.
- [GT36] G. Gamow and E. Teller. “Selection Rules for the β -Disintegration.” In: *Physical Review* 49 (12 June 1936), pp. 895–899. DOI: 10.1103/PhysRev.49.895.
- [GT58] M. L. Goldberger and S. B. Treiman. “Form Factors in β Decay and μ Capture.” In: *Physical Review* 111 (1 July 1958), pp. 354–361. DOI: 10.1103/PhysRev.111.354.
- [GT92] F. Glück and K. Tóth. “Order- α radiative corrections for semileptonic decays of polarized baryons.” In: *Physical Review D* 46.5 (Sept. 1992), pp. 2090–2101.
- [GZ01] S. Gardner and C. Zhang. “Sharpening Low-Energy, Standard-Model Tests via Correlation Coefficients in Neutron β Decay.” In: *Physical Review Letters* 86.25 (June 2001), pp. 5666–5669.
- [GZ56] S. S. Gershtein and Ia. B. Zel’dovich. “Meson Corrections in the Theory of Beta Decay.” In: *Journal of Experimental and Theoretical Physics* 2 [ZETF 29] (1956 [1955]), 576–577 [698–699].
- [Han85] H. H. Hansen. “Evaluation of K-shell and Total Internal Conversion Coefficients for Some Selected Nuclear Transitions.” In: *European Applied Research Reports, Nuclear Science Technology* 6.4 (1985), pp. 777–816.
- [Her+77] S. W. Herb et al. “Observation of a Dimuon Resonance at 9.5 GeV in 400-GeV Proton-Nucleus Collisions.” In: *Physical Review Letters* 39 (5 Aug. 1977), pp. 252–255. DOI: 10.1103/PhysRevLett.39.252.
- [Hic12] Kevin P. Hickerson. “The Physics of Ultracold Neutrons and Fierz Interference in Beta Decay.” PhD thesis. California Institute of Technology, 2012.
- [HM76] H. H. Hansen and D. Mouchel. “Internal Conversion Coefficient for the 165.8 keV Transition in ^{139}La .” In: *Zeitschrift für Physik* 276 (1976), pp. 303–307.
- [Hoe03] Seth Hoedl. “Novel Proton Detectors, Ultra-Cold Neutron Decay and Electron Backscatter.” PhD thesis. Princeton University, 2003.
- [Hol12] A. T. Holley. “Report: UCNA 2010 Polarimetry (ver. 2.3).” UCNA electronic logbook analysis note #443. Sept. 2012.
- [Hol+12] A. T. Holley et al. “A high-field adiabatic fast passage ultracold neutron spin flipper for the UCNA experiment.” In: *Review of Scientific Instruments* 83.7 (2012), p. 073505. DOI: 10.1063/1.4732822.
- [Hol12] Adam T. Holley. “Ultracold Neutron Polarimetry in a Measurement of the β Asymmetry.” PhD thesis. North Carolina State University, 2012.

- [Hol74] B. R. Holstein. “Recoil effects in allowed beta decay: The elementary particle approach.” In: *Reviews of Modern Physics* 46.4 (1974), pp. 789–814.
- [HS68] R. S. Hager and E. C. Seltzer. “Internal conversion tables part I: K-, L-, M-shell conversion coefficients for $Z=30$ to $Z=103$.” In: *Nuclear Data Sheets. Section A* 4.1–2 (1968), pp. 1–11. DOI: 10.1016/S0550-306X(68)80002-3.
- [HT09] J. C. Hardy and I. S. Towner. “Superallowed $0^+ \rightarrow 0^+$ nuclear β decays: A new survey with precision tests of the conserved vector current hypothesis and the standard model.” In: *Physical Review C* 79 (5 May 2009), p. 055502. DOI: 10.1103/PhysRevC.79.055502.
- [Ign90] V.K. Ignatovich. *The Physics of Ultracold Neutrons*. Oxford University Press, 1990.
- [Ito+07] T. M Ito et al. “A multiwire proportional chamber for precision studies of neutron β decay angular correlations.” In: *Nuclear Instruments and Methods A* 571.3 (2007), pp. 676–686. DOI: 10.1016/j.nima.2006.11.026.
- [Iva+11] V. Ivanchenko et al. “Recent improvements in Geant4 Electromagnetic Physics Models and Interfaces.” In: *Progress in Nuclear Science and Technology* 2 (2011), pp. 898–903.
- [JTW57a] J. D. Jackson, S. B. Treiman, and H. W. Wyld Jr. “Coulomb corrections in allowed beta transitions.” In: *Nuclear Physics* 4 (1957), pp. 206–212. DOI: 10.1016/0029-5582(87)90019-8.
- [JTW57b] J. D. Jackson, S. B. Treiman, and H. W. Wyld Jr. “Possible Tests of Time Reversal Invariance in Beta Decay.” In: *Physical Review* 106 (3 May 1957), pp. 517–521. DOI: 10.1103/PhysRev.106.517.
- [Kas+75] N. T. Kashoukeev et al. “Production of ultracold neutrons by the method of rotating flat neutron mirrors.” In: *Nuclear Instruments and Methods* 126.1 (1975), pp. 43–48. DOI: 10.1016/0029-554X(75)90228-1.
- [Kib+08] T. Kibédi et al. “Evaluation of theoretical conversion coefficients using BrIcc.” In: *Nuclear Instruments and Methods A* 589.2 (2008), pp. 202–229. DOI: 10.1016/j.nima.2008.02.051.
- [KL11] F. G. Kondev and S. Lalkovski. “Nuclear Data Sheets for $A = 207$.” In: *Nuclear Data Sheets* 112 (2011). Data extracted from the ENSDF database, version 201102, pp. 707–853.
- [KM73] Makoto Kobayashi and Toshihide Maskawa. “CP-Violation in the Renormalizable Theory of Weak Interaction.” In: *Progress of Theoretical Physics* 49.2 (1973), pp. 652–657. DOI: 10.1143/PTP.49.652.
- [Kon43] Emil Jan Konopinski. “Beta-Decay.” In: *Reviews of Modern Physics* 15 (4 Oct. 1943), pp. 209–245. DOI: 10.1103/RevModPhys.15.209.
- [KR75] V. E. Krohn and G. R. Ringo. “ G_A/G_V measured in the decay of polarized neutrons.” In: *Physics Letters B* 55.2 (1975), pp. 175–177. DOI: 10.1016/0370-2693(75)90436-0.
- [KRP36] Franz N. D. Kurie, J. R. Richardson, and H. C. Paxton. “The Radiations Emitted from Artificially Produced Radioactive Substances. I. The Upper Limits and Shapes of the β -Ray Spectra from Several Elements.” In: *Physical Review* 49 (5 Mar. 1936), pp. 368–381. DOI: 10.1103/PhysRev.49.368.

- [KU35] E. J. Konopinski and G. E. Uhlenbeck. “On the Fermi Theory of β -Radioactivity.” In: *Physical Review* 48 (1 July 1935), pp. 7–12. DOI: 10.1103/PhysRev.48.7.
- [Lau11] B. Lauss. “Commissioning of the new high-intensity ultracold neutron source at the Paul Scherrer Institut.” In: *Journal of Physics: Conference Series* 312 (2011), p. 052005. DOI: 10.1088/1742-6596/312/5/052005.
- [Lia+97] P. Liaud et al. “The measurement of the beta asymmetry in the decay of polarized neutrons.” In: *Nuclear Physics A* 612.1 (1997), pp. 53–81. DOI: 10.1016/S0375-9474(96)00325-9.
- [Liu02] Chen-Yu Liu. “A Superthermal Ultra-Cold Neutron Source.” PhD thesis. Princeton University, June 2002.
- [Liu+03] C.-Y. Liu et al. “An apparatus to control and monitor the para-D₂ concentration in a solid deuterium, superthermal source of ultra-cold neutrons.” In: *Nuclear Instruments and Methods A* 508.3 (2003), pp. 257–267. DOI: 10.1016/S0168-9002(03)01666-8.
- [LMH+10] J. Liu, M. P. Mendenhall, A. T. Holley, et al. “Determination of the Axial-Vector Weak Coupling Constant with Ultracold Neutrons.” In: *Physical Review Letters* 105.18 (Oct. 2010), p. 181803. DOI: 10.1103/PhysRevLett.105.181803.
- [LRY49] T. D. Lee, M. Rosenbluth, and C. N. Yang. “Interaction of Mesons with Nucleons and Light Particles.” In: *Physical Review* 75 (5 Mar. 1949), pp. 905–905. DOI: 10.1103/PhysRev.75.905.
- [Lus+69] V. I. Lushchikov et al. “Observation of Ultracold Neutrons.” In: *JETP Letters* 9.1 (1969), 23–26 [Pis. ZhETF 40–45].
- [LY56] T. D. Lee and C. N. Yang. “Question of Parity Conservation in Weak Interactions.” In: *Physical Review* 104.1 (Oct. 1956), pp. 254–258.
- [LY57] T. D. Lee and C. N. Yang. “Parity Nonconservation and a Two-Component Theory of the Neutrino.” In: *Physical Review* 105 (5 Mar. 1957), pp. 1671–1675. DOI: 10.1103/PhysRev.105.1671.
- [Mak05] Mark F. Makela. “Polarized Ultracold Neutrons: their transport in diamond guides and potential to search for physics beyond the standard model.” PhD thesis. Virginia Polytechnic Institute and State University, 2005.
- [Mam10] Russell R. Mammei. “Thin Films for the Transport of Polarized Ultracold Neutrons for Fundamental Symmetry Study.” PhD thesis. Virginia Polytechnic Institute and State University, 2010.
- [Mar+08] J. W. Martin et al. “TRIUMF Ultracold Neutron Source.” Mar. 2008. URL: <http://www.triumf.ca/sites/default/files/SEEC-UCN.pdf>.
- [Mär+09] B. Märkisch et al. “The new neutron decay spectrometer Perkeo III.” In: *Nuclear Instruments and Methods A* 611.2–3 (2009), pp. 216–218. DOI: 10.1016/j.nima.2009.07.066.
- [Mat91] E. Mathieson. *Induced charge distributions in proportional detectors*. 1991. URL: http://www.inst.bnl.gov/programs/gasnobledet/publications/Mathieson's_Book.pdf (visited on 01/23/2014).

- [MBM76] C. L. Morris, W. J. Braithwaite, and C. F. Moore. “A stable light pulser for gain stabilizing photomultiplier tubes.” In: *Nuclear Instruments and Methods* 136 (1976), pp. 197–198.
- [Men+13] M. P. Mendenhall et al. “Precision measurement of the neutron β -decay asymmetry.” In: *Physical Review C* 87 (3 Mar. 2013), p. 032501. DOI: 10.1103/PhysRevC.87.032501.
- [Mid] *MidasWiki*. 2013. URL: <https://midas.triumf.ca> (visited on 11/05/2013).
- [Mor+02] C. L. Morris et al. “Measurements of Ultracold-Neutron Lifetimes in Solid Deuterium.” In: *Physical Review Letters* 89 (27 Dec. 2002), p. 272501. DOI: 10.1103/PhysRevLett.89.272501.
- [Mor+09] C. L. Morris et al. “Multi-wire proportional chamber for ultra-cold neutron detection.” In: *Nuclear Instruments and Methods A* 599.2–3 (2009), pp. 248–250. DOI: 10.1016/j.nima.2008.11.099.
- [Mun+13] D. Mund et al. “Determination of the Weak Axial Vector Coupling $\lambda = g_A/g_V$ from a Measurement of the β -Asymmetry Parameter A in Neutron Beta Decay.” In: *Physical Review Letters* 110 (17 Apr. 2013), p. 172502. DOI: 10.1103/PhysRevLett.110.172502.
- [Nak10] K. Nakamura et al. (Particle Data Group). “The Review of Particle Physics.” In: *Journal of Physics G* 37 (2010), p. 075021.
- [Nic+05] J. S. Nico et al. “Measurement of the neutron lifetime by counting trapped protons in a cold neutron beam.” In: *Physical Review C* 71 (5 May 2005), p. 055502. DOI: 10.1103/PhysRevC.71.055502.
- [Nie88] Harald Niederreiter. “Low-discrepancy and low-dispersion sequences.” In: *Journal of Number Theory* 30.1 (1988), pp. 51–70. DOI: 10.1016/0022-314X(88)90025-X.
- [NT60] T. G. Northrop and E. Teller. “Stability of the Adiabatic Motion of Charged Particles in the Earth’s Field.” In: *Physical Review* 117 (1 Jan. 1960), pp. 215–225. DOI: 10.1103/PhysRev.117.215.
- [Pat+09] R. W. Pattie Jr. et al. “First Measurement of the Neutron β Asymmetry with Ultracold Neutrons.” In: *Physical Review Letters* 102.1 (Jan. 2009), p. 012301. DOI: 10.1103/PhysRevLett.102.012301.
- [Pat12] Robert W. Pattie Jr. “A Precision Measurement of the Neutron β Asymmetry Using Ultracold Neutrons.” PhD thesis. North Carolina State University, 2012.
- [PHY13] R. W. Pattie, K. P. Hickerson, and A. R. Young. “Limits on tensor coupling from neutron β decay.” In: *Physical Review C* 88 (4 Oct. 2013), p. 048501. DOI: 10.1103/PhysRevC.88.048501.
- [Pla+08] B. Plaster et al. “A solenoidal electron spectrometer for a precision measurement of the neutron β -asymmetry with ultracold neutrons.” In: *Nuclear Instruments and Methods A* 595.3 (2008), pp. 587–598. DOI: 10.1016/j.nima.2008.07.143.
- [Pla+12] B. Plaster et al. “Measurement of the neutron β -asymmetry parameter A_0 with ultracold neutrons.” In: *Physical Review C* 86 (5 Nov. 2012), p. 055501. DOI: 10.1103/PhysRevC.86.055501.

- [Red+76] S. B. Reddy et al. “On the conversion of the 192keV transition in ^{114}In .” In: *Current Science (India)* 45.22 (1976).
- [Rio+11] R. Rios et al. “Sealed drift tube cosmic ray veto counters.” In: *Nuclear Instruments and Methods A* 637.1 (2011), pp. 105–108. DOI: 10.1016/j.nima.2010.12.098.
- [RW83] Wayne W. Repko and Chong-en Wu. “Radiative corrections to the end point of the tritium β decay spectrum.” In: *Physical Review C* 28 (6 Dec. 1983), pp. 2433–2436. DOI: 10.1103/PhysRevC.28.2433.
- [Sak56] Shoichi Sakata. “On a Composite Model for the New Particles.” In: *Progress of Theoretical Physics* 16.6 (1956), pp. 686–688. DOI: 10.1143/PTP.16.686.
- [Sal+14] D. J. Salvat et al. “Storage of ultracold neutrons in the magneto-gravitational trap of the UCN τ experiment.” In: *Physical Review C* 89 (5 May 2014), p. 052501. DOI: 10.1103/PhysRevC.89.052501.
- [Sau+04] A. Saunders et al. “Demonstration of a solid deuterium source of ultra-cold neutrons.” In: *Physics Letters B* 593.1–4 (2004), pp. 55–60. DOI: 10.1016/j.physletb.2004.04.048.
- [Sau+13] A. Saunders et al. “Performance of the Los Alamos National Laboratory spallation-driven solid-deuterium ultra-cold neutron source.” In: *Review of Scientific Instruments* 84 (2013), p. 013304. DOI: 10.1063/1.4770063.
- [Sch+95] K. Schreckenbach et al. “A new measurement of the beta emission asymmetry in the free decay of polarized neutrons.” In: *Physics Letters B* 349.4 (1995), pp. 427–432. DOI: 10.1016/0370-2693(95)00228-D.
- [Sem+97] J. Sempau et al. “An algorithm for Monte Carlo simulation of coupled electron-photon transport.” In: *Nuclear Instruments and Methods B* 132.3 (1997), pp. 377–390. DOI: 10.1016/S0168-583X(97)00414-X.
- [Ser+05] A. Serebrov et al. “Measurement of the neutron lifetime using a gravitational trap and a low-temperature Fomblin coating.” In: *Physics Letters B* 605.1–2 (2005), pp. 72–78. DOI: 10.1016/j.physletb.2004.11.013.
- [Ser11] A. P. Serebrov. “Supersource of ultracold neutrons at the WWR-M reactor and the program of fundamental research in physics.” In: *Crystallography Reports* 56.7 (2011), pp. 1230–1237. DOI: 10.1134/S1063774511070303.
- [SF10] A. P. Serebrov and A. K. Fomin. “Neutron lifetime from a new evaluation of ultracold neutron storage experiments.” In: *Physical Review C* 82 (3 Sept. 2010), p. 035501. DOI: 10.1103/PhysRevC.82.035501.
- [Sha71] R. T. Shann. “Electromagnetic Effects in the Decay of Polarized Neutrons.” In: *Il Nuovo Cimento* 5 A.4 (Oct. 1971), pp. 591–596.
- [Sir67] A. Sirlin. “General Properties of the Electromagnetic Corrections to the Beta Decay of a Physical Nucleon.” In: *Physical Review* 164.5 (Dec. 1967), pp. 1767–1775.
- [SM57] E. C. G. Sudarshan and R. E. Marshak. “The Nature of the Four Fermion Interaction.” In: *Proceedings of Padua-Venice Conference on Mesons and Newly Discovered Particles*. Sept. 1957.

- [SM58] E. C. G. Sudarshan and R. E. Marshak. “Chirality Invariance and the Universal Fermi Interaction.” In: *Physical Review* 109 (5 Mar. 1958), pp. 1860–1862. DOI: 10.1103/PhysRev.109.1860.2.
- [Sob67] I. M. Sobol’. “On the distribution of points in a cube and the approximate evaluation of integrals.” In: *USSR Computational Mathematics and Mathematical Physics* 7.4 (1967), pp. 86–112. DOI: 10.1016/0041-5553(67)90144-9.
- [Ste75] A. Steyerl. “A “neutron turbine” as an efficient source of ultracold neutrons.” In: *Nuclear Instruments and Methods* 125.3 (1975), pp. 461–469. DOI: 10.1016/0029-554X(75)90265-7.
- [Ste+86] A. Steyerl et al. “A new source of cold and ultracold neutrons.” In: *Physics Letters A* 116.7 (1986), pp. 347–352. DOI: 10.1016/0375-9601(86)90587-6.
- [TH10] I. S. Towner and J. C. Hardy. “The evaluation of V_{ud} and its impact on the unitarity of the Cabibbo-Kobayashi-Maskawa quark-mixing matrix.” In: *Reports on Progress in Physics* 73.4 (Mar. 2010), p. 046301. DOI: 10.1088/0034-4885/73/4/046301.
- [Tul96] J. K. Tuli. “Evaluated nuclear structure data file.” In: *Nuclear Instruments and Methods A* 369.2–3 (1996), pp. 506–510. DOI: 10.1016/S0168-9002(96)80040-4.
- [TW49] J. Tiomno and John A. Wheeler. “Charge-Exchange Reaction of the μ -Meson with the Nucleus.” In: *Reviews of Modern Physics* 21 (1 Jan. 1949), pp. 153–165. DOI: 10.1103/RevModPhys.21.153.
- [Wal+09] P. L. Walstrom et al. “A magneto-gravitational trap for absolute measurement of the ultra-cold neutron lifetime.” In: *Nuclear Instruments and Methods A* 599.1 (2009), pp. 82–92. DOI: 10.1016/j.nima.2008.11.010.
- [Wei58] Steven Weinberg. “Charge Symmetry of Weak Interactions.” In: *Physical Review* 112 (4 Nov. 1958), pp. 1375–1379. DOI: 10.1103/PhysRev.112.1375.
- [Wil00] D. H. Wilkinson. “Limits to second-class nucleonic and mesonic currents.” In: *The European Physical Journal A - Hadrons and Nuclei* 7 (3 2000), pp. 307–315. DOI: 10.1007/s100500050397.
- [Wil68] F. L. Wilson. “Fermi’s Theory of Beta Decay.” In: *American Journal of Physics* 36.12 (Dec. 1968), pp. 1150–1160. DOI: 10.1119/1.1974382.
- [Wil82] D. H. Wilkinson. “Analysis of Neutron β -Decay.” In: *Nuclear Physics A* 377 (1982), pp. 474–504.
- [Wil89] D. H. Wilkinson. “Evaluation of Beta-Decay I. The traditional phase space factors.” In: *Nuclear Instruments and Methods A* 275 (1989), pp. 378–386.
- [Wil90] D. H. Wilkinson. “Evaluation of Beta-Decay II. Finite mass and size effects.” In: *Nuclear Instruments and Methods A* 290 (1990), pp. 509–515.
- [Wil93] D. H. Wilkinson. “Evaluation of beta-decay Part III. The complex gamma function.” In: *Nuclear Instruments and Methods A* 335.1–2 (1993), pp. 305–309. DOI: 10.1016/0168-9002(93)90285-P.
- [Wil95a] D. H. Wilkinson. “Evaluation of Beta-Decay IV. The complex gamma function; practicalities.” In: *Nuclear Instruments and Methods A* 365 (1995), pp. 203–207.

- [Wil95b] D. H. Wilkinson. “Evaluation of Beta-Decay V. The Z-independent outer radiative corrections for allowed decay.” In: *Nuclear Instruments and Methods A* 365 (1995), pp. 497–507.
- [Wil97] D. H. Wilkinson. “Evaluation of Beta-Decay VI. The Z-dependent outer radiative corrections for allowed decay.” In: *Nuclear Instruments and Methods A* 401 (1997), pp. 275–280.
- [Wil98] D. H. Wilkinson. “Evaluation of Beta-Decay VII. The Z-independent outer radiative corrections for unique-forbidden decay.” In: *Nuclear Instruments and Methods A* 406 (1998), pp. 89–92.
- [Wre+11] C. Wrede et al. “Preparation of ^{114m}In low energy conversion electron sources.” In: *Nuclear Instruments and Methods B* 269 (2011), pp. 1113–1116. DOI: 10.1016/j.nimb.2011.02.076.
- [Wu+57] C. S. Wu et al. “Experimental Test of Parity Conservation in Beta Decay.” In: *Physical Review* 105 (4 Feb. 1957), pp. 1413–1415. DOI: 10.1103/PhysRev.105.1413.
- [Yer+97] B. Yerozolimsky et al. “Corrigendum: Corrected value of the beta-emission asymmetry in the decay of polarized neutrons measured in 1990.” In: *Physics Letters B* 412.3–4 (1997), pp. 240–241. DOI: 10.1016/S0370-2693(97)01004-6.
- [You12] A. R. Young. “Radiative corrections to the β -asymmetry from effective field theory.” Private communication. Oct. 2012.
- [Yua06] Junhua Yuan. “Progress Towards a High Precision Measurement of the Neutron Spin–Electron Angular Correlation in Polarized Neutron β Decay with Ultra-Cold Neutrons.” PhD thesis. California Institute of Technology, 2006.
- [Yue+13] A. T. Yue et al. “Improved Determination of the Neutron Lifetime.” In: *Physical Review Letters* 111 (22 Nov. 2013), p. 222501. DOI: 10.1103/PhysRevLett.111.222501.
- [Zec12] B. W. Zeck. “MWPC Efficiency Update.” UCNA electronic logbook analysis note #459. Sept. 2012.
- [Zel59] Ya. B. Zel’dovich. “Storage of cold neutrons.” In: *Journal of Experimental and Theoretical Physics* 9 [ZETF 36] (June 1959), 1389–1390 [1952–1953].
- [Zwe64] G. Zweig. “An SU(3) Model for Strong Interaction Symmetry and its Breaking II.” In: *CERN-8419-TH-412* (1964).